

**The Relationships between Sea Surface Temperature Anomalies
and Clouds, Water Vapor and their Radiative Effects**

By
Thomas C. Peterson

Department of Atmospheric Science
Colorado State University
Fort Collins, Colorado



**Department of
Atmospheric Science**

Paper No. 482

THE RELATIONSHIPS BETWEEN SEA SURFACE
TEMPERATURE ANOMALIES AND CLOUDS, WATER VAPOR
AND THEIR RADIATIVE EFFECTS

by

Thomas C. Peterson

Department of Atmospheric Science
Colorado State University
Fort Collins, Colorado 80523

Summer, 1991

Atmospheric Science Paper No. 482

Research Supported by
NASA Grant NAG-1-865
and a NASA Global Change Fellowship

This paper was also submitted in partial fulfillment of the
requirements for the Degree of Doctor of Philosophy.

ABSTRACT

THE RELATIONSHIPS BETWEEN SEA SURFACE TEMPERATURE ANOMALIES AND CLOUDS, WATER VAPOR, AND THEIR RADIATIVE EFFECTS

An observational study of climatological relationships between sea surface temperature anomalies (SSTAs) and clouds, water vapor, and their radiative effects was conducted. The goal of this research project is to identify and quantify cloud and water vapor radiative feedback loops through an observational study, using sea surface temperature anomalies as a surrogate for global climate change. The relationship of an atmospheric variable to the SSTA was determined by using a Least Absolute Deviations (LAD) regression analysis between 6 year monthly anomaly data sets of both variables at each grid point over the open ocean. The slope of the LAD regression line was used to define the relationship. How well the LAD regression line represented the data was determined by using a Multivariate Randomized Block Permutation test to calculate the probability that data points better fitted to that LAD regression line could occur by random chance alone. These analyses were performed on anomaly data sets of: high, middle, low and total cloudiness; high, middle, low and total clear sky water vapor; albedo; reflected flux; outgoing longwave radiation (OLR); and net radiation. In addition, the relationships between these atmospheric variables and the El Niño–Southern Oscillation was examined. The radiative effects of the relationships between all three levels of clear sky water vapor anomalies and SSTAs was determined by using a two stream radiative transfer model at each grid point. Also, an in depth analysis of two months of data at three different locations was performed.

The results of this research indicate that there are strong, regionally varying relationships between SSTAs and cloud anomalies, water vapor anomalies, and their radiative

effects. In much of the tropics and South Pacific Convergence Zone, high clouds increased with increases in SSTA while in the subtropical stratocumulus regions low clouds decreased with increases in SSTAs. Averaged over the entire data set region, total cloudiness increased with increases in SSTAs. Yet, because optically thick low clouds decreased while optically thin high clouds increased, the average reflected flux decreased. Over most of the open ocean, clear sky water vapor increased at all levels in association with increases in SSTAs. The observed changes in water vapor high in the troposphere had the greatest radiative effect of any of the three layers of water vapor. However, the decrease in OLR caused by increases in clear sky water vapor was only a small portion of the change in OLR that occurred in association with increases in SSTAs. Net flux increased with increases in SSTAs in response to decreases in both OLR and reflected flux.

While this research does not attempt to predict SSTAs, the results can be used to predict changes in cloud, water vapor, and their radiative effects that should be associated with any given SSTA at any grid point. In addition, these results provide observational evidence in support of the position that both the cloud and water vapor radiative feedback loops, which are important in many global warming scenarios, are positive.

Thomas Carl Peterson
Department of Atmospheric Science
Colorado State University
Fort Collins, Colorado 80523
Summer 1991

ACKNOWLEDGEMENTS

I like to think that I work fairly independently. But when I look over this dissertation, I see the handiwork of many people. I'd like to gratefully acknowledge their contributions here, starting with my advisor, Professor Thomas Vonder Haar, and committee, Professors Paul Mielke, Jr., David A. Randall, and Wayne Schubert. Almost all the acknowledgements I've read in dissertations start out with thanks to their advisor and committee. I used to think this was just necessary politics, but no longer. Many times over the course of this research I've dropped in unannounced on my advisor or committee members seeking guidance, answers, or sometimes just reassurance on a course taken. They were always gracious and helpful. And I want them to know that not only their aid, but also the open armed nature in which it was offered, was very much appreciated.

Many other people, too, deserve clear acknowledgements and expressions of gratitude: Ian Wittmeyer for assistance with ISCCP TOVS data, Lola Olson of NASA Goddard Space Flight Center for her efforts to get me the sixth year of ISCCP TOVS data I needed in time for me to use it, Richard Reynolds and Diane Marsico of the Climate Analysis Center for supplying SST data, Dave Randel for various technical assistance especially regarding imaging, Paul Stackhouse for providing his two stream radiative transfer model along with assistance and advice on using it, Kelly Dean for assistance with data and programing, Andy Jones for the many day to day answers to specific programing and other problems that saved me months of time, Judy Sorbie-Dunn for assistance with figures, G. Garrett Campbell for too many different things to list here, and to family and friends for their encouragement.

This research was supported by NASA Grant NAG-1-865 and a NASA Global Change Fellowship.

TABLE OF CONTENTS

1	Introduction	1
2	Cloud – SSTA Relationships	8
2.1	Introduction	8
2.2	Data	10
2.2.1	Cloud	10
2.2.2	SST	13
2.3	Methods	14
2.4	Results	19
2.5	Discussion	41
3	Clear Sky Water Vapor – SSTA Relationships	46
3.1	Introduction	46
3.2	Data	48
3.2.1	Water Vapor	48
3.2.2	SST	54
3.3	Method	59
3.4	Results	59
3.5	Discussion	72
4	Basic Radiation Parameters – SSTA Relationships	77
4.1	Introduction	77
4.2	Data	78
4.2.1	Radiation Parameters	78
4.2.2	SST	78
4.3	Methods	80
4.4	Results	80
4.4.1	Albedo	80
4.4.2	Outgoing Longwave Radiation	94
4.4.3	Net Radiation	95
4.5	Discussion	100
5	Comparative Analysis of the Radiative Effects of Cloud–SSTA and Clear Sky Water Vapor–SSTA Relationships in Contributing to the Relationship between Outgoing Longwave Radiation and SSTA	111
5.1	Introduction	111
5.2	Methods	113
5.2.1	Data	113
5.2.2	The Two Stream Radiative Transfer Model	114

5.3	Results	124
5.3.1	Changes in Clear Sky OLR	124
5.3.2	Changes in OLR due to changes in clear sky OLR	133
5.3.3	The Contribution of Changes in Clear Sky OLR to changes in OLR	149
5.4	Discussion	150
6	ENSO Teleconnections and the Role of Circulation in Cloud–SSTA and Water Vapor–SSTA Relationships	155
6.1	Introduction	155
6.2	Data	157
6.3	Methods	158
6.4	Results	164
6.4.1	Global SSTA–ENSO	164
6.4.2	Clouds–ENSO	167
6.4.3	Water Vapor–ENSO	173
6.4.4	Basic Radiation Parameters–ENSO	179
6.5	Discussion	184
7	Case Study Analyses	186
7.1	Introduction	186
7.2	Data	187
7.3	Methods	191
7.4	Results	191
7.4.1	Region 1: California Stratocumulus Deck	193
7.4.2	Region 2: South Pacific Convergence Zone	198
7.4.3	Region 3: The Southeastern Pacific Ocean	206
7.5	Discussion	219
8	Summary and Conclusions	222
	References	227
	Appendix A: List of Acronyms and Abbreviations	235
	Appendix B: Statistical Techniques	237
B.1	LAD: Least Absolute Deviations	237
B.2	MRBP: Multivariate Randomized Block Permutation	238
B.3	Fisher’s Exact Test	239
	Appendix C: The Relationships between the Eastern Tropical Pacific SSTA and Global SSTAs, Clouds, Water Vapor, and Radiation Parameters	240
C.1	Introduction	240
C.2	Methods	240
C.3	Results	240
C.4	Discussion	241

LIST OF FIGURES

2.1	Distribution of surface marine <i>in situ</i> observations for the month of October 1986.	15
2.2	Sample grid point's cloud and SST anomaly data.	16
2.3	Probability versus LAD slope for total cloud-SSTA analysis.	18
2.4	Zonal averages of cloud-SSTA LAD slope.	21
2.5	Zonal averages of cloud-SSTA LAD slope for grid points with $P \leq 0.05$	22
2.6	Probability versus LAD slope for total cloud-SSTA analysis for both full data set analysis and analysis of June, July, and August.	25
2.7	Contour plot of Total Cloud-SSTA LAD slope.	26
2.8	Contour plot of Total Cloud-SSTA LAD slope for June, July, and August.	27
2.9	Contour plot of Total Cloud-SSTA LAD slope for December, January, and February.	28
2.10	Probability versus LAD slope for high cloud-SSTA analysis for both full data set analysis and analysis of June, July, and August.	29
2.11	Contour plot of High Cloud-SSTA LAD slope.	30
2.12	Contour plot of High Cloud-SSTA LAD slope for June, July, and August.	31
2.13	Contour plot of High Cloud-SSTA LAD slope for December, January, and February.	32
2.14	Probability versus LAD slope for Middle Cloud-SSTA analysis for both full data set analysis and analysis of June, July, and August.	33
2.15	Contour plot of Middle Cloud-SSTA LAD slope.	34
2.16	Contour plot of Middle Cloud-SSTA LAD slope for June, July, and August.	35
2.17	Contour plot of Middle Cloud-SSTA LAD slope for December, January, and February.	36
2.18	Probability versus LAD slope for Low Cloud-SSTA analysis for both full data set analysis and analysis of June, July, and August.	37
2.19	Contour plot of Low Cloud-SSTA LAD slope.	38
2.20	Contour plot of Low Cloud-SSTA LAD slope for June, July, and August.	39
2.21	Contour plot of Low Cloud-SSTA LAD slope for December, January, and February.	40
2.22	Total cloud cover versus Total Cloud-SSTA LAD slope.	42
3.1	Zonally averaged ISCCP TOVS water vapor - Total.	55
3.2	Zonally averaged ISCCP TOVS water vapor - Low.	56
3.3	Zonally averaged ISCCP TOVS water vapor - Middle.	57
3.4	Zonally averaged ISCCP TOVS water vapor - High.	58
3.5	Probability versus Total PW-SSTA LAD regression slope.	61
3.6	Probability versus Low PW-SSTA LAD regression slope.	62
3.7	Probability versus Middle Level PW-SSTA LAD regression slope.	63

3.8	Probability versus High PW–SSTA LAD regression slope.	64
3.9	Zonal averages of PW–SSTA LAD slopes.	66
3.10	Contour plot of Total PW–SSTA LAD regression slopes.	67
3.11	Contour plot of Low PW–SSTA LAD regression slopes.	68
3.12	Contour plot of Middle PW–SSTA LAD regression slopes.	69
3.13	Contour plot of High PW–SSTA LAD regression slopes.	70
3.14	Total, High, Middle, and Low Water Vapor–SSTA LAD slope versus SST. . . .	71
3.15	Four scatter plots of the relationship between water vapor–SSTA LAD slope values and cloud–SSTA LAD slope values.	73
4.1	Probability versus Albedo–SSTA LAD regression slope.	82
4.2	Contour plot of Albedo–SSTA LAD regression slope.	84
4.3	Contour plot of Albedo–SSTA LAD regression slope for June–July–August. . .	85
4.4	Contour plot of Albedo–SSTA LAD regression slope for December–January– February.	86
4.5	Probability versus Reflected Flux–SSTA LAD regression slope.	88
4.6	Contour plot of Reflected Flux–SSTA LAD regression slopes for full year analysis.	89
4.7	Contour plot of Reflected Flux–SSTA LAD regression slopes for analysis of March, April, and May.	90
4.8	Contour plot of Reflected Flux–SSTA LAD regression slopes for analysis of June, July, and August.	91
4.9	Contour plot of Reflected Flux–SSTA LAD regression slopes for analysis of September, October, November.	92
4.10	Contour plot of Reflected Flux–SSTA LAD regression slopes for analysis of December, January, and February.	93
4.11	Probability versus OLR–SSTA LAD regression slope.	96
4.12	Contour plot of OLR–SSTA LAD regression slopes.	97
4.13	Contour plot of OLR–SSTA LAD regression slope for June–July–August. . . .	98
4.14	Contour plot of OLR–SSTA LAD regression slope for December–January–February.	99
4.15	Probability versus Net Radiation–SSTA LAD regression slope.	101
4.16	Contour plot of Net Radiation–SSTA LAD regression slope.	102
4.17	Contour plot of Net Radiation–SSTA LAD regression slope for June–July–August.	103
4.18	Contour plot of Net Radiation–SSTA LAD regression slope for December– January–February.	104
4.19	Zonal average values for radiation–SSTA LAD analysis.	108
4.20	Zonal average values for radiation–SSTA LAD analysis for grid points with P ≤ 0.05	109
5.1	Zonally averaged top-of-the-atmosphere clear sky long wave flux from ERBS and model output.	120
5.2	ERBS clear sky long wave flux (top) and baseline model calculated long wave flux at the top of the atmosphere.	122
5.3	Difference between ERBS clear sky long wave flux and baseline model calcu- lated long wave flux at the top of the atmosphere.	123
5.4	The clear sky radiative effect of changes in water vapor as a function of latitude.	127
5.5	The clear sky radiative effect of changes in water vapor as a function of latitude for grid points with low P -values.	128

5.6	The change in clear sky greenhouse effect due to changes in total water vapor as a function of SST.	129
5.7	The change in clear sky greenhouse effect due to changes in high water vapor as a function of SST.	130
5.8	The change in clear sky greenhouse effect due to changes in middle level water vapor as a function of SST.	131
5.9	The change in clear sky greenhouse effect due to changes in low level water vapor as a function of SST.	132
5.10	Contour plot of the change in clear sky greenhouse effect due to changes in total water vapor.	134
5.11	Contour plot of the change in clear sky greenhouse effect due to changes in high water vapor.	135
5.12	Contour plot of the change in clear sky greenhouse effect due to changes in middle level water vapor.	136
5.13	Contour plot of the change in clear sky greenhouse effect due to changes in low level water vapor.	137
5.14	The radiative effect due to changes in water vapor as a function of latitude. . .	139
5.15	The radiative effect due to changes in water vapor as a function of latitude for grid points with low P-values.	140
5.16	The radiative effect due to changes in total water vapor as a function of SST. .	141
5.17	The radiative effect due to changes in high water vapor as a function of SST. .	142
5.18	The radiative effect due to changes in middle level water vapor as a function of SST.	143
5.19	The radiative effect due to changes in low level water vapor as a function of SST.	144
5.20	Contour plot of the change in greenhouse effect due to changes in total water vapor.	145
5.21	Contour plot of the change in greenhouse effect due to changes in high water vapor.	146
5.22	Contour plot of the change in greenhouse effect due to changes in middle level water vapor.	147
5.23	Contour plot of the change in greenhouse effect due to changes in low level water vapor.	148
5.24	The percent of the change in OLR due to changes in clear sky water vapor versus SST.	151
5.25	Contour plot of the percent of change in OLR due to changes in clear sky water vapor.	152
6.1	Eastern tropical Pacific SST Anomalies and SOI for Nimbus-7 cloud data set times.	159
6.2	Eastern tropical Pacific SST Anomalies and SOI for ISCCP TOVS water vapor data set times.	160
6.3	The number of grid points with low P-values associated with the SOI at various lags and leads, for Total Clouds and SSTA.	162
6.4	The number of grid points with low P-values associated with the SOI at various lags and leads, for Total Water Vapor and SSTA.	163
6.5	Contour plot of the LAD slope from the analysis between SSTA and the SOI for times corresponding to the Nimbus-7 cloud data set.	165

6.6	Contour plot of the LAD slope from the analysis between SSTA and the SOI for times corresponding to the ISCCP TOVS water vapor data set.	166
6.7	Contour plot of the LAD slope from the analysis between total cloudiness and the SOI.	168
6.8	Contour plot of the LAD slope from the analysis between high clouds and the SOI.	169
6.9	Contour plot of the LAD slope from the analysis between middle level clouds and the SOI.	170
6.10	Contour plot of the LAD slope from the analysis between low clouds and the SOI.	171
6.11	Contour plot of the LAD slope from the analysis between total water vapor and the SOI.	174
6.12	Contour plot of the LAD slope from the analysis between high water vapor and the SOI.	175
6.13	Contour plot of the LAD slope from the analysis between middle level water vapor and the SOI.	176
6.14	Contour plot of the LAD slope from the analysis between low water vapor and the SOI.	177
6.15	Contour plot of the LAD slope from the analysis between OLR and the SOI. .	180
6.16	Contour plot of the LAD slope from the analysis between reflected flux and the SOI.	181
6.17	Contour plot of the LAD slope from the analysis between net flux and the SOI.	182
7.1	Case study regions.	192
7.2	Average conditions in region one.	194
7.3	LAD slope and probability for cloud-SSTA and PW-SSTA relationships at case study region one.	196
7.4	The difference in observed clouds, clear sky precipitable water, and SST between March 1984 and March 1985 at case study region one.	197
7.5	Average low clouds and the difference between March 1984 and March 1985 low clouds as a function of time of day for the westernmost part of case study region 1.	199
7.6	Comparison of optical thickness of low clouds between March 1984 and March 1985 in case study region 1.	200
7.7	Average conditions in region two.	202
7.8	LAD slope and probability for cloud-SSTA and PW-SSTA relationships at case study region two.	203
7.9	The difference in observed clouds, clear sky precipitable water, and SST between March 1984 and March 1985 at case study region two.	205
7.10	Average high clouds and the difference between March 1984 and March 1985 high clouds as a function of time of day for the central part of case study region 1.	207
7.11	Comparison of optical thickness of high clouds between March 1984 and March 1985 in case study region 2.	208
7.12	Average conditions in region three.	209
7.13	LAD slope and probability for PW-SSTA relationships at case study region three.	211

7.14	The difference in observed clouds, clear sky precipitable water, and SST between March 1984 and March 1985 at case study region three.	212
7.15	Values for low water vapor-SSTA LAD slopes, probability, and grid points removed from analysis due to land or ice for a zonal band at 56.25°S.	214
7.16	Average Total Clouds, Low Clouds, Low Precipitable Water, and SST along the 56.25°S latitude band.	215
7.17	Number of TOVS soundings and type of SST analysis along the latitude band centered at 56.25°S.	217
7.18	Standard deviations of low level clear sky water vapor and SST for the latitude band centered at 56.25°S.	218
C.1	A global plot of the slope of the LAD analysis of total clouds and the eastern tropical Pacific SSTA analyzed with the atmospheric variable leading 4 months ahead of the SSTA.	242
C.2	A global plot of the slope of the LAD analysis of total clouds and the eastern tropical Pacific SSTA analyzed with the atmospheric variable lagging 4 months behind the SSTA.	243
C.3	A global plot of the slope of the LAD analysis of total clouds and the eastern tropical Pacific SSTA analyzed with the atmospheric variable lagging 2 months behind the SSTA.	244
C.4	A global plot of the slope of the LAD analysis of total water vapor and the eastern tropical Pacific SSTA analyzed with the atmospheric variable leading 4 months ahead of the SSTA.	245
C.5	A global plot of the slope of the LAD analysis of total water vapor and the eastern tropical Pacific SSTA analyzed with the atmospheric variable lagging 4 months behind the SSTA.	246
C.6	A global plot of the slope of the LAD analysis of total water vapor and the eastern tropical Pacific SSTA analyzed with the atmospheric variable lagging 2 months behind the SSTA.	247
C.7	A global plot of the slope of the LAD analysis of global SSTAs and the eastern tropical Pacific SSTA analyzed with the global SSTAs lagging 2 months behind the eastern tropical Pacific SSTA for the time period corresponding to the Nimbus-7 cloud data set.	248
C.8	A global plot of the slope of the LAD analysis of global SSTAs and the eastern tropical Pacific SSTA analyzed with the global SSTA lagging 2 months behind the tropical SSTA for the time period corresponding to the ISCCP TOVS water vapor data set.	249
C.9	A global plot of the slope of the LAD analysis of high clouds and the eastern tropical Pacific SSTA analyzed with the atmospheric variable lagging 2 months behind the SSTA.	250
C.10	A global plot of the slope of the LAD analysis of middle clouds and the eastern tropical Pacific SSTA analyzed with the atmospheric variable lagging 2 months behind the SSTA.	251
C.11	A global plot of the slope of the LAD analysis of low clouds and the eastern tropical Pacific SSTA analyzed with the atmospheric variable lagging 2 months behind the SSTA.	252

C.12	A global plot of the slope of the LAD analysis of high water vapor and the eastern tropical Pacific SSTA analyzed with the atmospheric variable lagging 2 months behind the SSTA.	253
C.13	A global plot of the slope of the LAD analysis of middle water vapor and the eastern tropical Pacific SSTA analyzed with the atmospheric variable lagging 2 months behind the SSTA.	254
C.14	A global plot of the slope of the LAD analysis of low water vapor and the eastern tropical Pacific SSTA analyzed with the atmospheric variable lagging 2 months behind the SSTA.	255
C.15	A global plot of the slope of the LAD analysis of albedo and the eastern tropical Pacific SSTA analyzed with the radiation variable lagging 2 months behind the SSTA.	256
C.16	A global plot of the slope of the LAD analysis of reflected flux and the eastern tropical Pacific SSTA analyzed with the radiation variable lagging 2 months behind the SSTA.	257
C.17	A global plot of the slope of the LAD analysis of OLR and the eastern tropical Pacific SSTA analyzed with the radiation variable lagging 2 months behind the SSTA.	258
C.18	A global plot of the slope of the LAD analysis of net radiation and the eastern tropical Pacific SSTA analyzed with the radiation variable lagging 2 months behind the SSTA.	259

LIST OF TABLES

2.1	Average LAD slope values for total, high, middle, and low clouds–SSTA LAD analysis.	20
3.1	Average PW–SSTA LAD	60
3.2	Percentage of grid points with low P-values.	60
4.1	Nimbus-7 Earth Radiation Budget instrument channels.	79
4.2	Area averaged values of the Albedo–SSTA LAD regression slope.	81
4.3	Area averaged values of the Reflected Flux–SSTA LAD regression slope.	94
4.4	Area averaged values of the OLR–SSTA LAD regression slope.	95
4.5	Area averaged values of the Net Radiation–SSTA LAD regression slope.	100
4.6	Summation of area averaged values of LAD regression slopes.	105
4.7	Summation of area averaged values of LAD regression slopes for grid points with $P \leq 0.05$	105
5.1	Model bands.	117
5.2	Comparison of model runs.	119
5.3	Model sensitivity to baseline water vapor.	125
5.4	Average change in clear sky greenhouse effect due to water vapor changes associated with 1°C increase in SSTA.	125
5.5	Average change in greenhouse effect due to water vapor changes associated with 1°C increase in SSTA.	138
5.6	Comparison of the radiative effect of change in clear sky water vapor to the change in OLR.	150
6.1	Number of cloud LAD analysis grid points with P-value ≤ 0.05	172
6.2	Number of water vapor LAD analysis grid points with P-value ≤ 0.05	178
6.3	Number of radiation parameter LAD analysis grid points with P-value ≤ 0.05	183
B.1	A 2 x 2 Cross-classification Table.	239

Chapter 1

INTRODUCTION

The climate is changing. Of that there is little doubt. A cursory look at historical climatology reveals a global climate that is always in flux, with climate changes occurring on many different time scales:

~1 year — we observe the El Niño affecting the lives of fishermen off the coast of Peru and through teleconnections many other people around the globe (Philander, 1990).

~10 years — we observe fluctuations in the Sahel rainfall that can bring famine to Africa and alter hurricane landfall frequency on the U.S. eastern seaboard (Gray, 1990b).

~100 years — we have records of climatic events such as “the little ice age” that affected Europe from the 13th to 18th Century (Bryson, 1977).

~1000+ years — there are the true ice ages with glacial ice a mile thick in Wisconsin and warm periods such as the Alleröd Epoch (Budyko, 1982).

Currently the atmospheric science community and, indeed, much of the world is involved in a debate over CO₂ induced climate change: Will the anthropogenic increases in CO₂ cause global warming? How much warming? Where? When? What will be the human costs or benefits? What policy changes could be enacted that would moderate the effects? What are the cost/benefit ratios of such policies?

That CO₂ can cause warming is not debated. Carbon dioxide is a greenhouse gas. It allows the transmittance of most short wave solar energy through the atmosphere, but absorbs some long wave energy radiated up from the earth. The more CO₂, the more IR energy is absorbed. The greater the greenhouse effect, the higher the surface temperature needed to obtain the earth-atmosphere’s radiative equilibrium temperature. Hence, the earth’s surface will warm until the earth-atmosphere system radiates out to space the

same amount of energy that it absorbs from the sun. There is little question about this, as Schneider says, “The future is . . . based on physics” (Kerr, 1989).

However, the exact physics are debated. The first question is the importance of an incremental increase in CO₂. Carbon dioxide is a minor atmospheric constituent (about 0.03%). Pre-industrial concentrations of about 270-280 ppm have increased to about 350 ppm. This is a large percentage increase, but it is still only a small fraction of the atmosphere. In addition, the radiative effect of any IR absorbing gas is logarithmic so that each additional incremental increase in CO₂ produces progressively less radiative effect. Though several other anthropogenic gases, such as methane, also have a distinct greenhouse effect, the actual radiative impact of projected increases in all the anthropogenic greenhouse gases is fairly small, certainly nowhere near large enough to directly cause the major warming predicted in some of the global warming scenarios. This predicted warming is achieved through various positive feedback loops.

The feedbacks are where the physics get most interesting and most debated. There are two prime atmospheric variables which cause radiative feedback loops: water vapor and clouds. These two feedback loops produce one-half to four-fifths of the predicted warming due to a doubling of CO₂ (Lindzen, 1990a). The essence of these loops are: atmospheric and surface temperature changes caused by increases in carbon dioxide, methane, and other anthropogenic greenhouse gases cause changes in evaporation and condensation which alter the water vapor and clouds in the atmosphere. Changes in atmospheric water vapor have clearly understood radiative effects: increases in the water vapor content of any layer of the atmosphere increases the greenhouse effect. Yet, changes in total column water vapor produce different changes in the greenhouse effect depending on the vertical distribution of the water vapor changes. For example, “even though water vapor near the ground increases with increasing temperature, a smaller absolute decrease at upper levels can lead to a negative feedback” (Lindzen, 1990b). Changes in clouds, on the other hand, do not have such simple radiative effects because clouds reflect solar radiation as well as absorb and re-radiate IR radiation. The cloud albedo depends on cloud phase (ice or water), particle size, particle concentrations, cloud thickness, and cloud structure. In

addition, the radiative effect of changes in cloud albedo also depends on the albedo of the Earth's surface below the cloud. The IR impact is primarily a function of cloud elevation (temperature) and cloud thickness. Various combinations of these factors can result in positive or negative cloud radiative feedbacks. Furthermore, there is a close —yet not exact— relationship between changes in water vapor and changes in clouds.

Most of the analysis of these global warming feedback loops comes from general circulation model (GCM) and other numerical experiments. While there is often strong agreement between different GCM experiment results, this does not stop the debate. One criticism of using GCMs in analysis of cloud feedback loops is that the GCM may have the right amount of clouds in the baseline simulation but for the wrong reasons, in which case changes in clouds could not be reliably predicted (Campbell, 1990). Even if the correct clouds are present in the model for the correct reasons, their optical thickness might not be correct. An example that illustrates the importance of this concern is a fairly recent change in the British Meteorological Office's climate model's ice content of layer clouds which reduced its predicted warming in response to doubling of CO₂ by 60% (Lindzen, 1990a). "Most scientists view the cloud radiative feedback problem to be the 'Achilles Heel' of GCMs" (Cotton, 1991). However, the water vapor feedback loop "is the most important positive feedback in current large scale climate models —despite the popular emphasis on feedbacks from cloud cover" (Lindzen, 1990b). Much of the atmosphere's response to surface heating, such as cumulus convection, is, by necessity, a sub-grid scale process for GCMs and therefore must be parameterized. Convective parameterizations tend to moisten the atmosphere at all levels, creating a positive water vapor radiative feedback. While such parameterizations are the modelers' best representation of the physics of the earth-atmosphere system, the appropriateness of some of the effects of such parameterizations are debated (Lindzen, 1990a).

There are also possible effects relevant to global warming scenarios that are too poorly understood to be included in GCMs. For example, Charlson *et al.* (1987) proposed a link between oceanic phytoplankton, atmospheric sulphur, cloud albedo, and climate. In keeping with the assumption of negative feedback loops inherent in the Gaia theory

(Lovelock, 1979, 1986), they see a possible negative feedback loop starting with increases (decreases) in sea surface temperature anomalies (SSTAs) which increases (decreases) the growth of oceanic phytoplankton which in turn increases (decreases) their excretion of dimethylsulphide which increases (decreases) the escape of oceanic dimethylsulphide into the atmosphere where the dimethylsulphide reacts to form sulphate and methane sulphonate aerosol which act as cloud condensation nuclei (CCN). This increase (decrease) in CCN would then make the clouds more reflective by increasing (decreasing) droplet concentrations and decreasing (increasing) droplet size which decreases (increases) the incident solar radiation entering the ocean which in turn decreases (increases) the SSTA thereby completing the negative feedback loop. The current state of our understanding of ocean-atmosphere-biosphere interactions makes much of this hypothesis speculative and an error in any one link in this long chain can nullify the whole hypothesis. However, to the extent that the time scales of this and other possible Gaia theory related negative feedback loops are within the time scales of the observations, these feedback loops would be included in an observational analysis though they may not be able to be isolated and understood.

The radiative effect of all potential cloud and water vapor feedback loops in global climate change may someday be understood through joint observations and modeling. In the meantime, can cloud and water vapor feedback loops can be examined observationally through an analogy to CO₂ induced global warming? Over land, the hydrologic cycle is greatly affected by vegetation. Since vegetation might change drastically in response to global warming, any currently available observational analogies over land will be missing this major component. However, over the ocean the hydrologic cycle is not greatly affected by vegetation. Therefore, simply using sea surface temperatures (SST), one can draw an analogy to global warming.

Raval and Ramanathan (1989) did just that. They looked at the clear sky greenhouse effect versus SST and found that there is a larger greenhouse effect over warmer waters. The implication they see is that "the coupling between surface temperature and the greenhouse effect will lead to a strong positive feedback on any perturbations to the

present climate.” The problem with their analogy, however, is that they are essentially drawing an analogy between latitude and global warming. Since SSTs generally increase as one moves equatorward, their analogy and the implications they draw from it indicate that they expect the greenhouse effect at a location at 40°N, would change, due to CO₂ induced global warming, to be like the greenhouse effect at a location perhaps 38°N. While this may indeed be correct, there are basic general circulation characteristics that such an analogy cannot take into account.

The research presented in this paper is an observational study of the cloud and water vapor feedback loops that uses a very different analogy. Instead of implying that the effect of global warming is similar to moving equatorward, our analogy is that global warming is similar to the warmer than average times at that location. While it is most likely a major error to assume that CO₂ induced global warming would warm all locations over the ocean, the relationships we determine between local SSTAs and radiative feedbacks could be used with any positive or negative SST predictions for that area: use of this analogy does not commit us to the assumption that all locations over the ocean would warm.

The goal of this research is to use this analogy to identify geographical variation of the changes in cloud and water vapor that are associated with sea surface temperature anomalies and then to quantify their radiative effects. In order to make use of this analogy, we needed long term data sets. Therefore, all of our data sets were 72 months long. From these long term data sets, monthly anomaly data sets were created based on the average value for each of the 12 months of the year. The relationship between, for example, cloud anomalies and SSTAs, was determined using a Least Absolute Deviations (LAD) regression analysis between the two anomaly data sets at each grid point. The slope of the regression line defined the relationship between the two variables. How well the LAD regression line represented the data was determined by using a Multivariate Randomized Block Permutation (MRBP) test to calculate the probability (P) that data points better fitted to that LAD regression line could occur by random chance. (Appendix A is a list of frequently used acronyms and abbreviations.)

The first step of this research was to determine the relationship between clouds at various levels and SSTA. This analysis indicated several regions of strong cloud anomaly-SSTA relationships. For example, in much of the tropics, high clouds increase with increasing SSTA while in the subtropical stratocumulus decks, low clouds decreased with increasing SSTA. Next, the relationship between water vapor at various levels and SSTA was examined. For almost the entire global ocean, clear sky water vapor increased with increasing SSTA. Unfortunately, concurrent cloud and water vapor data sets were not available. Therefore, relationships between cloud anomalies and clear sky water vapor anomalies could not be directly determined. However, indirect analysis could be used. For example, in regions where high clouds increased with increasing SSTA, clear sky water vapor high in the troposphere also increased with increasing SSTA.

Using basic radiation parameters, the radiative effects of both of these relationships were examined. As one would expect, outgoing longwave radiation (OLR) decreased with increasing SSTA in regions where high clouds increased with increasing SSTA. However, some or all of this decrease in OLR was compensated for by increases in reflected flux due to increases in albedo. The most important radiation parameter, net flux, showed the strongest response to SSTAs in the subtropical stratocumulus decks where low clouds decreased with increases in SSTA with a change in net flux as high as $8 \text{ W}\cdot\text{m}^{-2}\cdot\text{K}^{-1}$. This is where the positive radiative feedback was the greatest. The magnitude of greenhouse effect due to changes in clear sky water vapor associated with increases in SSTA was determined by applying a two stream radiative transfer model to results from the water vapor-SSTA LAD analyses at each grid point and was found to be about $0.75 \text{ W}\cdot\text{m}^{-2}\cdot\text{K}^{-1}$ or only about 13% of the magnitude of the total change in OLR per degree of SSTA.

These analyses allow for an observational quantification of the cloud and water vapor radiative feedbacks, as related to SSTA, throughout the global oceans. However, before drawing general conclusions from these analyses, two additional questions needed to be addressed. The first question is how much of these results are caused by altered circulation and how much are caused by local effects of SSTAs. This question is addressed in Chapter 6 with the answer being that the observed effect is related to local SSTAs only or in regions

where SSTAs and altered circulation are closely related, such as the eastern tropical Pacific, it is impossible to isolate the two different effects. The second question involves the scale of the interactions. For example, in the South Pacific Convergence Zone (SPCZ) high clouds are found to increase with increasing SSTAs. If this relationship is a very localized phenomena, where high clouds decrease at one grid point while they increase at the next grid point in response to gradients in SSTAs, then the cloud feedback when averaged over a large region may be negligible and the results of the research may not be relevant to large scale CO₂ induced warming of the ocean surface. Examination of this question in the case study analyses presented in Chapter 7 reveals that the observed interactions are large scale phenomena: that even if averaged over a large region, which the global warming–positive SSTA analogy implies, the feedback would still be apparent.

Therefore, the observational analogy to global climate change used for this research, while not perfect by any means, does have some validity. However, ocean surface temperature changes resulting from increased CO₂ depend not only on the direct radiative effects of CO₂ and the associated cloud and water vapor feedbacks, but also on the changes in global circulation. Clearly in regions of coastal upwelling, changes in winds can have much greater effect on SST than changes in net radiation. This research does not attempt to predict SST. That we will leave to coupled ocean–atmosphere circulation models. What this research can indicate, in a very quantitative fashion, is what changes in clouds, water vapor and their radiative effects a GCM should see for any particular SSTA at any particular place in the global ocean. On a near global average though, this observational research supports the global warming scenario that warming of the ocean surface will produce cloud and water vapor changes that lead to positive radiative feedbacks.

Chapter 2

CLOUD – SSTA RELATIONSHIPS

2.1 Introduction

The cloud radiative feedback loop is widely considered to be important in global climate change, including global warming. “The size of the observed net cloud forcing is about four times as large as the expected value of radiative forcing from a doubling of CO₂. The shortwave and longwave components of cloud forcing are about ten times as large as those for a CO₂ doubling. Hence, small changes in the cloud-radiative forcing fields can play a significant role as a climate feedback mechanism” (Ramanathan *et al.*, 1989). Furthermore, modeling work such as that by Slingo (1990) determined that top-of-the-atmosphere radiative forcing by doubled carbon dioxide concentration could be balanced by modest absolute increases of ~3.5-5.0% in amount of low clouds. Therefore, a prime question that needs to be answered is: what would be the response of low and all other clouds to global warming induced by increases in carbon dioxide and other greenhouse gases?

General circulation model (GCM) studies have tried to answer this question through theory and numerical simulation. Rather than looking at GCM results from a doubled CO₂ simulation, Cess *et al.* (1990) compared the response of 19 atmospheric GCMs to changes in the fixed ocean temperature. Their results showed that for a +2°C SSTA simulation minus the –2°C SSTA simulation the average change in cloudiness was –2.1%. This means that for every degree C that the ocean warms, the average cloudiness decreases ~0.5%. The models’ results did range from –4.4% to –0.3% for the difference between the two simulations. But all 19 models showed a decrease. The results of this study “show that the gross climate sensitivities of the various models range over about a factor of three, but

that virtually all of these differences can be accounted for by differences in cloud feedbacks produced by the various models. . . . Even before the GCM Intercomparison Project results were analyzed, many researchers had concluded that uncertainties about the effects of clouds are a key obstacle to reliable quantitative climate change predictions (Charney, 1979)” (Randall, 1990a).

Mokhov’s (1985, 1990a, 1990b) observational studies of the relationship between total cloud amount and surface temperature found quite different results than the GCM numerical experiments. He found that on a hemispheric average there was a general tendency for total cloud amount to increase with an increase in surface temperature (Mokhov, 1985). On a zonally averaged basis in the Northern Hemisphere over oceans, Mokhov (1990a, 1990b) reported a decrease in total cloud amount associated with increases in surface temperatures between 58°N and 22°N. His minimum zonal average linear regression value of $\sim -1\% \cdot K^{-1}$ was at 35°N. Equatorward of 22°N, total cloud amount increased in association with increases in surface temperatures with a maximum zonal average value of $\sim 1\% \cdot K^{-1}$ at 10°N. At the equator, his zonal average linear regression value was 0.

As part of a continuing effort to better understand cloud changes in response to changes in SST this research performs a similar observational analysis. Observational analyses can be complimentary to the numerical simulations with data providing factual information about the ocean/atmosphere system. However, there are distinct limits to the global applicability of the results from the observational analogy to global warming used in this research. For example, the entire global ocean never has a uniform $+2^{\circ}C$ SSTA for a year followed by a $-2^{\circ}C$ SSTA for a year, so we have had to use the naturally occurring local SSTA in our analysis. Since a positive SSTA at any particular location may be related to a negative SSTA at another location, the atmospheric effects we see associated with the positive SSTA may be related to the changes in both locations and therefore would not be totally indicative of warming over the entire ocean.

Even knowing the changes in the percent of cloudiness associated with changes in SSTAs will not answer all the questions about the radiative effects of these changes. For example, the sign of the net radiative effect of cirrus clouds varies with their optical

depth and location. “Generally, tropical and mid-latitude cirrus clouds cause a warming effect until the optical depths become large. For optical depths greater than about 12 for tropical cirrus, and about 5 for mid-latitude cirrus, an increase in cloud will cause a cooling tendency” (Platt, 1981). In Chapter 4 we will look at changes in the basic radiation parameters including net radiation and in Chapter 5 we will address the question of how much of the observed radiative effects are due to changes in clouds and how much are due to changes in clear sky water vapor. However, the analysis presented in this chapter will be crucial in providing a physical interpretation for the observed changes in radiation.

2.2 Data

2.2.1 Cloud

The cloud data set used in this study is the percentage of cloud cover derived from the polar orbiting Nimbus-7 satellite’s Temperature Humidity Infrared Radiometer (THIR) and Total Ozone Mapping Spectrometer (TOMS) data. The following description of this data set is gleaned from Stowe *et al.* (1988):

For the cloud data set, the relevant one of the two channels that the THIR scanning radiometer measures is the 11.5 μm (10.5 to 12.5 μm) window channel. Ground resolution at the sub-satellite point for this channel is 6.7 kilometers. At a nadir angle of 50°, where interorbit coverage is achieved at the equator, the ground resolution is 13 x 24 km.

The TOMS instrument is a single monochromator whose field of view (FOV) is scanned perpendicularly to the orbital plane through the satellite subpoint by a rotating mirror. The TOMS FOV is 50 x 50 km at nadir and increases to 150 x 200 km at the extreme off nadir position. The UV backscattered radiation is measured at six wavelengths from 0.313 to 0.380 μm sequentially in three-degree steps along the scan, which spans 51 degrees to either side of nadir (Heath *et al.*, 1978). The 0.360 and 0.380 μm wavelengths, which are not absorbed by ozone, are included to provide an estimate of the UV reflectivity of a surface below or within the atmosphere. Measurements are also made of the incoming solar irradiance at these wavelengths, which are used to compute directional albedos from the backscattered radiances. The estimate of reflectivity at these two wavelengths are then averaged to create a 0.37 μm UV surface reflectivity.

Three of the data fields used in the Air Force 3-D Cloud Nephanalysis (Fye, 1978) are used in the Nimbus-7 cloud analysis, but the only one used in the domain of our research is the Surface Temperature Analysis. Over water, the analysis uses sea surface temperature measurements reported by ships every six hours and by satellite remote sensing, twice daily. Initially, a five-layer atmospheric general circulation model is used to analyze the state of the atmosphere at a grid resolution of 320 km. This analysis is interpolated to a resolution of 160 km, and climatological lapse rates are used to extrapolate the temperature from the gradient level (60 hPa above the surface) to the surface. Empirically derived diurnal temperature corrections are then applied to the surface temperature field.

Two independent cloud detection algorithms are combined by a bispectral algorithm into one value of cloud amount. The infrared algorithm is a threshold technique based on the 11.5 μm radiance. In this technique, the Air Force surface temperature is converted into an equivalent blackbody radiative temperature (i.e., the expected clear-sky temperature that should be detected by the 11.5 μm channel of THIR when no clouds are within its FOV) by subtracting an empirical atmospheric water vapor attenuation adjustment. This adjustment was derived from collocated and concurrent observations of sea surface temperature and 11.5 μm radiance data from a NOAA scanning radiometer (Brower *et al.*, 1976). Since the standard deviations of the Air Force surface temperatures at local noon and midnight, the time of the Nimbus-7 overpasses, are “near zero” for open ocean areas, the cloud/no cloud threshold could be set close to the surface temperature. However, a close to surface temperature cloud/no cloud threshold will result in a systematic overestimation cloud amount because when cloud elements are smaller than the FOV of the radiometer the scene will be classified as totally cloud covered. Therefore, a modification was made to the cloud/no cloud threshold to adjust for this error. The low/mid cloud threshold is based on the climatological lapse rate between the surface and 2 km altitude for the appropriate month as computed from the NCAR monthly climatology (Jenne *et al.*, 1974). The mid/high cloud threshold is similarly calculated except the altitude is 7 km for latitudes between 0 and 30 degrees, 6 km for latitudes between 30 and 60 degrees, and 4 km for latitudes greater than 60 degrees.

One advantage of UV surface reflectivity is that it is much less dependent on solar illumination angle and satellite viewing angle than is the visible. This is due to stronger Rayleigh scattering at $0.37 \mu\text{m}$, which diffuses much of the UV that reaches the surface, and upon reflection, scatters the UV again in passing through the atmosphere before being sensed by the satellite. Clear scene ocean reflectivities are 6-8%. A reflectivity of 8% was therefore chosen to represent 0% cloud amount with a linear relationship from 8% to 50% reflectivity corresponding to a 0% to 100% cloud amount range.

The UV reflectivity is affected by cloud thickness, however this is of minor concern because the bispectral algorithm mainly uses the UV cloud amount estimate as a correction for the IR algorithm when the latter indicates that either low clouds or no clouds are present. Low clouds are relatively easy for the UV to detect accurately because of the large contrast between reflectance of the ice-free surface and the low clouds. The actual process of the bispectral cloud algorithm involves a weighting of the cloud amounts from the two algorithms with the weighting factors decreasing the influence of the UV reflectivities as the satellite zenith angle increases. When the UV algorithm indicates less clouds than the IR algorithm, the IR algorithm's low, then middle and then high clouds amounts, in that order, are decreased to agree with the bispectral total clouds amount. When the UV algorithm indicates more cloud than the IR algorithm, the IR algorithm's low cloud amount is increased so that, when added to the IR estimates of middle and high cloud amount, agrees with the bispectral algorithm's total cloud amounts.

Based on a theoretical sensitivity analysis and on an empirical comparison between cloud amount estimated by an analyst, using GOES images and auxiliary meteorological data, and by the Nimbus-7 algorithms, the systematic errors of the Nimbus-7 estimates, relative to the analyst, are less than 10% and the random errors range from 7% to 16%. The errors of the satellite cloud estimates may be lower than these estimates since the analyst contributes systematic and random error to the comparison. The UV algorithm rarely causes the bispectral algorithm results to depart by more than 10% from the IR algorithm. Thus, the nighttime cloud estimates, which use the IR algorithm solely, should only be slightly less accurate than the daytime estimates, with the exception of geographical regions where low level cloud systems are prevalent, e.g., the west coast of subtropical

continents where the marine stratocumulus tend to be underestimated at night. However, since this research uses anomalies rather than the actual cloud amounts, a minor bias in the average cloud amount does not have much impact on this research.

The analysis from 9 sub-target areas (~ 165 km x 165 km) are averaged into the value for the ~ 500 km x 500 km target area twice a day. Each target area spans 4.5° of latitude while the longitude varies, with the longitude interval starting at 4.5° near the equator and increasing poleward with the longitude interval being 9.0° at 60° N. These target area values are then averaged into monthly values. This data set of monthly averaged percent cloud cover by high, middle, low, and total clouds is available for 72 months, from April 1979 through March 1985. These six years are an interesting time to study cloud-SSTA relationships because they include the strong 1982 ENSO event.

2.2.2 SST

Since the cloud data set is derived from satellite measurements, we felt it was important to use a SST data set that is grounded with *in situ* data to avoid any dependent relationships between algorithms to derive SST from satellite observations in cloudy conditions and the clouds we are going to relate to the SST. For this reason we used the Climate Analysis Center's (CAC) monthly averaged SST data set. During the early part of the Nimbus-7 data set, the CAC's SST data set is based solely on *in situ* data from ships and buoys and extends only from 60° North to 40° South. Starting in January 1982, CAC's SST analysis was blended with satellite data and covers the entire globe. These data are on a $2^\circ \times 2^\circ$ grid.

Figure 2.1 gives an example of one month's *in situ* surface observations. After initial quality control checks are done on these surface observations the remaining approximately 100,000 *in situ* observations for the month are used to compute an initial gridded field. This initial grid undergoes more screening tests and spacial filtering before the final *in situ* SST grid is created. A satellite SST grid is created in much the same manner which is then blended with *in situ* data by "using the *in situ* analysis to define 'benchmark' temperature values in regions of frequent *in situ* observations and the satellite analysis to define the shape of the field in regions with little or no *in situ* data" (Reynolds, 1988).

Verification of both the *in situ* and blended *in situ*-satellite SST data was performed using quality-controlled drifting buoy data. The results show that the modulus of the monthly buoy-to-analysis biases (i.e., the average of the absolute value of the monthly biases) was 0.15 °C for *in situ* analysis and 0.09 °C for blended analysis (Reynolds, 1988).

2.3 Methods

The first step in the analysis procedure was to create anomaly data sets from both the cloud data and the SST data. These anomalies are monthly, based on the average value for that month for the six years from April 1979 through March 1985. For example, the average percentage of low cloud amount for January was calculated at each grid point from the 6 Januaries in the data set. From this average, anomaly values of percentage of low cloud amount were calculated at each grid point for each of the 6 Januaries. For the SST anomaly data set, after the monthly averages and anomalies were calculated on CAC's 2 x 2 degree grid, the final step was to regrid the data to produce a weighted average anomaly value for the center of each of the Nimbus-7 4.5° x 4.5° grid boxes (500 x 500 km at the equator).

The relationship between each grid point's SST anomaly and the overlying cloud anomaly was defined by using a Least Absolute Deviations (LAD) regression analysis (Narula and Wellington, 1982; Seneta, 1983). The choice of LAD rather than Least Square Deviations (LSD) regression analysis, which includes the orthogonal eigenvector approach, is simply to avoid the overwhelming influence on LSD regression analyses by a very few substantial deviations (Wong *et al.*, 1989). (For details on LAD and other statistical techniques used in this research, see Appendix B.) In the total cloud-SSTA LAD analysis, for example, the 72 pairs (one pair for each month in the data set) of total cloud and SST anomalies at each grid point have a LAD regression analysis performed on them as shown in Figure 2.2. The units of the LAD regression slope are the increase (+) or decrease (-) of cloud anomaly in percent of cloud cover per 1 degree C increase in SST anomaly. The slope of the LAD regression analysis defines the cloud anomaly-SST anomaly relationship and can be plotted on maps. For a seasonal analysis, 18 pairs of data points go into each grid point's LAD analysis instead of 72.

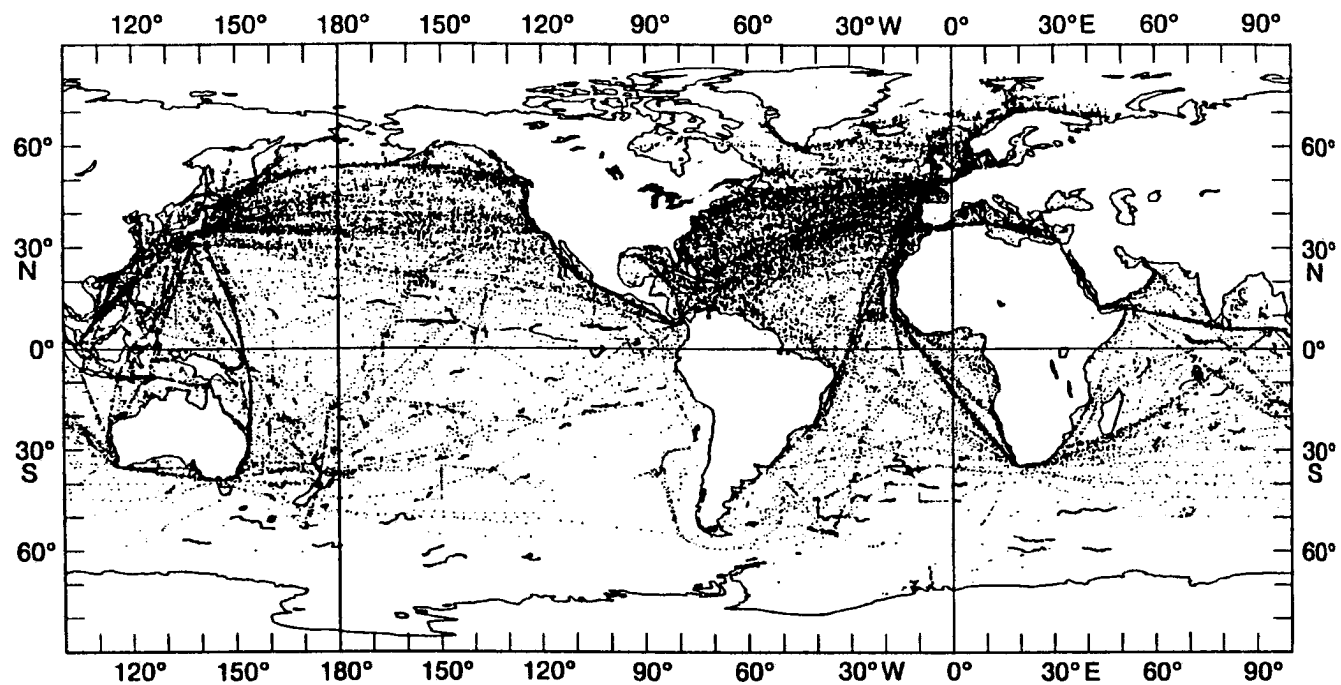


Figure 2.1: Distribution of the surface marine *in situ* observations for the month of October 1986. Drifting buoys may be distinguished as nearly continuous wiggly lines. From Reynolds (1988).

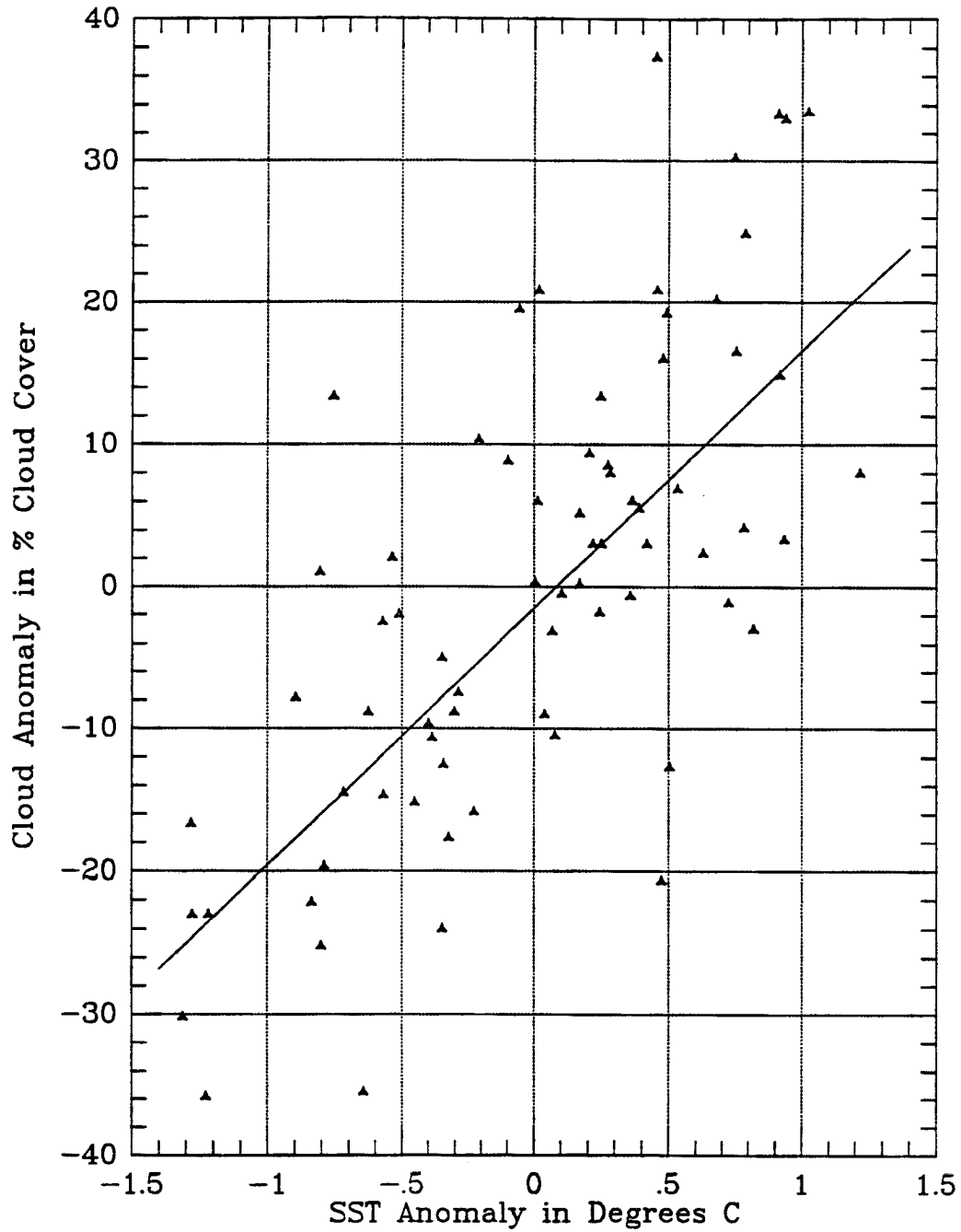


Figure 2.2: One sample grid point's cloud and SST anomaly data along with the Least Absolute Deviations (LAD) regression analysis line calculated from these data. This particular example is for total clouds at the grid point centered at 2.25° North and 164.25° West in the central tropical Pacific. This particular grid box has a high LAD slope of 18 and a low P-value of 6×10^{-11} . Based on data from April 1979 through March 1985.

LAD regression analysis can determine a slope value at each grid point even if the distribution of the 72 pairs of anomaly data points is totally random. Therefore, some measure of the probability of the distribution of the data points being random is necessary to evaluate the significance we should place on the LAD slope value. This was accomplished by using a Multivariate Randomized Block Permutation (MRBP) test at each grid point (Mielke, 1984, 1986). Since the LAD analysis regression line predicts a cloud anomaly \hat{y}_i for each SST anomaly x_i and we have the observed cloud anomaly y_i from the data, we used these values in the MRBP test to determine the probability that the distribution of the y_i s is random. (For details on MRBP and other statistical techniques used in this research, see Appendix B.) The probability or P-value that the MRBP returns ranges from 0 to 1 and represents the probability that a event more extreme than the one described by the arrangement of the 72 data points around the LAD slope line could occur by random chance alone. A P-value of 0.05 means that there is a 5% chance that such a data arrangement could occur by random chance. One advantage of the MRBP is that no *a priori* assumption of data distribution is needed. This test was run at each grid point with some interesting results.

By comparing the MRBP P-values with the LAD slopes we found that not only did the LAD analysis do an adequate job of defining the relationship between cloud anomalies and SST anomalies, but that it also did a fairly good job indicating where there was no relationship: as Figure 2.3 shows, where the P-values were large, the absolute value of the LAD slope was small. For total clouds, of the 181 grid points with LAD slope values between -1 and 1 , only 5 had P-values less than 0.05 whereas for the other 847 grid points, 510 had P-values less than 0.05. Where the absolute value of the LAD slope was larger, the P-values tended to be smaller, however, each grid point's P-value was not small enough to indicate that there was no chance, practically speaking, that the data could be distributed like that by random chance alone.

If the data distributions were due to random chance, then the LAD slope values and the probability values would also be randomly distributed geographically as well. If the data distributions were due to physical processes at work in the ocean/atmosphere system,

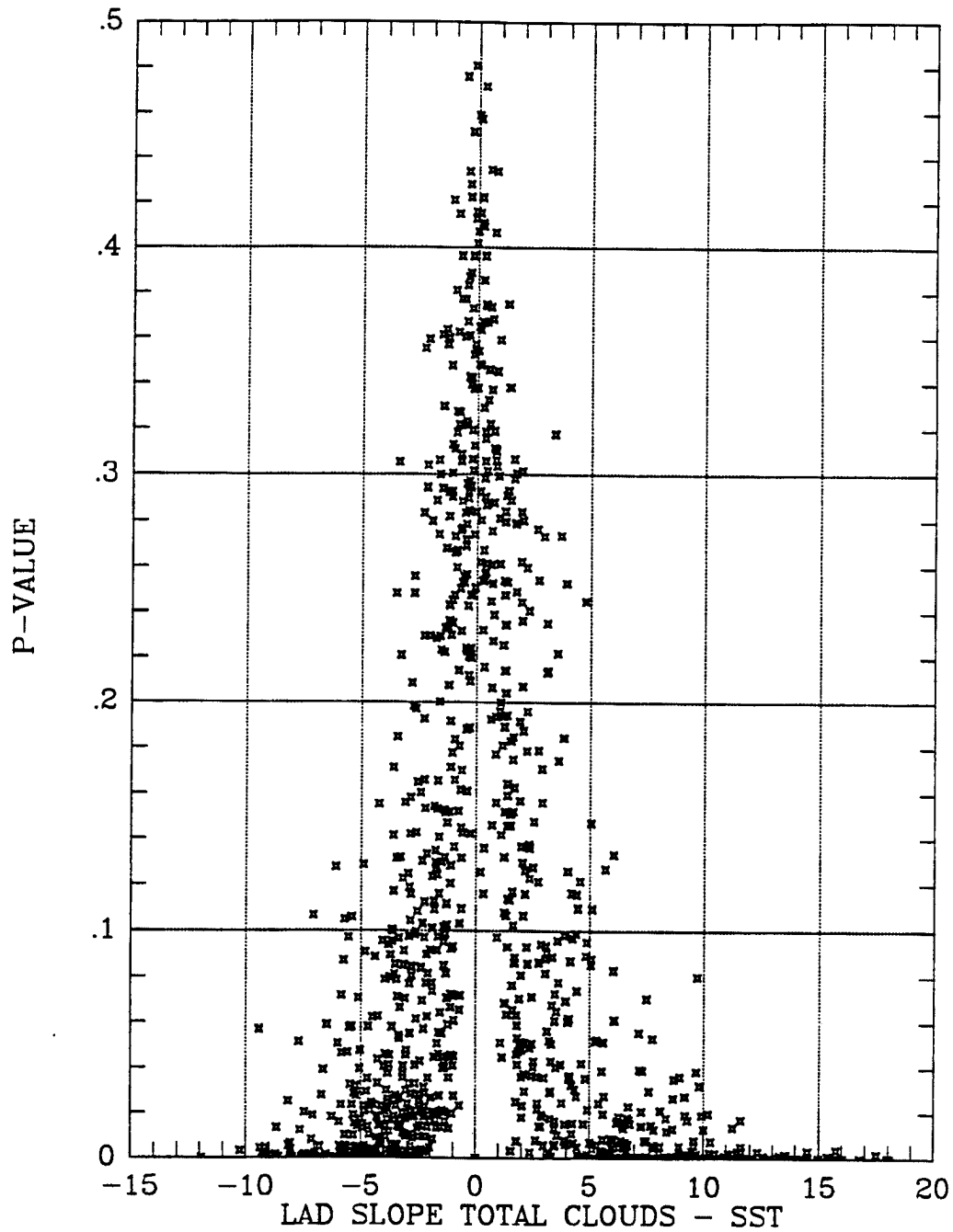


Figure 2.3: A scatter plot of the Probability that each grid point's data, a sample of which is shown in Figure 2.2, are a random distribution versus the value of the LAD slope. This example is for total clouds-SSTA LAD analysis. Based on data from April 1979 through March 1985.

then there would likely be good spacial correlation in LAD slope and P-values. Therefore, we examined the geographical distribution of the P-values simply using latitude as the sole geographic descriptor. For this we used a two sided Fisher's Exact test (Berry and Mielke, 1985; Fisher, 1958) to determine the likelihood that the distribution of these P-values with regards to latitude was random. (For details on the Fisher's Exact test and other statistical techniques used in this research, see Appendix B.) For total clouds, a simple four box diagram with the latitudinal qualification being poleward or equatorward of 12° and the P-value cut off being 0.05, returned a P-value of 4.0×10^{-11} . More precise latitudinal cut off values have returned P-values for other cloud types as low as 6.0×10^{-89} . These extremely low P-values related to simple latitudinal variations indicates that there is definitely a strong signal being picked up by the LAD analysis which is related to some physical process that varies with latitude. In other words, while the low P-values at individual grid boxes indicate that the signal is real, the regionality of the LAD slope and P-value distributions provides convincing evidence that the LAD slope values are indicative of real physical processes instead of random noise.

2.4 Results

Area weighted averages for the LAD regression slope of cloud anomaly versus SST anomaly from 60°N to 40°S vary with cloud type and are shown in Table 2.1 for all grid points and for those grid points with probability values less than or equal to 0.05. On average, total cloudiness increases with increasing SSTA. The percentage of high clouds increased the most, while low clouds decreased with increases in SSTA. No data set corrections based on cloud overlap assumptions were made. Therefore, some of the globally averaged decreases in slope of low clouds may have occurred because the increase in high clouds obscured the satellite's view of low clouds. In certain regions, however, the opposite may have occurred: a decrease in high clouds leading to observed increases in low clouds because of less obscuration by high clouds. "Correcting" the data using a relatively simple random overlap assumption might decrease such errors in analysis of low clouds. However, when high clouds are obscuring low clouds, the changes in low clouds in association with

Table 2.1: Slope values of cloud–SSTA LAD regression for total, high, middle, and low clouds. Column 2 is the area weighted average for the entire open ocean from 60°N to 40°S. Column 3 is the same except only for those grid boxes with a probability value of less than or equal to 0.05. Columns 4 and 5 are the maximum and minimum LAD slopes for any grid box in the domain. The last column is the percent of the grid boxes with probabilities less than or equal to 0.05. Based on data from April 1979 through March 1985.

Cloud Type	All Prob	Prob \leq 0.05	Maximum	Minimum	Percent
Total	0.94	1.98	18.05	-11.93	50%
High	1.32	2.89	14.48	-11.73	41%
Middle	0.30	0.81	9.84	-11.44	42%
Low	-0.75	-1.46	3.54	-6.40	45%

changes in SSTAs can be of less concern from a top-of-the-atmosphere radiation balance point of view and it is understanding the changes in the top-of-the-atmosphere radiation balance that is the prime goal of this research. Therefore, no cloud overlap assumptions were made.

Zonal averages for the cloud–SSTA LAD slopes for all grid points and for only those grid points with $P \leq 0.05$ are plotted in Figures 2.4 and 2.5. As one might infer from Table 2.1, the magnitude of the LAD slopes are greater for the zonal averages of grid points with $P \leq 0.05$ than the zonal averages of all grid points, however, the sign of the zonally averaged LAD slope is generally the same. The zonally averaged total cloud–SSTA LAD slope has a maximum just north of the equator but switches crosses the 0 line at about 15–20° North and South. It remains negative for poleward of that latitude. Zonally averaged high cloud–SSTA LAD slopes are generally positive. For low P-value grid points, there is a distinct difference between the northern and southern hemisphere away from the tropics: the southern hemisphere has much higher LAD slopes. By contrast, zonally averaged low cloud–SSTA LAD slopes are fairly similar in the northern hemisphere as the southern hemisphere: almost uniformly negative with the lowest values between 20 and 35 degrees North and South. Zonally averaged middle cloud–SSTA LAD slopes increase like high clouds in the tropics but decrease like low clouds in the midlatitudes.

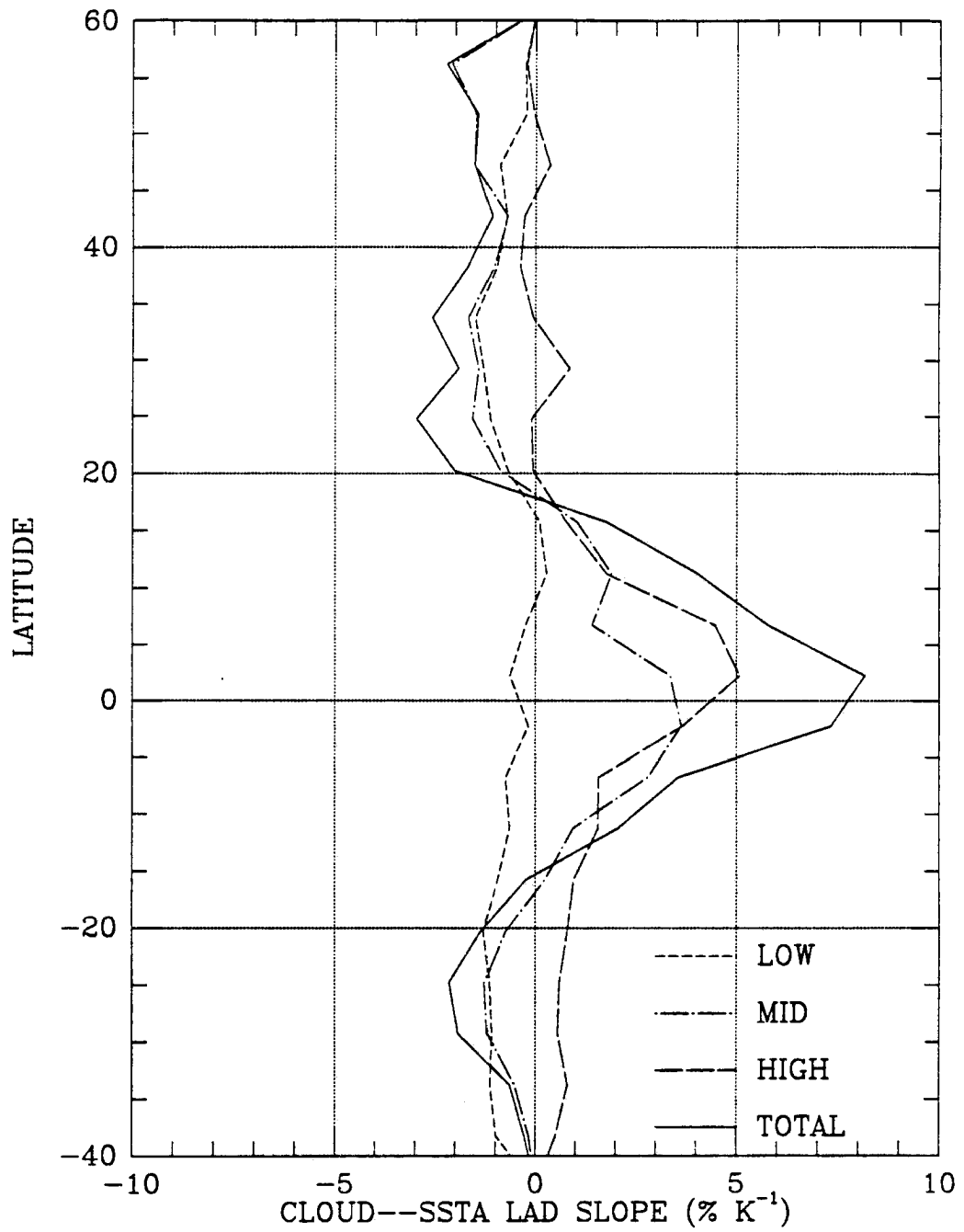


Figure 2.4: Zonal averages of cloud-SSTA LAD slopes of all grid points. Based on data from April 1979 through March 1985.

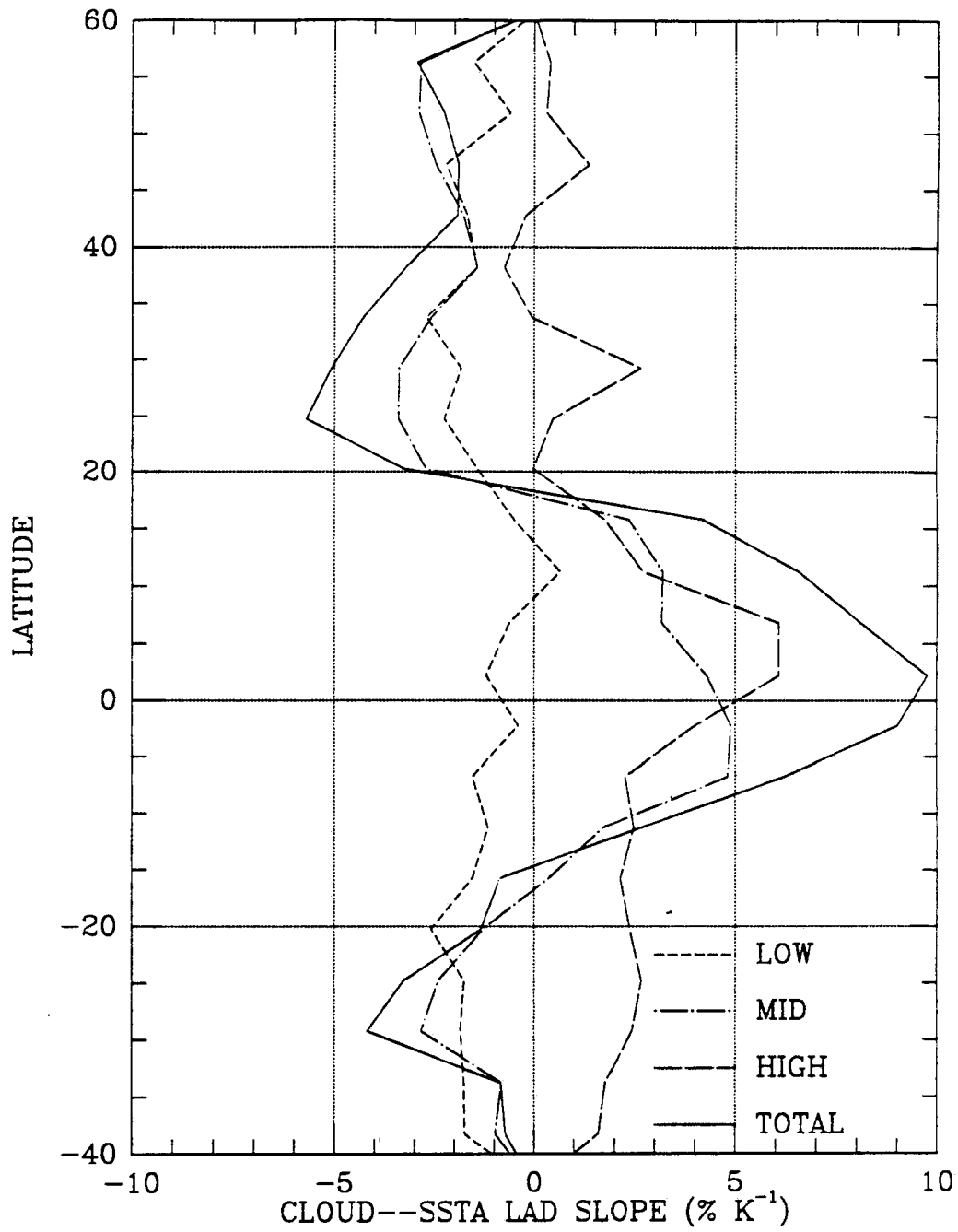


Figure 2.5: Zonal averages of cloud-SSTA LAD slopes of grid points with $P \leq 0.05$. Based on data from April 1979 through March 1985.

Global and zonal averages, however, tell only part of the story. The range in LAD slope values is also shown in Table 2.1. All of the grid points values used to report the maximum or minimum LAD slope values had P-values less than or equal to 0.05. A range of 18 to -12 may average out to 1 but the average may not be very indicative of what to expect at any particular location. The last column in Table 2.1 indicates the percentage of grid points with $P \leq 0.05$. Total clouds have the highest percent while high clouds have the lowest percent, all of which are in the 40-50% range. A grid point could have a high P-value for a number of reasons: there could be little relationship between cloudiness at that level and SSTA, there could be a relationship but the signal from it could be overwhelmed by a much stronger relationship to some other earth/ocean/atmosphere process that is unrelated to SSTAs, the cloud-SSTA relationship could be made noisier by the effects of higher level clouds, or the grid box may be in a transitional geographic zone where LAD slope values change from positive to negative with the seasonal LAD slope at that grid box changing from positive to negative with the seasons, making a year's data appear random. Whatever the reason for the high P-values, since we are unable to put too much faith in the ability of the LAD slope to represent the cloud-SSTA relationship when the probabilities are greater than 0.05 for any particular grid box, the global contour plots of the LAD slope values which are on many of the following pages only show those grid boxes with $P \leq 0.05$.

Figure 2.6 shows the distribution of probability versus LAD slope for both the full data set analysis and analysis of just June, July, and August for total cloud-SSTA. Clearly the seasonal analysis is noisier than the full data set analysis. Also evident from examination of this figure is there are many positive and negative LAD slope values associated with low P-values. As examination of Figure 2.7 reveals, the positive and negative LAD slope grid points with low P-values display strong regionality with the positive total cloud-SSTA LAD slope values —total cloudiness increasing in association with increases in SSTA— clustered in the tropics and the South Pacific Convergence Zone. Negative total cloudiness-SSTA LAD slope grid points with low P-values tend to be in higher latitudes and in the subtropical subsidence regions. Seasonal analysis for June, July, and August

and December, January, and February are shown in Figures 2.8 and 2.9 and reveal that the negative LAD slope regions associated with stratocumulus decks tend to be large in summer than winter.

High cloud–SSTA LAD analysis grid points with low P-values tend to have positive LAD slopes, as revealed by Figure 2.10. Figures 2.11, 2.12, and 2.13 show strong regional-ity with equatorial region showing up strongly. The South Pacific Convergence Zone also appears to be revealed in these figures as regions of positive high cloud–SSTA LAD slopes. As one would expect, the subtropical stratocumulus subsidence regions where there are few high clouds do not appear in these figures with the exception of the region off the west coast of Australia. Only one significant region has LAD slope values that goes from positive to negative with the season in any of the cloud–SSTA analyses. That occurs in the high cloud–SSTA analysis of the oceanic region just South of Japan which has positive LAD slopes in winter and negative LAD slopes in summer.

Middle cloud–SSTA analysis has both positive and negative LAD slope values with low P-values, as indicated in Figure 2.14. Generally, as shown in Figures 2.15, 2.16, and 2.17, the main region with positive LAD slope values is along the equator with higher latitudes more likely to have negative LAD slopes. The main exception to this generality is along the SPCZ, where positive mid cloud–SSTA LAD slope values show up strongest in winter.

Low P-value grid points for low cloud–SSTA LAD analysis are most likely to have negative LAD slopes, as shown in Figure 2.18. Also evident in this figure, the magnitude of the low P-value grid point LAD slopes is smaller for low cloud–SSTA analysis than for mid-, high-, or total cloud–SSTA analyses. The dominant location for low P-value low cloud–SSTA negative LAD slope grid points is in subtropical stratocumulus subsidence regions. This negative low cloud–SSTA relationship appears to be strongest in the summer. Equatorial regions where low clouds decrease in association with increases in SSTA are regions where high, middle, and total clouds increase in association with increases in SSTA.

Examination of all the seasonal figures reveals some north/south movement with the season, with certain features being farther north during June, July, and August than December, January, and February.

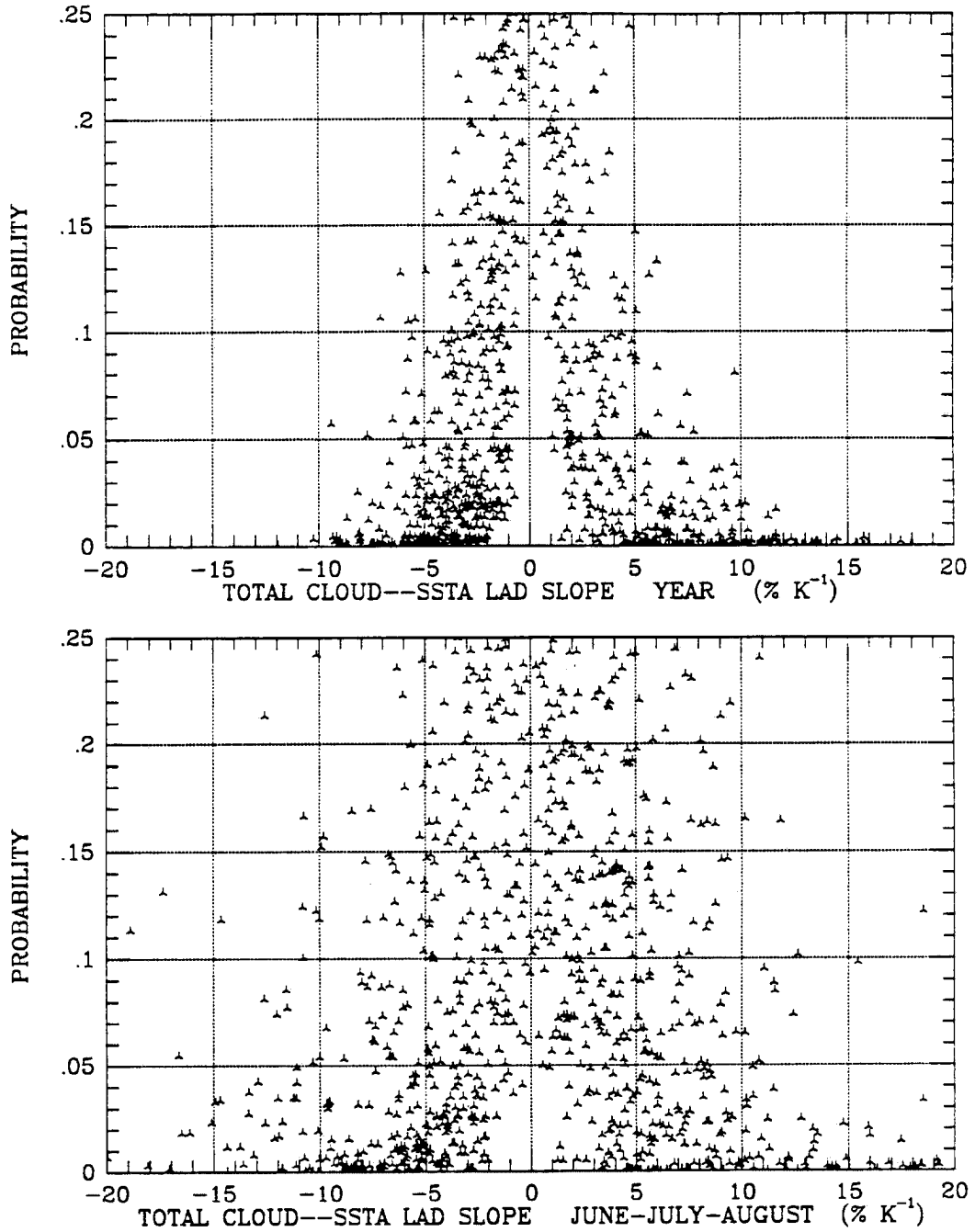


Figure 2.6: Probability versus LAD slope for total cloud-SSTA analysis for both full data set analysis (top) and analysis of June, July, and August (bottom). Based on data from April 1979 through March 1985.

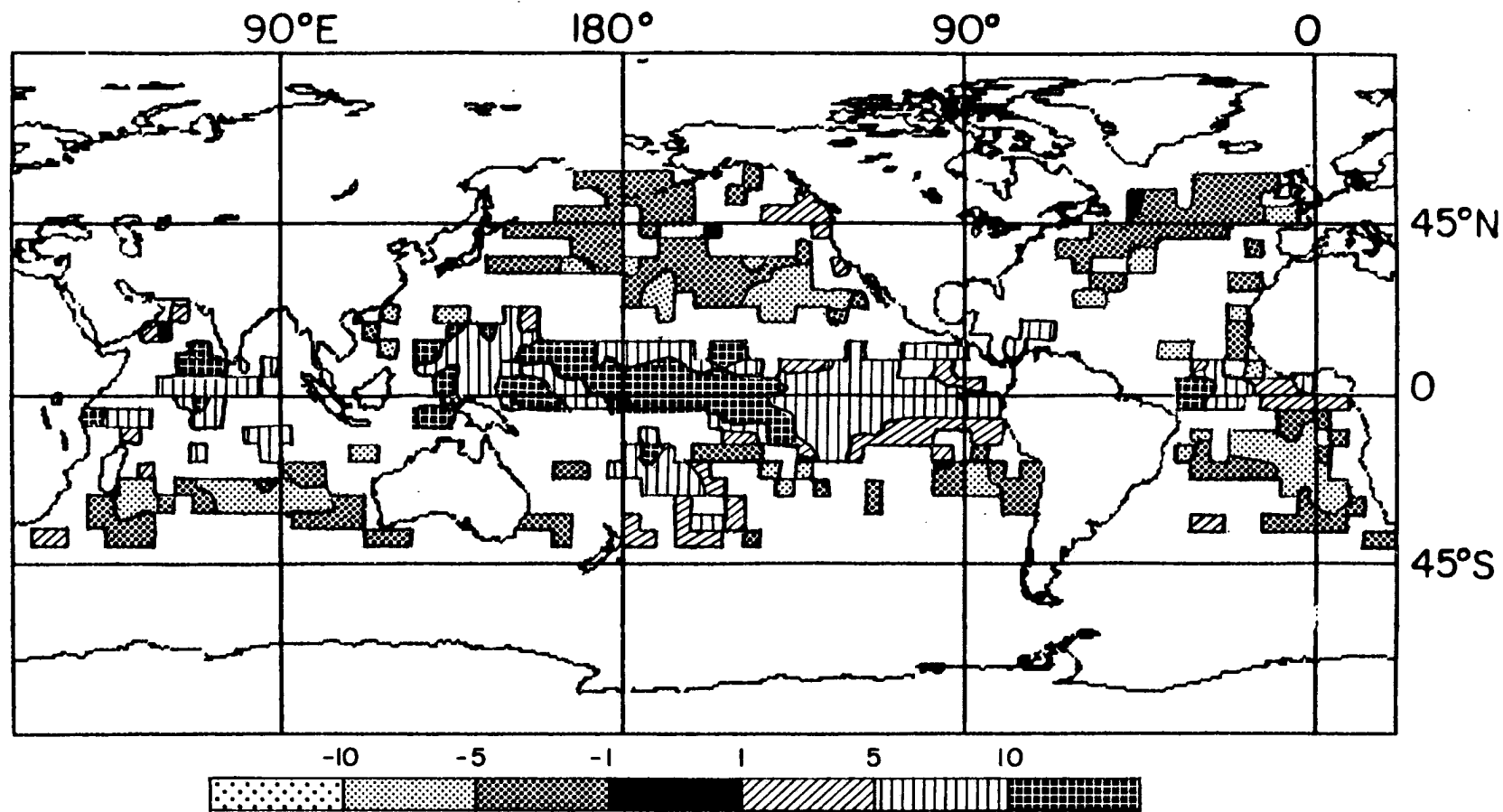


Figure 2.7: Total Cloud-SSTA LAD slope. Contour plot from 60°N to 40°S (the extent of the SST data) of the slope of the Least Absolute Deviations (LAD) regression relating total cloud anomalies and SST anomalies at each grid point as shown in Figure 2.2. Values are in units of change in percent of cloud cover per one degree C increase in SST anomaly. Only grid boxes with $P \leq 0.05$ are shown. Based on data from April 1979 through March 1985.

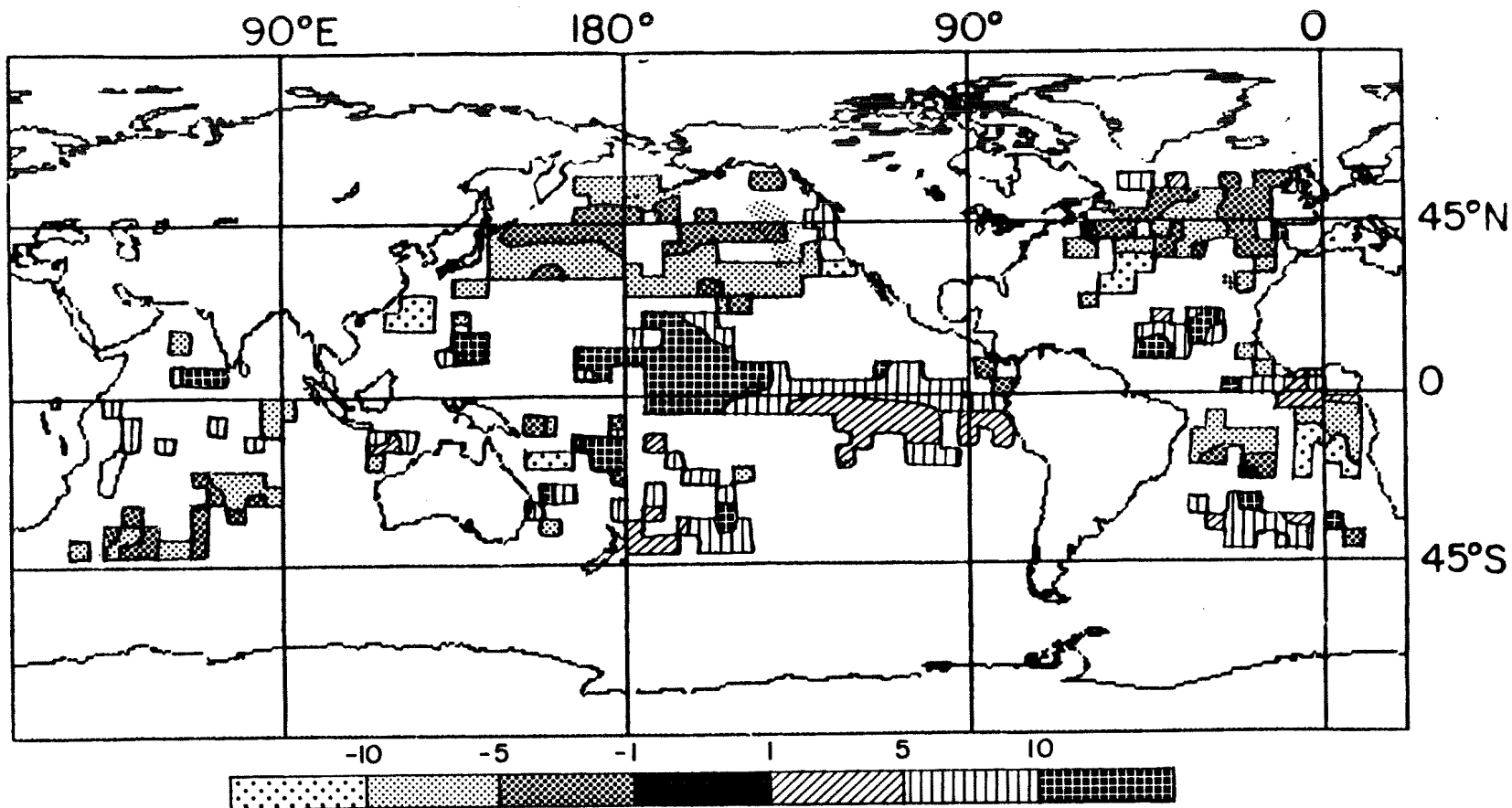


Figure 2.8: Total Cloud-SSTA LAD slope, June, July, August. Contour plot from 60°N to 40°S (the extent of the SST data) of the slope of the Least Absolute Deviations (LAD) regression relating total cloud anomalies and SST anomalies at each grid point as shown in Figure 2.2. Values are in units of change in percent of cloud cover per one degree C increase in SST anomaly. Only grid boxes with $P \leq 0.05$ are shown. This analysis is for the months of June, July, and August. Based on data from April 1979 through March 1985.

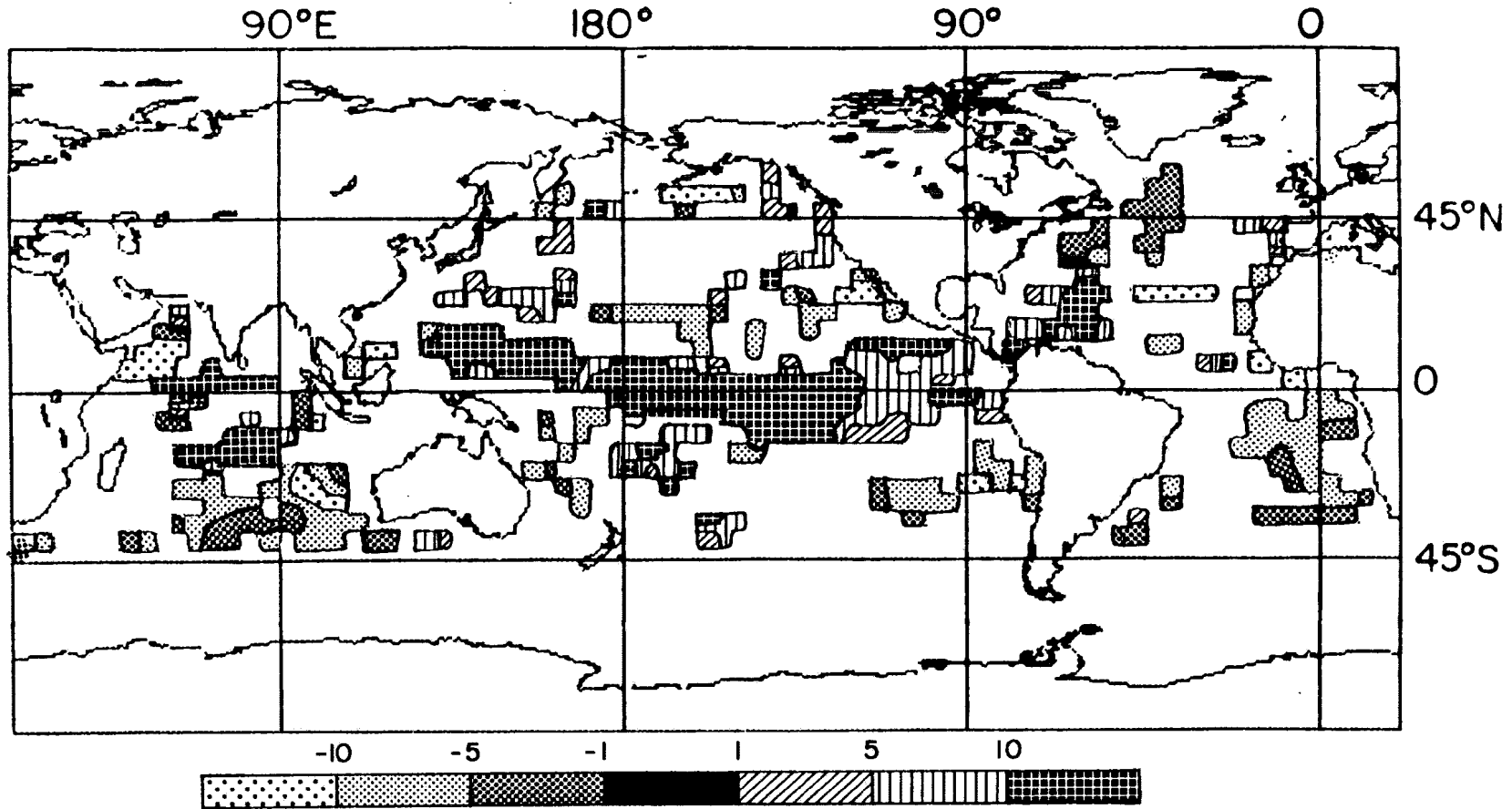


Figure 2.9: Total Cloud-SSTA LAD slope, December, January, February. Contour plot from 60°N to 40°S (the extent of the SST data) of the slope of the Least Absolute Deviations (LAD) regression relating total cloud anomalies and SST anomalies at each grid point as shown in Figure 2.2. Values are in units of change in percent of cloud cover per one degree C increase in SST anomaly. Only grid boxes with $P \leq 0.05$ are shown. This analysis is for the months of December, January, and February. Based on data from April 1979 through March 1985.

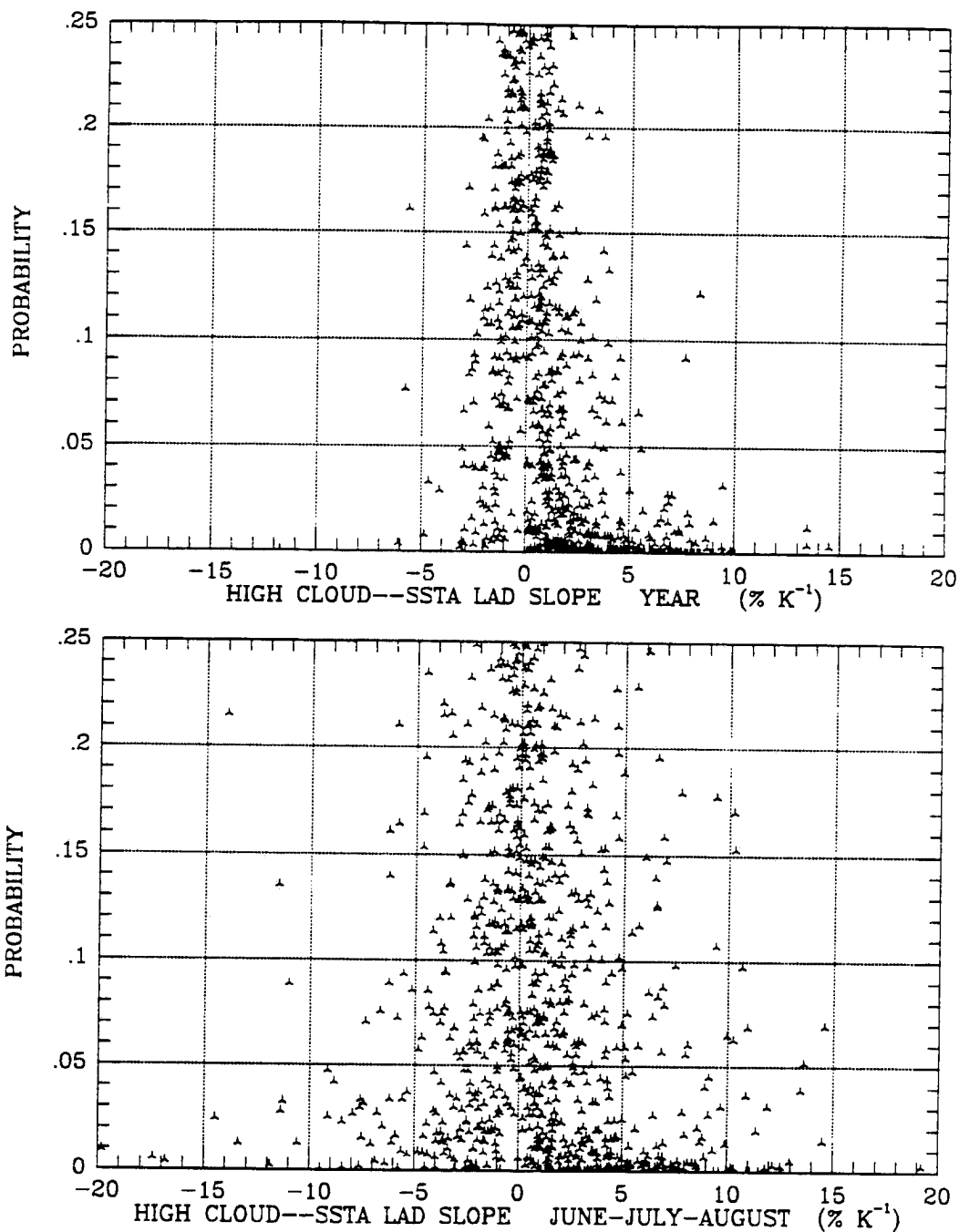


Figure 2.10: Probability versus LAD slope for high cloud-SSTA analysis for both full data set analysis (top) and analysis of June, July, and August (bottom). Based on data from April 1979 through March 1985.

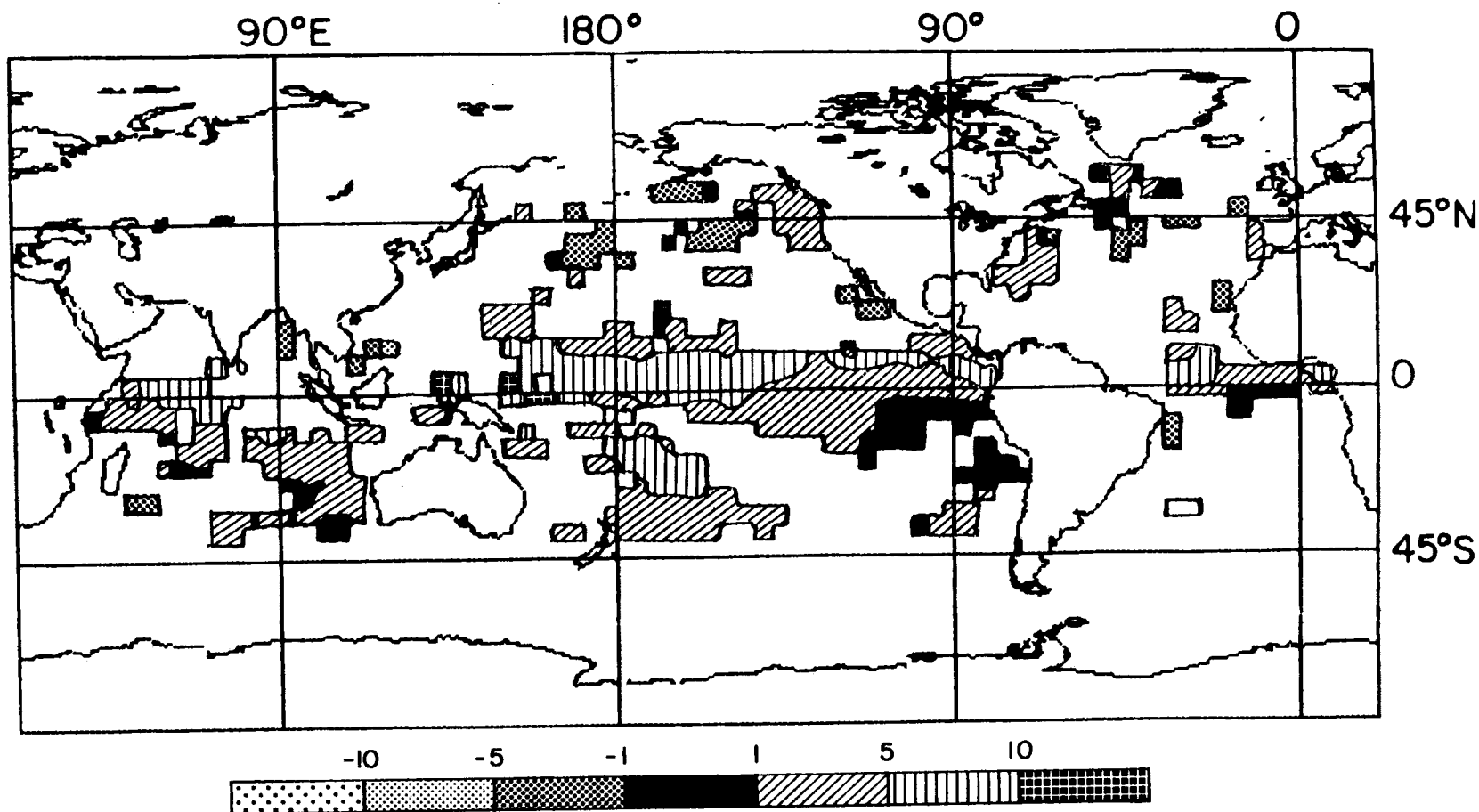


Figure 2.11: High Cloud-SSTA LAD slope. Contour plot from 60°N to 40°S (the extent of the SST data) of the slope of the Least Absolute Deviations (LAD) regression relating high cloud anomalies and SST anomalies at each grid point as shown in Figure 2.2. Values are in units of change in percent of cloud cover per one degree C increase in SST anomaly. Only grid boxes with $P \leq 0.05$ are shown. Based on data from April 1979 through March 1985.

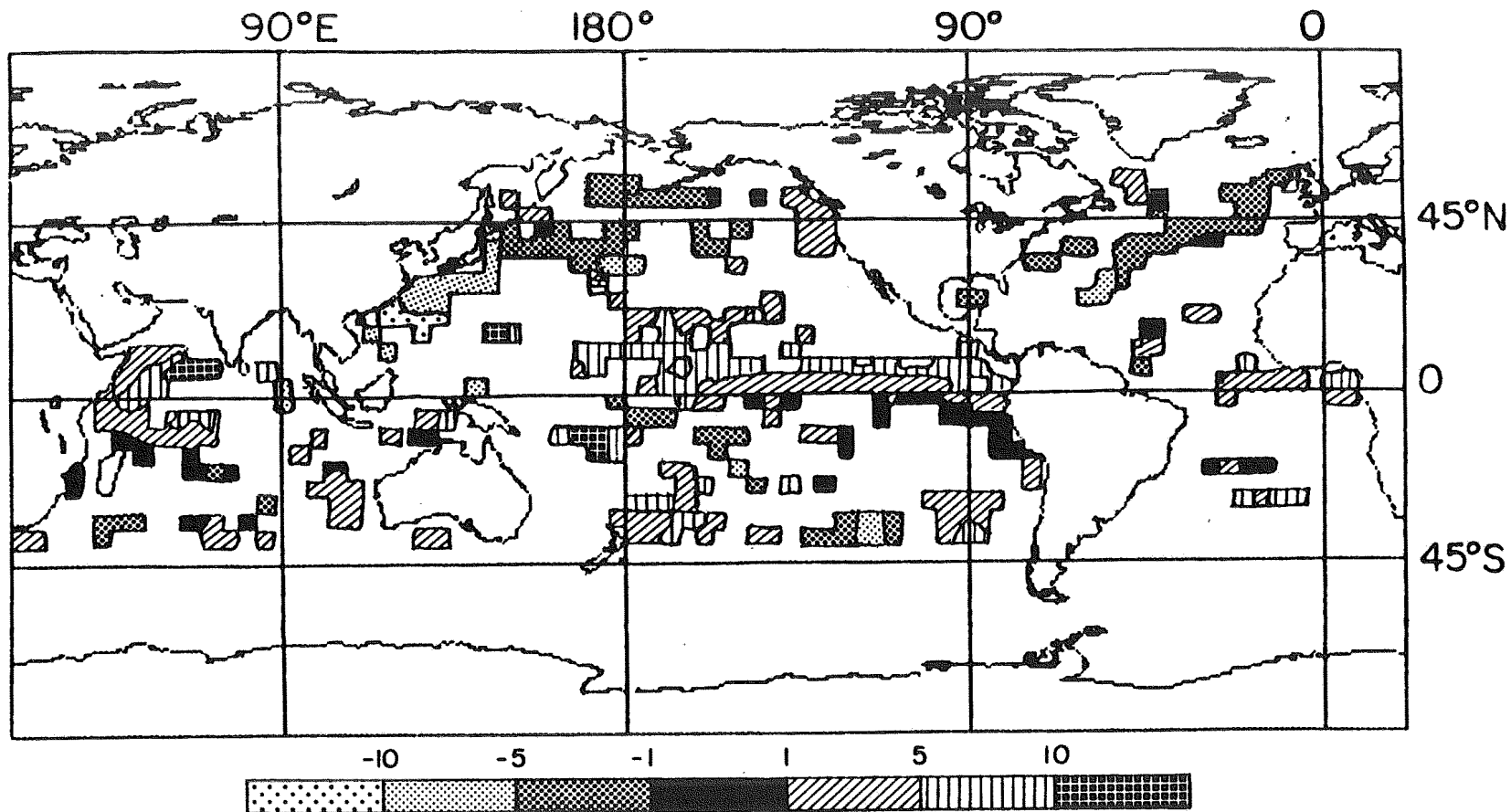


Figure 2.12: High Cloud-SSTA LAD slope, June, July, August. Contour plot from 60°N to 40°S (the extent of the SST data) of the slope of the Least Absolute Deviations (LAD) regression relating high cloud anomalies and SST anomalies at each grid point as shown in Figure 2.2. Values are in units of change in percent of cloud cover per one degree C increase in SST anomaly. Only grid boxes with $P \leq 0.05$ are shown. This analysis is for the months of June, July, and August. Based on data from April 1979 through March 1985.

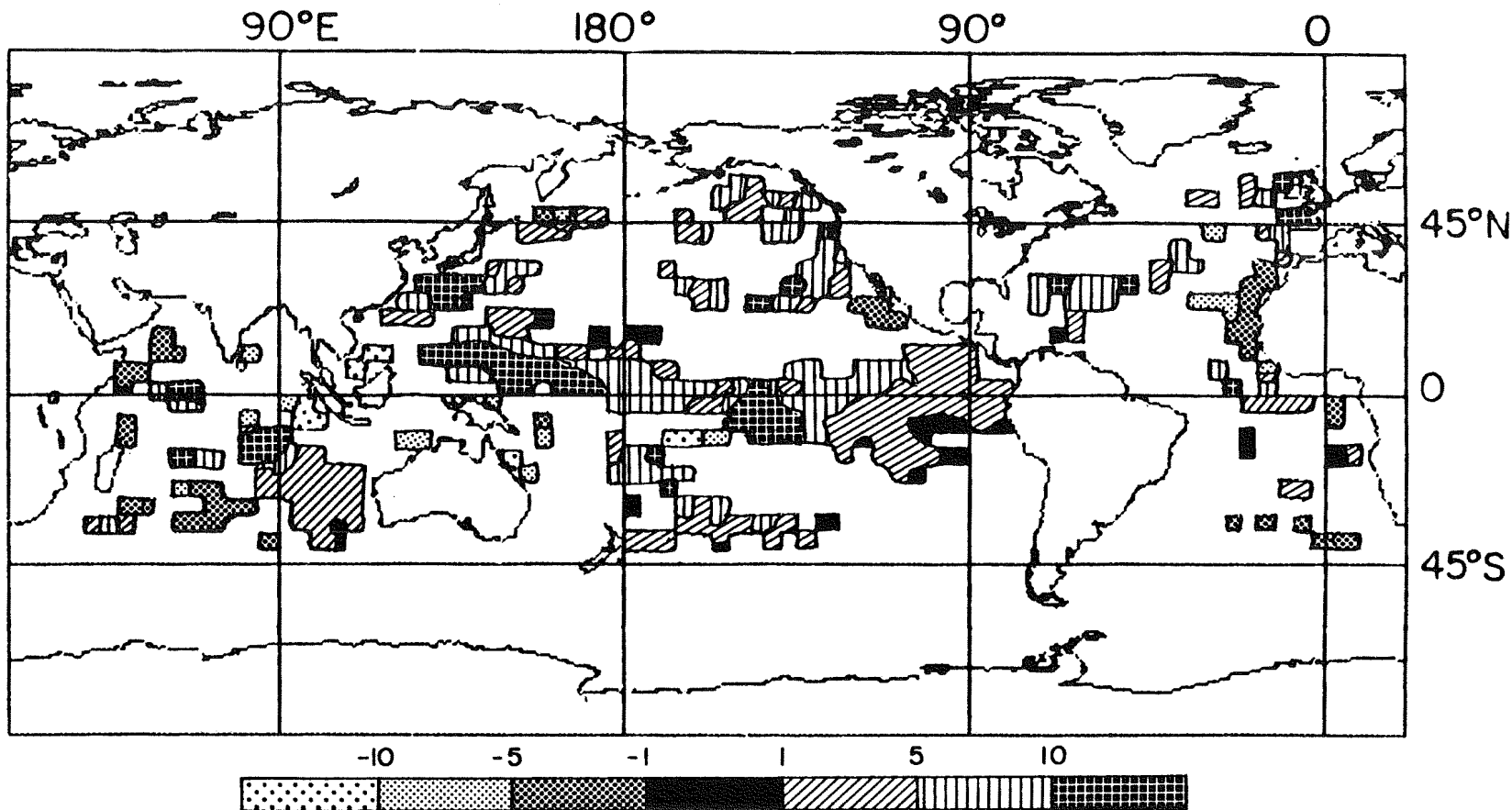


Figure 2.13: High Cloud-SSTA LAD slope, December, January, February. Contour plot from 60°N to 40°S (the extent of the SST data) of the slope of the Least Absolute Deviations (LAD) regression relating high cloud anomalies and SST anomalies at each grid point as shown in Figure 2.2. Values are in units of change in percent of cloud cover per one degree C increase in SST anomaly. Only grid boxes with $P \leq 0.05$ are shown. This analysis is for the months of December, January, and February. Based on data from April 1979 through March 1985.

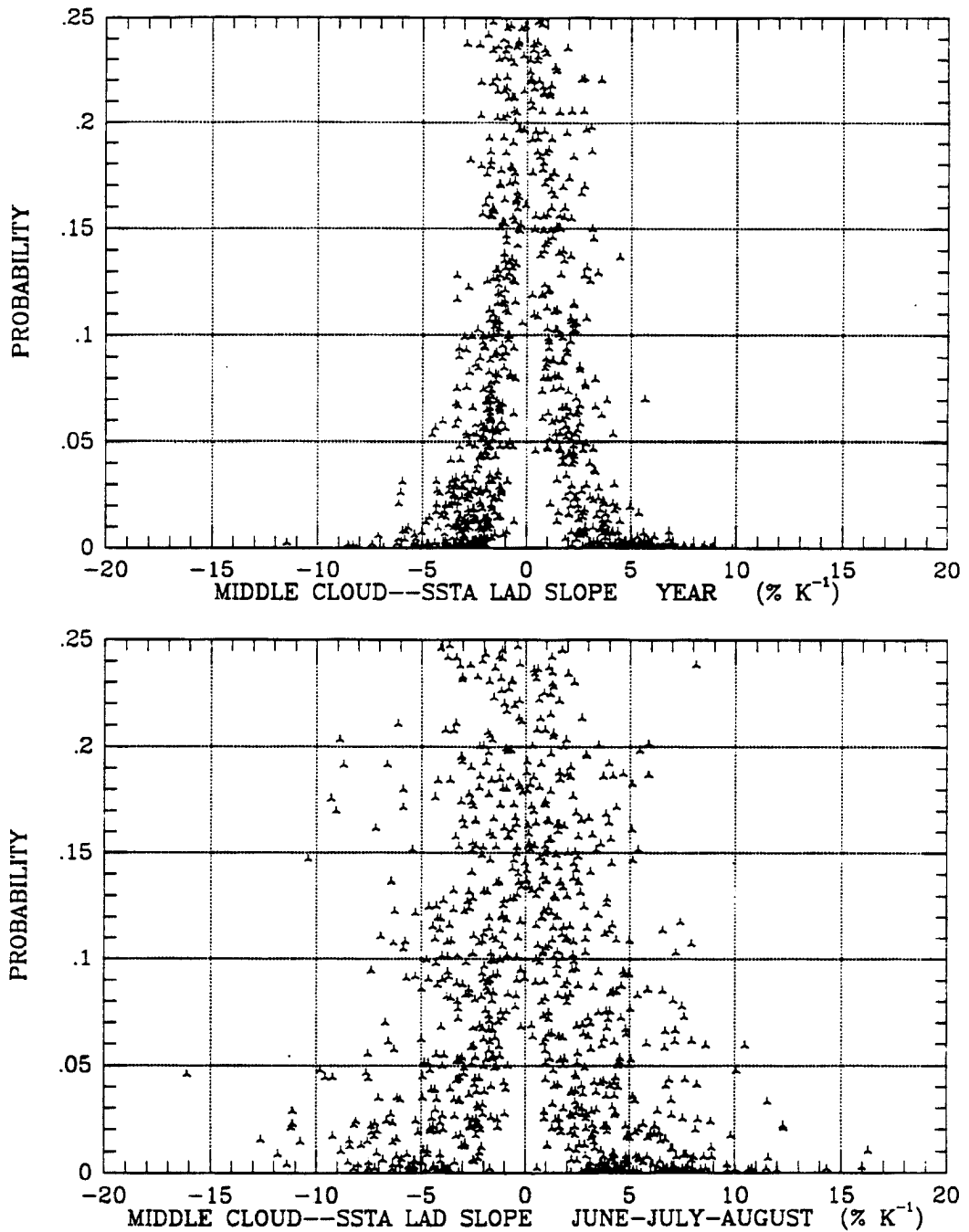


Figure 2.14: Probability versus LAD slope for middle cloud-SSTA analysis for both full data set analysis (top) and analysis of June, July, and August (bottom). Based on data from April 1979 through March 1985.

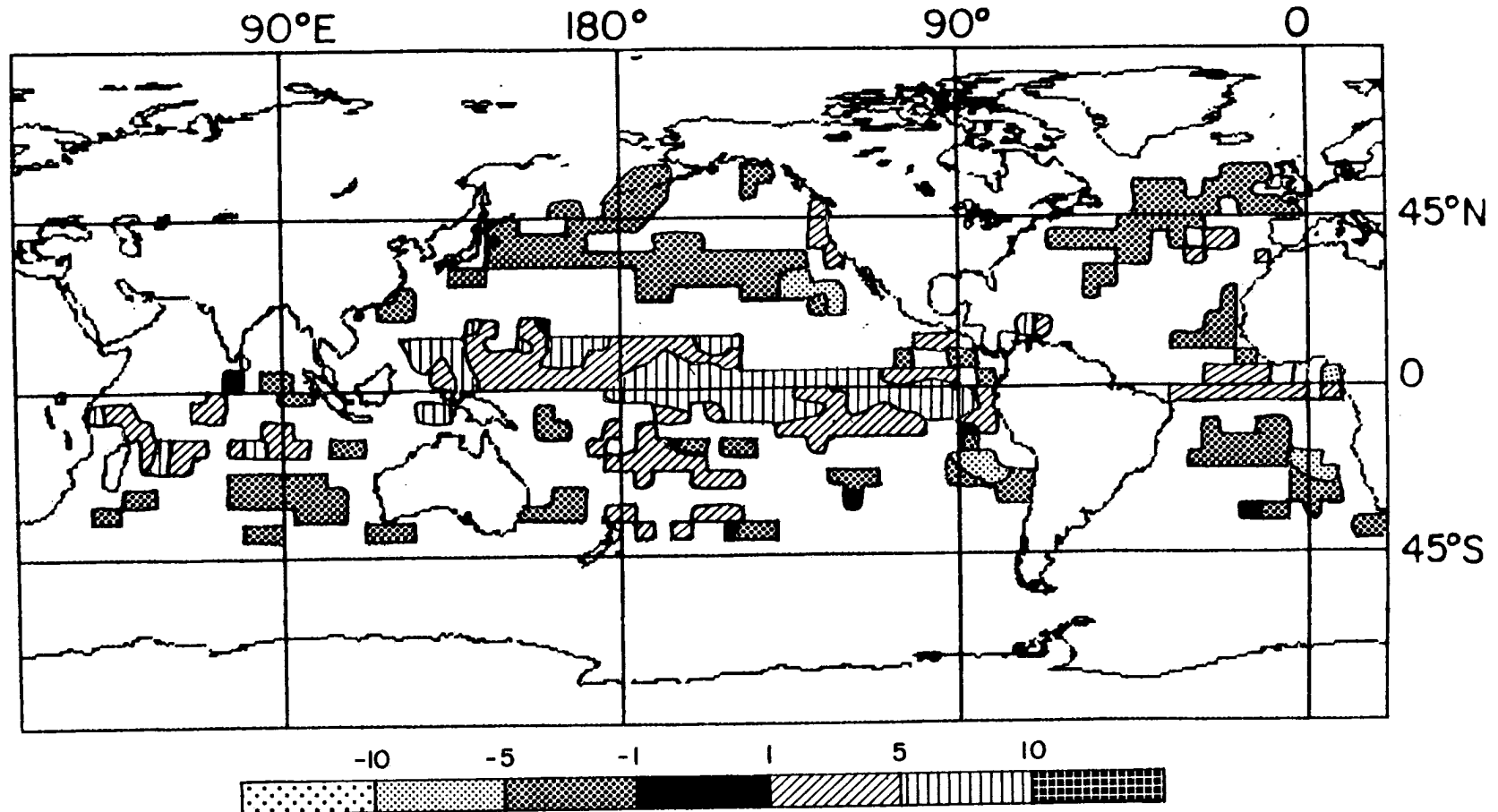


Figure 2.15: Middle Cloud–SSTA LAD slope. Contour plot from 60°N to 40°S (the extent of the SST data) of the slope of the Least Absolute Deviations (LAD) regression relating middle cloud anomalies and SST anomalies at each grid point as shown in Figure 2.2. Values are in units of change in percent of cloud cover per one degree C increase in SST anomaly. Only grid boxes with $P \leq 0.05$ are shown. Based on data from April 1979 through March 1985.

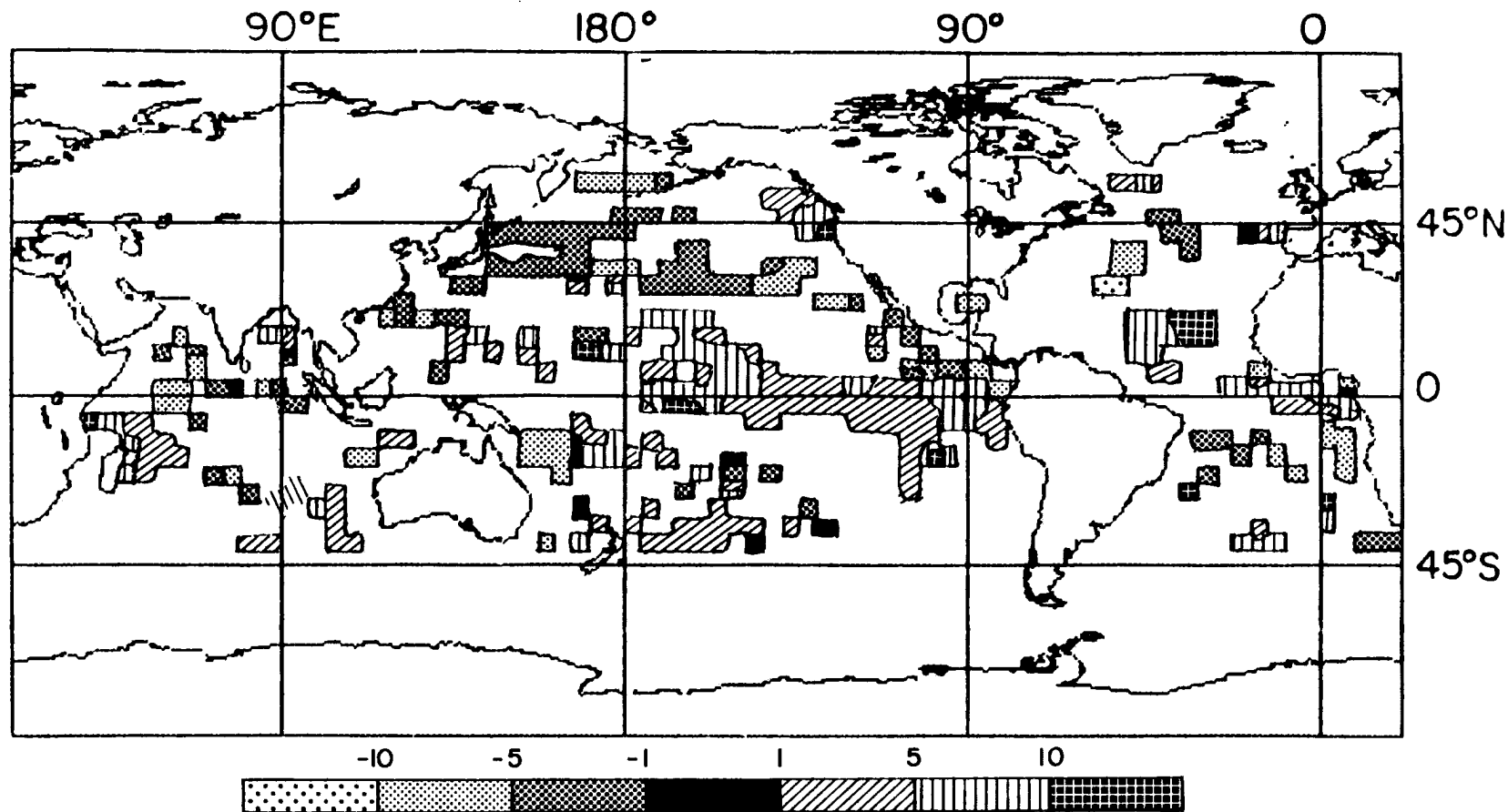


Figure 2.16: Middle Cloud-SSTA LAD slope, June, July, August. Contour plot from 60°N to 40°S (the extent of the SST data) of the slope of the Least Absolute Deviations (LAD) regression relating middle cloud anomalies and SST anomalies at each grid point as shown in Figure 2.2. Values are in units of change in percent of cloud cover per one degree C increase in SST anomaly. Only grid boxes with $P \leq 0.05$ are shown. This analysis is for the months of June, July, and August. Based on data from April 1979 through March 1985.

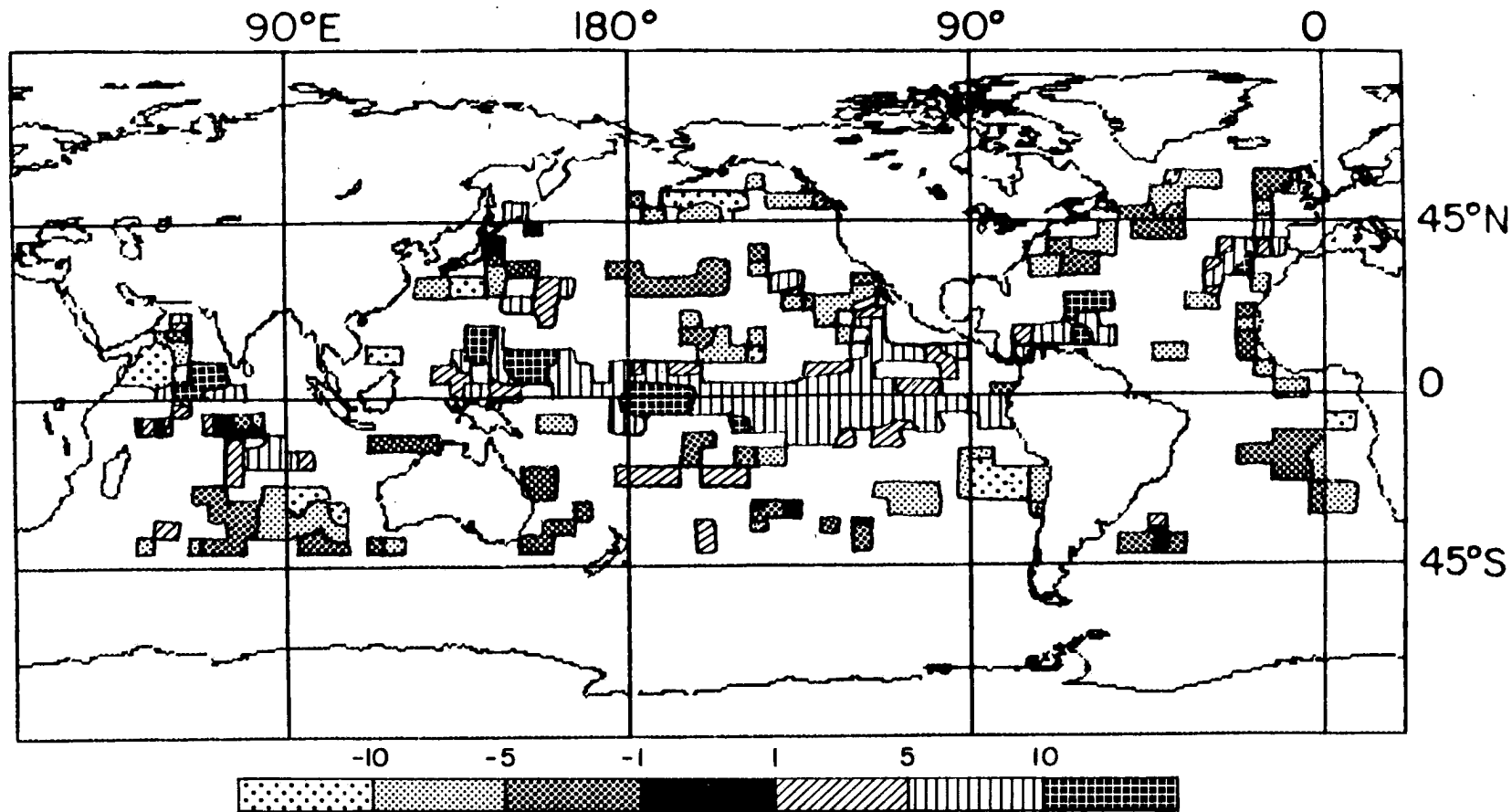


Figure 2.17: Middle Cloud-SSTA LAD slope, December, January, February. Contour plot from 60°N to 40°S (the extent of the SST data) of the slope of the Least Absolute Deviations (LAD) regression relating middle cloud anomalies and SST anomalies at each grid point as shown in Figure 2.2. Values are in units of change in percent of cloud cover per one degree C increase in SST anomaly. Only grid boxes with $P \leq 0.05$ are shown. This analysis is for the months of December, January, and February. Based on data from April 1979 through March 1985.

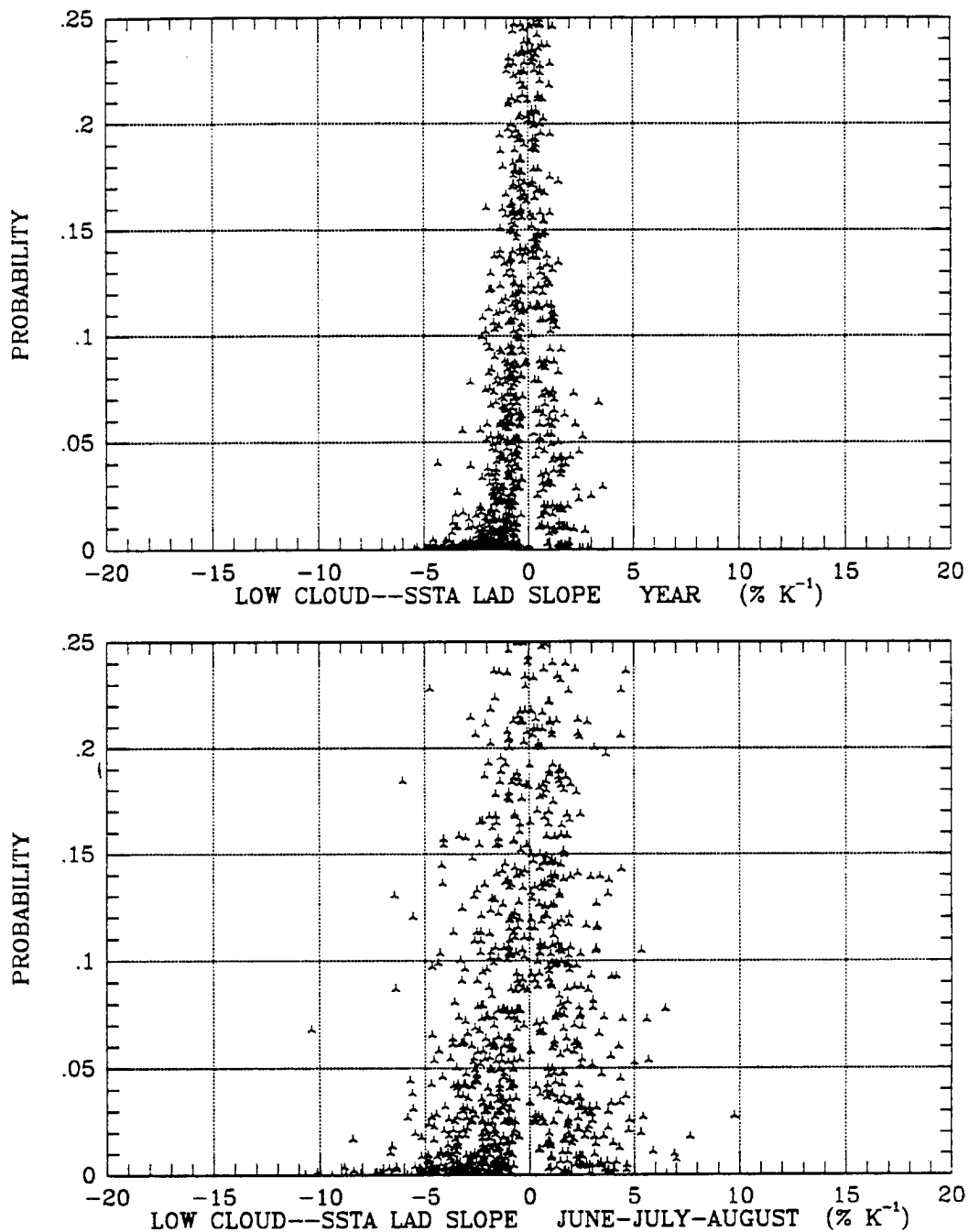


Figure 2.18: Probability versus LAD slope for low cloud-SSTA analysis for both full data set analysis (top) and analysis of June, July, and August (bottom). Based on data from April 1979 through March 1985.

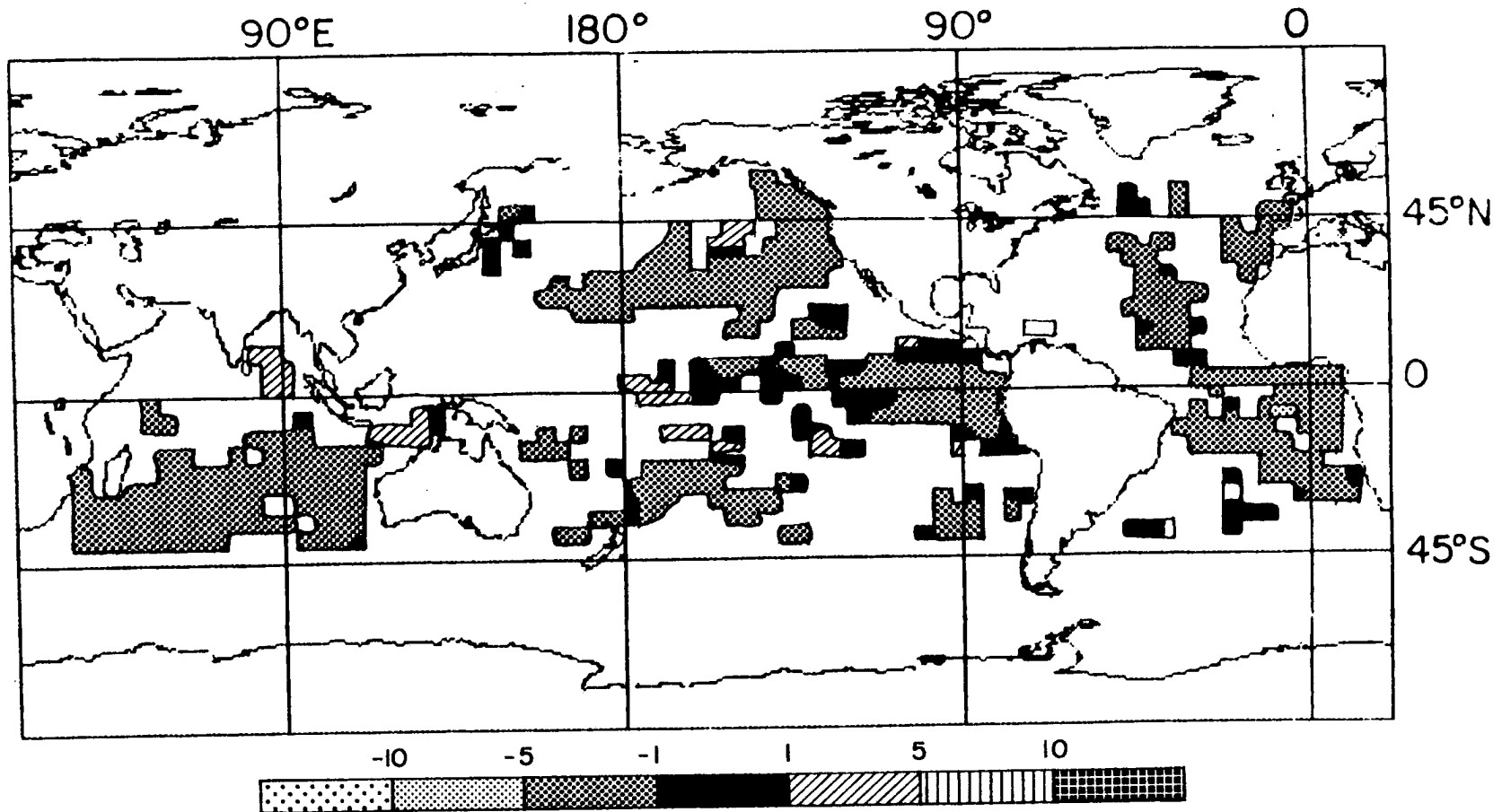


Figure 2.19: Low Cloud-SSTA LAD slope. Contour plot from 60°N to 40°S (the extent of the SST data) of the slope of the Least Absolute Deviations (LAD) regression relating low cloud anomalies and SST anomalies at each grid point as shown in Figure 2.2. Values are in units of change in percent of cloud cover per one degree C increase in SST anomaly. Only grid boxes with $P \leq 0.05$ are shown. Based on data from April 1979 through March 1985.

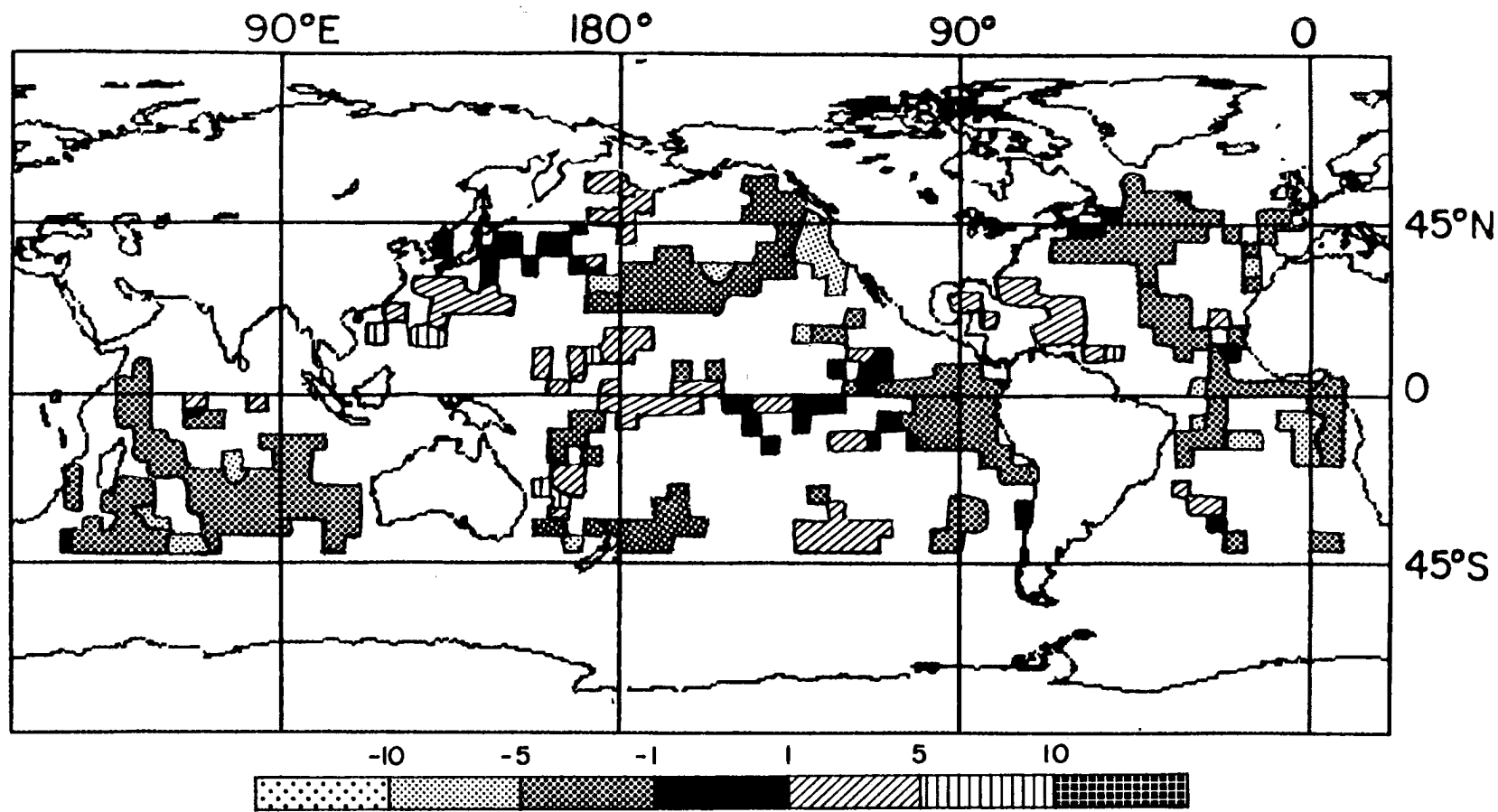


Figure 2.20: Low Cloud-SSTA LAD slope, June, July, August. Contour plot from 60°N to 40°S (the extent of the SST data) of the slope of the Least Absolute Deviations (LAD) regression relating low cloud anomalies and SST anomalies at each grid point as shown in Figure 2.2. Values are in units of change in percent of cloud cover per one degree C increase in SST anomaly. Only grid boxes with $P \leq 0.05$ are shown. This analysis is for the months of June, July, and August. Based on data from April 1979 through March 1985.

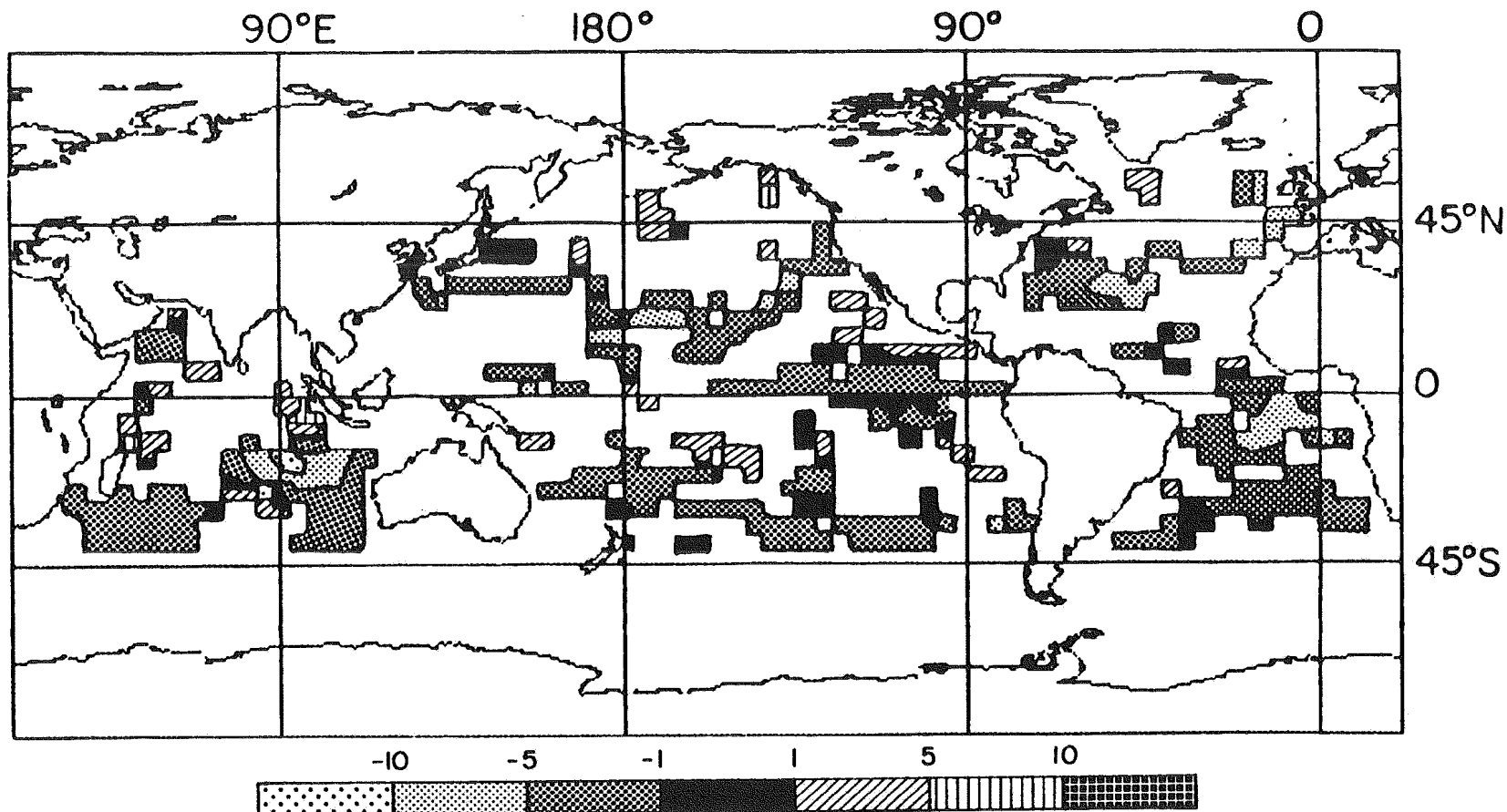


Figure 2.21: Low Cloud-SSTA LAD slope, December, January, February. Contour plot from 60°N to 40°S (the extent of the SST data) of the slope of the Least Absolute Deviations (LAD) regression relating low cloud anomalies and SST anomalies at each grid point as shown in Figure 2.2. Values are in units of change in percent of cloud cover per one degree C increase in SST anomaly. Only grid boxes with $P \leq 0.05$ are shown. This analysis is for the months of December, January, and February. Based on data from April 1979 through March 1985.

Also of importance from the perspective of understanding global change are the large areas of the world where there is no significant relationship between SST anomalies and various types of cloud anomalies. The high cloud results (Figures 2.11 - 2.13) show the largest areas with no strong cloud-SSTA relationship.

2.5 Discussion

The strong latitudinal variation of LAD slope values and some north/south movement with the seasonal cycle implies several possible physical explanations for relating these cloud anomaly-SSTA LAD slope relationships to other features in the ocean/atmosphere system. One possibility is simply sea surface temperature. Indeed, a strong correlation could be discerned between SST and the LAD slope because SST also has a strong latitudinal dependence and moves north/south with the seasons. Many researchers such as Chan and Lau (1988), Daniels and Vernekar (1988), and Gadgil *et al.* (1984) have linked tropical convection directly to SST. However, the strongly positive LAD slope in the region of the SPCZ defy widespread use of this direct SST explanation because the SPCZ is oriented at a high angle to the contours of SST over a region where the yearly average SST ranges from 28° in the North to 16° in the South. This, therefore, leaves us looking for another explanation.

Can the LAD slope value at various places simply be related to the average percent of cloud cover at that location? This, too, would seem logical since cloud cover couldn't, for example, decrease with increasing SST anomaly if there weren't any clouds there to begin with. To test this idea, we plotted LAD slope versus percent of total cloud cover in Figure 2.22. Examination of Figure 2.22 reveals no significant relationship between the two.

One explanation that does seem to work on a broad scale is relating LAD slope values to general circulation features. For example, the strongest negative values tend to be associated with regions of high average pressure associated with large scale Hadley Cell subsidence, while the strongest positive values are located in regions of lower average pressure in or not far from the ascending branch of the Hadley Cell. This analysis fits well

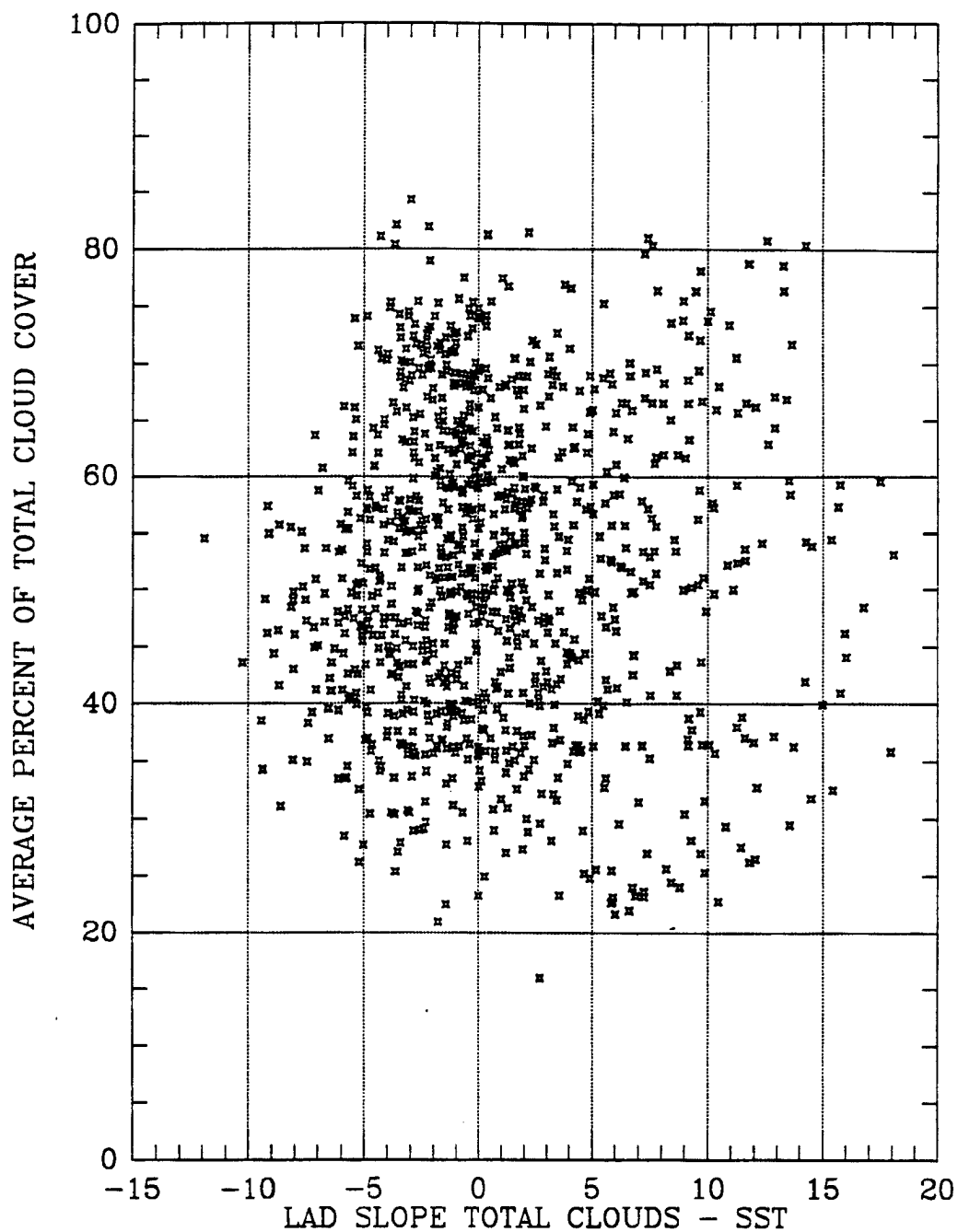


Figure 2.22: Scatter plot of average annual percent of total cloud cover versus the slope of the Least Absolute Deviations (LAD) regression analysis performed on total cloud anomaly versus SST anomaly. There appears to be no significant correlation between the percent of cloud cover and the value of the LAD slope. Based on data from April 1979 through March 1985.

with the general location of the dominant features shown in global plots of cloud–SSTA LAD slope and the north/south movement with the seasons.

Due to the effects of the general circulation, the mechanisms by which SST anomalies affect the atmosphere vary depending on whether the grid point is in a region of strong subsidence or not. Near the equator and along the SPCZ where average vertical motion is upwards or weakly downwards, several mechanisms may account for the observed positive LAD slope. With increasing SST anomaly, evaporation increases so more water vapor is available to form more clouds, and the equivalent potential temperature at the surface increases, so the atmosphere is less stable. While negative SST anomalies would decrease evaporation, “the mechanism of increased subsidence being driven by negative SST anomalies” (Love, 1985) would also diminish convection.

In the subtropical regions with negative LAD slopes, these mechanisms do not have the same end result. An increase in SST anomaly will still lead to more evaporation but not to more cloudiness. This is due to the nature of the cloudiness in this region. These are regions where the Nimbus-7 cloud data indicate there are few or no high clouds and as Figure 2.11 shows, except off the west coast of Australia, there are no low P-value grid points for high clouds–SSTA analysis. The cloud–SSTA effect is therefore confined to lower-level clouds. This can include both low clouds and middle clouds because “the mid cloud altitude range for the Nimbus-7 climatology is 2-7 km for 30°N to 30°S. Therefore, stratocumulus could easily be classified as midlevel cloud” (Stowe *et al.*, 1989).

In these subtropical subsidence regions, cold SST anomalies cool the marine boundary layer and strengthen the inversion thereby encouraging the formation of stable stratus or stratocumulus cloud decks which can have a very high percentage of cloud coverage. Warm SST anomalies, on the other hand, would warm the marine boundary layer, raising and weakening the inversion layer and making the lapse rate in the boundary layer less stable. Such changes promote the breakup of stratocumulus decks into cumulus humilis clouds through mechanisms such as cloud-top entrainment instability (Randall, 1980). The percent of cloud coverage associated with this cumulus humilis regime is much less than that associated with a stable stratocumulus deck, therefore the percent of cloud cover would decrease with increasing SST anomaly.

In the northern hemisphere where the data extends significantly poleward of the subtropical subsidence regions, the cloud-SSTA relationship as indicated by the LAD slope does not conform to large scale generalizations. However, smaller regions may have their own distinct physical processes at work. For instance, south of Japan where the high cloud-SSTA LAD slope is positive in winter and the region of positive LAD values for high clouds in the NE Pacific off the coast of Washington and British Columbia where seasonal analysis reveals that the high cloud-SSTA LAD slope values are higher in winter than summer, the positive high cloud-SSTA LAD slopes could be a result of extratropical waves feeding off increased land/sea temperature contrasts. The LAD value for low clouds in the NE Pacific off the coast of Washington is negative while high, middle, and total cloud LAD values are positive. This, therefore, is quite likely one of the locations where the observed decrease in low clouds with increasing SST anomaly is due to obscuration by increases in higher clouds.

Away from land, the northern oceans' weakly negative cloudiness-SSTA LAD slopes indicate that cloudiness tends to decrease with increases in SSTA. Seasonal analysis indicates that this negative relationship is strongest during the summer. These regions may be areas where atmospheric anomalies are driving SST anomalies. A decrease in cloudiness would increase the solar flux into the northern oceans which would increase the surface temperature. In these latitudes, a decrease in cloudiness is also associated with an increase in atmospheric pressure. A high pressure area's light winds would decrease evaporation since evaporation is related to wind speed. A decrease in evaporation would decrease the surface cooling due to latent heat flux, thereby contributing to warm SST anomalies as well. The thermocline in the northern ocean is shallowest during the summer and the solar flux is highest, therefore this effect should show up strongest during the summer months.

The whole basic premise for most regions that the SST anomaly is affecting the atmosphere instead of vice versa must be acknowledged as incomplete in any location. The time span of changes in SST is so much greater than the average time span of clouds that it is tempting to view SST as the independent variable, the driving force. However, that is far from the case in the actual ocean/atmosphere system. In addition to the

obvious effect of cloud shading cooling the ocean, in middle latitudes, SST variations are often affected by large-scale atmospheric disturbances such as increased winds enhancing ocean mixing, thereby decreasing SST (Nitta, 1986). Though strong recurring atmospheric patterns may be required to set up certain SST anomaly patterns, that “does not dispel the sea-to-air feedback possibility” (Namias *et al.*, 1988). Indeed, whatever the cause of the SST anomaly, the SST anomaly changes the flux of sensible and latent heat into the atmosphere. And these changes can affect clouds through a variety of mechanisms including, but not limited to, those proposed earlier. In addition, the observed response may, in part, be a result of fluctuations in the spacial patterns of SST, which this study does not address.

Though the quantitative radiation effects won't be addressed until Chapters 4 and 5, the strong relationship between cloud anomalies and SST anomalies suggests that there will be a cloud radiative feedback loop to global warming. The present research using SSTAs as a substitute for global warming implies that the sign of the cloud radiative feedback loop would be positive because low clouds, the clouds which cool the planet, tend to decrease with increasing SST anomaly while high clouds, the clouds that can warm the planet depending on their optical depth, tend to increase with increasing SSTA. This research found that on average, total cloudiness increased with increasing SSTA while Cess *et al.* (1990) reported that all 19 GCMs indicated cloudiness decreased with increasing SSTAs. Though Cess *et al.* (1990) gave few details about these changes in cloudiness, directly comparing these two results may not be appropriate because our results are for the open ocean from 60°N to 40°S while the GCM averages were for the entire Earth. Comparing our results with Mokhov (1990a, 1990b) we find distinct similarities and differences in the zonal average of the total cloud–surface temperature relationship. Both results show positive values in the tropics and negative in the midlatitudes. However, Mokhov's zonal average value went to 0 at the equator while ours is near the maximum value at the equator. Also, his maximum and minimum values were ~ 1 and $-1 \text{ \%}\cdot\text{K}^{-1}$ while ours are much larger, ~ 8 and $-3 \text{ \%}\cdot\text{K}^{-1}$ for all grid points.

Chapter 3

CLEAR SKY WATER VAPOR – SSTA RELATIONSHIPS

3.1 Introduction

Water vapor is *the* principal greenhouse gas (Intergovernmental Panel on Climate Change, 1990). It is highly transparent to short wave radiation, highly absorbent to long wave radiation, and very abundant. This makes analysis of water vapor crucial to our understanding of clear sky radiative feedback loops in global warming scenarios. However, such analysis can be very complex because unlike CO₂ and many of the other IR absorbing gases, water vapor is highly variable both in time and in space. Water vapor will also change phases, precipitate out and evaporate into the atmosphere.

One of the key questions in this and other research is: how will water vapor behave in response to warming due to increasing CO₂? Raval and Ramanathan (1989) determined that over oceans, the clear sky greenhouse effect was greater over regions with higher SSTs. They also found, based on microwave satellite soundings, that there was more water vapor integrated over the depth of the atmosphere over the warm tropical oceans than over colder oceans. Stephens (1990a) determined that water vapor in the atmosphere above oceans not only is related to SST, but that “negative water vapor anomalies more or less match the negative SST anomalies”. Since his research was done using data from a microwave sensor on a satellite, the water vapor anomaly that he could correlate with the SST anomaly was the water vapor integrated throughout the depth of the atmosphere. Furthermore, it was not necessarily the clear sky water vapor, because low frequency microwave sensors can “see” through clouds as long as large rain drops aren’t present. This means that the water vapor observed by microwave sensors would be weighted towards (1) water vapor near the surface where evaporation takes place and temperatures are warmest and (2) in clouds

where the relative humidity is near 100 percent. The greenhouse radiative effects of (1) can be small because the radiative temperature of the water vapor is close to the radiative temperature of the surface and the radiative effects of (2) can also be small because the IR radiative effects of water vapor inside the cloud is small compared to the IR radiative effects of the cloud droplets or crystals.

Lindzen (1990a) states that “it is primarily the distribution of infrared absorbers above 5 km (rather than below 5 km) that is important for containing the heat carried away from the earth’s surface.” The clear sky greenhouse effect of water vapor is greater the higher in the atmosphere the water vapor is located because water vapor at higher, colder levels will radiate less long wave radiation out to space. Therefore, it is important to understand not only how water vapor changes over regions of changing SSTA, but also how water vapor changes at various, especially high, levels in the atmosphere. Microwave satellites, while giving accurate insights into integrated water vapor, cannot give information on water vapor at different levels. However, satellite observations using several specific infrared wavelengths can give information on water vapor at several different levels in the atmosphere. Relating this water vapor data to SST data can provide insights into how water vapor changes over areas of positive and negative SST anomalies. Understanding how water vapor at various levels in the atmosphere responds to warming of SST is important in evaluating the clear sky greenhouse effect predicted in many global warming scenarios.

Despite some agreement “on the fundamental importance of the upper tropospheric water vapor budget to the question of global warming” (Lindzen, 1990b), there is a fair amount of debate currently underway on just how the water vapor high in the atmosphere behaves because “even though water vapor near the ground increases with increasing temperature, a smaller absolute decrease at upper levels can lead to a negative feedback” (Lindzen, 1990b). Some of this debate centers around the interaction between tropical cloud clusters and the clear sky around the cloud clusters. If the cloud clusters get larger and deeper, what happens to the clear sky water vapor in the upper troposphere? Since Chapter 2 indicated where tropical cloudiness increased in association with SSTA, the

research in this chapter should be able to indicate how clear sky water vapor changes with SSTA in these same regions and by implication how clear sky water vapor changes in relation to changes in cloudiness.

3.2 Data

3.2.1 Water Vapor

Satellite based precipitable water measurements have been taken operationally since 1978 by the TIROS-N, or NOAA series of operational polar orbiting satellites (Schwalb, 1978). Utilizing a complement of seven orbiters, the NOAA system follows two previous operational programs. The Television and Infrared Observation Satellite (TIROS) research and development system, initiated on April 1, 1960, lead to the first operational U.S. polar orbiting satellite program, the TIROS Operational System (TOS) (for overview see Colorado State University, 1982). The launch of nine TOS Environmental Science Services Administration (ESSA) satellites were followed by six Improved TOS (ITOS) platforms which carried sensors capable of higher quality observations of the atmosphere. Since then, the NOAA series of satellites (TIROS-N, and NOAA 6-11) has provided uninterrupted global coverage by up to two satellites since the October 13, 1978 launch of TIROS-N.

The NOAA satellites have a near-polar sun synchronous orbit with a 102 minute period (Schwalb, 1978). The odd numbered orbiters (including TIROS-N) have afternoon ascending nodes, while NOAA 6, 8, and 10 have morning descending nodes. This orbital strategy allows for a 90 degree orbital plane separation (to reduce the number of redundant observations) and thus up to four separate observations per day for a given region when two satellites are operational. A regular launch schedule was key in the continuous coverage by these satellites despite their relatively short two year expected lifetime (Wittmeyer, 1990a).

The TIROS Operational Vertical Sounder

Carried aboard these platforms is the TIROS Operational Vertical Sounder (TOVS) instrument package for retrieval of atmospheric temperature, ozone, and water content. The TOVS system is made up of the second generation High Resolution Infrared Radiation

Sounder (HIRS/2), the Microwave Sounding Unit (MSU), and the Stratospheric Sounding Unit (SSU) (Werbowetzki, 1981). The HIRS/2 and MSU are used for retrieval of vertical moisture profiles.

Both the HIRS/2 and the MSU instruments are cross-track scanners, capable of sensing a swath 2250 km wide. The HIRS/2 spectrometer has 19 infrared and one visible channel, and are operated simultaneously during each scan. A HIRS/2 scan takes 6.4 seconds in 56 steps, with a field of view (FOV) ranging from 17.4 km at sub-satellite point, to a 58.5 km cross-track by 29.9 km along-track FOV at end of scan.

Calibration is performed every 256 seconds, or every 40 scans, to maintain accurate radiometric observation throughout the life of the sensor (Lauritson *et al.*, 1979). Operational calibration consists of using all channels to view an internal warm target, as well as space, to aid in converting Earth viewed radiometric counts to radiance values. The time equivalent of three scans is required for calibration, and no HIRS/2 data are collected during this time.

The MSU has four channels to sense radiation in the 5.5 mm oxygen absorption band. A MSU scan takes 25.6 seconds and consists of 11 steps, with nadir resolution of 109 km. Calibration is performed during nominal data collection which allows for uninterrupted MSU observation of the atmosphere. At the end of each scan, the spectrometer views space before observing two internal targets. These values are corrected with measurements made by platinum resistance thermometers and known National Bureau of Standards space radiometric values. The spectrometer then returns to start the next Earth-view scan (Wittmeyer, 1990a).

TOVS Operational Retrieval Method

The individual scan spot data from the HIRS/2, MSU, and the third TOVS instrument, the Stratospheric Sounding Unit (SSU), is then processed to convert the 27 channel radiances to vertical profiles of temperature, water content, and ozone. The TOVS processing system consists of four modules (Werbowetzki, 1981), and is operated by the National Environmental Satellite, Data, and Information Service (NESDIS). Operationally ingested digital count data collected during one orbital period is fed into the TIROS preprocessor,

which applies various corrections and calibrations, and appends navigational information to the output. The TIROS Atmospheric Radiance Module (TARM) takes the corrected single FOV radiance data from the preprocessor and produces soundings with resolution of 250 km. The input single FOV data are grouped into 7 by 9 arrays for which tests for clouds are performed. Such tests are required since HIRS/2 infrared moisture channels, sensing radiation in water vapor absorption bands, can not be used under cloudy scene conditions due to the opaque nature of clouds at these wavelengths. The TARM uses multispectral information to determine the number of cloudy FOV's, and if four or more are deemed clear, then the centroid of the clear FOV's describes the 250 km box based on the weighted average of the clear sky radiances. If fewer than four FOV's are clear, then the N*, or adjacent pair, method (Smith and Woolf, 1976) is used to extract a clear column radiance value from the partly cloudy scene. If the above methods fail, then the box is said to be cloudy, and radiances from channels not subject to cloud contamination are averaged to produce temperature soundings in the higher layers, where little water vapor is found.

The third module, the TIROS Stratospheric Mapper (TSM), applies limb corrections and maps SSU data to conform spatially to the HIRS/2 and MSU data. TSM output, along with output from TARM, is sent to the TIROS Retrieval Module (TRET). The TRET accesses a coefficient data base which is needed to generate the temperature and water vapor profiles as calculated by the method of eigenvector regression (Smith and Woolf, 1976). The weekly updated regression coefficients are made using quasi-collocated radiosonde data, as well as space based radiance measurements, and are stratified within five latitude zones. Up to 25,000 soundings per day are theoretically possible using the above method, at the nominal 250 km resolution. However, a more modest figure of 8000 per day are operationally generated (Wittmeyer, 1990a).

The above description of the TOVS retrieval method was based on written descriptions from NESDIS. However, in response to concerns that were expressed by Randall (1990b) that TOVS actually doesn't use the three major IR water vapor channels in its water vapor retrievals, we called people working on the TOVS retrievals to get a better

understanding of the retrieval method. According to Fleming (1991), the TOVS water vapor retrievals do not use the three prime water vapor channels (10 at $8.30\mu\text{m}$, 11 at $7.30\mu\text{m}$, and 12 at $6.7\mu\text{m}$). They don't use these channels because they don't know how to model them properly. They do, however, use several other channels that "see some water vapor". These include channels 5 at $14.00\mu\text{m}$, 6 at $13.70\mu\text{m}$, 7 at $13.40\mu\text{m}$, 13 at $4.57\mu\text{m}$, and 14 at $4.52\mu\text{m}$. The weighting function of these channels have the level of peak energy contributions ranging from 1,000 hPa for channel 13 to 600 hPa for channel 5 (Werbowetzki, 1981). Fleming (1991) did not express much concern about the ability to accurately retrieve water vapor data from information provided by these channels. Instead, he expressed more concern about two other possible sources of error. One of these was the problems of using rawinsondes as ground truth, since rawinsondes are often under or in clouds where the air is more moist than the clear sky between clouds that TOVS examines. The second problem arises from terminating the water vapor retrieval at 300 mb. This was done to assist in comparison to rawinsondes which seldom record moisture above 300 mb. But such a termination changes the shape of the weighting functions, particularly in the water vapor channels.

ISCCP and ISCCP TOVS

The long term water vapor data set used in this research was the International Satellite Cloud Climatology Project (ISCCP) TOVS monthly precipitable water data which is a global 2.5×2.5 degree gridded water vapor data set available from July 1983 to 1989. ISCCP has precipitable water analysed for 5 layers: 1000-800, 800-680, 680-560, 560-440, and 440-310 hPa. These are the standard ISCCP layers used for their cloud analysis. The water vapor in them was derived from TOVS. The National Environmental Satellite, Data, and Information Service (NESDIS) makes an operational TOVS sounding product with precipitable water in three layers: 1000-700 hPa, 700-500 hPa, and 500 hPa and up with an individual accuracy goal of 30% per layer (Kidwell, 1988). To create the ISCCP precipitable water amounts, the total precipitable water in a layer is subdivided into 2 hPa thick layers based on the assumption that the relative humidity of the original layer was constant. The temperature of the 2 hPa layers were linearly interpolated from the TOVS

Sounding Product. "Since there is a small error in assuming a constant relative humidity over the original layers, the final values at 2 hPa intervals are adjusted so that their sum is equal to the original TOVS layer mean water amounts" (Rossow and Kachmar, 1988).

Since 5 separate layers are not needed for purposes of this research, we combined the ISCCP TOVS data into three layers: 1000-800 hPa (low), 800-560 hPa (middle), and 560-310 hPa (high), as well as total precipitable water. Combining a couple of the levels of the ISCCP TOVS data set also brings our data closer to the original TOVS Sounding Product.

TOVS Evaluation

Approximately 8,000 TOVS soundings are processed daily. This provides not only good spacial resolution, but when averaged over a month, the errors in individual soundings are smoothed. This is not to say that the TOVS soundings actually represent the true water vapor in the atmosphere. Since the TOVS sounding tropospheric retrievals cannot be performed during times of total clouds, though they may during times of partial cloud cover, ISCCP TOVS data will have a distinct bias towards clear sky values. Which is exactly what we are looking for in this research.

Early TOVS evaluation was done by Gruber and Watkins (1979) and showed the ability of the system to adequately sense atmospheric moisture content under certain conditions. In regions of cloud free air the retrieval scheme produces layer moisture values comparable to quasi-collocated radiosonde observations. However, TOVS retrievals overestimate moisture content in high pressure regimes where dry, sinking air can be found (Wittmeyer, 1990a). Too much moisture in the retrievals of subtropical ridges, such as off the west coast of South America, was also found by Robertson (1990) in his comparison between the European Centre for Medium Range Weather Forecasts (ECMWF) water vapor, which uses TOVS soundings as a data source, and water vapor retrieved from microwave satellite data. Since the retrieval scheme forces a profile that is representative of mean conditions, the dry scenario is not well represented. Similarly, the water content of a deep moist layer is underestimated. Long term means of total column moisture are biased toward the land based mean conditions because the first guess fields generated are from

collocated radiosonde data (Wittmeyer, 1990a). However, a recent evaluation of TOVS soundings, as compared with aircraft dropwindsonde data, over tropical oceans was done by Khalsa and Steiner (1987) and concluded that “although TOVS cannot detect sharp features such as inversions, it can return the coarse features of the atmospheric temperature and humidity to the extent that useful stability indices can be formed.” For our use, we need to be able to see coarse features in humidity and we don’t need to be too concerned about general biases in the data: since the data set to be used in our analysis is the anomaly data set, the mean value in a region (whether it is biased a little high or a little low) is not germane to this research.

Analysis of the standard deviation of the ISCCP TOVS water vapor data (Wittmeyer, 1990b) indicates that it is not high where one might expect. For example, the standard deviation of water vapor determined by microwave retrieval (Tjemkes, 1990) indicates that total water vapor is highly variable in regions of transient midlatitude cyclones while ISCCP TOVS water vapor does not indicate strong deviations there. For September 1987, Tjemkes’ (1990) total water vapor retrieval from the SSM/I had a standard deviations in the North Pacific as high as 2.0 cm with several small regions in excess of 1.5 cm; while Wittmeyer’s (1990b) analysis of the standard deviation of ISCCP TOVS total water vapor for the same month had maximum in this region of 0.9 cm with several areas as high as 0.8 cm. Some of the reason for this difference lies in the TOVS bias towards clear areas. The ISCCP TOVS lower standard deviation in these regions probably indicates that the water vapor in the clear areas between the transient cyclones is not as variable as water vapor retrievals that are made in both clear and cloudy conditions as the Tjemkes retrievals reported above were. In addition, the smoothing effect of using weekly-updated regression coefficients based on quasi-collocated radiosonde data also makes ISCCP TOVS less variable on a daily basis. However, much short term variability would be filtered out anyway by our use of monthly anomalies.

Though soundings are carefully screened for cloud contamination, a possible source of error to the soundings may occur if the sounding mistakenly perceives the top of low clouds as the sea surface. Asking whether this error would make the TOVS retrieval too

moist or too dry caused considerable debate at NESDIS, with no one positive which way the error would be (Gardner, 1991).

The TOVS data quality question that is germane to this research is the question of trends. Data from several different satellites went into this data set. Furthermore, the TOVS retrieval algorithms may not have remained exactly the same during these 6 years. Therefore, we have looked at the year to year variations in the ISCCP TOVS water vapor as shown in Figures 3.1-3.4. Analysis of the year to year changes in zonally averaged water vapor retrievals indicates no clear trend in the data. Therefore, no adjustments were made to the water vapor values provided by ISCCP TOVS.

Despite being a 6 year data set, 72 months of valid ISCCP TOVS data was not available. No ISCCP TOVS water vapor data was available for the month of May 1986, though other missing data problems were fairly minor. The ISCCP TOVS grid consists of 10,368 grid points. Of these, 5,777 were removed from this analysis due to land or sea ice consideration. Of the remaining 4,591 grid points, 245 had one additional month of missing data and 15 had two additional months of missing data.

3.2.2 SST

The SST data set used was the same Climate Analysis Center's monthly SST data used in Chapter 2. However, the dates of the available ISCCP TOVS data that were used, July 1983 through June 1989, were times when the CAC's SST data set covered the full globe. After the appropriate monthly anomaly data set was created based on averages for those six years, the 2 x 2 degree SST data was transformed into the 2.5 x 2.5 degree ISCCP TOVS grid by interpolating nearby SST anomaly values to obtain an SST anomaly value for near the center of the TOVS grid box. To avoid land/ocean effects, grid boxes with more than 5% land were flagged so they would not be included in the analysis. Similarly, to avoid ocean/ice effects, grid boxes which had near center monthly SST value for any of the 72 months of this study of less than -1.5 degrees C (-1.8°C is the freezing point of sea water) were flagged and excluded from the analysis as well.

The CAC has several different techniques for deriving their monthly average SST depending on the availability of various types of data. Each month's SST data has a flag

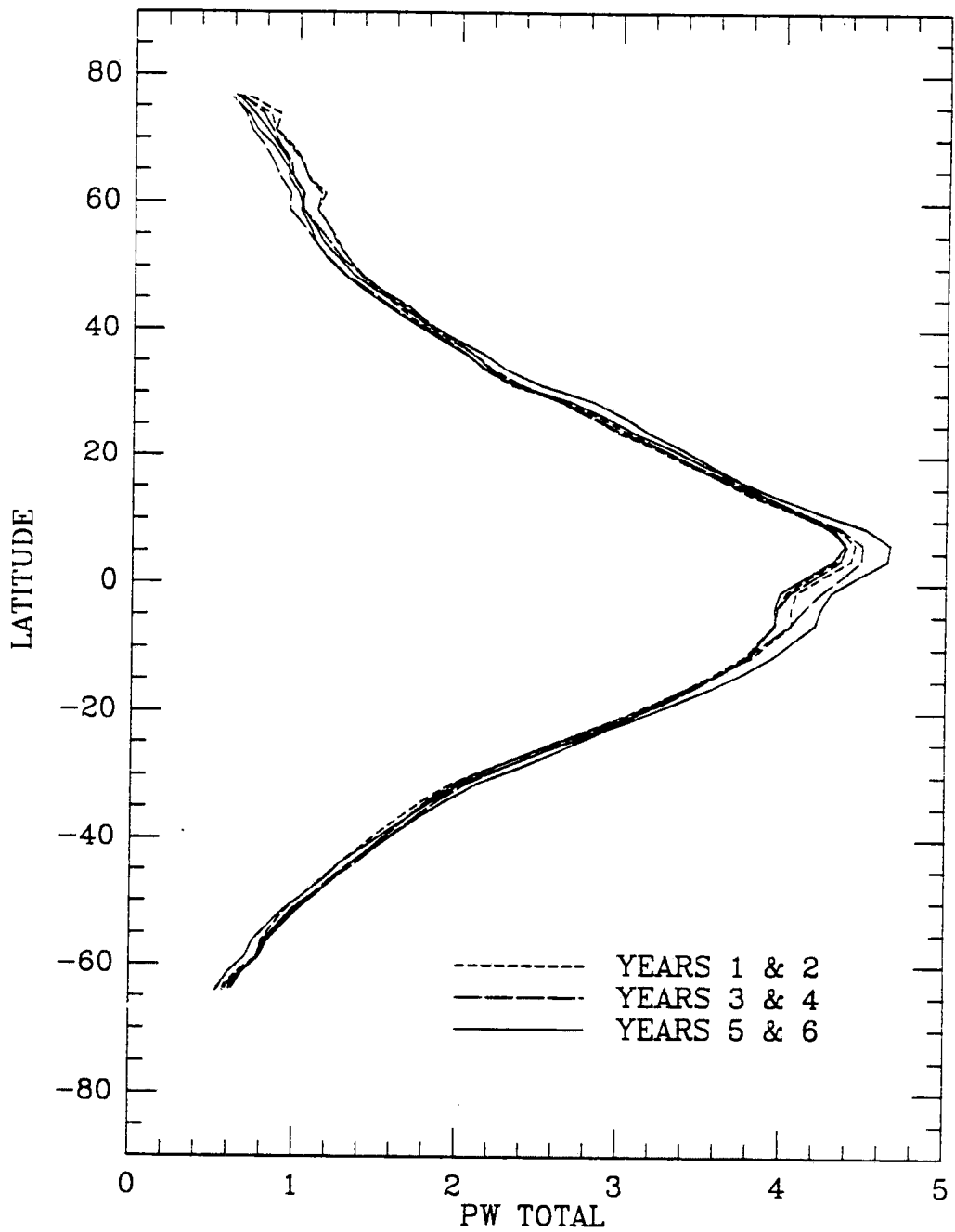


Figure 3.1: Zonally averaged Total ISCCP TOVS water vapor. The years run from July to June, 1983 to 1989. Units are in cm of liquid equivalence.

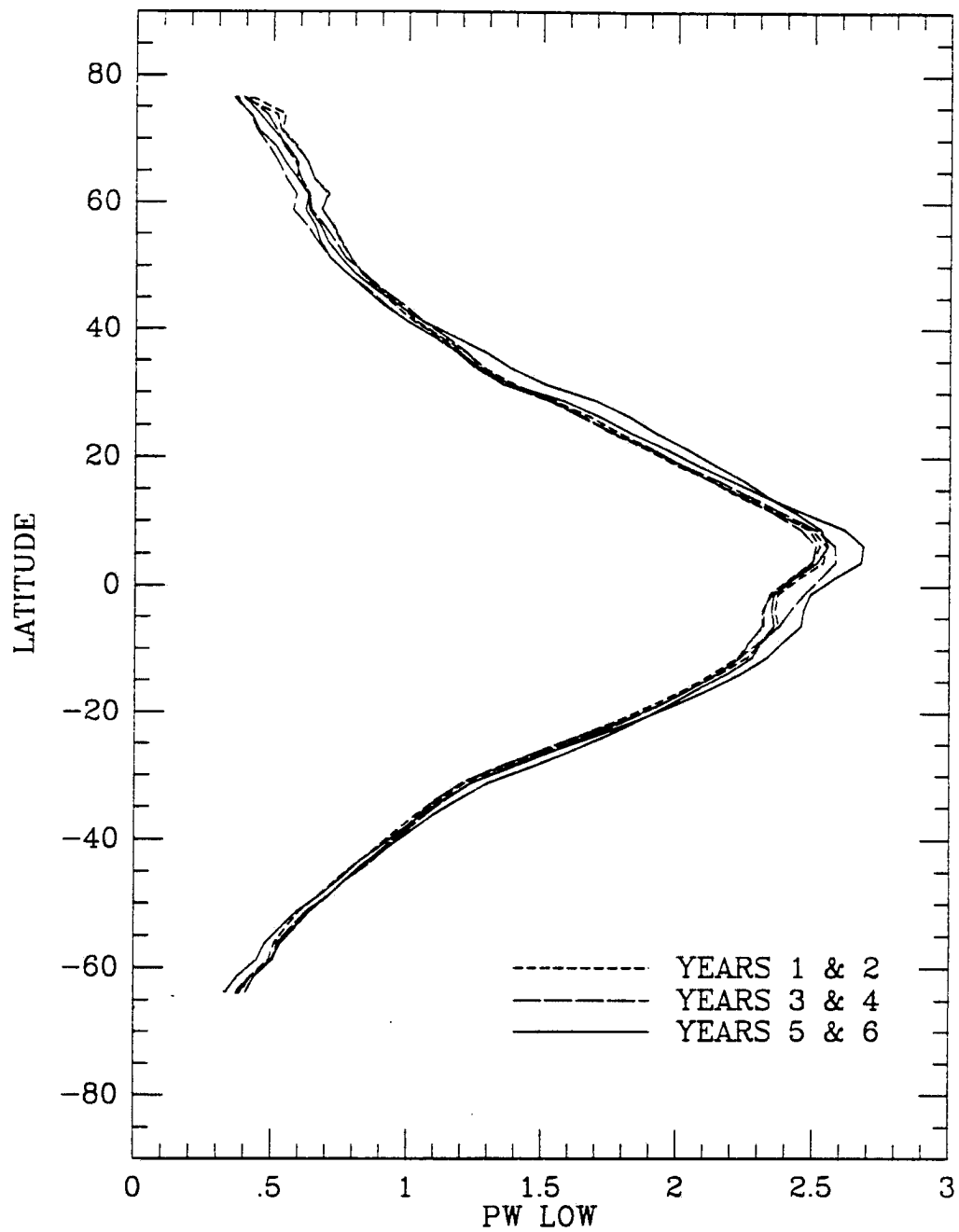


Figure 3.2: Zonally averaged Low ISCCP TOVS water vapor. The years run from July to June, 1983 to 1989. Units are in cm of liquid equivalence.

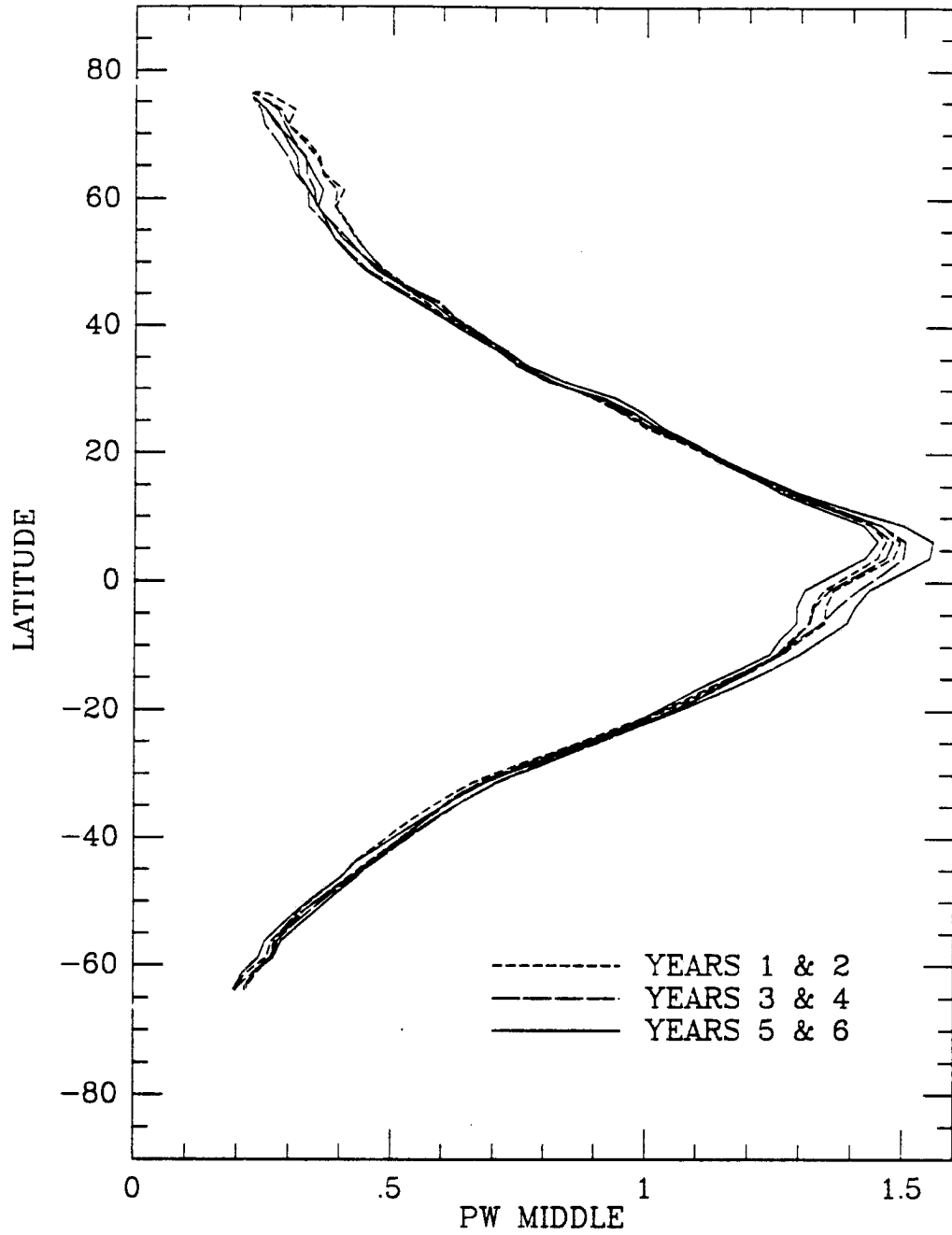


Figure 3.3: Zonally averaged Middle level ISCCP TOVS water vapor. The years run from July to June, 1983 to 1989. Units are in cm of liquid equivalence.

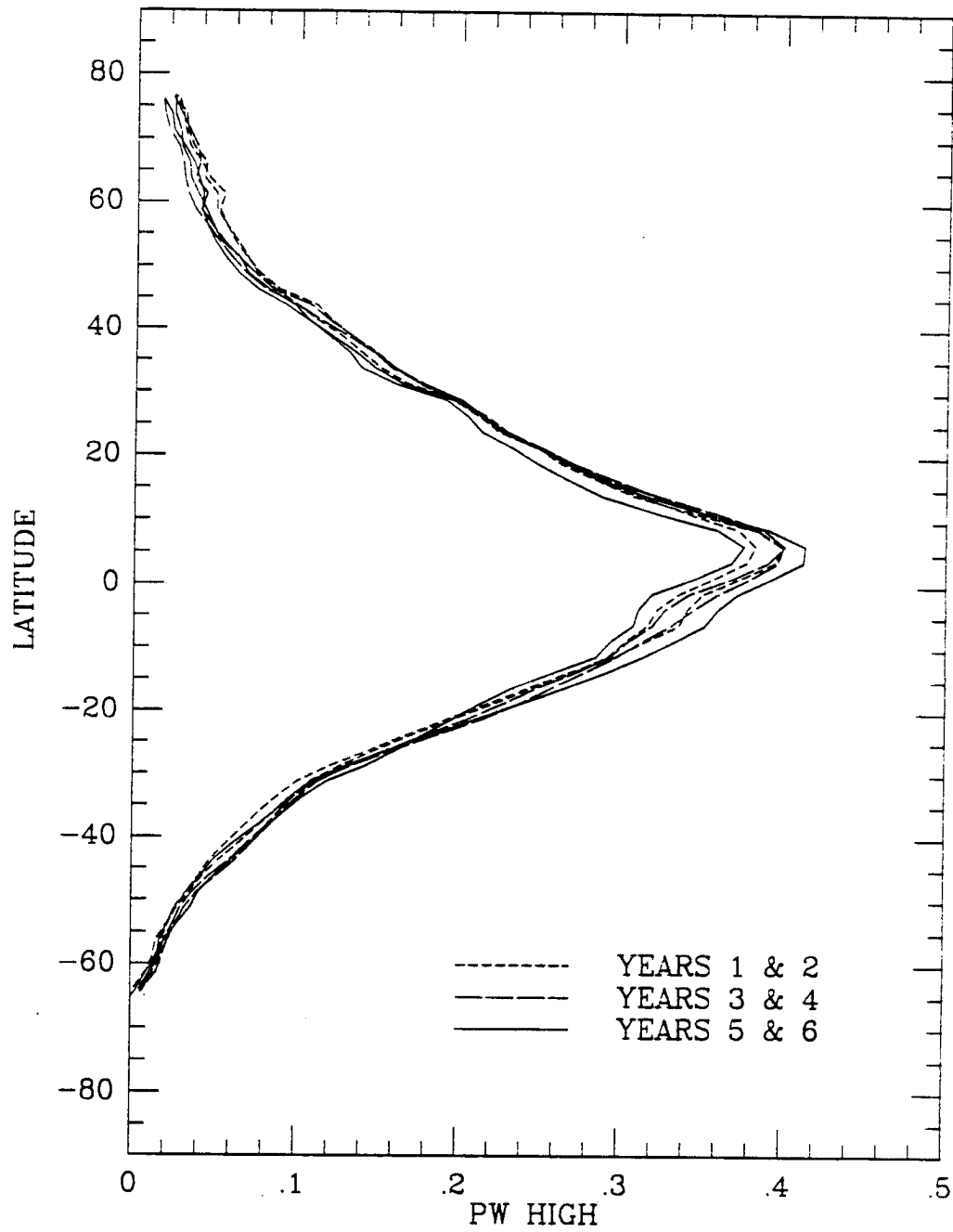


Figure 3.4: Zonally averaged High ISCCP TOVS water vapor. The years run from July to June, 1983 to 1989. Units are in cm of liquid equivalence.

for each grid box indicating which type of analysis was used to determine the SST. For type 1, the blended SST value is anchored by *in situ* analysis and there are at least 5 *in situ* observations per month. Type 5's SST value is determined by relaxation of the *in situ* analysis with satellite forcing and the number of satellite observations is at least 10 per month. For type 6, the blended SST value is determined by relaxation of the *in situ* analysis with the satellite forcing set to zero and there are less than 10 satellite observations per month (Reynolds, 1988). The area weighted average for the entire research area is 25 months of type 1, 44 months of type 5, and 2 months of type 6.

3.3 Method

A LAD regression analysis between the water vapor anomaly data sets and the SST anomaly data set was performed in a manner similar to that described in Chapter 2 with only two differences. The first is the number of analyses performed. With a finer grid scale in the ISCCP TOVS versus Nimbus-7 data set and no poleward limitations on the SST data set, once grid boxes with more than 5% land and grid boxes with sea ice were removed, there were still 4,591 grid points to perform the LAD analysis on. The second difference was with the number of months used in the analysis. Unlike the 6 year Nimbus-7 data set, the six years of ISCCP TOVS had some missing data. The full year LAD analysis at each grid point was usually performed using 71 data points instead of 72.

3.4 Results

On a global average, the water vapor–SSTA LAD slope at all levels is positive. Examination of Table 3.1 reveals that on a global average, a 1°C increase in SSTA is associated with a 0.122 cm increase in precipitable water. Summation of the average LAD slope values for low, middle, and high precipitable water vapor (PW) is 0.121. Such close agreement indicates that this technique is robust. Looking only at grid points with a P-value less than or equal to 0.05, indicating a low probability that the data was randomly distributed, the globally averaged values increase at all levels. Evidently grid points with higher LAD slopes have a greater likelihood of having low P-values.

Table 3.1: Area averaged values of PW-SSTA LAD slope. Units are $\text{cm}\cdot\text{K}^{-1}$. Based on data from July 1983 through June 1989.

TOVS PW	All Prob	Prob ≤ 0.05
Total	0.122	0.165
Low	0.071	0.090
Middle	0.038	0.057
High	0.012	0.023

Table 3.2: Number and percentage of PW-SSTA LAD regression grid points with low P-values. Based on data from July 1983 through June 1989.

PW Grid Points:	All Prob	Prob ≤ 0.05	Percent ≤ 0.05
Total	4591	3078	66%
Low	4591	3340	73%
Middle	4591	2710	59%
High	4591	2069	45%

Figures 3.5, 3.6, 3.7, and 3.8 indicate that this is indeed the case. Examination of these figures also reveals that there are very few grid points with negative PW-SSTA LAD slopes that also have low P-values. Since these figures cut off some of the more extreme values in the interest of clarity, remember that the handful of grid points with LAD slopes less than zero and low P-values is out of a total of 4,591 grid points. While the different scales necessary for these figures and the heavy overlapping of data points at positive LAD values and very small P-values makes it difficult for direct comparisons between these results, one can still conclude that the weakest signal appears to be in precipitable water high in the troposphere. Indeed, looking at Table 3.2 reveals that High PW-SSTA regression had the lowest percent of grid points with low P-values while Low PW-SSTA had the highest.

Figure 3.9 shows the zonally averaged values for the water vapor-SSTA LAD slopes. The highest values for total, low, and middle level water vapor-SSTA LAD slopes are just north of the equator. However, the highest values for upper tropospheric water vapor-SSTA LAD slope occurs about 15°S . All zonally averaged LAD slope values approach 0

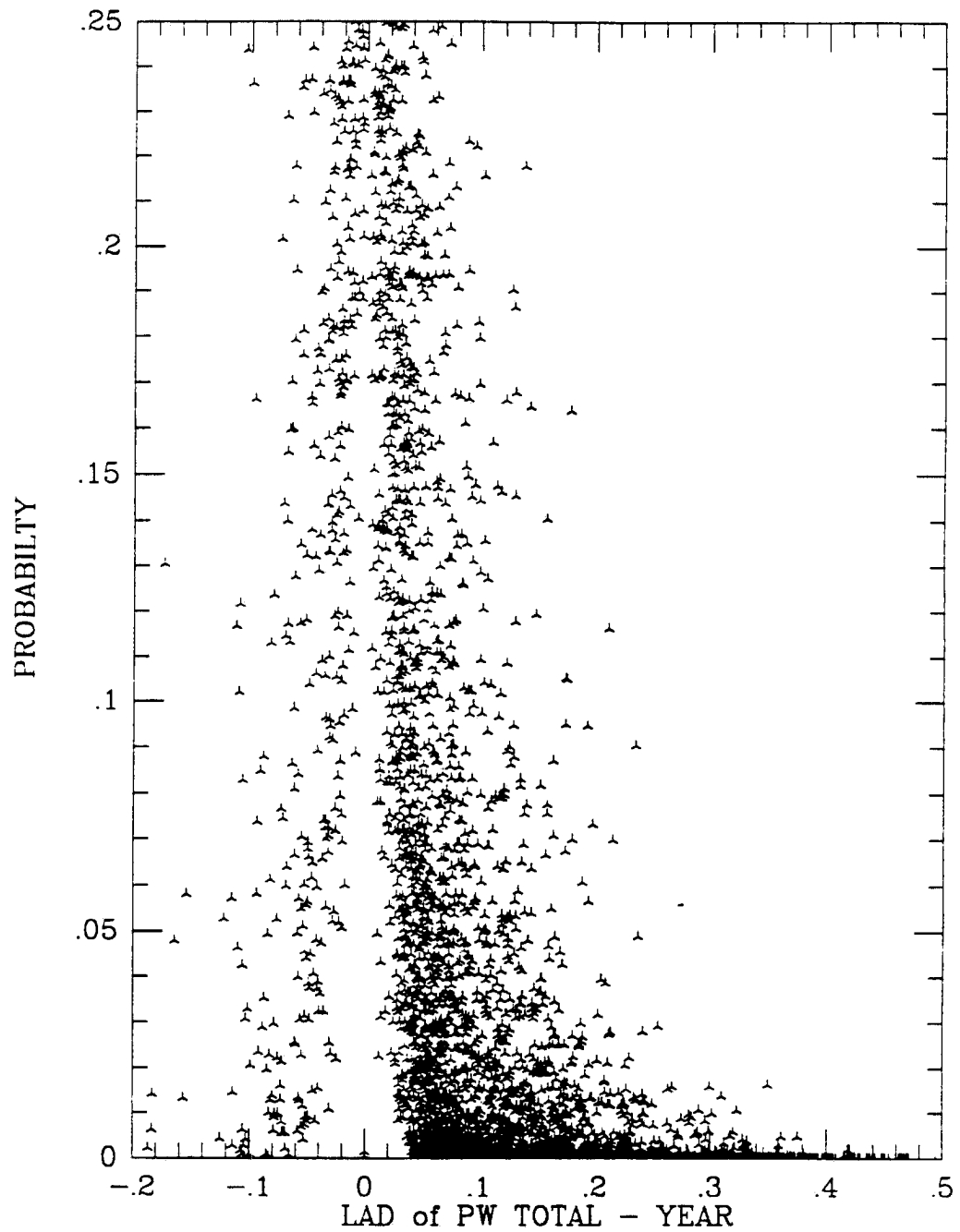


Figure 3.5: Scatter plot of Total PW-SSTA LAD regression slope values versus the Probability that the data was randomly distributed around the regression line. The P-value is unitless and the LAD slope has units of $\text{cm}\cdot\text{K}^{-1}$. Based on data from July 1983 through June 1989.

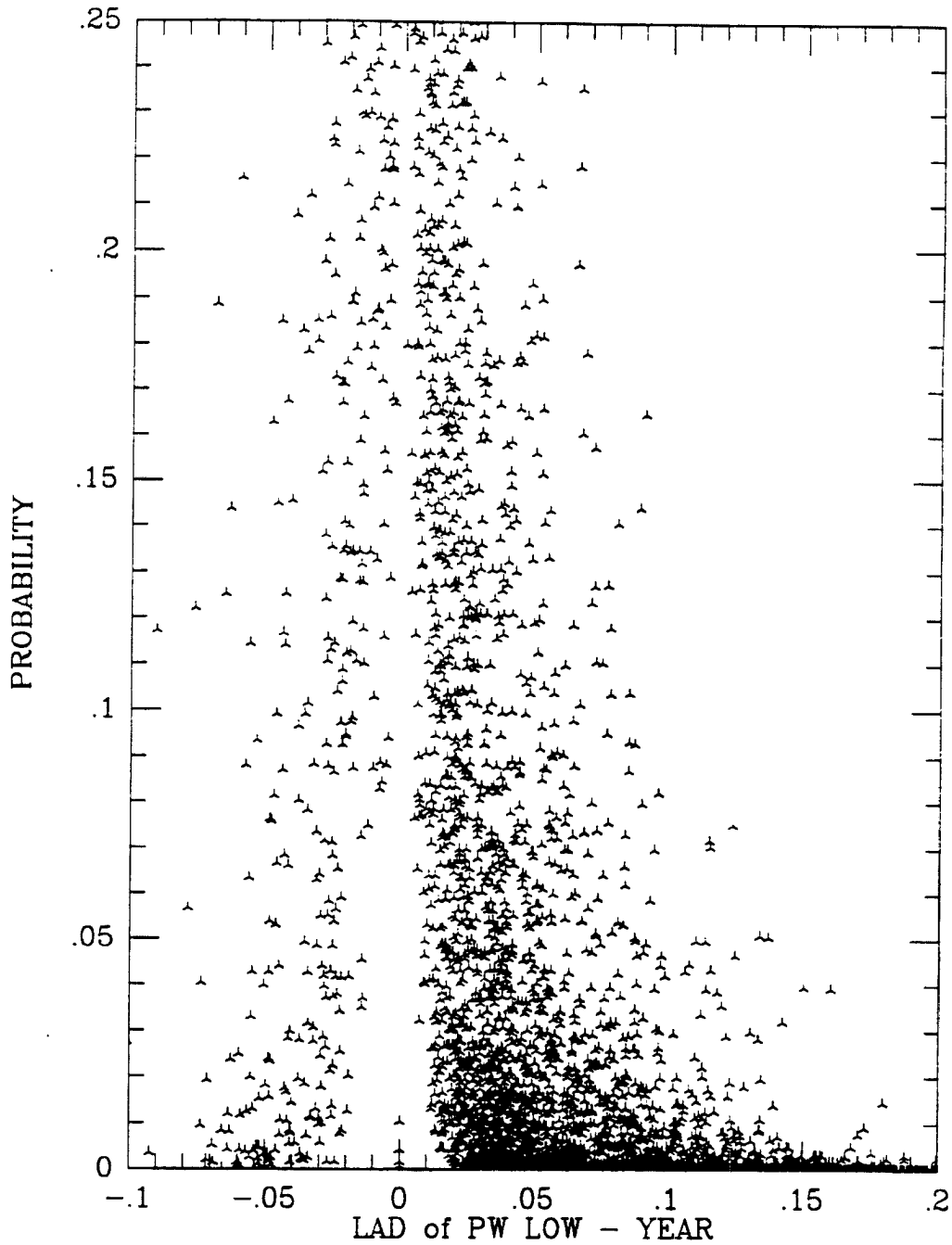


Figure 3.6: Scatter plot of Low PW-SSTA LAD regression slope values versus the Probability that the data was randomly distributed around the regression line. The P-value is unitless and the LAD slope has units of $\text{cm}\cdot\text{K}^{-1}$. Based on data from July 1983 through June 1989.

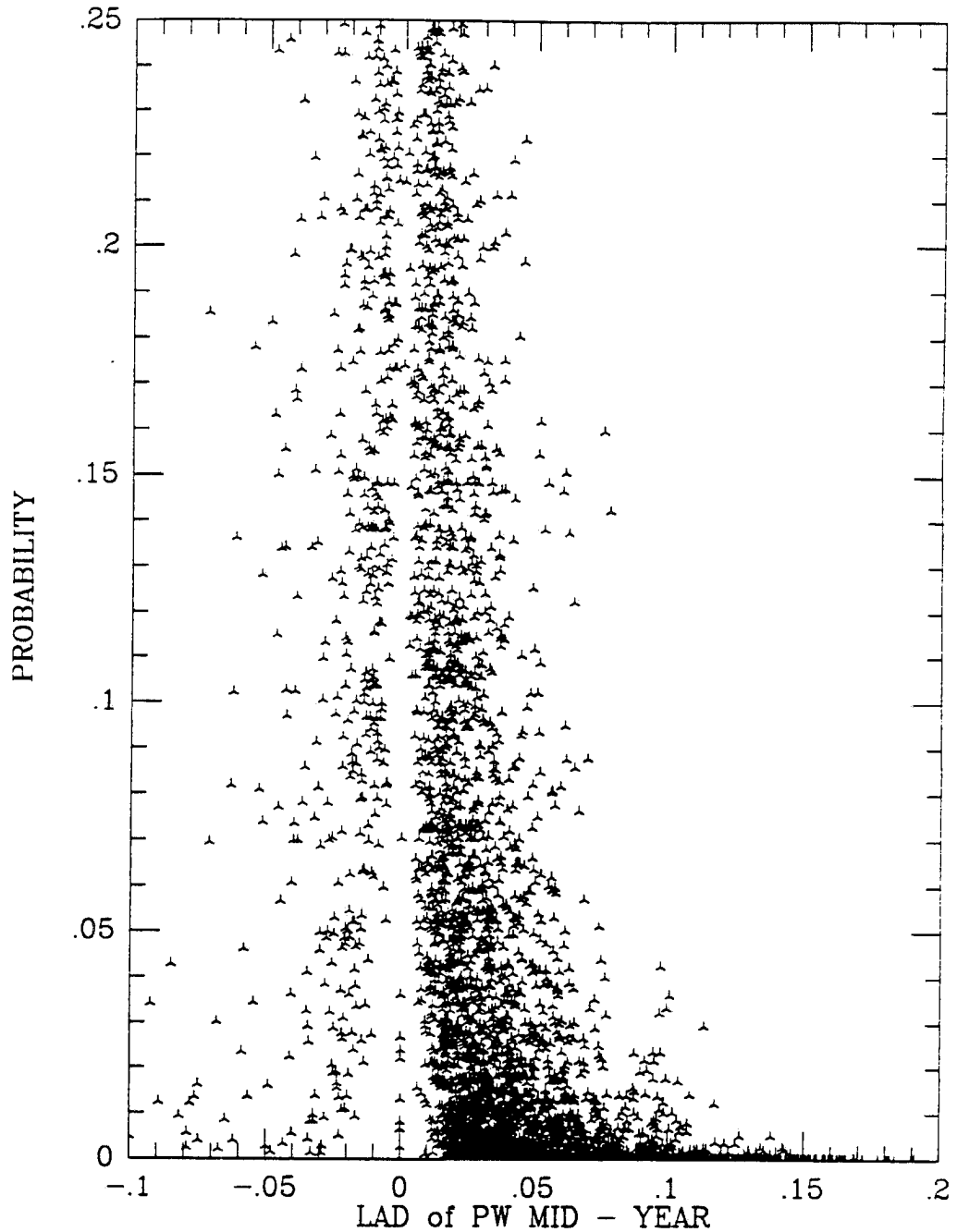


Figure 3.7: Scatter plot of Middle Level PW-SSTA LAD regression slope values versus the Probability that the data was randomly distributed around the regression line. The P-value is unitless and the LAD slope has units of $\text{cm}\cdot\text{K}^{-1}$. Based on data from July 1983 through June 1989.

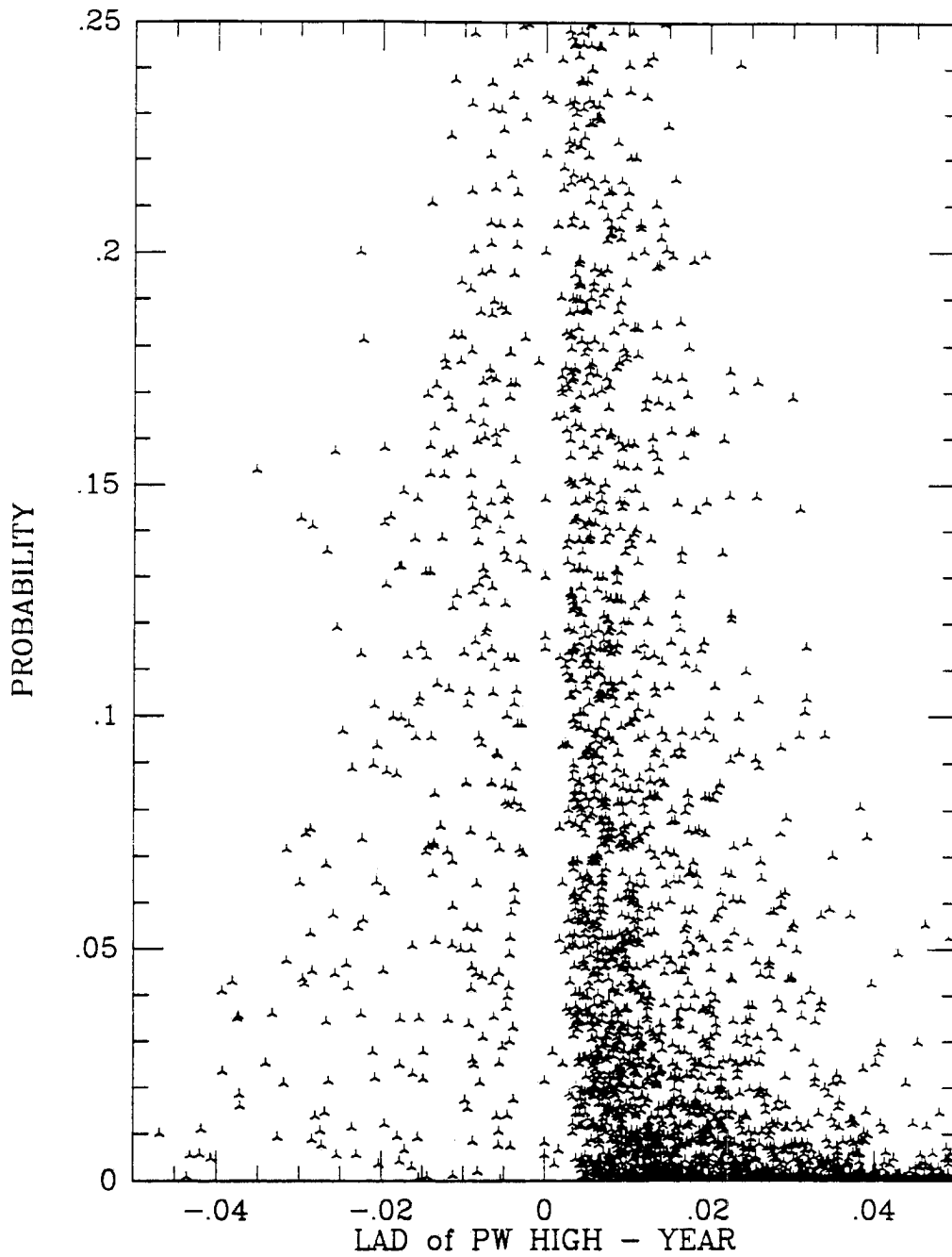


Figure 3.8: Scatter plot of High PW-SSTA LAD regression slope values versus the Probability that the data was randomly distributed around the regression line. The P-value is unitless and the LAD slope has units of $\text{cm}\cdot\text{K}^{-1}$. Based on data from July 1983 through June 1989.

near 60° North and South, with the southern hemisphere having negative zonally averaged total and low water vapor–SSTA LAD slopes south of 60°S.

However, the previously referred to table and figures cannot indicate anything about possible clumping of low P-value grid points. For that analysis we need to examine Figures 3.10, 3.11, 3.12, and 3.13. Such examination reveals that the 73% to 45% of the grid points that had low P-values were definitely not scattered randomly around the globe but instead showed strong regional clumping.

The strongest positive PW–SSTA LAD regression relationship for all levels is in the central tropical Pacific Ocean and in the tropical Indian Ocean. Generally, the farther from the equator, the lower the LAD slope.

The strongest negative PW–SSTA LAD regression relationship is in low levels of the atmosphere in a region off the SW tip of South America. Another, smaller region of negative PW–SSTA relationship is off the SE coast of Greenland. This again is most dominant in low levels of the atmosphere. A short distance SW of Indonesia is a small region of negative PW–SSTA relationship, but this area is most significant in the middle and upper troposphere. These are about the only significant regions with negative PW–SSTA slopes with low P-values.

Seasonal LAD analysis of PW–SSTA relationship were made on all 4 water vapor data sets. Examination of images of the seasonal LAD analyses revealed that the seasonal signal has regional variability on a smaller space scale than full year analyses. Also, unlike the cloud–SSTA LAD relationship, the water vapor–SSTA relationship does not show any clear north/south movement with the seasons. Examination of the region off the SW coast of South America with a negative PW–SSTA relationship revealed that this region had a negative PW–SSTA LAD slopes in each of the 4 seasons.

Examination of Figure 3.14 reveals the relationship between the water vapor–SSTA LAD slope and the average SST. Though there is a lot of scatter, it is clear from this figure that the highest LAD slopes are over the warmest waters. Also, below about 20°C, the relationship is quite uniform. Only above 20°C do the LAD slopes significantly increase with increases in SST. Interestingly, this appears to be true for water vapor at all levels of the troposphere.

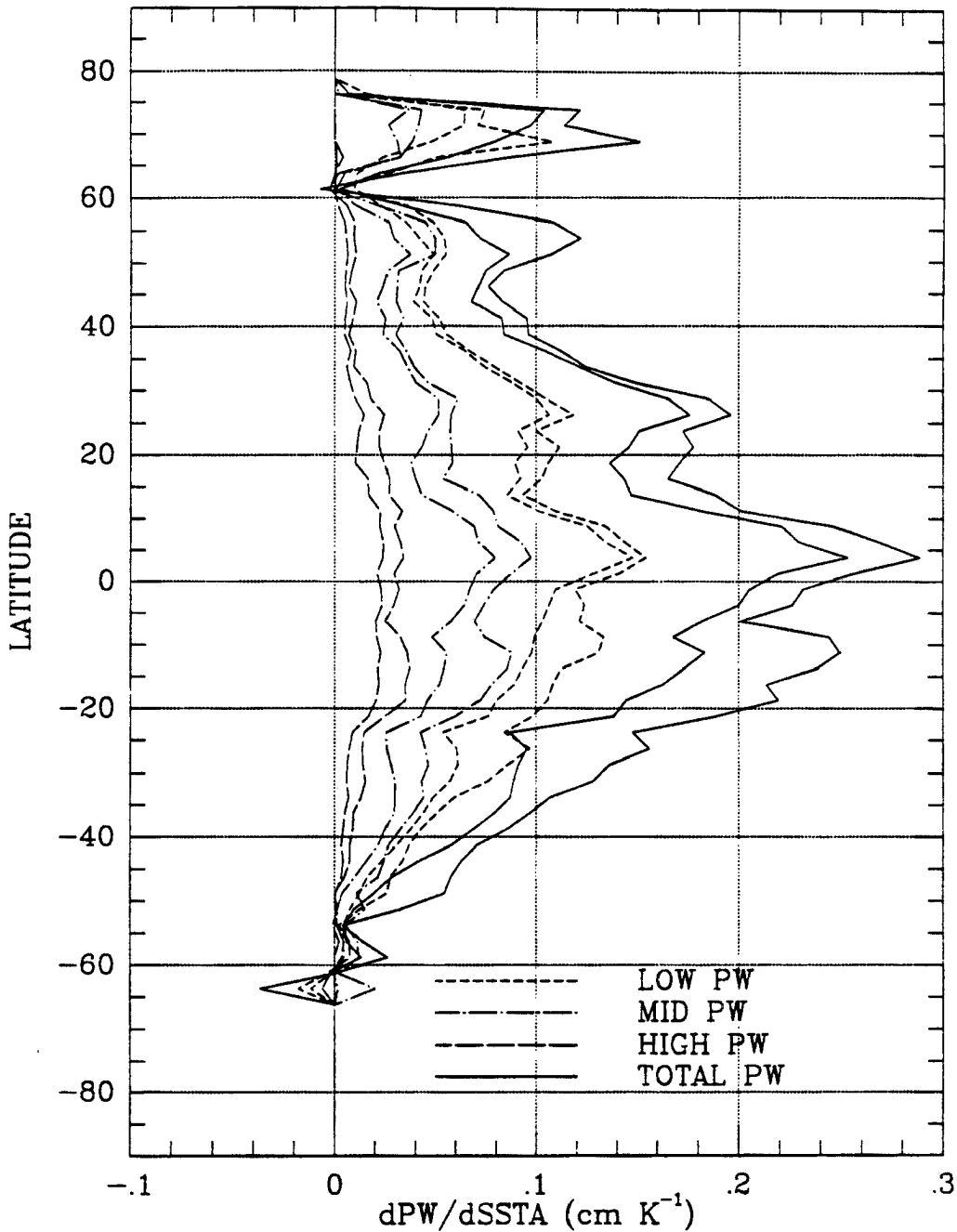


Figure 3.9: Zonal averages for total, high, middle, and low PW-SSTA LAD slopes. Each level has two lines. One line is the zonal average for all grid points and the other line is the zonal average LAD slope values only for grid points with $P \leq 0.05$. In all cases, where the value is positive, the higher values are for the low P-value grid points. In the small regions where the LAD slope is negative, the low P-value grid points have lower zonal averages. Units are $cm \cdot K^{-1}$. Based on data from July 1983 through June 1989.

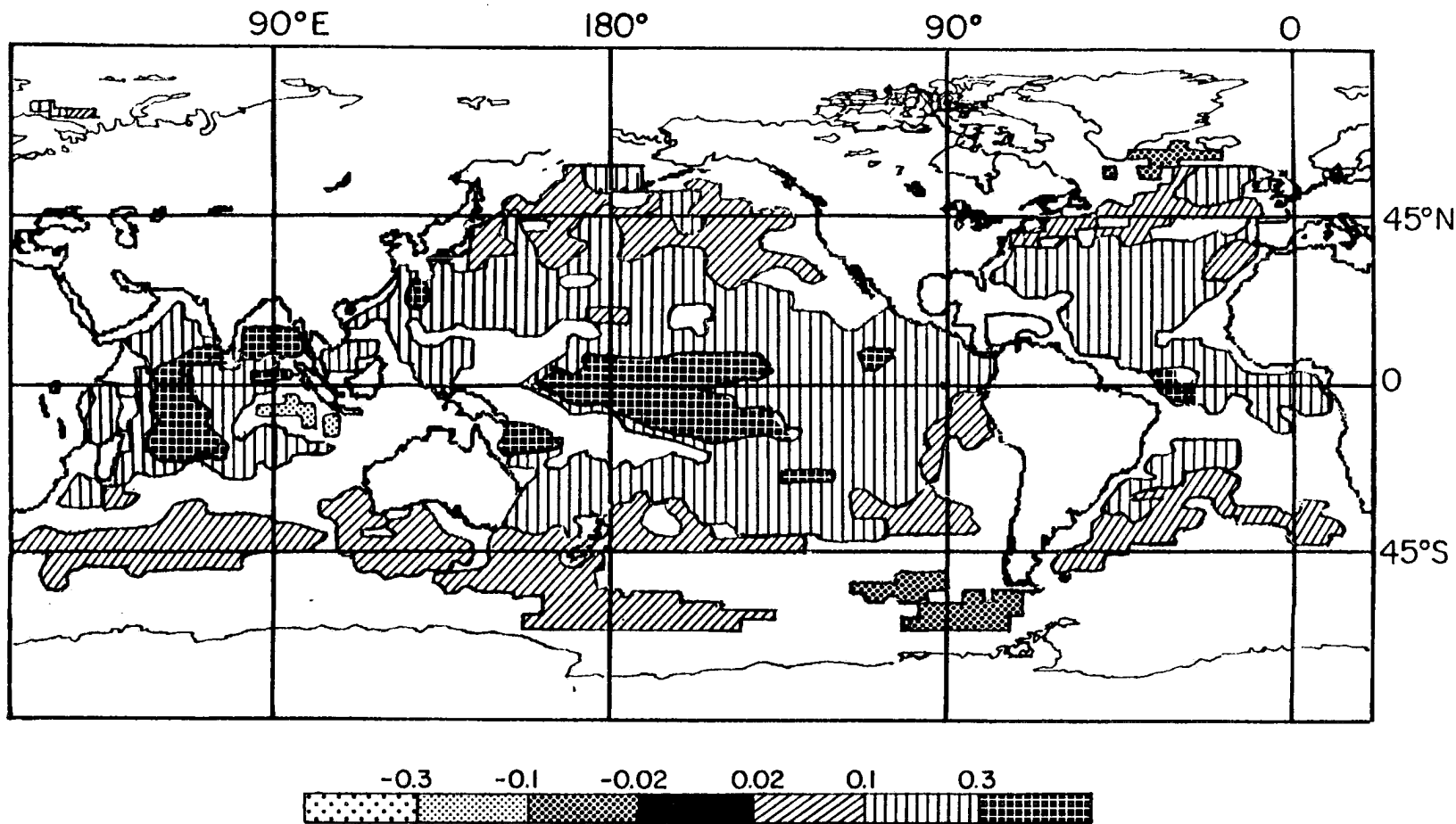


Figure 3.10: Contour plot of Total PW-SSTA LAD regression slopes showing areas where the grid points had a P-value less than or equal to 0.05. Figure is of the full data set analysis. Units are $\text{cm}\cdot\text{K}^{-1}$. Based on data from July 1983 through June 1989.

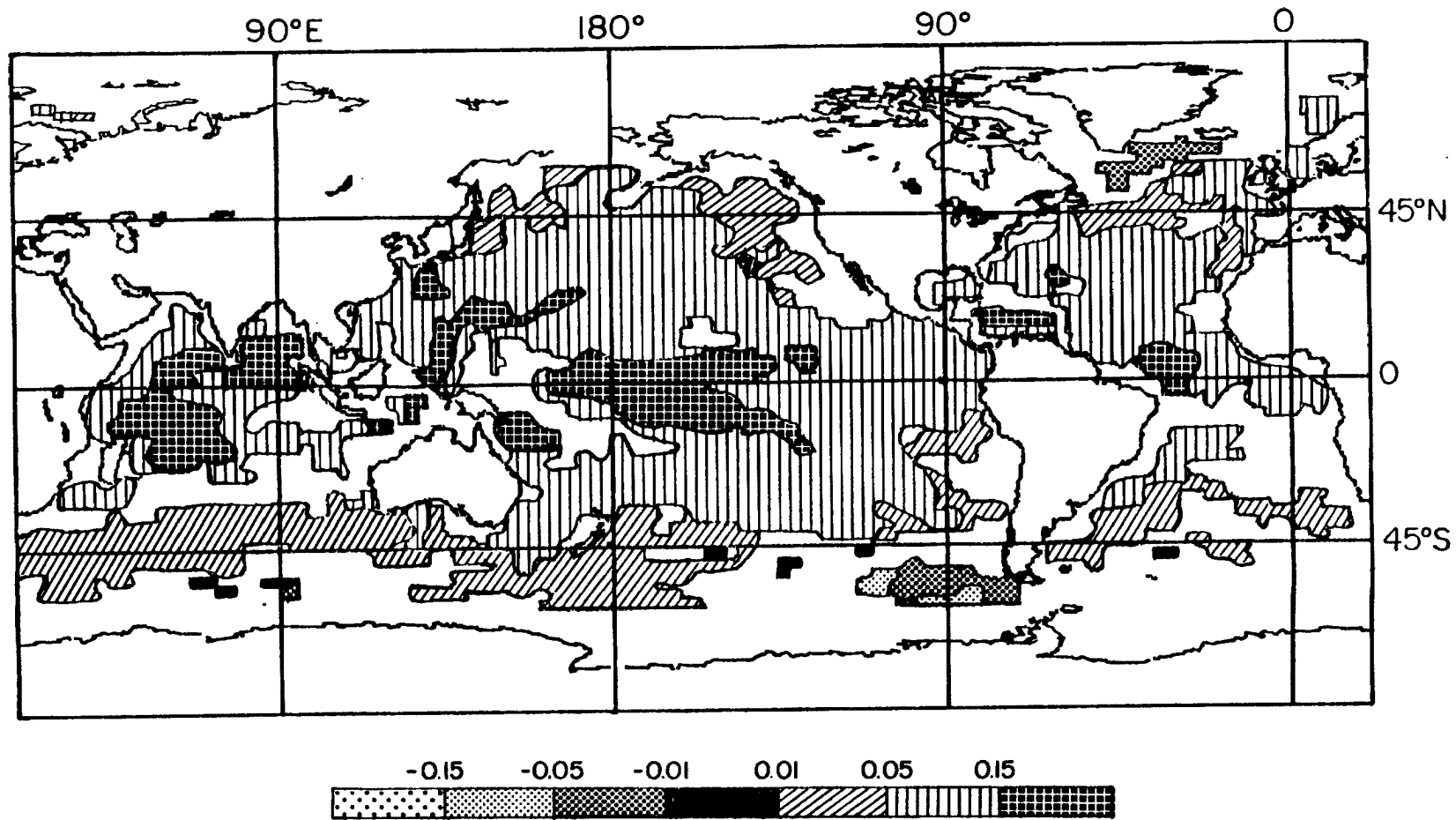


Figure 3.11: Contour plot of Low PW-SSTA LAD regression slopes showing areas where the grid points had a P-value less than or equal to 0.05. Figure is of the full data set analysis. Units are $\text{cm}\cdot\text{K}^{-1}$. Based on data from July 1983 through June 1989.

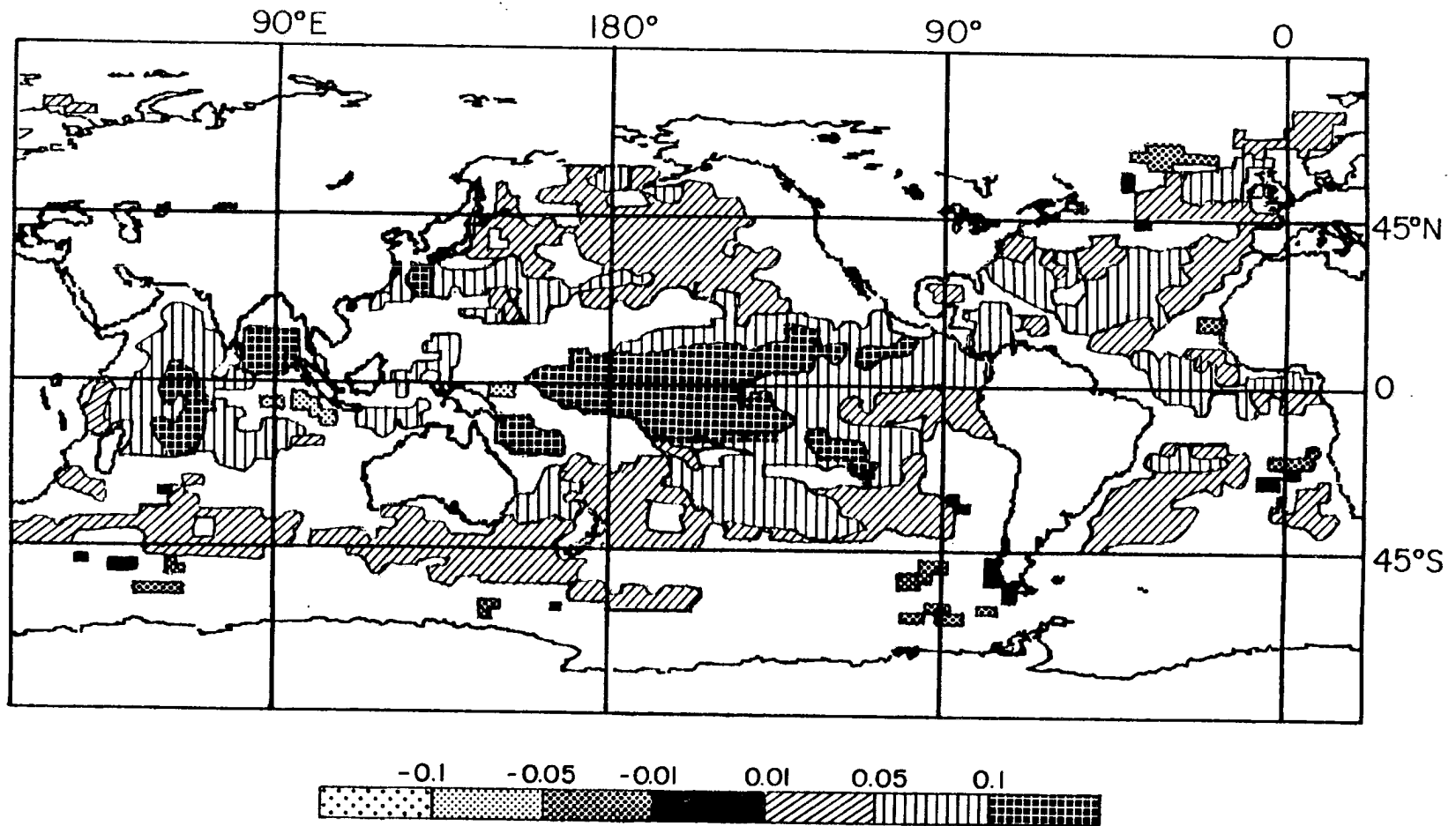


Figure 3.12: Contour plot of Middle PW-SSTA LAD regression slopes showing areas where the grid points had a P-value less than or equal to 0.05. Figure is of the full data set analysis. Units are $\text{cm}\cdot\text{K}^{-1}$. Based on data from July 1983 through June 1989.

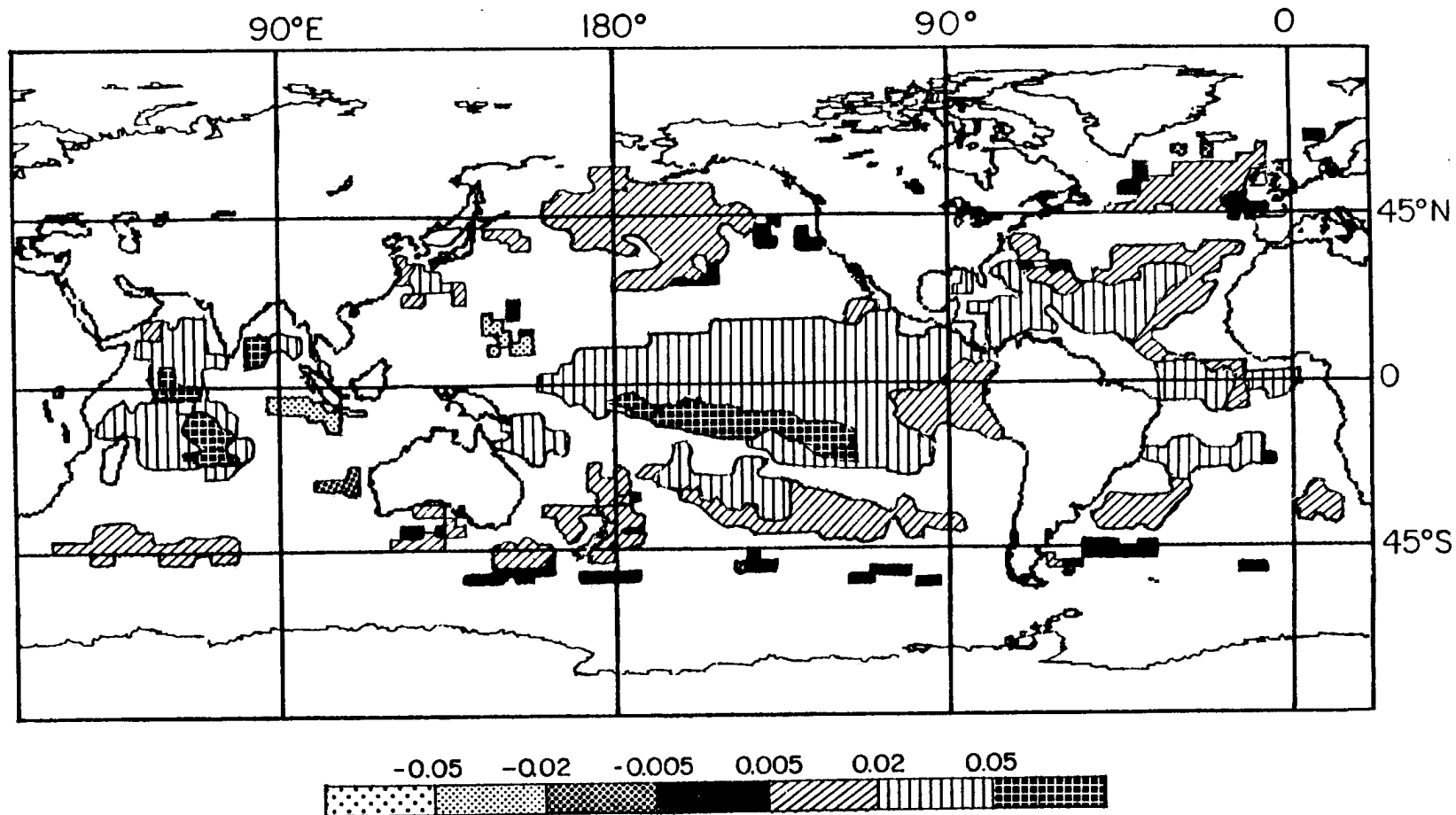


Figure 3.13: Contour plot of High PW-SSTA LAD regression slopes showing areas where the grid points had a P-value less than or equal to 0.05. Figure is of the full data set analysis. Units are $\text{cm}\cdot\text{K}^{-1}$. Based on data from July 1983 through June 1989.

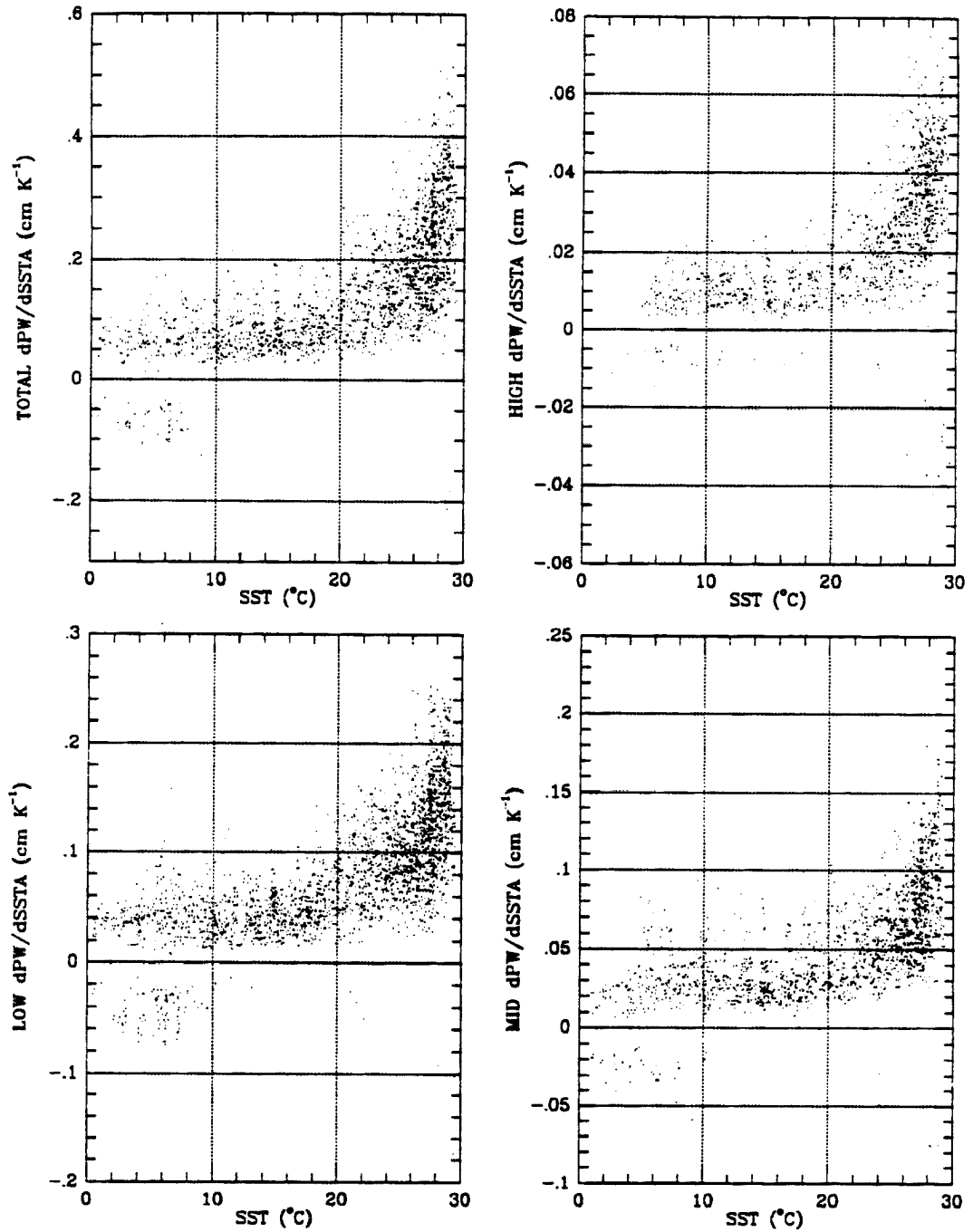


Figure 3.14: Total, high, middle, and low water vapor-SSTA LAD slopes plotted against SST. Only grid points with $P \leq 0.05$ are shown. Units for the water vapor-SSTA LAD slope are $\text{cm} \cdot \text{K}^{-1}$ and SST is in degrees C. Based on data from July 1983 through June 1989.

The cloud and water vapor data sets overlap for only 22 months. This is too short a period of time to create an adequate anomaly data set with the seasonal cycle removed which allow us to perform a direct cloud–water vapor LAD analysis. Therefore, to look at the relationship between changes in cloudiness and changes in clear sky water vapor, we interpolated the cloud–SSTA LAD slopes and probabilities into the finer ISCCP grid and compared only grid points with $P \leq 0.05$ for both cloud– and water vapor–SSTA LAD analysis. Figure 3.15 gives some indication of the relationships between changes in cloudiness and changes in clear sky water vapor. In interest of brevity, only four of the 16 possible combinations of clouds and water vapor are shown. One generality revealed by this figure is that the larger the increase in clouds with increases in SSTA, the larger the increase in water vapor with increases in SSTA. This is true for all the cloud levels and water vapor levels plotted. Another feature revealed by Figure 3.15 is that generally whether clouds increase or decrease with increases in SSTA at that grid point, clear sky water vapor will increase with increases in SSTA.

3.5 Discussion

Lindzen (1990a) hypothesizes that “although, in nature, warming increases water vapor near the ground, warming is also associated with more and deeper cumulus convection. This leads to drying of the upper troposphere (above 5 km).” A clear argument can be made to support this conclusion. Clouds in general are sometimes looked on as elements that dry the atmosphere because the precipitation that falls out of the cloud to the earth was formally water vapor in the atmosphere. Further, examining the change in cloud depth, a precipitating parcel of air that rises to the 5 km level before detraining from the cloud and evaporating puts more moisture into the cloud free region at 5 km elevation than a similar parcel rising to 6 km before detraining and subsiding to the 5 km level because some of the extra moisture condensed on the rise from 5 km to 6 km would have precipitated out during that rise.

However, clouds can also be looked upon as elements that moisten the atmosphere because clouds transport moist air from near the surface up to higher and dryer levels of

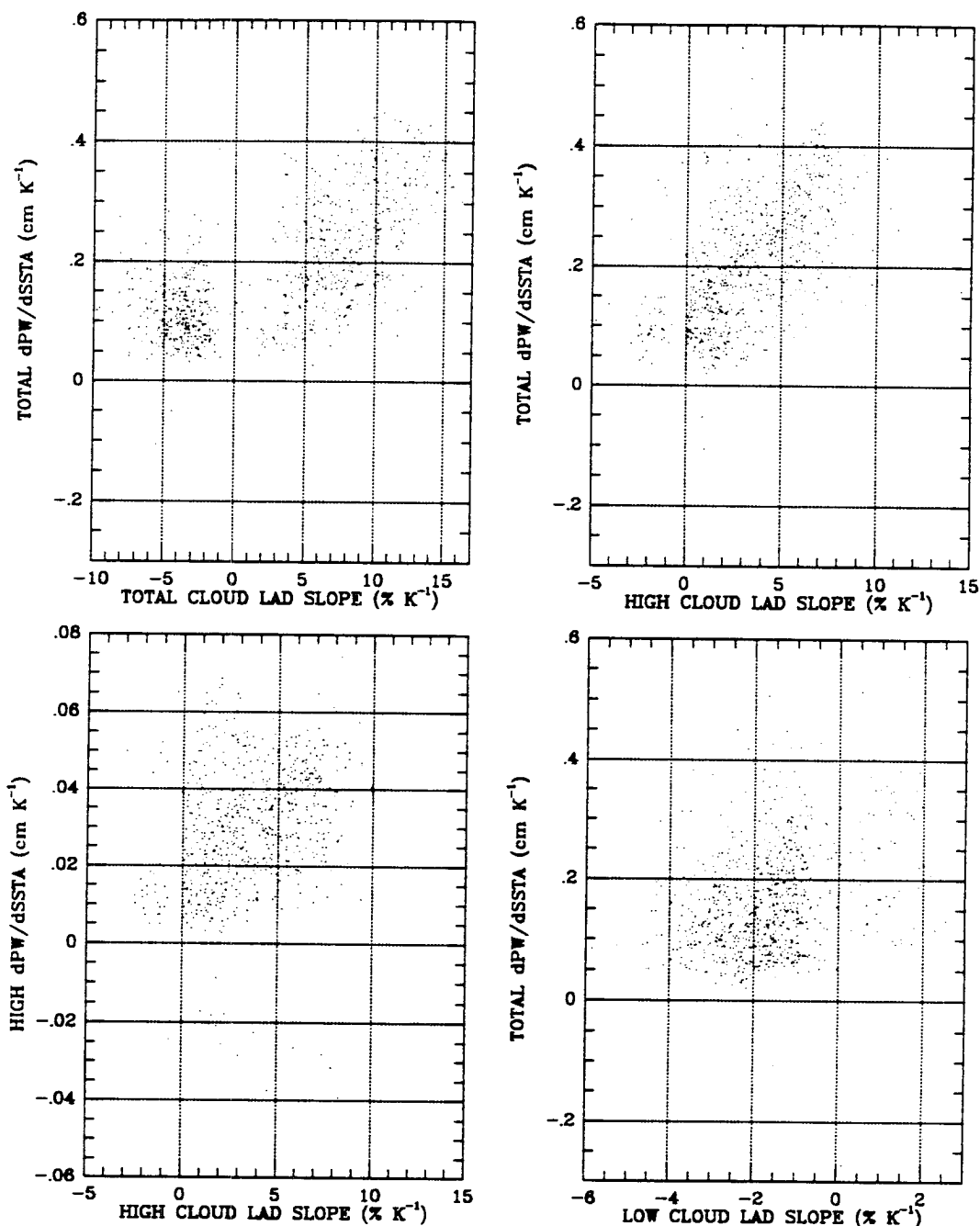


Figure 3.15: Four plots scatter plots of the relationship between water vapor-SSTA LAD slope values and cloud-SSTA LAD slope values. These include total water vapor versus total cloud, total water vapor versus high cloud, high water vapor versus high cloud, and total water vapor versus low cloud. Units for the water vapor-SSTA LAD slope are $\text{cm}\cdot\text{K}^{-1}$ and cloud-SSTA LAD slope units are $\%\cdot\text{K}^{-1}$. Cloud LAD and Probability values were interpolated to the finer ISCCP grid. Only grid points with $P \leq 0.05$ for both analyses were plotted. Based on data from July 1983 through June 1989 for water vapor and April 1979 through March 1985 for cloud data.

the atmosphere where they evaporate (Gray, 1990a). Further, a cloud parcel evaporating at the 5 km level would provide the same amount of moisture as a parcel rising to the 6 km level and then subsiding to 5 km if no precipitation fell out of the parcel on the rise from 5 to 6 km. In this example, though the moisture at 5 km would be the same in both cases, the moisture between 5 and 6 km would increase with higher detrainment.

The results of this research indicate that in most of the tropics where a strong positive relationship between high cloud anomalies and SST anomalies exists, there is also a strong positive relationship between high water vapor anomalies and SST anomalies. Furthermore, on a grid point by grid point examination, generally the greater the increase in high clouds with increases in SSTA the greater the increase in upper tropospheric water vapor per increase in SSTA. Therefore, either the observed changes in cloudiness in these locations, do not, as Lindzen hypothesized, lead to drying of the cloud free region on a climatological basis, or the drying effect of the increase cloudiness is overwhelmed by extra evaporation from a the warmer ocean surface and subsequent transport of water vapor, or the drying hypothesized by Lindzen is observed higher in the atmosphere than the TOVS water vapor retrievals extend which is 300 hPa.

One problem with the second explanation is that the dominant form of vertical moisture transport in the atmosphere is in clouds. However, we see a positive relationship between SST anomalies and water vapor anomalies at all levels no matter what the relationship between SST anomalies and cloud anomalies are. Even in regions where cloudiness decreases with increasing SST anomalies, water vapor increases. The only general trend in the water vapor-SSTA relationship is that a 1 degree SST anomaly is related to a larger increase in water vapor over warmer waters than colder waters. This is quite likely because saturation vapor pressure increase exponentially with increasing temperature as indicated by the Clausius-Clapeyron equation:

$$e_s = e_{s_0} \exp \left[\frac{L}{R_v} \left(\frac{1}{T_0} - \frac{1}{T} \right) \right]. \quad (3.1)$$

To give an example of the importance of the rate of increase of saturation vapor pressure with temperature, according to the Smithsonian Meteorological Tables, a 5 degree

increase in temperature from 0°C to 5°C causes saturation water vapor pressure to increase 2.6 hPa while a similar 5 degree increase in temperature from 20°C to 25°C causes an 8.3 hPa increase in saturation vapor pressure. This is in keeping with the increases in water vapor–SSTA LAD slopes over warmer waters once the annual average water temperature is above about 20°C. However, seasonal analysis did not show a clear increase in water vapor–SSTA LAD regression value in summer over winter even in areas with strong differences in average summer versus winter SST.

One would assume that more water vapor would evaporate from warmer oceans and therefore there would be strong positive water vapor–SSTA relationship in the lower troposphere. And this is indeed what we see from this data. The fact that the water vapor–SSTA signal is weaker higher in the troposphere is not surprising since the extra water vapor evaporated from a warmer surface would have to be transported vertically a considerable extent. The fact that the seasonal analysis did not show clear north/south variations does not mean that the water vapor–SSTA relationship is unaffected by altered global circulations. To further explore the relationship between global circulations and water vapor, Chapter 6 will examine teleconnections between global water vapor and the Southern Oscillation Index which is clearly related to changes in global circulation.

Two significant regions showed a negative water vapor–SSTA relationship: one near Antarctica off the SW coast of South America and other off the SE coast of Greenland. Many different possibilities need to be examined to explain these results. Because of the special nature of these negative low water vapor–SSTA LAD slope regions, one of these regions will be examined in greater depth in the case study part of this research which will be presented in Chapter 7.

On an area average basis, the analysis presented in this chapter indicated that clear sky water vapor increased ~ 0.15 cm in association with a 1°C increase in SSTA. An analysis of 14 atmospheric GCMs run with a uniform -2°C SSTA and a $+2^\circ\text{C}$ SSTA revealed a global average increase of ~ 0.20 cm water vapor per degree increase in SSTA (Randall, 1990b). Caution must be exercised in comparing these two results because the numerical simulation results are for the entire earth with artificially set SSTAs while

the observations presented here are limited to the ice free, open oceans with naturally occurring SSTAs. However, given the nature of the uncertainties, the average results are quite comparable. Whether in a GCM or observed, the radiative effects of increases in clear sky water vapor should be the same: an increase in the greenhouse effect. The following chapter will directly examine the radiative changes associated with SSTAs.

Chapter 4

BASIC RADIATION PARAMETERS – SSTA RELATIONSHIPS

4.1 Introduction

The goal of this research project is to identify and quantify cloud and water vapor radiative feedback loops through an observational study, using sea surface temperature anomalies as a surrogate for global climate change. The changes in clouds in association with changes in SSTAs identified in Chapter 2 and the changes in water vapor associated with changes in SSTAs identified in Chapter 3 imply that there will also be changes in radiation associated with changes in SSTA. The actual radiative effects would be observed in the changes in albedo (and hence reflected flux), outgoing long wave radiation (OLR), and net radiation. The goal of the research presented in this chapter is to quantify the radiative effects of the cloud- and water vapor-SSTA relationships.

Cess *et al.* (1990) looked at these parameters in their comparison of 19 GCMs simulations with global SSTAs set at $+2^{\circ}\text{C}$ and at -2°C . They found that global average ΔOLR per degree C increase in SSTA averaged $2.46 \text{ W}\cdot\text{m}^{-2}\cdot\text{K}^{-1}$ with a range from 1.65 to $3.13 \text{ W}\cdot\text{m}^{-2}\cdot\text{K}^{-1}$. Since, for conditions typical of the earth, the ΔOLR per one degree C increase in surface temperature would be about $3.3 \text{ W}\cdot\text{m}^{-2}\cdot\text{K}^{-1}$ without feedback mechanisms (Cess *et al.*, 1990), a change of $2.46 \text{ W}\cdot\text{m}^{-2}\cdot\text{K}^{-1}$ represents a positive warming feedback of about $0.84 \text{ W}\cdot\text{m}^{-2}\cdot\text{K}^{-1}$. The change in reflected flux averaged $-0.72 \text{ W}\cdot\text{m}^{-2}\cdot\text{K}^{-1}$ with a range from 0.83 to $-2.08 \text{ W}\cdot\text{m}^{-2}\cdot\text{K}^{-1}$. This decrease in reflected flux is in keeping with the models' decreases in cloudiness with increases in SSTA which was the opposite of our cloud-SSTA analysis reported in Chapter 2. Adding the radiative effects of the change in reflected flux to the decrease in OLR from the expected change due to increases in surface temperature and one gets an average net warming effect of $1.56 \text{ W}\cdot\text{m}^{-2}\cdot\text{K}^{-1}$ from the GCM numerical simulations.

4.2 Data

4.2.1 Radiation Parameters

One advantage with this part of the research is that unlike cloud percentages and water vapor amounts, there are no complex algorithms used to derive the necessary parameters for this research from the observed radiation. For they are the basic observed radiation parameters. Four radiation parameters are used in the research presented in this chapter. They are albedo, reflected flux (albedo multiplied by incident solar radiation), outgoing longwave radiation, and net radiation (which is the difference between absorbed solar and outgoing IR). The monthly averaged radiation parameter data used in this research came from the Nimbus-7 satellite for the same time period, April 1979 to March 1985, as the cloud data used in the research presented in Chapter 2, and was available in the same 4.5 x 4.5 degree (at the equator) grid as the cloud data (Kyle *et al.*, 1985).

The radiation parameter data came from three separate groups of sensors on Nimbus-7, which independently monitored the spectral and total solar irradiances, as well as the earth solar reflected and earth infrared emitted radiation fluxes for both wide and narrow angle field-of-views. Descriptions and performances of the three instruments can be found in Jacobowitz *et al.* (1984). Table 4.1 gives the spectral intervals for the Nimbus-7's ERB channels. The scanner responsible for the narrow field-of-view channels 15-22 failed in June 1980, but data from these channels was used in calibration studies (Randel, 1990). Careful pre-launch and post-launch studies of the radiometric qualities of the sensors has allowed for additional calibration applied directly to the primary data (Jacobowitz, 1984). Of special concern with any long-term satellite data set is possible instrument degradation such as a slow change in sensitivity of the sensor. For this data set, "these instrument-related long-term trends are essentially removed by the new global adjustment algorithm" (Kyle *et al.*, 1985).

4.2.2 SST

The SST data used for this research is exactly the same data set used with the cloud data in Chapter 2: a monthly anomaly data set based on CAC's monthly SST for the region from 60°N to 40°S for the period April 1979 through March 1985.

Table 4.1: Nimbus-7 Earth Radiation Budget instrument channels and their spectral intervals. Channels 1-10 are the ERB solar channels, channels 11-14 are the fixed wide-angle FOV channels, and channels 15-22 are the ERB scanning channels with a narrower FOV.

Channel	Wavelength limits (μm)
1	0.2 - 3.8
2	0.2 - 3.8
3	0.2 - 50
4	0.536 - 2.8
5	0.698 - 2.8
6	0.395 - 0.508
7	0.344 - 0.460
8	0.300 - 0.410
9	0.275 - 0.360
10	0.2 - 50
11	<0.2 - >50
12	<0.2 - >50
13	0.2 - 3.8
14	0.695 - 2.8
15-18	0.2 - 4.8
19-22	4.5 - 5.0

4.3 Methods

The analysis procedure for these data sets was the same as described earlier: using LAD to determine the radiation parameter–SSTA relationship and then MRBP to determine the likelihood that the observed data points were randomly distributed around the LAD regression line. All the data analyzed in this chapter had the same maximum of high probability values and minimum of low probability values at a LAD slope of 0. Grid points with probabilities less than or equal to 0.05 are plotted on the maps. Again we found the low P-value grid boxes were clustered in distinct regions indicating a strong significance to the data in those regions.

4.4 Results

4.4.1 Albedo

The albedo is a basic measurement of the total reflected energy of the earth expressed as a percentage of incident energy. Since this research takes place over the ocean, changes in the albedo of the surface can be ignored as long as we remove areas of ice cover, which we have done. The albedo of the atmosphere is primarily, but not solely, affected by clouds. Most atmospheric constituents either do not affect the albedo or are uniformly dispersed so they would not vary the albedo from month to month. Some atmospheric pollutants, such as dust off the Sahara Desert, can vary the atmosphere's albedo, but those effects are clearly second order effects compared to changes in cloud cover.

Changing the percentage of cloud cover can obviously have a profound effect on the albedo. However, other cloud changes can have a significant effect on albedo even with unchanged cloud percentage. These changes can include changes in phase between ice and water, changes in liquid or ice water path lengths, and changes in the geometry or fractal size of the clouds. To show up in this monthly analysis, these changes would have to occur with some distinct relationship to SST anomalies.

There are two ways to look at the albedo change. One is looking directly at the percentage change in reflectance. This should be most closely linked to changes in clouds. Another is to look at the changes in reflected energy per unit area per time that the change

Table 4.2: Albedo. Area averaged values from 60°N to 40°S of the LAD regression slope of percent change in albedo per 1°C increase in SST. Units are %·K⁻¹. Column 4 is the percent of the grid points with $P \leq 0.05$. Based on data from April 1979 through March 1985.

Season	All Prob	Prob ≤ 0.05	Percent
Full Year	-0.14	-0.16	49%
Mar-Apr-May	0.21	0.47	36%
Jun-Jul-Aug	-0.19	-0.37	42%
Sep-Oct-Nov	-0.04	-0.09	35%
Dec-Jan-Feb	-0.17	-0.11	40%

in albedo produces. This would be linked not only to changes in clouds but also to the season in which these changes occur. For example, at 50 degrees North, a 10% increase in the albedo would produce a much larger increase in reflected flux during the summer when there is much more incident solar radiation than during the winter. Therefore, this analysis is divided into both albedo as a percentage and albedo effects in watts per square meter (reflected energy).

Albedo Percent

Examination of plots of probability versus LAD slope for albedo, shown in Figure 4.1, indicates that there are both positive and negative Albedo–SSTA LAD regression slopes with low P-values. It is also clear that there are more negative albedo anomaly–SSTA relationships than positive on a grid point basis. Area averages over the entire data set shown in Table 4.2, indicate a generally weakly negative LAD relationship. The small absolute values of the nearly global averages are a result of averaging both positive and negative values. The area average value for full year analysis of $-0.14 \text{ \%}\cdot\text{K}^{-1}$ represents averaging LAD slope with absolute values frequently in the range of 1 or 2. Values from full year LAD analysis, however, rarely had an absolute value greater than 3 % per degree K. Seasonal analysis was definitely noisier than full year analysis, but still had few grid points with an absolute value greater than $5 \text{ \%}\cdot\text{K}^{-1}$.

Grid points with positive and negative Albedo–SSTA relationship are not randomly distributed around the globe. As Figures 4.2, 4.3, and 4.4 illustrates, there are distinct

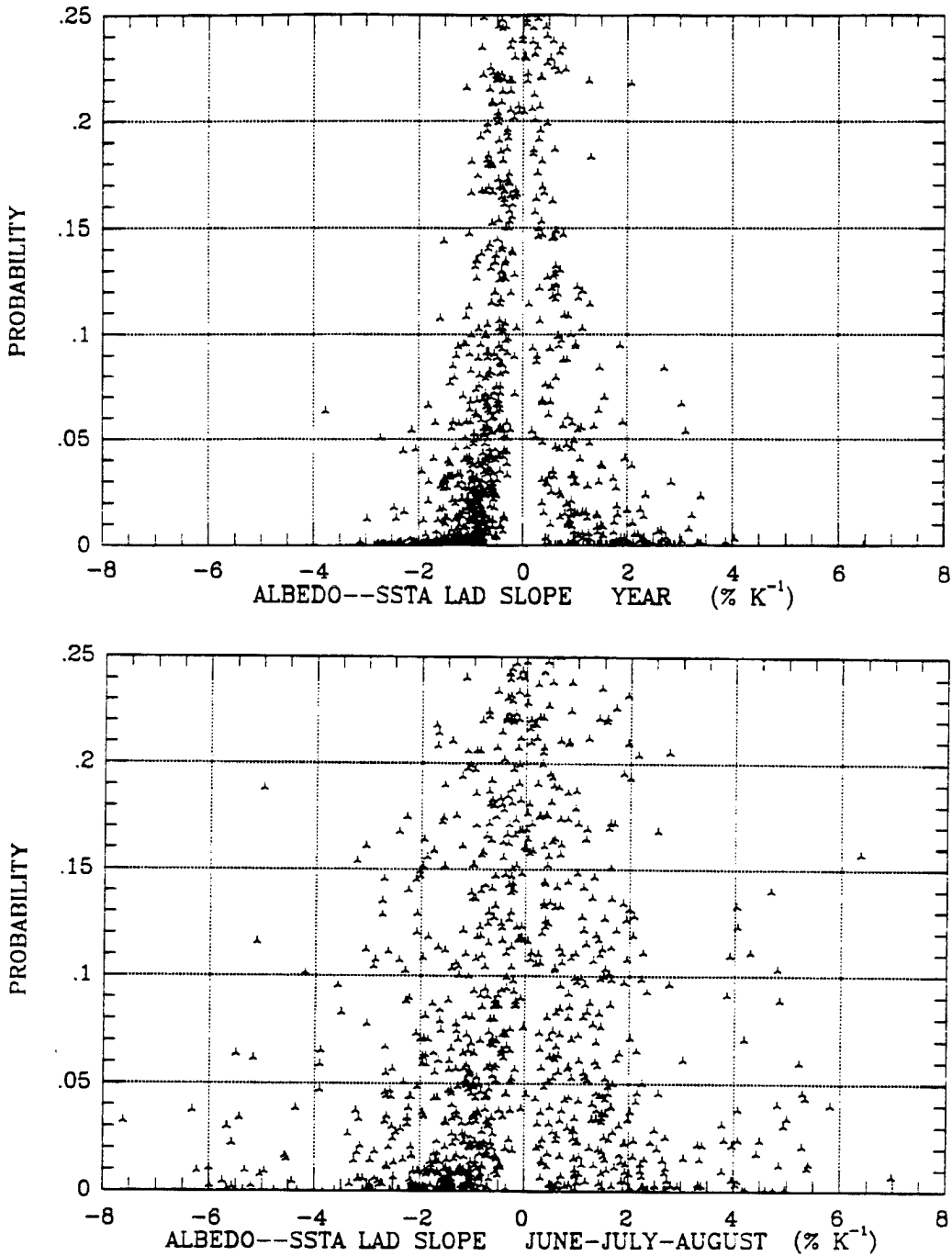


Figure 4.1: Scatter plots of Albedo-SSTA LAD slope versus the Probability that the data was randomly distributed around the regression line. Top is for the full year, bottom is seasonal analysis for June-July-August which was very similar to the scatter plot for December-January-February analysis. Units are unitless for the P-value and $\% \cdot K^{-1}$ for the LAD slope. Based on data from April 1979 through March 1985.

regions with strong and statistically significant positive relationships and negative relationships. It is clear that for the full year analysis, the strongest positive relationship is in the tropics and along the SPCZ. The strongest negative relationship is in stratocumulus regions off the west coast of continents. Seasonal analysis, shown in Figures 4.3 and 4.4, indicates that the negative relationship is strongest during the summer. Also, the SPCZ is more clearly defined by the albedo–SSTA LAD analysis in the summer. Both positive and negative regions tend to move north and south with the sun.

Examination of Table 4.2 indicates that the nearly global average Albedo–SSTA LAD slope values are positive for only the months of March–April–May. This is due mainly to a large region in the eastern tropical Pacific ocean south of the equator which has strong positive LAD values for these months.

Reflected Flux: Albedo’s Effect on Radiation

Simply multiplying the Albedo–SSTA LAD values by incident solar would not provide an accurate representation of the reflected flux–SSTA relationship because the strong seasonal variation due to day length and zenith angle changes would not be properly incorporated. To accurately examine the relationship between SSTA and the radiative effect of changes in albedo, we first created a reflected flux anomaly data set. This was created by multiplying the albedo anomaly data set used in the previous subsection by the average incident solar radiation at that grid point for that month. The average incident solar radiation represents essentially all the incident joules of solar radiation per square meter for the month divided by the number of seconds in the month. The incident solar radiation data, given in watts per square meter, came from the Nimbus-7 data set. The actual values of incident solar radiation at, for example, 40 degrees N latitude and 180 degrees longitude for the month of May, varied slightly from year to year. A decrease in the reflected flux means less solar radiation is being reflected, hence more solar radiation is being absorbed by the earth-atmosphere system.

The LAD regression slopes of full year analysis of the reflected flux–SSTA, shown in in the top of Figure 4.5 varies from about $-10 \text{ W}\cdot\text{m}^{-2}\cdot\text{K}^{-1}$ to $10 \text{ W}\cdot\text{m}^{-2}\cdot\text{K}^{-1}$ with a few

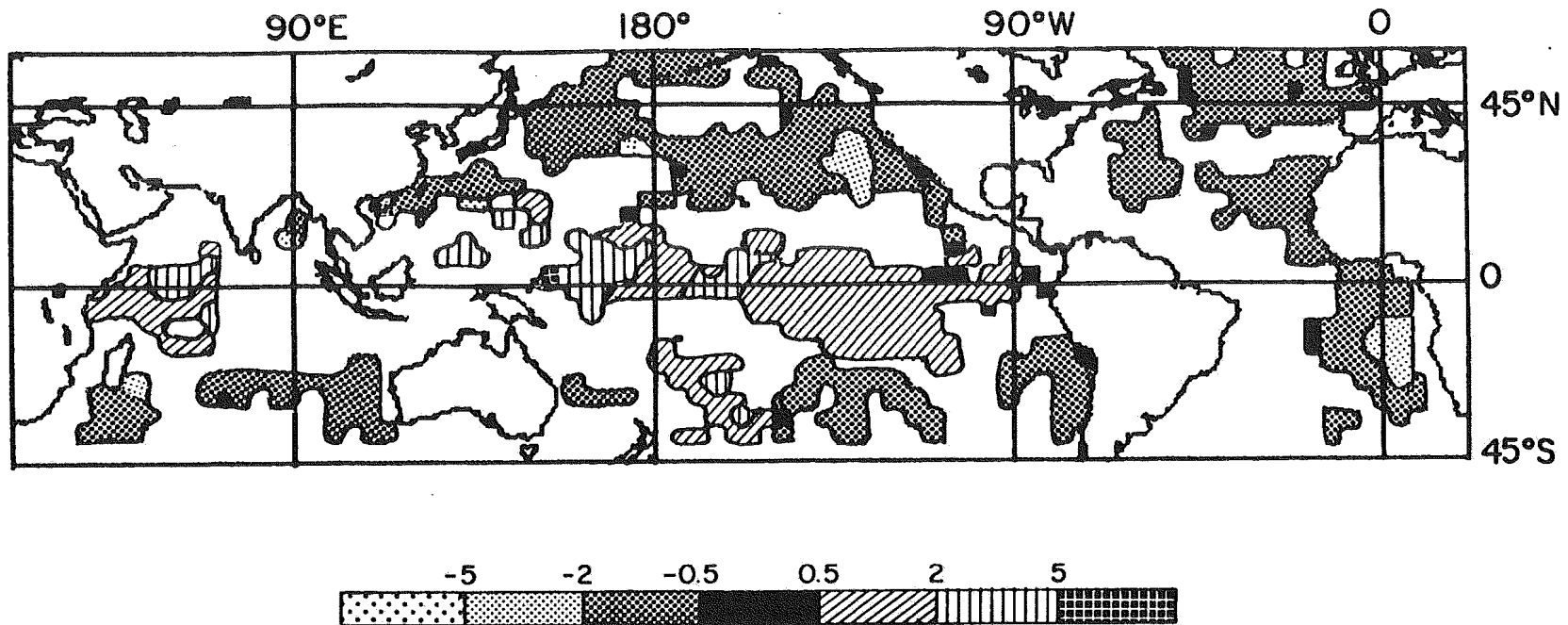


Figure 4.2: Contour plot of Albedo-SSTA LAD regression slopes showing areas where grid points had a P-value less than or equal to 0.05. Units are $\% \cdot K^{-1}$. Due to limits on SST data, this analysis is available only from 60°N to 40°S. Based on data from April 1979 through March 1985.

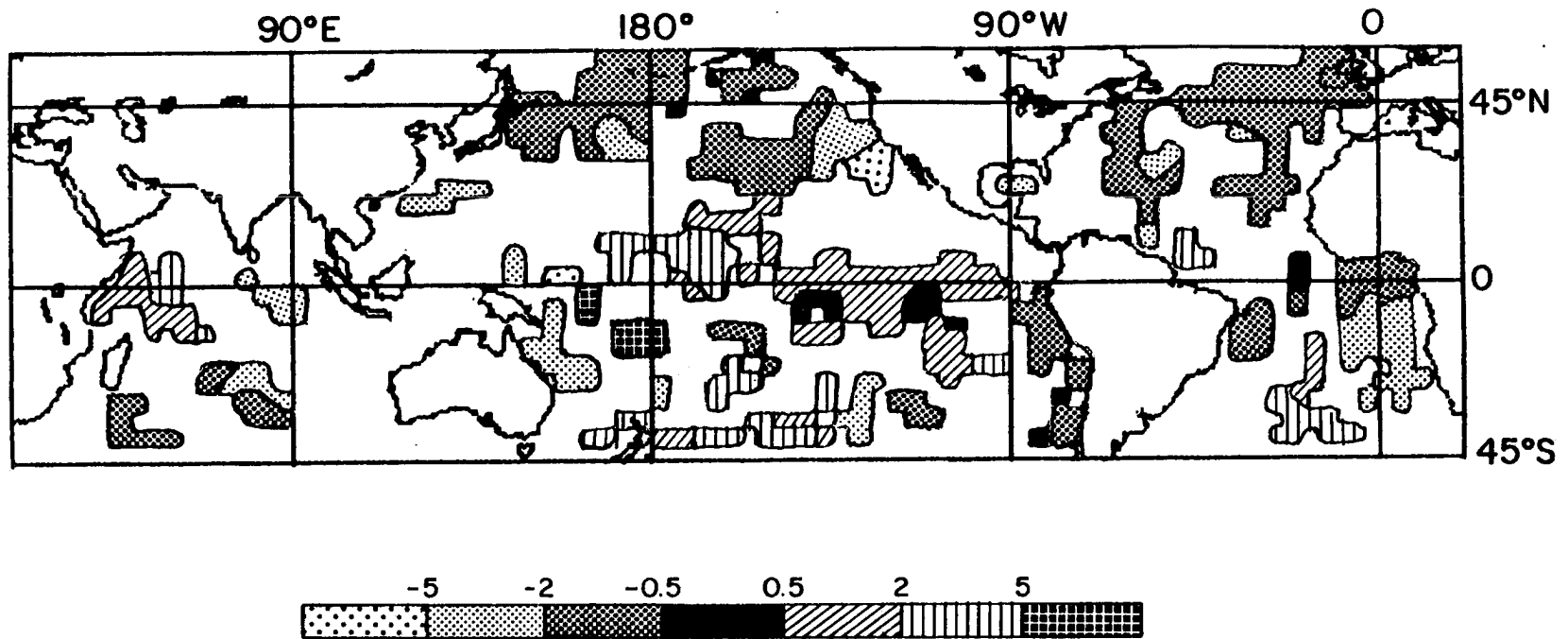


Figure 4.3: Contour plot of Albedo-SSTA LAD regression slope for June-July-August showing areas where grid points had a P-value less than or equal to 0.05. Units are $\% \cdot K^{-1}$. Based on data from April 1979 through March 1985.

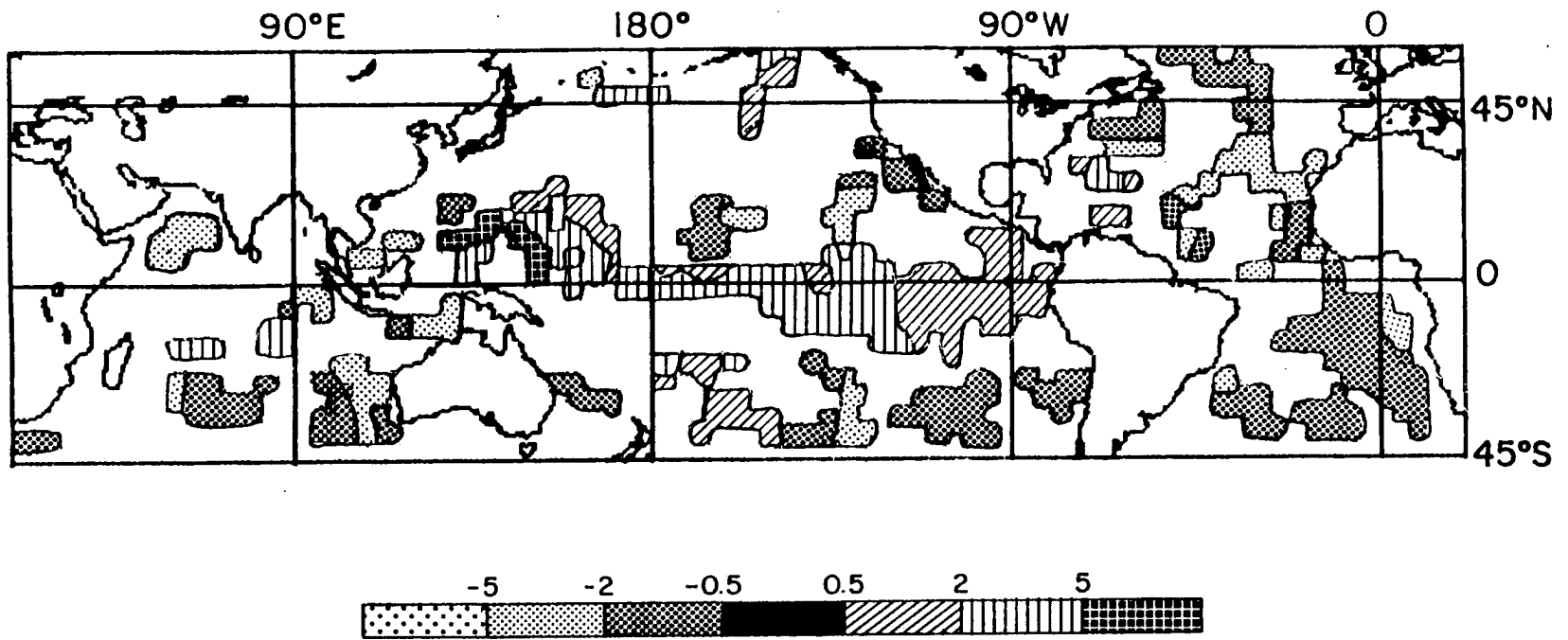


Figure 4.4: Contour plot of Albedo-SSTA LAD regression slope for December-January-February showing areas where grid points had a P-value less than or equal to 0.05. Units are $\% \cdot K^{-1}$. Based on data from April 1979 through March 1985.

grid points outside that range. Seasonal analysis, shown in the bottom of Figure 4.5, is much the same only noisier.

There were 1039 grid boxes analyzed. The analysis using the full 72 month data set (full year analysis, not seasonal) had $P \leq 0.05$ at 514 grid boxes for albedo-SSTA and 526 grid boxes for reflected flux-SSTA. Albedo-SSTA analysis had 14 grid points with low P-values that did not have the low P-values for reflected flux-SSTA, while the reflected flux-SSTA analysis had 26 grid points with low P-values that did not have low P-values for the albedo-SSTA analysis. Therefore, the location of regions with P-values less than or equal to 0.05 is very similar between analysis of albedo and the reflective flux. Examination of regions on these contour plots indicates that they are almost identical in terms of which grid points have low P-values. The place where the plots diverge is in the seasonal relative amounts.

As shown in Table 4.3, the area averaged value of the LAD slope of the reflective flux and the LAD slope for just those grid points with low P-values are small: $\sim -0.4 \text{ W}\cdot\text{m}^{-2}\cdot\text{K}^{-1}$. This again is a result of averaging regions with positive and regions with negative LAD slopes. Since Table 4.3 indicates a change in sign of the global average value with the seasons (negative in June-July-August and December-January-February while positive in March-April-May and September-October-November), Figures 4.7, 4.8, 4.9, and 4.10 give the seasonal analysis for all four seasons for grid points with P-value less than or equal to 0.05. The highly positive global average in March-April-May is caused by the large positive eastern tropical Pacific region clearly shown in Figure 4.7.

As these figures can illustrate, the only areas of positive LAD slopes, where positive SST anomalies are associated with positive albedo anomalies and their radiative effects are the tropical Pacific ocean, a region in the western tropical Indian ocean, and the South Pacific Convergence Zone. All other regions with low P-values are negative, with the strongest negative LAD regression slopes being in stratocumulus subsidence regions off the western coasts of continents. Compared to the albedo-SSTA analysis in the previous section, the regions in high latitudes with the same values for the LAD of albedo for summer and winter, show a much higher summer versus winter LAD of the reflective flux.

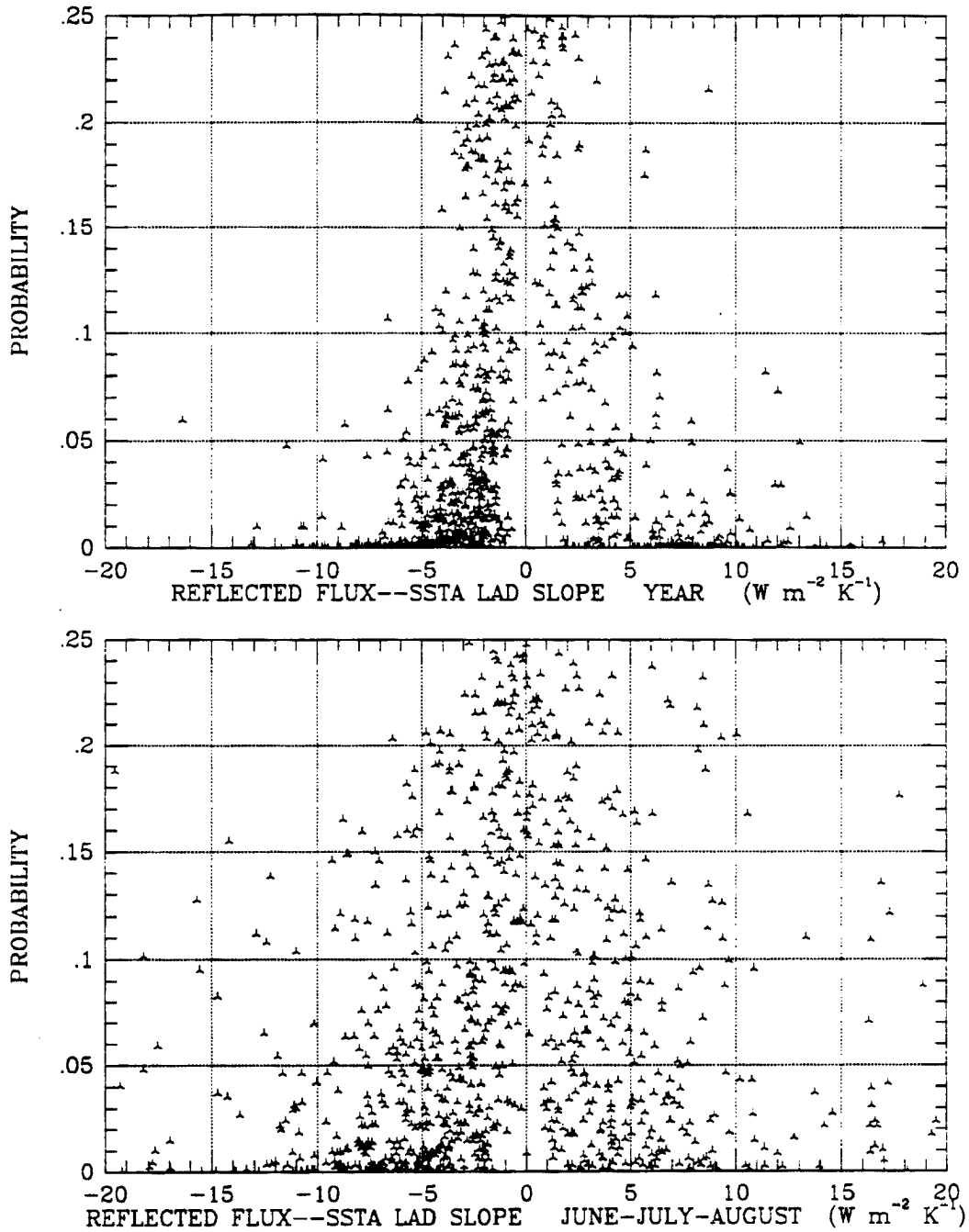


Figure 4.5: Scatter plots of Reflected Flux-SSTA LAD slope values versus the Probability that the data was randomly distributed around the regression line. Top is for the full year, bottom is seasonal analysis for June-July-August which was very similar to the scatter plot for December-January-February analysis. Units are unitless for the P-value and $W \cdot m^{-2} \cdot K^{-1}$ for the LAD slope. Based on data from April 1979 through March 1985.

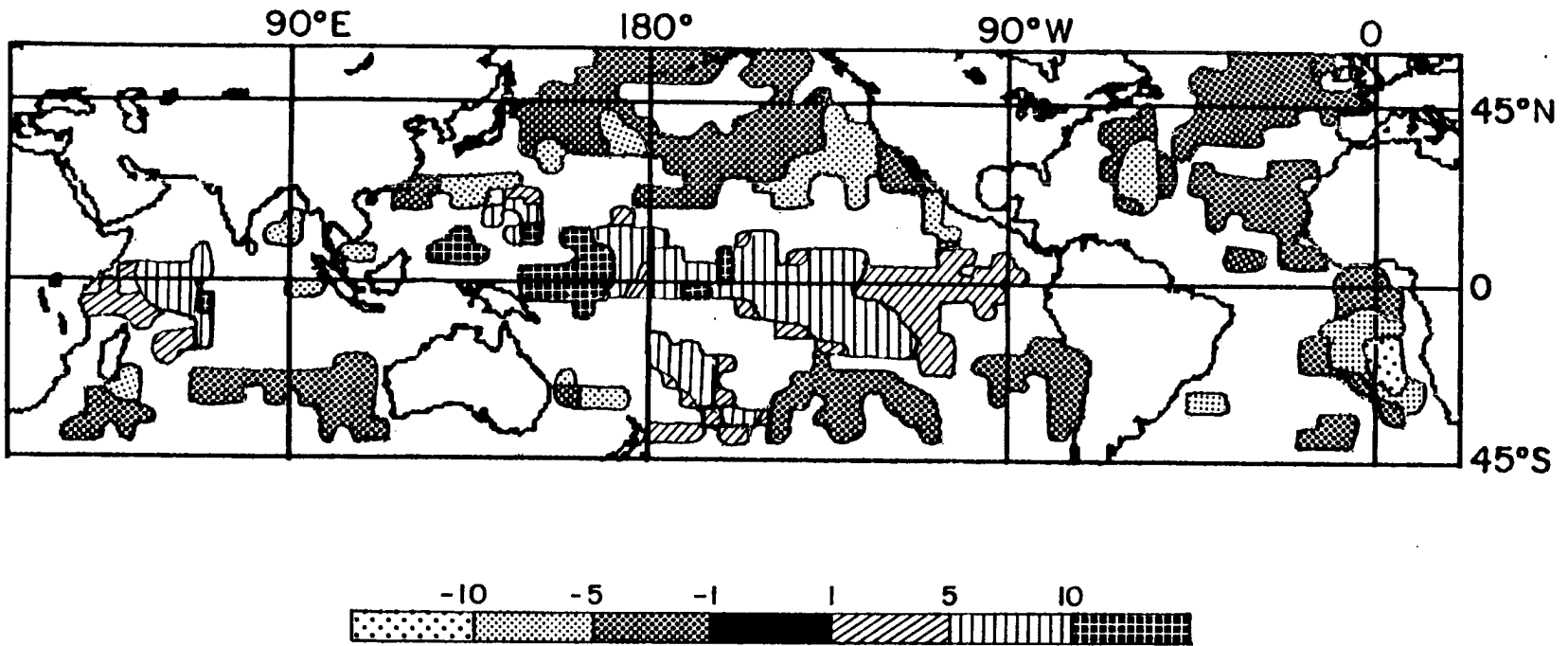


Figure 4.6: Contour plot of Reflected Flux-SSTA LAD regression slopes showing areas where grid points had a P-value less than or equal to 0.05. This analysis is for the entire 72 month data set. Units are $W \cdot m^{-2} \cdot K^{-1}$. Based on data from April 1979 through March 1985.

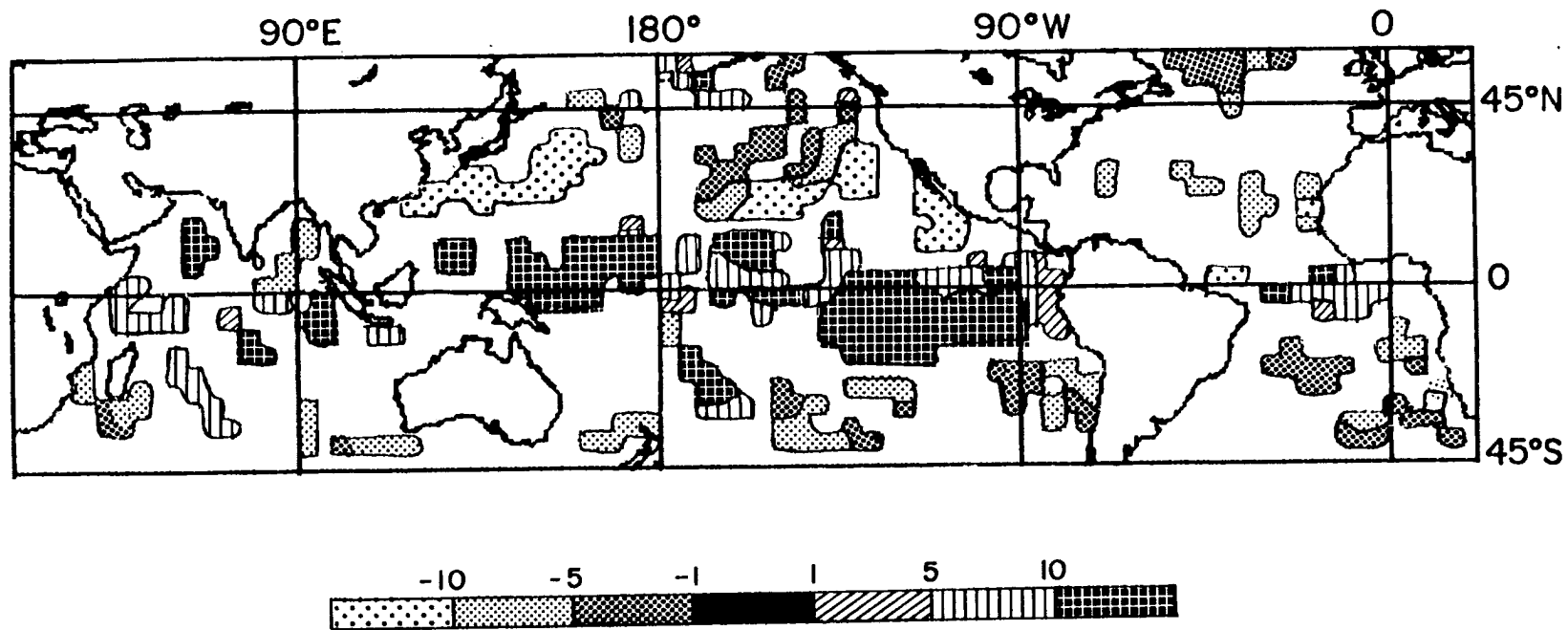


Figure 4.7: Contour plot of Reflected Flux-SSTA LAD regression slopes showing areas where grid points had a P-value less than or equal to 0.05. This analysis is for the months of March, April, and May. Units are $W \cdot m^{-2} \cdot K^{-1}$. Based on data from April 1979 through March 1985.

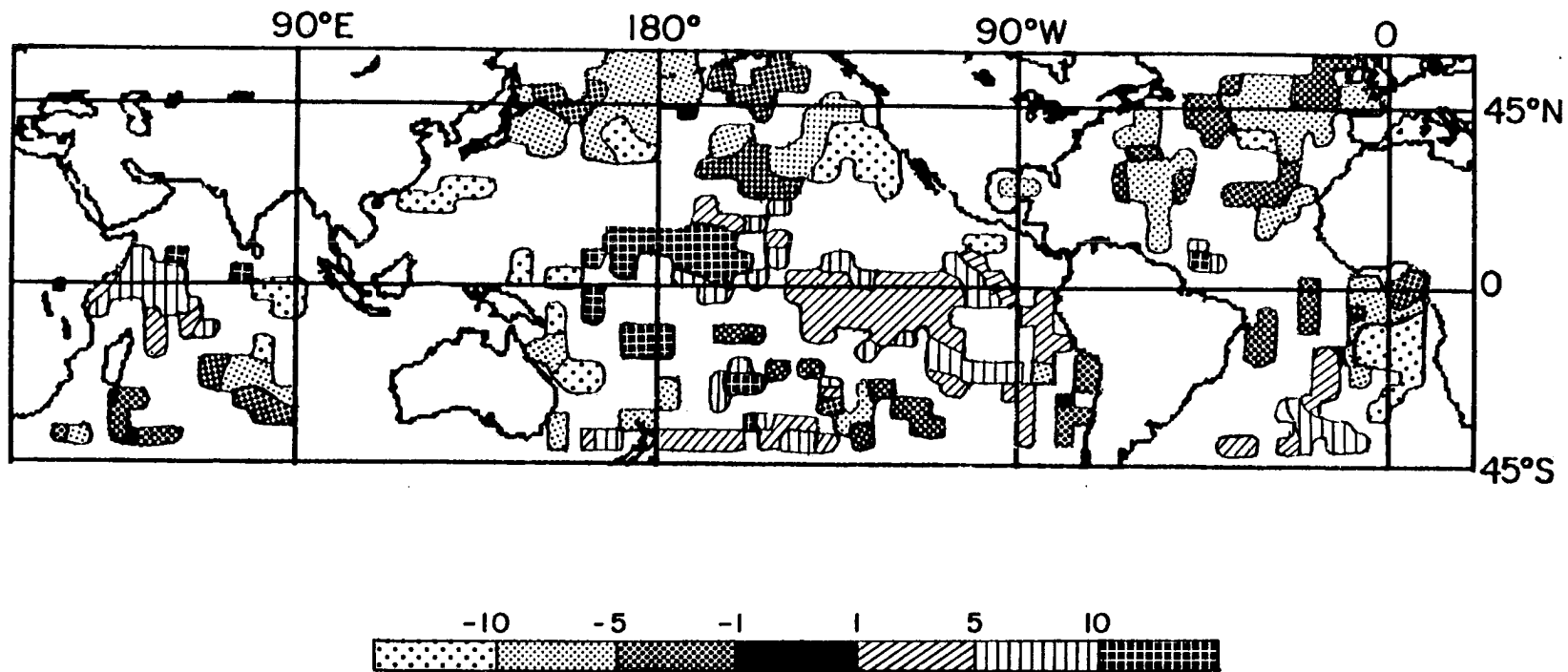


Figure 4.8: Contour plot of Reflected Flux-SSTA LAD regression slopes showing areas where grid points had a P-value less than or equal to 0.05. This analysis is for the months of June, July, and August. Units are $W \cdot m^{-2} \cdot K^{-1}$. Based on data from April 1979 through March 1985.

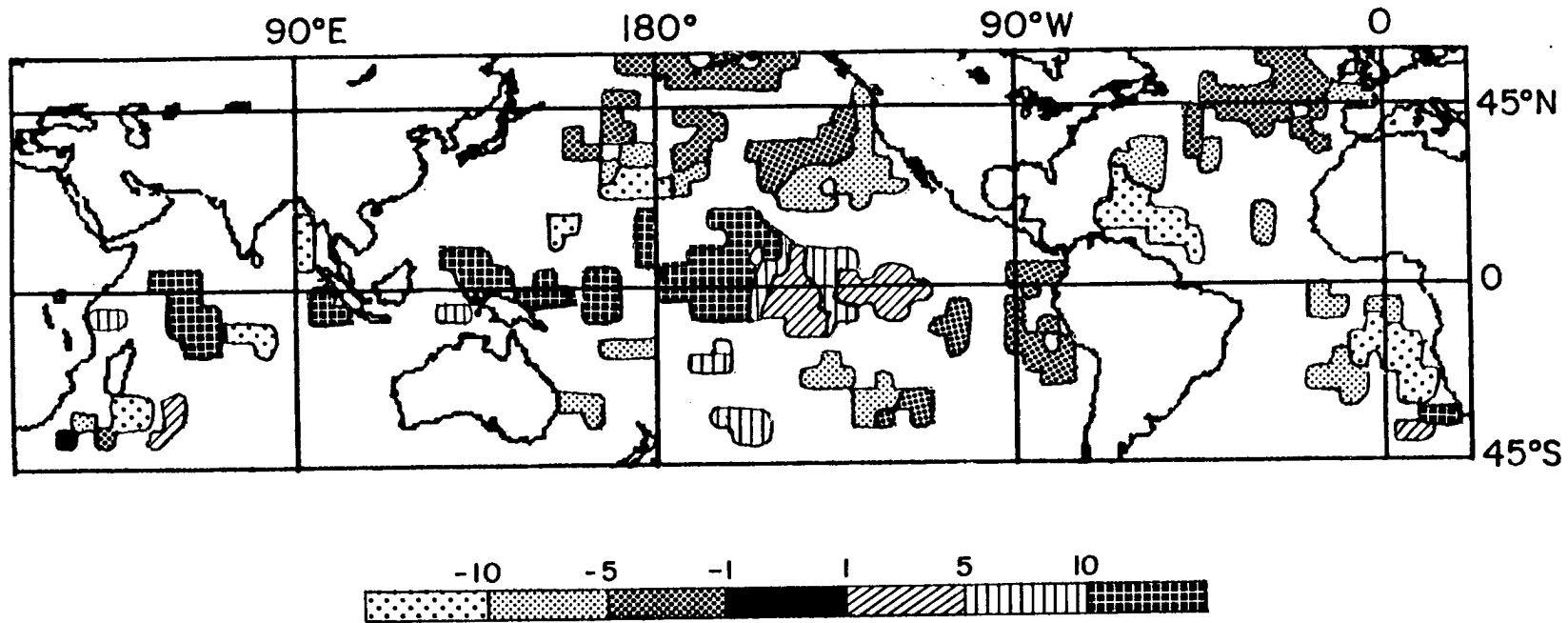


Figure 4.9: Contour plot of Reflected Flux-SSTA LAD regression slopes showing areas where grid points had a P-value less than or equal to 0.05. This analysis is for the months of September, October, and November. Units are $W \cdot m^{-2} \cdot K^{-1}$. Based on data from April 1979 through March 1985.

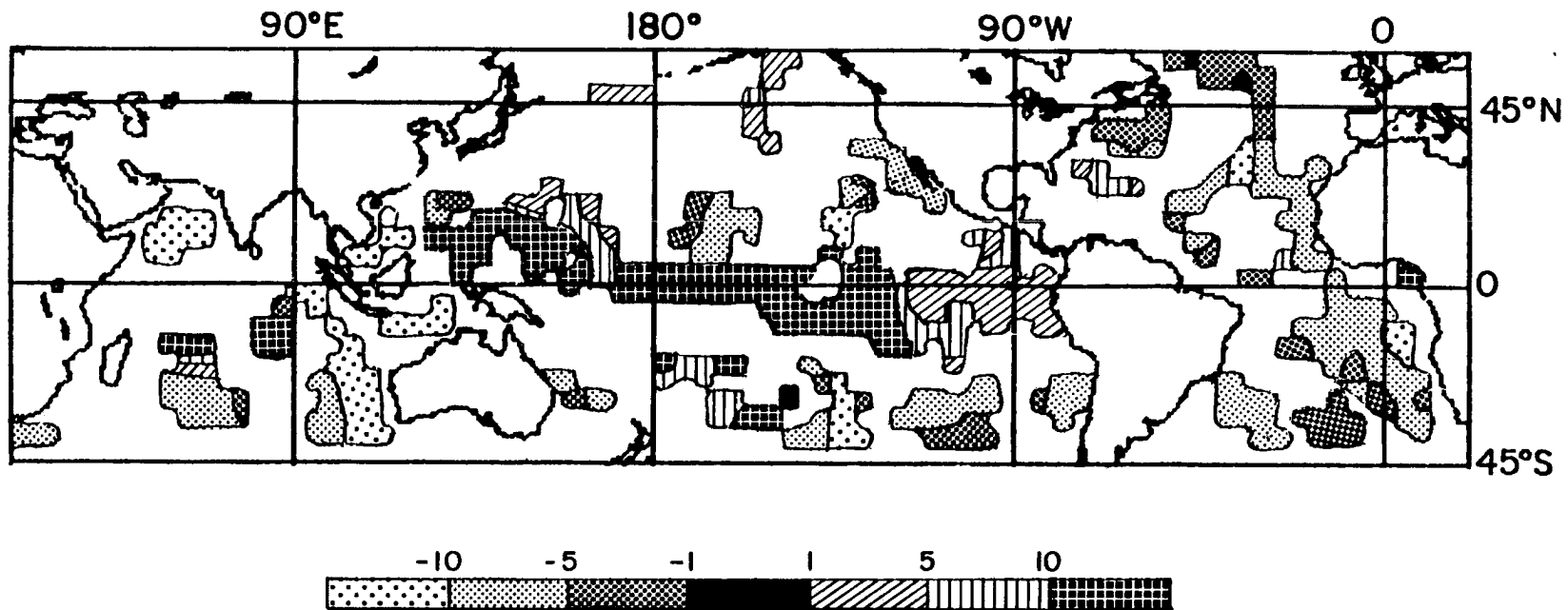


Figure 4.10: Contour plot of Reflected Flux-SSTA LAD regression slopes showing areas where grid points had a P-value less than or equal to 0.05. This analysis is for the months of December, January, and February. Units are $\text{W}\cdot\text{m}^{-2}\cdot\text{K}^{-1}$. Based on data from April 1979 through March 1985.

Table 4.3: Reflected Flux–SSTA LAD slope. Area averaged values from 60°N to 40°S in the LAD regression value of the $W \cdot m^{-2}$ effect of the change in albedo per 1°C increase in SST. Units are $W \cdot m^{-2} \cdot K^{-1}$. Column 4 is the percent of grid points with $P \leq 0.05$. Based on data from April 1979 through March 1985.

Season	All Prob	Prob ≤ 0.05	Percent
Full Year	-0.37	-0.39	51%
Mar-Apr-May	0.90	1.89	38%
Jun-Jul-Aug	-0.82	-1.69	43%
Sep-Oct-Nov	0.14	0.20	35%
Dec-Jan-Feb	-0.64	-0.39	40%

4.4.2 Outgoing Longwave Radiation

Without cloud or clear sky greenhouse effect, an increase in SST would lead to an increase in outgoing long wave radiation. At the high end of sea surface temperatures, 29°C, outgoing IR radiation would increase at $6.3 W \cdot m^{-2}$ per 1 degree increase in SST. At the low end of sea surface temperatures, 0°C, outgoing IR radiation would increase at $4.7 W \cdot m^{-2}$ per 1 degree increase in SST. With the greenhouse effect, this averages about $3.3 W \cdot m^{-2}$ (Cess *et al.*, 1990). If the greenhouse effect was a constant or a function of latitude or latitude and longitude only, then the observed OLR–SSTA LAD slope would be some fraction of the values stated earlier. However, the area averaged OLR–SSTA LAD slope was $-1.6 W \cdot m^{-2} \cdot K^{-1}$, as shown in Table 4.4. Again, these near global averages are a combination of both positive and negative LAD slope values. But as Figure 4.11 shows, the negative LAD values dominate over positive LAD values, especially at grid points with very small P-values.

Figure 4.12 shows little OLR–SSTA relationship in the subtropical stratocumulus regions off the west coasts of Africa, North America, and Australia. Much of the tropics and the SPCZ show up as a decrease in OLR with increases in SSTA as does a region off the west coast of South America near 90°W which stretches very far south. Examination of the seasonal analysis of June-July-August and December-January-February shown in Figures 4.13 and 4.14, reveals that this negative OLR–SSTA relationship in the South Pacific near 90°W is primarily a wintertime phenomena. Generally, though, poleward of

Table 4.4: Area averaged values from 60°N to 40°S of the OLR–SSTA LAD slope. Units are $\text{W}\cdot\text{m}^{-2}\cdot\text{K}^{-1}$. Column 4 is the percent of grid boxes with $P \leq 0.05$. Based on data from April 1979 through March 1985.

Season	All Prob	Prob ≤ 0.05	Percent
Full Year	-1.6	-3.2	43%
Mar-Apr-May	-2.8	-5.4	40%
Jun-Jul-Aug	-1.0	-1.8	38%
Sep-Oct-Nov	-2.0	-4.3	36%
Dec-Jan-Feb	-1.6	-4.4	34%

the tropics, OLR increases with increasing SSTA and the effect is more pronounced in the summer hemisphere.

4.4.3 Net Radiation

In this analysis, a positive value for net radiation means that the earth-atmosphere system is gaining radiant energy. The area average value for net radiation–SSTA LAD regression slope is $1.9 \text{ W}\cdot\text{m}^{-2}\cdot\text{K}^{-1}$ as shown in Table 4.5. For grid points with P-values less than or equal to 0.05, the average value goes up to $3.5 \text{ W}\cdot\text{m}^{-2}\cdot\text{K}^{-1}$. As Figure 4.15 illustrates, the LAD slope of net radiation–SSTA is predominately positive. Net radiation–SSTA LAD analysis had the lowest number of grid points with P-values less than or equal to 0.05, though only a few less than the OLR–SSTA LAD analysis. This should, perhaps, be expected because even in regions where there is a clear positive correlation between cloud anomalies and SST anomalies, the change in cloud radiative effects due to changes in albedo and OLR can balance out enough to create an unclear or noisy signal in net radiation.

Figures 4.16, 4.17, and 4.18 reveal the regionality of low P-value net radiation–SSTA LAD analysis. There are no clear zonally oriented regions, especially near the equator which were common in the analyses of other variables. However, there are distinct regions oriented North-South, particularly along the west coast of continents. These are primarily regions where low clouds decrease with increasing temperature, where the albedo decreases but OLR does not change much. As the seasonal plots in Figures 4.17 and 4.18 can

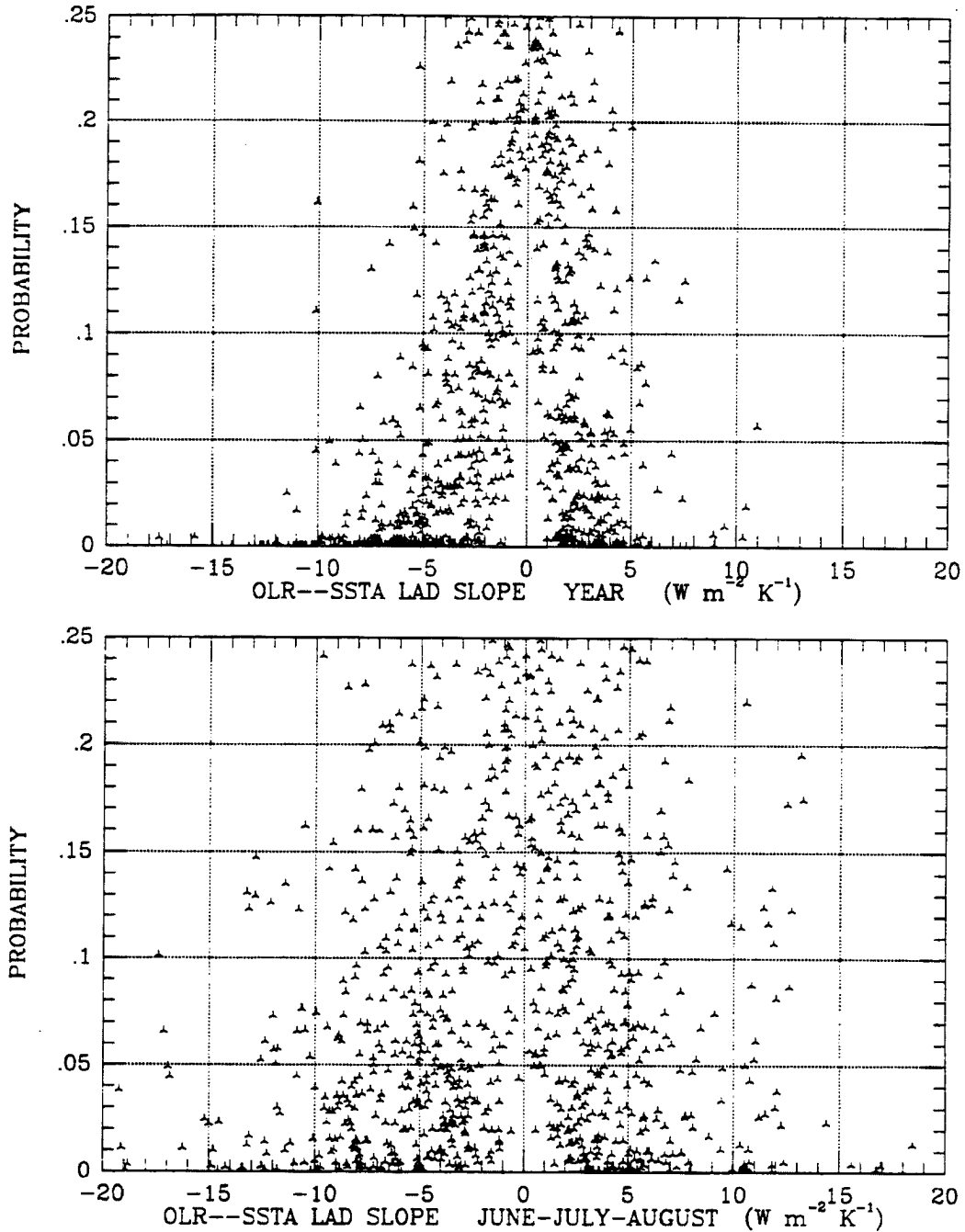


Figure 4.11: Scatter plots of OLR--SSTA LAD slope values versus the Probability that the data was randomly distributed around the regression line. Top is for the full year, bottom is seasonal analysis for June-July-August which was very similar to the scatter plot for December-January-February analysis. Units are unitless for the P-value and $\text{W}\cdot\text{m}^{-2}\cdot\text{K}^{-1}$ for the LAD slope. Based on data from April 1979 through March 1985.

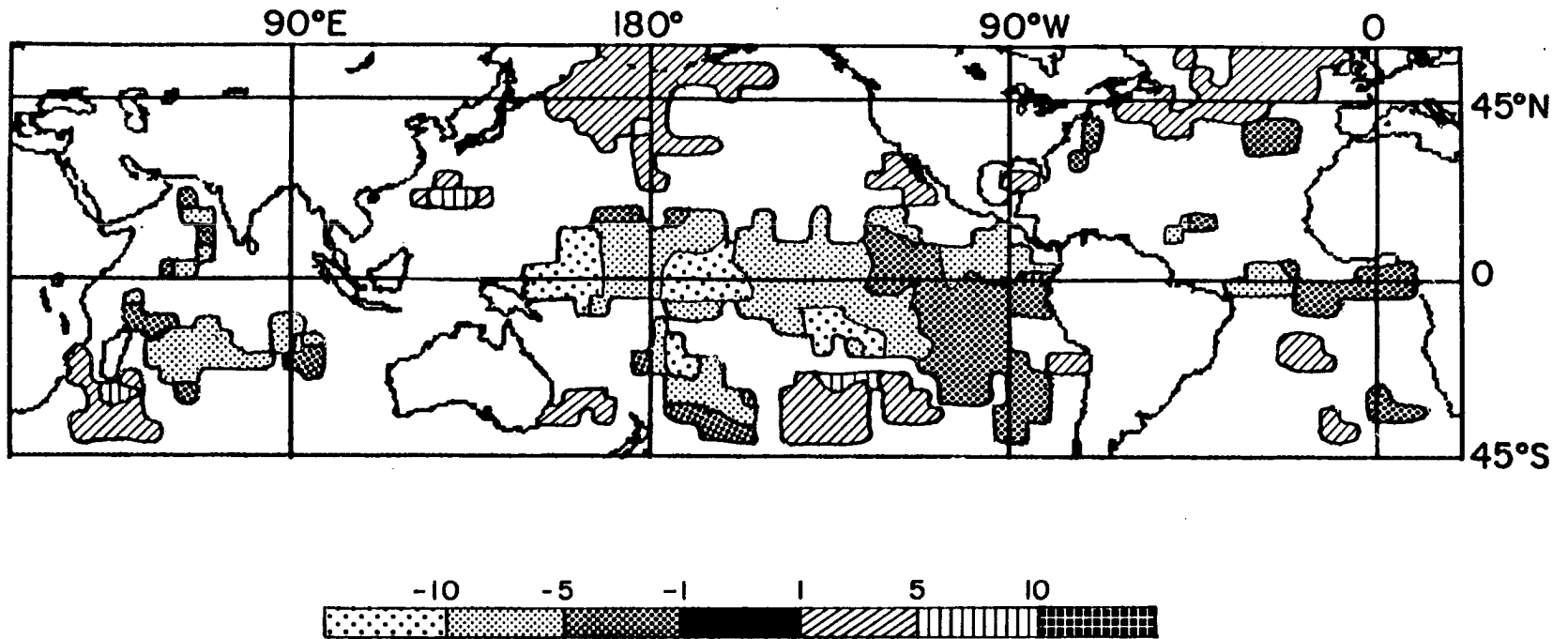


Figure 4.12: Contour plot of OLR-SSTA LAD regression slopes showing areas where grid points had a P-value less than or equal to 0.05. Units are $W \cdot m^{-2} \cdot K^{-1}$. Based on data from April 1979 through March 1985.

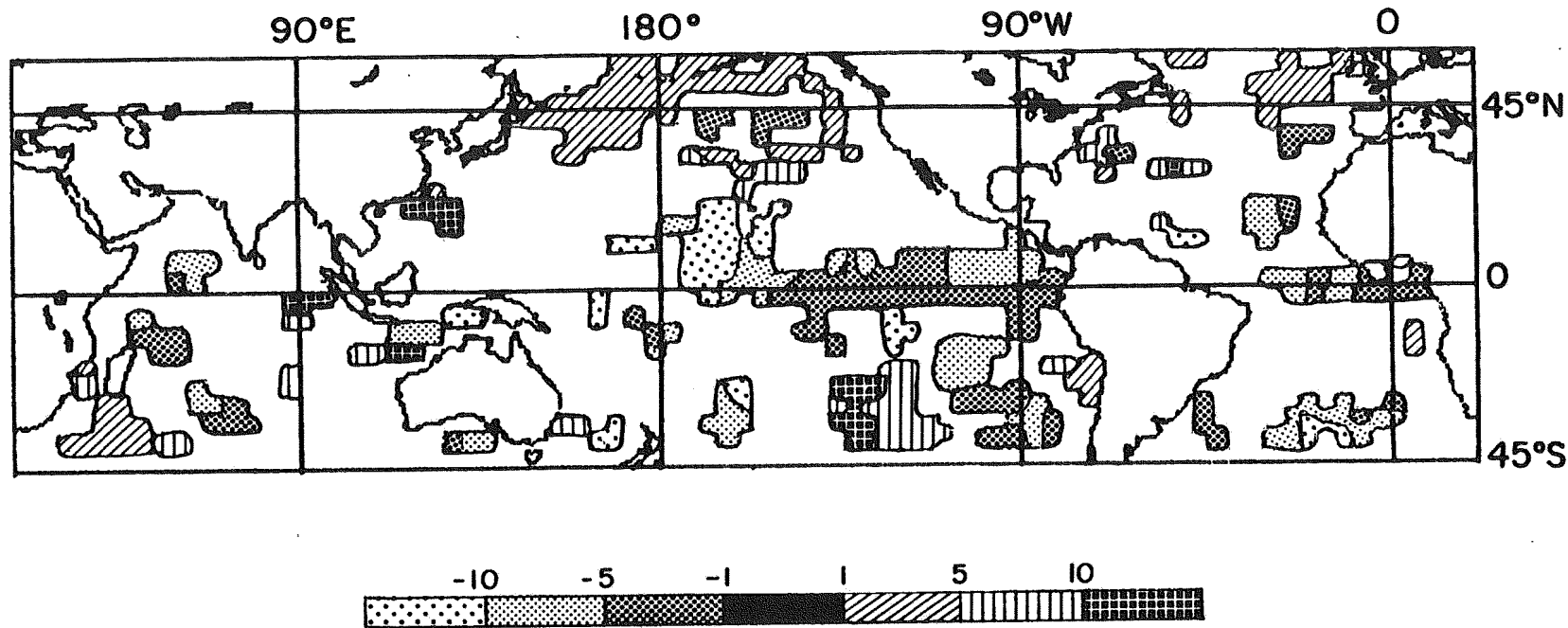


Figure 4.13: Contour plot of OLR-SSTA LAD regression slope for June-July-August showing areas where grid points had a P-value less than or equal to 0.05. Units are $W \cdot m^{-2} \cdot K^{-1}$. Based on data from April 1979 through March 1985.

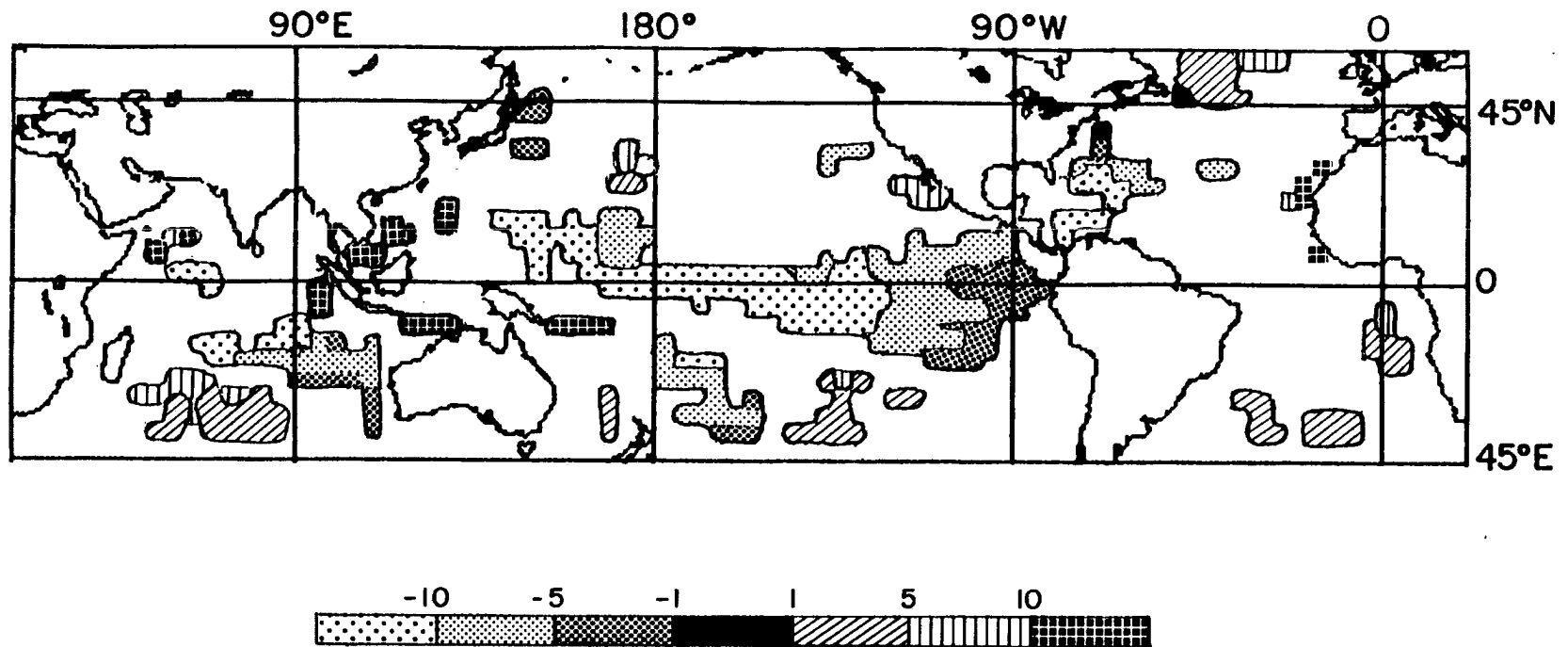


Figure 4.14: Contour plot of OLR-SSTA LAD regression slope for December-January-February showing areas where grid points had a P-value less than or equal to 0.05. Units are $W \cdot m^{-2} \cdot K^{-1}$. Based on data from April 1979 through March 1985.

Table 4.5: Net Radiation. Area averaged values from 60°N to 40°S in the LAD regression value of the $W \cdot m^{-2}$ of net radiation per $1^\circ C$ increase in SST. Units are $W \cdot m^{-2} \cdot K^{-1}$. Column 4 is the percent of grid points with $P \leq 0.05$. Based on data from April 1979 through March 1985.

Season	All Prob	Prob ≤ 0.05	Percent
Full Year	1.9	3.5	43%
Mar-Apr-May	1.6	4.0	31%
Jun-Jul-Aug	1.7	3.8	34%
Sep-Oct-Nov	1.9	4.1	33%
Dec-Jan-Feb	2.1	4.7	37%

highlight, the effect of SSTA on stratocumulus decks off the west coast of continents is strongest in summer. Also, unlike albedo- and OLR-SSTA analyses, the SPCZ is not clear in any of the plots of net radiation-SSTA LAD slopes.

4.5 Discussion

On a global basis, the changes in net radiation is going to be equal to the sum of the changes in outgoing long wave radiation and the changes in solar energy absorbed by the earth-atmosphere system. Assuming solar energy is a constant, which is valid for our purposes here, the change in absorbed solar energy is due primarily to changes in the albedo. Table 4.6 gives the average LAD value for the reflected flux-SSTA, the OLR-SSTA, followed by the sum of these two quantities. The sum has the sign reversed, though, for easier comparison to the average value for the LAD of net radiation-SSTA because a decrease in outgoing IR radiation leads to an increase in net radiation. Similarly, a decrease in the reflected flux means less solar radiation being reflected and therefore more solar radiation is being absorbed, hence an increase in the net radiation. For the full year, the difference between the average net radiation-SSTA LAD slope and the sum of the average reflected flux-SSTA and average OLR-SSTA LAD slopes is only 2.6%. The same analysis for grid points with P-values less than or equal to 0.05, shown in Table 4.7, has a difference between the sum of the average reflected flux-SSTA and average OLR-SSTA LAD slopes and the net radiation-SSTA LAD slope of only 1.4%. This small difference is a strong indication that this analysis technique is robust.

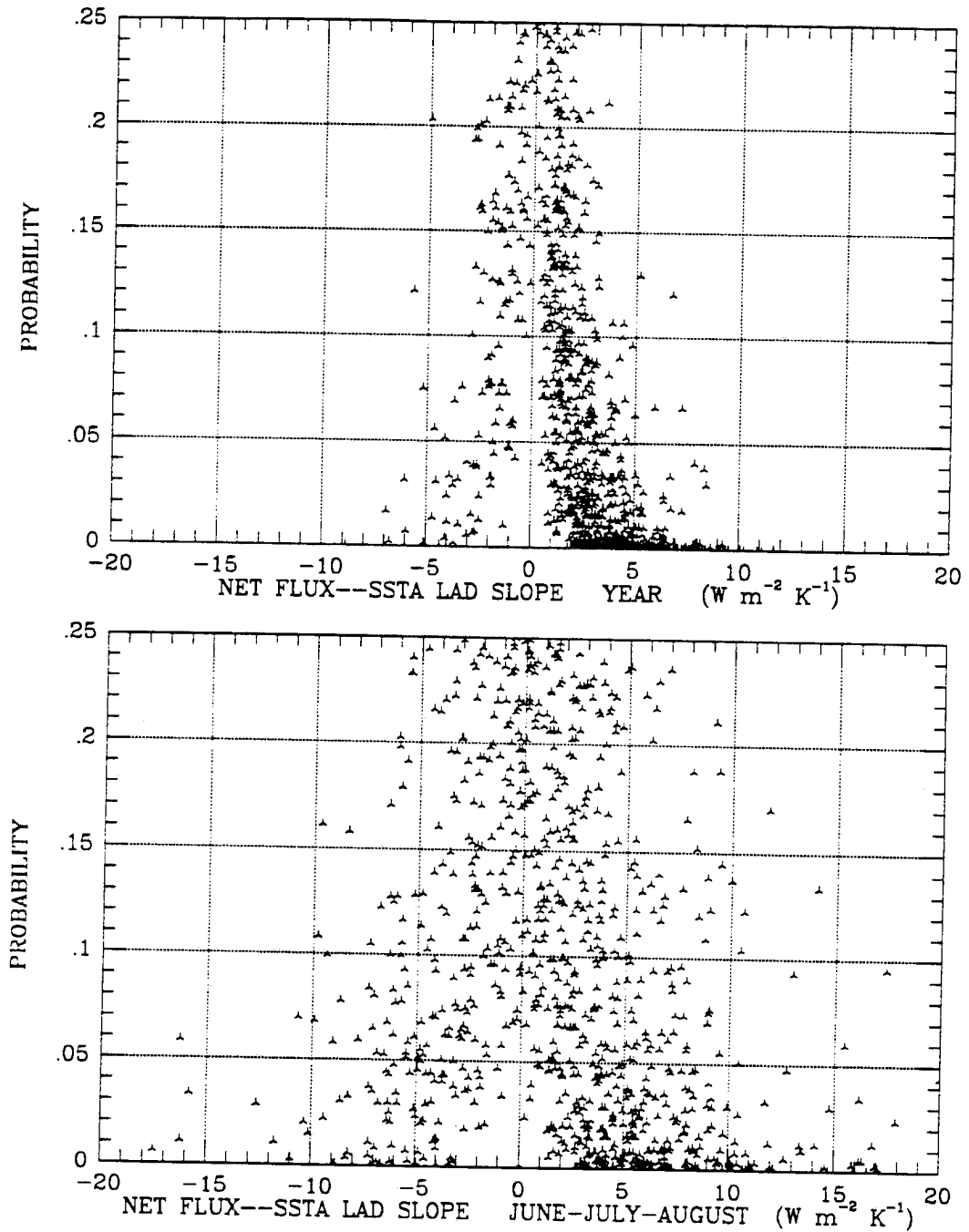


Figure 4.15: Scatter plots of Net Radiation--SSTA LAD slope values versus the Probability that the data was randomly distributed around the regression line. Top is for the full year, bottom is seasonal analysis for June-July-August which was very similar to the scatter plot for December-January-February analysis. Units are unitless for the P-value and $W \cdot m^{-2} \cdot K^{-1}$ for the LAD slope. Based on data from April 1979 through March 1985.

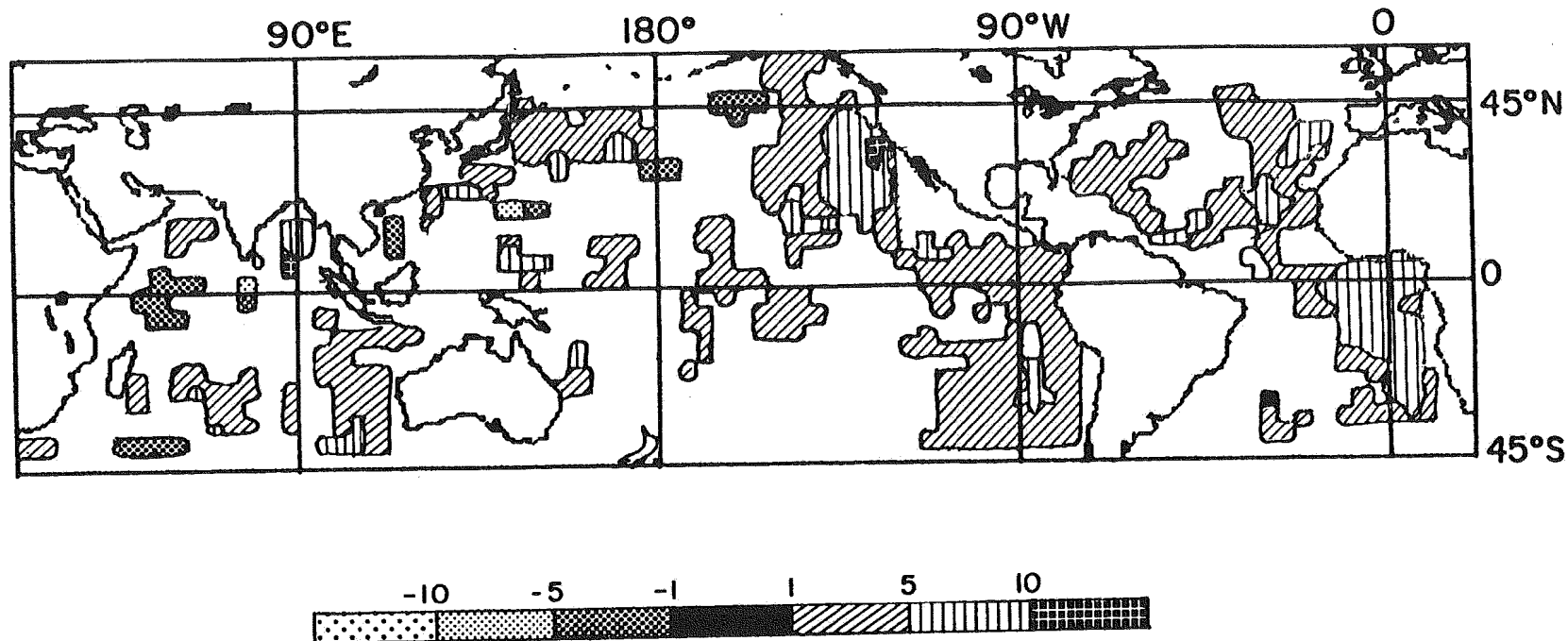


Figure 4.16: Contour plot of Net Radiation-SSTA LAD regression slope showing areas where grid points had a P-value less than or equal to 0.05. Units are $W \cdot m^{-2} \cdot K^{-1}$. Based on data from April 1979 through March 1985.

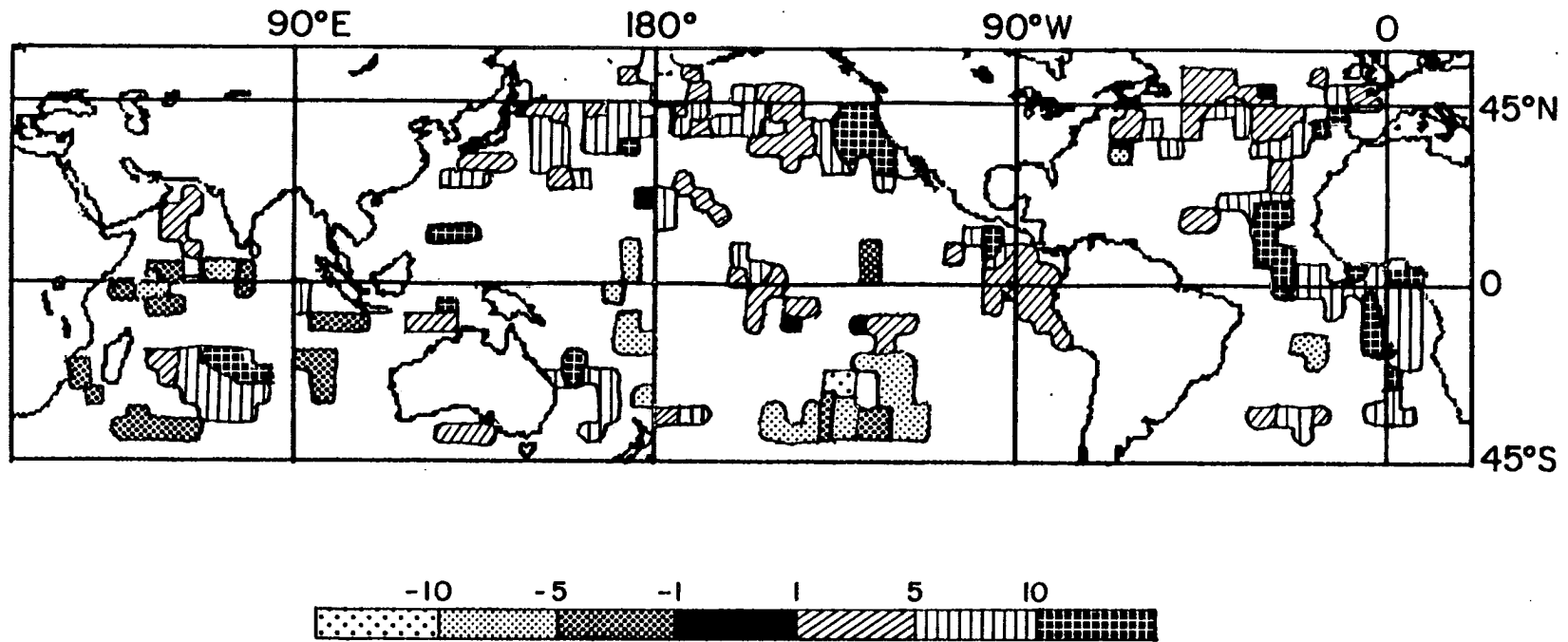


Figure 4.17: Contour plot of Net Radiation-SSTA LAD regression slope for June-July-August showing areas where grid points had a P-value less than or equal to 0.05. Units are $W \cdot m^{-2} \cdot K^{-1}$. Based on data from April 1979 through March 1985.

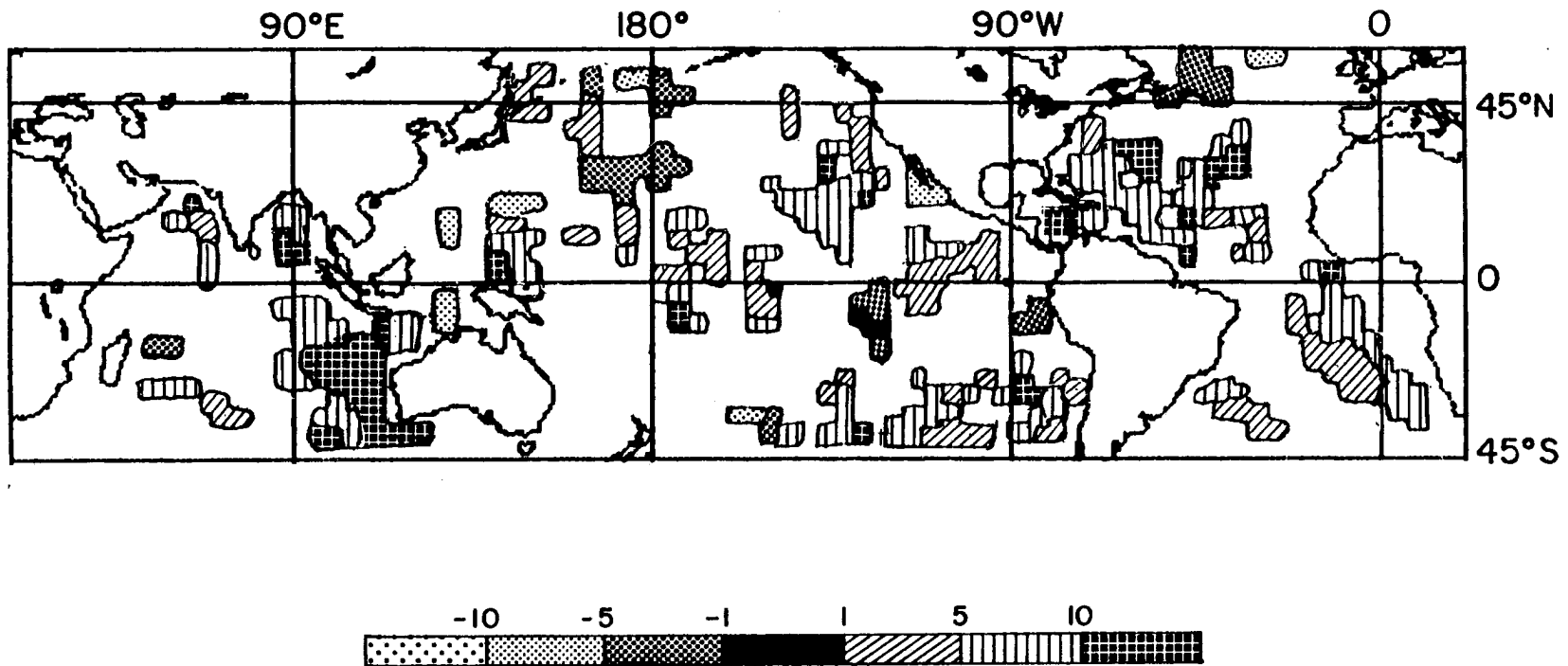


Figure 4.18: Contour plot of Net Radiation-SSTA LAD regression slope for December-January-February showing areas where grid points had a P-value less than or equal to 0.05. Units are $W \cdot m^{-2} \cdot K^{-1}$. Based on data from April 1979 through March 1985.

Table 4.6: Comparison of area averages of radiation parameters-SSTA LAD slopes from 60°N to 40°S. Column 4 is the sum of the average reflected flux-SSTA LAD slope and the average OLR-SSTA LAD slope multiplied by -1. The last column is the difference between the sum (of OLR-SSTA and reflected flux-SSTA LAD slope) and the average net radiation-SSTA LAD slope (column 5). All units are $\text{W}\cdot\text{m}^{-2}\cdot\text{K}^{-1}$. Based on data from April 1979 through March 1985.

Season	Ref. Flux	OLR	Sum	Net	Diff
Full Year	-0.37	-1.57	1.94	1.89	-0.05
Mar-Apr-May	0.90	-2.80	1.90	1.60	-0.30
Jun-Jul-Aug	-0.82	-1.01	1.83	1.65	-0.18
Sep-Oct-Nov	0.14	-1.98	1.88	1.93	0.05
Dec-Jan-Feb	-0.64	-1.61	2.25	2.11	0.14

Table 4.7: Comparison of area averages of radiation parameters-SSTA LAD slopes from 60°N to 40°S for grid points with probability values ≤ 0.05 . Column 4 is the sum of reflected flux-SSTA LAD slope and the OLR-SSTA LAD slope multiplied by -1. The last column is the difference between the sum (of OLR-SSTA and reflected flux-SSTA LAD slope) and the average net radiation-SSTA LAD slope (column 5). All units are $\text{W}\cdot\text{m}^{-2}\cdot\text{K}^{-1}$. Based on data from April 1979 through March 1985.

Season	Ref. Flux	OLR	Sum	Net	Diff
Full Year	-0.39	-3.16	3.55	3.50	-0.05
Mar-Apr-May	1.89	-5.41	3.52	3.98	0.46
Jun-Jul-Aug	-1.69	-1.81	3.50	3.79	0.29
Sep-Oct-Nov	0.20	-4.31	4.11	4.11	0.00
Dec-Jan-Feb	-0.39	-4.39	4.78	4.66	-0.12

The bottom line for this research is net radiation. If there were no feedbacks, the net radiation should decrease—that is, the earth should radiate more out to space than it receives—with increases in SSTA. This should be $\sim -3.3 \text{ W}\cdot\text{m}^{-2}\cdot\text{K}^{-1}$ (Cess *et al.*, 1990). Yet net radiation increased $\sim 3 \text{ W}\cdot\text{m}^{-2}\cdot\text{K}^{-1}$. This is clearly indicative of positive feedback mechanisms associated with SSTAs. These positive feedback mechanisms take the form of both changes in reflected flux and changes in OLR associated with changes in SSTA.

As mentioned in the introduction to this chapter, Cess *et al.* (1990) reported that the average GCM determined change in OLR associated with a 1°C increase in SSTA was $2.46 \text{ W}\cdot\text{m}^{-2}\cdot\text{K}^{-1}$. Since for conditions average for the earth, OLR should increase $3.3 \text{ W}\cdot\text{m}^{-2}\cdot\text{K}^{-1}$ (Cess *et al.*, 1990), this represents a positive warming feedback of $0.84 \text{ W}\cdot\text{m}^{-2}\cdot\text{K}^{-1}$. This modeling study also found that reflected flux decreased by an average of $0.72 \text{ W}\cdot\text{m}^{-2}\cdot\text{K}^{-1}$. The net positive radiative feedback, therefore, was $1.56 \text{ W}\cdot\text{m}^{-2}\cdot\text{K}^{-1}$. Our observational study's results indicated that the change in reflected flux is the same sign as the models' but only about half as great. It decreases despite the observational evidence that clouds increase with SSTA. The change in OLR, however, was significantly different, rather than an increase that the models' had, our results showed a significant decrease. The effect on net radiation appears to be fairly similar, but the values reported here for the model results were after the expected $3.3 \text{ W}\cdot\text{m}^{-2}\cdot\text{K}^{-1}$ increase in radiation was subtracted. Therefore, again, this observational study reports a significantly larger positive net radiation–SSTA feedback. However, it should be noted that the model results were averaged over the entire globe while our observational analysis was only for the open ocean from 60°N to 40°S .

To break down the global averages somewhat, Figure 4.19 is a plot of the zonal average of these radiation parameters and Figure 4.20 is the same except only using those grid points with $P \leq 0.05$. To adjust to a sign convention where positive represents an increase in energy in the earth/ocean/atmosphere system, OLR–SSTA and reflected flux–SSTA LAD slopes were multiplied by -1 . On a zonally averaged basis, the net flux–SSTA LAD slope was always positive: increases in SSTA are associated with increases in net energy in all latitude circles from 60°N to 40°S . Changes in reflected flux and changes in OLR exhibit

a distinct out of phase relationship so that even in the tropics, the significant decreases in OLR are largely balanced by increases in reflected flux. However, the net effect is still positive. While Tables 4.6 and 4.7 show that for the entire open ocean from 60°N to 40°S, the sum of the area weighted average OLR–SSTA LAD slope and the average reflected flux–SSTA LAD slope came very close to equaling the average net radiation–SSTA LAD slope, this does not hold true on a zonally averaged basis. While Figure 4.19 comes close, because the grid points with low P-values were different for OLR–SSTA, reflected flux–SSTA and net radiation–SSTA analysis, we shouldn't expect Figure 4.20 to balance at each zonal band.

However, neither global averages nor zonal averages are necessarily representative of any particular location since the averages often reflect averaging of regions with negative and regions with positive values. One of the key features shown in this analysis is that the region where net radiation changes significantly with SSTA is not where OLR changes. Much has been written about possible radiative feedback loops associated changes in tropical cirrus (e.g. Somerville *et al.*, 1989; Lindzen, 1990a; Stephens *et al.*, 1990; and Platt, 1981) and changes in water vapor at high elevations as a result of strong tropical convection (Lindzen, 1990a). While these are real concerns, this research indicates that for the most part, these factors largely cancel each other out. The largest increases in net radiation associated with increases in SSTA occurs in regions where low clouds decrease with increases in SSTA. Therefore, as Slingo (1990) stated, low clouds may be one of the major keys to understanding radiative feedback loops in global warming.

With any research of this type, it is important to understand the link between clouds and albedo (and albedo's radiative effects). As noted in Chapter 2, for this same time period, total clouds increased with SSTA, yet this research indicated that albedo and reflected flux both decreased with SSTA. This means that the average cloud got less reflective. This appears to be because low, optically thick clouds decreased while high, optically thin clouds increased. Though the regionality of much of the change in radiation with SSTAs seems closely related to the changes in clouds with SSTAs discussed in Chapter 2, we must still consider the radiative importance of changes in clear sky water vapor. In

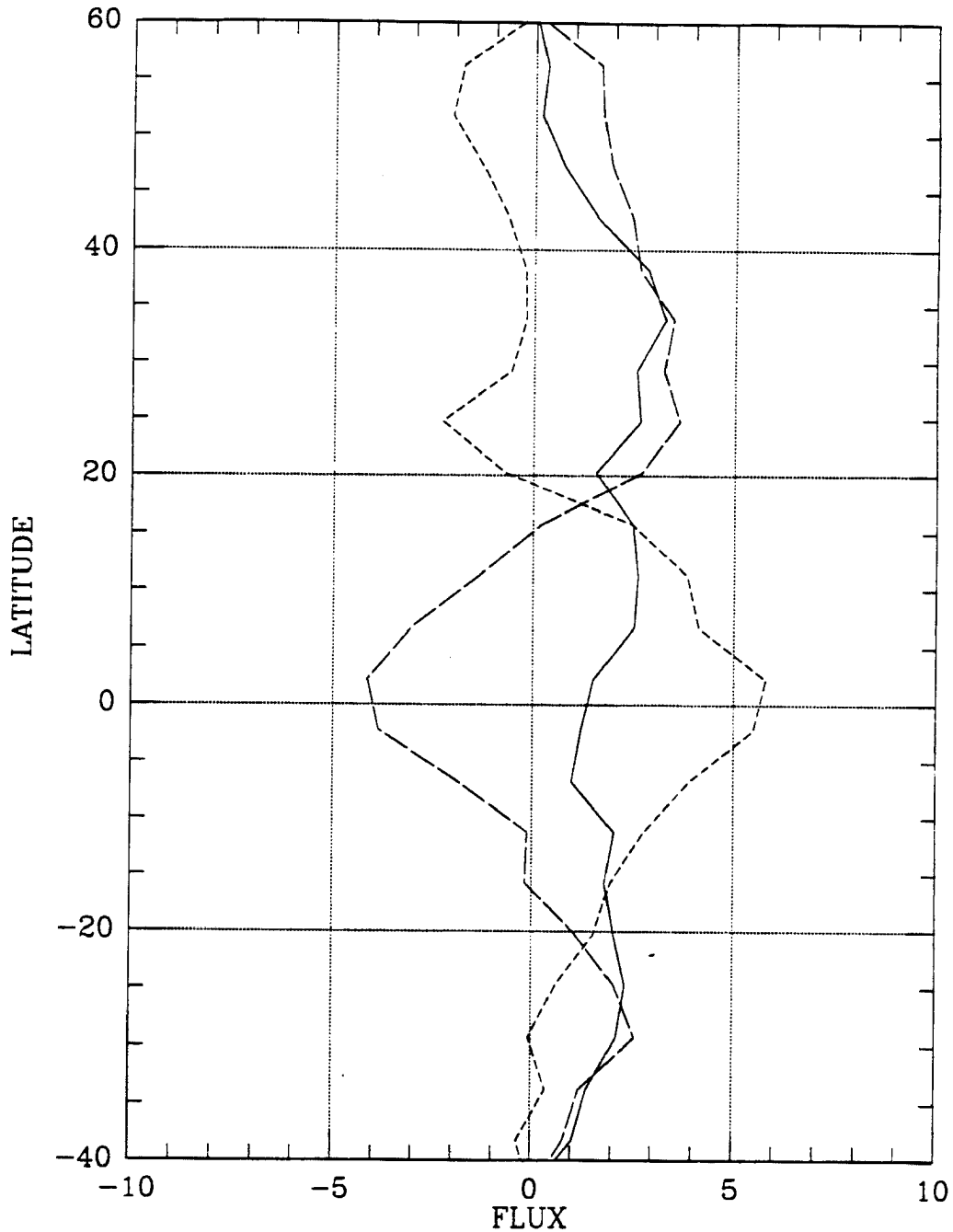


Figure 4.19: Zonal average values for net radiation-SSTA LAD slope (solid line), OLR-SSTA LAD slope (short dash line), and reflected flux-SSTA LAD slope (long dash line). A positive value for net radiation indicates that the earth/ocean/atmosphere system gained more radiation than it lost. To adjust to this sign convention, the values for OLR-SSTA and reflected flux-SSTA LAD slopes have been multiplied by -1 , because a decrease in OLR causes an increase in net radiation as does a decrease in reflected flux. All units are $\text{W}\cdot\text{m}^{-2}\cdot\text{K}^{-1}$. Based on data from April 1979 through March 1985.

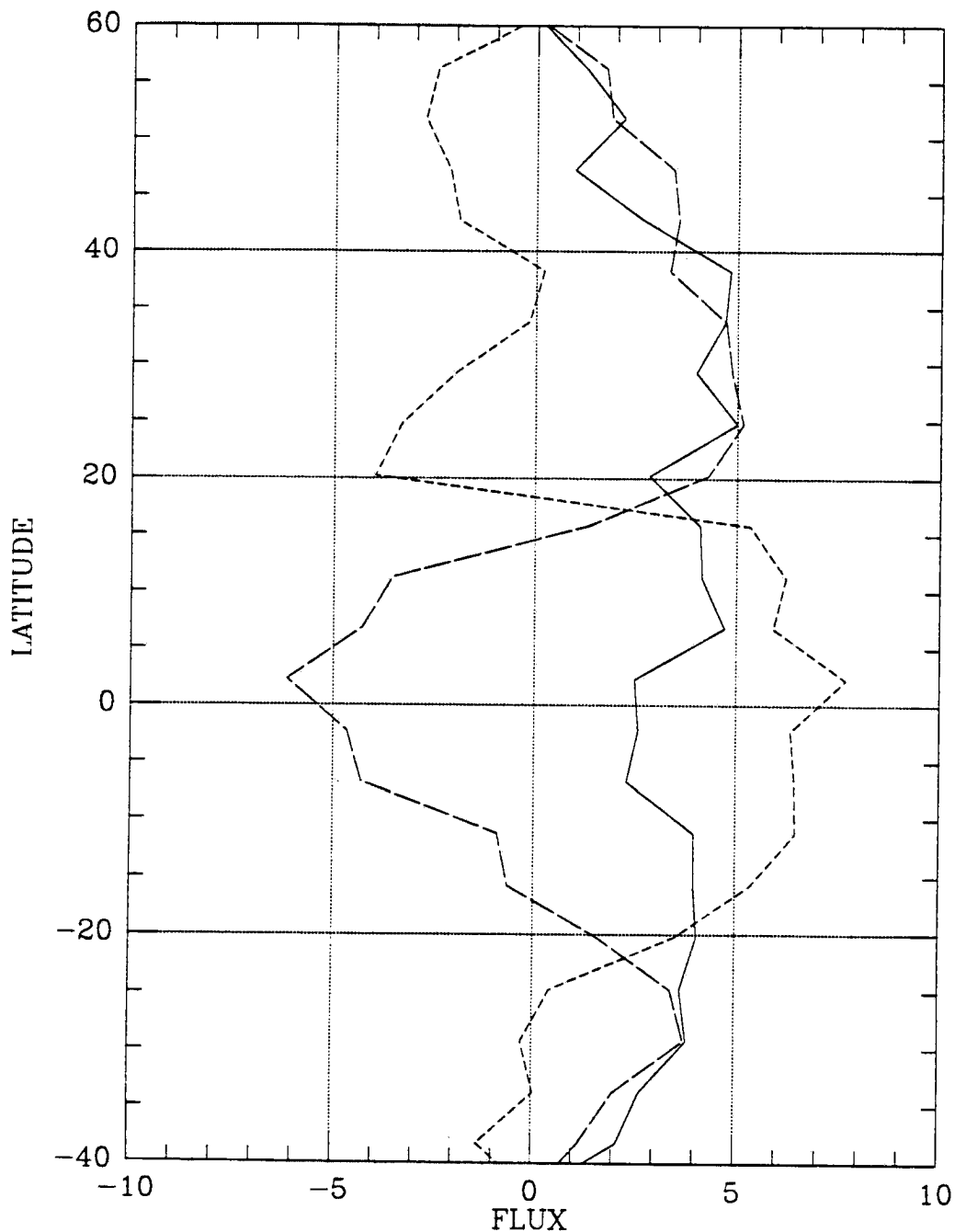


Figure 4.20: Zonal average values for net radiation-SSTA LAD slope (solid line), OLR-SSTA LAD slope (short dash line), and reflected flux-SSTA LAD slope (long dash line). A positive value for net radiation indicates that the earth/ocean/atmosphere system gained more radiation than it lost. To adjust to this sign convention, the values for OLR-SSTA and reflected flux-SSTA LAD slopes have been multiplied by -1 , because a decrease in OLR causes an increase in net radiation as does a decrease in reflected flux. Only grid points with $p \leq 0.05$ were used to create the zonal averages. All units are $\text{W}\cdot\text{m}^{-2}\cdot\text{K}^{-1}$. Based on data from April 1979 through March 1985.

the following chapter, we will try to determine how much of the change in OLR is due to changes in clouds and how much is due to changes in clear sky water vapor.

Chapter 5

COMPARATIVE ANALYSIS OF THE RADIATIVE EFFECTS OF CLOUD–SSTA AND CLEAR SKY WATER VAPOR–SSTA RELATIONSHIPS IN CONTRIBUTING TO THE RELATIONSHIP BETWEEN OUTGOING LONGWAVE RADIATION AND SSTA

5.1 Introduction

In Chapter 4, we showed that there was a strong observational relationship between SST anomalies and anomalies in basic radiation parameters such as albedo, outgoing longwave radiation, and net radiation. In Chapter 3, we determined that there was a strong relationship between clear sky water vapor anomalies and SST anomalies. Since water vapor is a major infrared radiation absorbing and emitting gas, the observed changes in water vapor would result in changes in IR radiation. Water vapor's absorption of solar energy does have an effect on albedo by decreasing the amount of solar energy available to reflect. However, since water vapor's effect on albedo is minor, its effect on IR radiation will produce a non-canceling effect on the net radiation.

It is important to this research project to understand how much of the observed changes in OLR and net radiation are due to changes in cloudiness and how much are due to changes in clear sky greenhouse effect. In addition, it is important to our understanding of the clear sky greenhouse effect to determine what level in the atmosphere's changes in water vapor has the greatest effect on IR radiation given the range of naturally observed variations in water vapor at that level. This is important because "even though water vapor near the ground increases with increasing temperature, a smaller absolute decrease at upper levels can lead to a negative (radiative) feedback" (Lindzen, 1990b).

"Both the greenhouse effect of and the feedback by water vapor have been explored in many model studies of climate. By contrast, few studies have attempted to use global

observations to examine the details of this feedback” (Stephens and Greenwald, 1990a). Two of the observational studies that have are Raval and Ramanathan (1989) and Stephens and Greenwald (1990). Using Earth Radiation Budget Experiment (ERBE) clear sky OLR and SST data, Raval and Ramanathan (1989) determined that the clear sky greenhouse effect increased with increasing SST. Stephens and Greenwald (1990a) took the analysis one step further by using not only ERBE clear sky OLR and SST data but also Scanning Multichannel Microwave Radiometer (SMMR) derived integrated water vapor that was coincident in both space and time. Again the results indicate that the clear sky greenhouse effect increases with increasing SST and that this is due to increases in the integrated clear sky water vapor. Since SST tends to increase with decreasing latitude and since both used averages around latitude belts which significantly diminishes random error (Raval and Ramanathan, 1989) the analogy to global warming applicable to these studies is that the clear sky radiative effect caused by CO₂ induced global warming is similar to moving equatorward. This is quite different from our examination of local changes over varying SSTAs. Another element that these studies could not address was the radiative effects of clear sky water vapor at different levels in the atmosphere.

The magnitude of the radiative effect of clear sky water vapor may be very significant. Lindzen (1990b) states that “the positive feedback that arises from using convective parameterizations which tend to moisturize the atmosphere at all levels when there is warming is the most important positive feedback in current large scale climate models — despite the popular emphasis on feedbacks from cloud cover.” Cess *et al.* (1990) states that “for conditions typical of the Earth” a one degree increase in surface temperature would result in a $3.3 \text{ W}\cdot\text{m}^{-2}$ increase in outgoing long wave radiation. However, climate models that contain a positive water vapor feedback mechanism, in which a warmer atmosphere contains more water vapor, “typically give” a $2.2 \text{ W}\cdot\text{m}^{-2}$ increase in outgoing longwave radiation for a 1°C increase in surface temperature. The average of the 19 atmospheric GCMs analyzed in Cess *et al.* (1990) was a $2.34 \text{ W}\cdot\text{m}^{-2}\cdot\text{K}^{-1}$ change in clear sky OLR. Thus the changes in water vapor associated with a 1°C increase in surface temperature results in $\sim 1 \text{ W}\cdot\text{m}^{-2}$ decrease in outgoing long wave radiation.

5.2 Methods

To determine the radiative effects of changes in clear sky water vapor from the changes in clear sky water vapor associated with SST anomalies determined in Chapter 3, a two stream radiative transfer model was run at each of the ISCCP grid points over the oceans. The model output included flux up from the surface and flux up at the top of the atmosphere. Subtracting flux up at the top of the atmosphere from flux up at the surface gives the greenhouse effect (Schneider, 1990). Without varying the surface temperature, and hence IR radiation up from the surface, water vapor was added or subtracted to the atmosphere in the quantity and vertical distribution associated with a 1°C increase in SSTA as determined in Chapter 3. The model was then run again and a new top-of-the-atmosphere flux determined. This process was repeated with just changing the water vapor at one layer in the atmosphere using that level's water vapor-SSTA LAD slope to determine which level's changes in water vapor has the greatest effect on clear sky OLR.

Clouds were not included in this modeling effort so the results apply only to clear sky fluxes. It is quite likely that temperatures at various levels in the atmosphere also have distinct relationships to SSTA that would impact on clear sky radiative fluxes. However, no changes in temperature were considered in this analysis. Even the SST was not altered though increases or decreases in water vapor associated with a 1°C increase in SSTA were used in the analysis. Temperatures remained fixed at all levels at each grid point so that the results would indicate the changes in clear sky radiative fluxes due solely to changes in water vapor.

5.2.1 Data

Since the PW-SSTA LAD analysis was performed on three different layers in the troposphere, the data used in this modeling analysis had to conform to these three layers. The baseline water vapor values used in this research were yearly averages taken directly from the ISCCP TOVS climatology for the surface to 800 hPa. However, above 800 hPa, the 800-680, 680-560, 560-440, and 440-310 hPa ISCCP TOVS layered water vapor values had to be combined into the two layers: 800-560 and 560-310 hPa. For atmospheric

temperatures at each grid point, yearly averaged ISCCP TOVS climatology was again used. Temperatures were used at 15, 50, 115, 245, 310, 560, and 800 hPa. The 15, 50, 115, and 245 hPa temperatures were levels supplied by ISCCP. The formulation of the model required temperatures at the top and bottom of each layer. Therefore, to correspond to the top and bottom of the layered values of water vapor, ISCCP temperatures at 900, 740, 620, 375, and 245 hPa were interpolated to derive the input temperatures at 800, 680, 560, and 310 hPa.

All input data varied from grid point to grid point on the 2.5 x 2.5 degree ISCCP grid and were based on full year or longer average values at that grid point. The surface temperature input to the model was the SST value averaged from the 72 months of SST data set used in Chapter 3. For changes in water vapor, the LAD slope values for water vapor at these levels presented in Chapter 3 were added to the climatological water vapor. The LAD slope values in Chapter 3 were in units of cm liquid water equivalence per degree K and therefore represent the changes in water vapor associated with a 1°C increase in SST at that grid point.

Since the ISCCP TOVS data set included no gridded values for ozone at different levels in the atmosphere, the IR radiative effects of O₃ were not included in this analysis. A constant standard distribution of CO₂ was assumed. Since ISCCP TOVS supplied no water vapor data above 310 hPa, we used an atmosphere in the model that had no water vapor above 310 hPa. Excluding O₃ and water vapor above 310 hPa would obviously lead to some errors in the analysis of clear sky IR radiation. The magnitude of these errors is evaluated following the description of the model.

5.2.2 The Two Stream Radiative Transfer Model

For this research, Paul Stackhouse kindly provided us with a 10 band, n-layer, two stream IR radiative transfer model. Mr. Stackhouse used an earlier 130 band version of this model in his M.S. degree research at CSU's Department of Atmospheric Science. Recently he modified the IR portion into a 10 band model. The decrease in the number of bands greatly decreased the model's computer run time while decreasing its accuracy only slightly. Details of a two stream model are presented in several review articles (e.g., Meador

and Weaver, 1980; Zdunkowski, *et al.*, 1980; and King and Harshvardhan, 1986). The description of the model in the following three subsections is taken, with some modification, from Stackhouse and Stephens (1991):

Basic Formulation of a the Two Stream Model

“The two stream equations for upward F^+ and downward F^- hemispheric fluxes can be written as

$$\mp \frac{dF^\pm(\tau)}{d\tau} = -(a + b)F^\pm(\tau) + b F^\mp(\tau) \quad (5.1)$$

where the upward and downward fluxes F^\pm (in $W \cdot m^{-2}$) are given by

$$\begin{aligned} F^+(\tau) &= \int_{-1}^0 \mu I(\tau, \mu) d\mu, \\ F^-(\tau) &= \int_0^1 \mu I(\tau, \mu) d\mu, \end{aligned} \quad (5.2)$$

and where $a = (1 - \omega_0)D$ is the fraction of the total extinction of the flux due to particle absorption. In this fraction, D is the diffusivity and $\tilde{\omega}_0$ is the single scatter albedo. The quantity b represents the fraction of diffuse flux scattered backwards from the layer (e.g., Stephens *et al.*, 1990).

“The two stream equations, written in the form of second order differential equations in F^+ and F^- , are then solved with appropriate specification of boundary conditions (e.g. Preisendorfer, 1976). The solutions to (5.1) are

$$F^\pm(\tau) = m_+ \eta_\pm \exp(\kappa\tau) + m_- \eta_\mp \exp(-\kappa\tau) + F s_{ir}^\pm(\tau), \quad (5.3)$$

where $\eta_\pm = 1 \pm \frac{a}{\kappa}$, $\kappa = [a(a + 2b)]^{\frac{1}{2}}$ and where $F s_{ir}^\pm(\tau)$ is the particular solution of the differential equation for the source term having units of flux. The constants m_\pm are found by applying boundary conditions at the top and bottom of an atmospheric layer assuming that the optical depth is zero at the top of a layer and τ^* at the bottom. As discussed by Flatau and Stephens (1988), (5.3) becomes unbounded as $\tau \rightarrow \infty$ through the presence of the term containing the positive exponential. A more stable expression of this solution is (Flatau and Stephens, 1988):

$$\begin{aligned} F^+(0) &= T F^+(\tau^*) + \mathcal{R} F^-(0) + S_{ir}^+(0) \\ F^-(\tau^*) &= \mathcal{R} F^+(\tau^*) + T F^-(0) + S_{ir}^-(\tau) \end{aligned} \quad (5.4)$$

where

$$\begin{aligned} S_{ir}^+(0) &= F_{s_{ir}^-}(0) - \mathcal{T}F_{s_{ir}^+}(\tau^*) - \mathcal{R}F_{s_{ir}^-}(0) \\ S_{ir}^-(\tau^*) &= F_{s_{ir}^-}(\tau^*) - \mathcal{R}F_{s_{ir}^+}(\tau^*) - \mathcal{T}F_{s_{ir}^-}(0) \end{aligned} \quad (5.5)$$

represents the total source terms for infrared (IR) wavelengths. The coefficients \mathcal{T} and \mathcal{R} are the diffuse transmittance and reflectance functions and are defined in Stephens and Tsay (1990). In this form, the exitant fluxes from the layer are expressed in terms of the incoming fluxes and (5.5) is a statement of the interaction principle for fluxes (e.g., contrast this statement with that defined in Stephens, 1988). The solution expressed by (5.5) is stable under the limits $\tau^* \rightarrow 0$ and $\tau^* \rightarrow \infty$ (e.g., Flatau and Stephens, 1988)" (Stackhouse and Stephens, 1991).

A model of the Molecular Absorption Spectra

"Molecular absorption is incorporated into the two stream model using narrow band absorption in the form of k -distributions and exponential sum fit approximations to the narrow band transmission functions for gaseous absorption. The absorbing gases included in this study are H_2O and CO_2 infrared wavelengths. For wavelengths greater than $3.8 \mu m$, the k -distribution method is applied to the bands shown in Table 5.1. The optical paths associated with each gas are computed using the simple pressure-temperature scaling parameterization with scaling constants given for each gas by Chou and Arking (1980), Chou and Arking (1981), and Chou and Peng (1983). Absorption in the $8 - 13 \mu m$ window region is modeled according to the parameterization of Kneizys *et al.* (1980).

"The transmittance of radiation for the 10 intervals of the infrared spectrum is thus defined as

$$T(u) \approx \sum_{i=1}^n w_i e^{-k_i u}. \quad (5.6)$$

Flux calculations are then performed for a particular k_i and summed according to (e.g., Stephens, 1984)

$$F_{\Delta\nu}^{\pm} = \sum_{i=1}^n w_i F_i^{\pm}(\tau_i = k_i u) \quad (5.7)$$

to determine the total broadband flux within the given spectral interval $\Delta\nu$ " (Stackhouse and Stephens, 1991).

Table 5.1: The ten bands used in the two stream radiative transfer model.

Wavenumber range(cm ⁻¹)	H ₂ O	CO ₂	O ₃
20.0-340.0	center		
340.0-540.0	wing		
540.0-620.0	wing	wing	
620.0-720.0	wing	center	
720.0-800.0	wing	wing	
800.0-980.0	wing		
980.0-1100.0	wing		center
1100.0-1380.0	wing		
1380.0-1900.0	center		
1900.0-2620.0	wing		

Treatment of Source Terms

“The azimuthally integrated thermal source at some internal level τ is given by:

$$S_{ir}^{\pm} = 2\pi(1 - \omega_0)\mathcal{B}_\nu(\tau) \quad (5.8)$$

where $\mathcal{B}_\nu(\tau)$ is the Planck emission function which is approximated as

$$\mathcal{B}_\nu(\tau) = B_0 + B'\tau, \quad (5.9)$$

with B_0 representing the Planck emission function at the top of the layer in question (i.e., $B_0 = \mathcal{B}_\nu(\tau = 0)$), and

$$B' = \frac{(B^* - B_0)}{\tau^*}, \quad (5.10)$$

where $B^* = \mathcal{B}_\nu(\tau^*)$. The particular solution for a source given by (5.9) and (5.10) is

$$F_{s_{ir}^{\pm}}(\tau) = \frac{2\pi}{D} \left[B_0 + B'\tau \pm \frac{B'}{x} \right] \quad (5.11)$$

where $x = a + 2b$.

“A problem arises when we apply the k-distribution to (5.11). Under conditions of pure molecular absorption, $\tau^* \rightarrow 0$ since k approaches zero for some bands. This results in spurious solutions and large errors in the atmospheric longwave cooling rates. We can avoid this problem by rearranging (5.11) to reduce the impact of τ^* in the denominator of (5.10). We do this using the interaction parameters \mathcal{R} and \mathcal{T} to obtain

$$S_{ir}^+(\tau = 0) = \frac{2\pi}{D} \left\{ B_0(1 - \mathcal{R}) - \mathcal{T}B^* + [B^* - B_0] \left[\frac{1 - \mathcal{T} + \mathcal{R}}{x\tau^*} \right] \right\} \quad (5.12)$$

$$S_{ir}^-(\tau = \tau^*) = \frac{2\pi}{D} \left\{ B^*(1 - \mathcal{R}) - \mathcal{T}B_0 - [B^* - B_0] \left[\frac{1 - \mathcal{T} + \mathcal{R}}{x\tau^*} \right] \right\}$$

where now the numerator of the final bracketed term is of the same order as the denominator. For the clear skies, $\omega_0 = 0$, $k = D$, $x = D$, $\mathcal{R} = 0$ and therefore, $\mathcal{T} = \exp(-D\tau^*)$. For $\tau^* \ll 1$ the Taylor series expansion gives $\mathcal{T} \approx 1 - D\tau^*$ and the factor $\frac{1 - \mathcal{T} + \mathcal{R}}{x\tau^*}$ reduces to order of 1" (Stackhouse and Stephens, 1991).

Model Evaluation

Since we did not have gridded O₃ data or information on water vapor above 310 hPa, even a 100% accurate model could not hope to duplicate the IR radiative flux. To see how much these data shortcomings would impact the model results, several model runs on McClatchey *et al.* (1972) soundings were made. These results are shown in Table 5.2. The first column represents the IR flux up at the top of the atmosphere using the O₃ data and the full depth water vapor data. The second column is flux up at the top of the atmosphere without considering any O₃ IR radiative effects. The third column is the flux up with the model as it was run for this research, without O₃ IR effects and no water vapor above 310 hPa. Not including O₃ radiative effects increases the IR leaving the Earth (decreasing the greenhouse effect) by $\sim 2.5 \text{ W}\cdot\text{m}^{-2}$ and not considering water vapor above 310 hPa increases outgoing IR by an addition $\sim 3 \text{ W}\cdot\text{m}^{-2}$. Given the appropriate weighting for the area covered by this research and the average top of the atmosphere IR flux is too high by $\sim 6.5 \text{ W}\cdot\text{m}^{-2}$, based solely on simulated evaluations of the model.

To evaluate the model using observational comparisons, the clear sky IR radiation values determined by a baseline model run were compared to the Earth Radiation Budget Satellite (ERBS) clear sky IR radiation. The model calculations were based on average SST temperature from 1983 to 1989, average water vapor based on TOVS data for the same time period, and climatological atmospheric temperatures from the ISCCP TOVS data set. The ERBS clear sky IR radiation data was an average for the year from June 1985 through May 1986. Hence, some differences, particularly localized maximums or

Table 5.2: Comparison of model runs on 4 different soundings. All values are for the flux up in units of $W \cdot m^{-2}$. The columns are for flux up at the top of the atmosphere for a model run with O_3 , without O_3 , and with no water above 310 hPa as well as no O_3 . The last column is difference between a full model run and the model run with no O_3 and no H_2O above 310 hPa.

Sounding	O_3	No O_3	No O_3 or $H_2O < 310 hPa$	Difference
Tropical	300.92	303.35	307.75	6.83
Mid Lat Summer	295.40	298.66	302.43	7.03
Mid Lat Winter	241.98	244.59	246.98	5.00
Sub Arctic Winter	206.79	208.74	209.58	2.79

minimums related to features such as a weak la Niña in 1986 versus averaged conditions for 1983–1989, could be expected.

Examination of the zonal average top of the atmosphere longwave flux from ERBS and baseline model output, shown in Figure 5.1, reveals that the model’s zonally averaged flux is significantly more than the observed values. Model sensitivity analysis shown in Table 5.2 would indicate perhaps a $7 W \cdot m^{-2}$ high bias in the model version used. However, the model output is frequently 20 or more $W \cdot m^{-2}$ higher than ERBS observations. Part of this high bias could be due to the total lack of aerosols in the model calculations. Also, a particularly appealing explanation for this discrepancy is cloud contamination of ERBS clear sky long wave top of the atmosphere flux. In support of this explanation is the large difference in clear sky fluxes in the tropics where high, thin cirrus could be hard to detect but would greatly lower outgoing IR radiation. The much smaller difference in the subtropics might be due to cloud contamination being caused by low clouds which have a much smaller effect on outgoing longwave radiation since they radiate at near surface temperatures.

However, this explanation may not be satisfactory. Stephens and Greenwald (1991a) summarize part of the work of Harrison *et al.* (1988) and Harrison *et al.* (1990) in evaluating ERBE fluxes by stating that “clear sky monthly averaged longwave fluxes are thought to overestimated by about $4 W \cdot m^{-2}$.” To examine this problem further, Figure 5.2 shows the observed clear sky long wave flux from ERBS and the calculated long wave

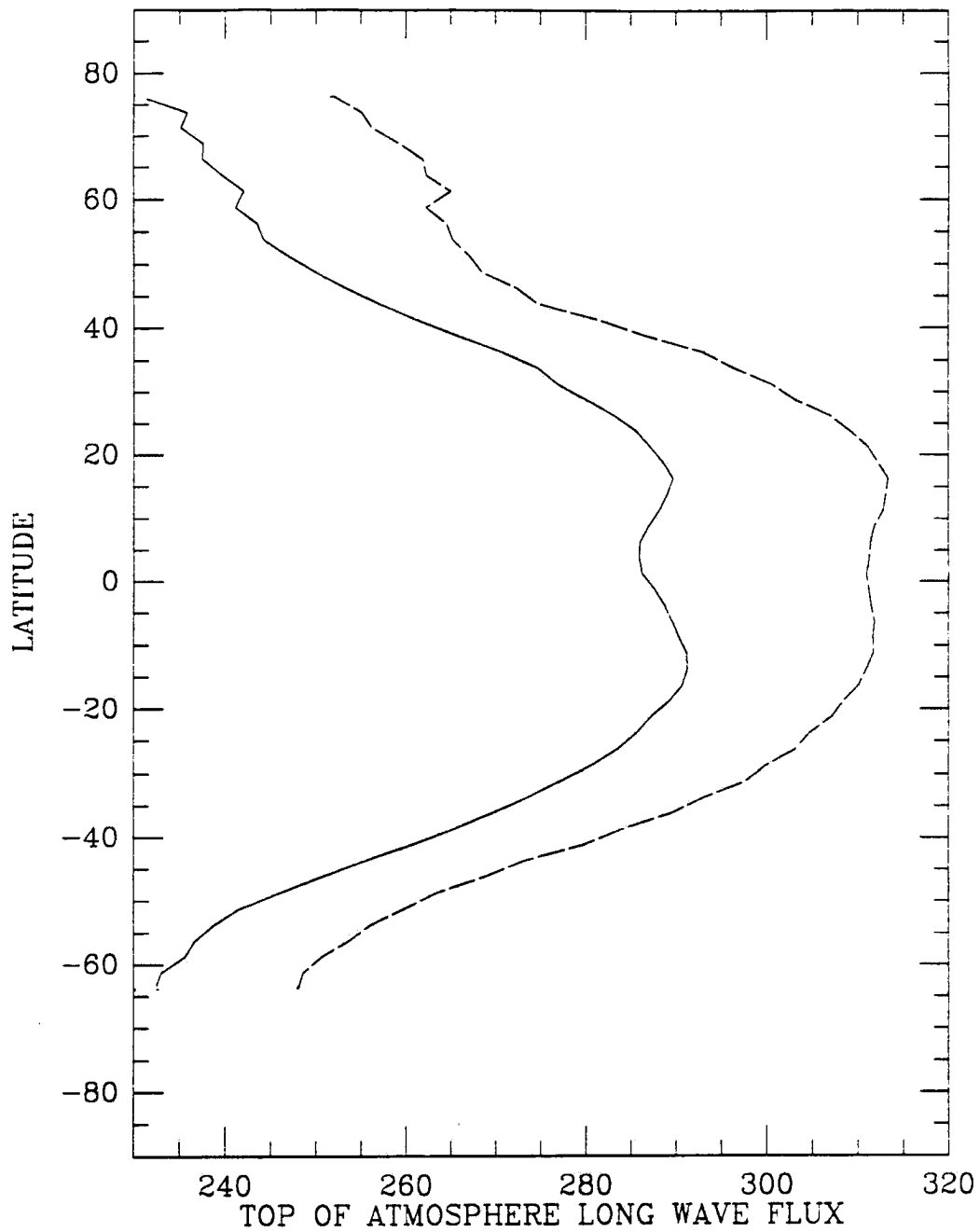


Figure 5.1: Zonally averaged top-of-the-atmosphere clear sky long wave flux from ERBS based on data from June 1985 through May 1986 (solid line) and the baseline model output from average temperature and water vapor data from July 1983 through June 1989 (dashed line). Values in $\text{W}\cdot\text{m}^{-2}$.

flux from the baseline run of the model at 4591 grid points. In addition, Figure 5.3 shows the difference between model calculations and ERBS observations. Generally, the model reproduces much of the general appearance of the observed (e.g., contour lines in approximately the same spacing and direction) with one notable exception: off the west coast of continents the model output has meridional components to contour lines while the observed contours are basically zonal. While this could be looked upon as a plus since it brings the model output more in line with the observed in those regions, it may simply be due to an error in the input data.

These regions where the model shows significantly less outgoing IR radiation than the zonal average are areas with cold water. For outgoing clear sky IR radiation to have values near the zonal average in these locations, as ERBS observations do, the troposphere in these regions must have less water vapor than the zonal average. While the data does show a gradient in tropospheric moisture, an overestimate of tropospheric moisture in these regions would lead to inappropriately small calculations of outgoing long wave radiation. Robertson (1991) and Robertson and Cohen (1990) indicate that European Centre for Medium Range Weather Forecasts (ECMWF) model output, which uses TOVS water vapor, overestimates the water vapor in these regions when compared to SSM/I observations of water vapor. Robertson believes this feature is probably in the ISCCP TOVS data as well as ECMWF, and is generally applicable to all subtropical ridges (see Chapter 3 for further evaluation of ISCCP TOVS water vapor).

Such differences would be a major concern if the goal of this research was to look at the magnitude of the clear sky greenhouse effect. However, the goal is to look at the radiative effect that changes in water vapor would cause. Therefore, the absolute magnitude of the baseline analysis is not as important as accurately understanding the magnitude of the changes. Since the analysis of the changes also have the limitations of no O₃ data nor water vapor data above 310 hPa, these limitations will not greatly effect the results though they do increase the outgoing IR radiation. However, the effect of inaccurate baseline water vapor data will still be present due to the logarithmic nature of the radiative effect of any gas. The same incremental increase in a radiatively active gas will have less of an effect on radiation if there is more of the gas there to begin with.

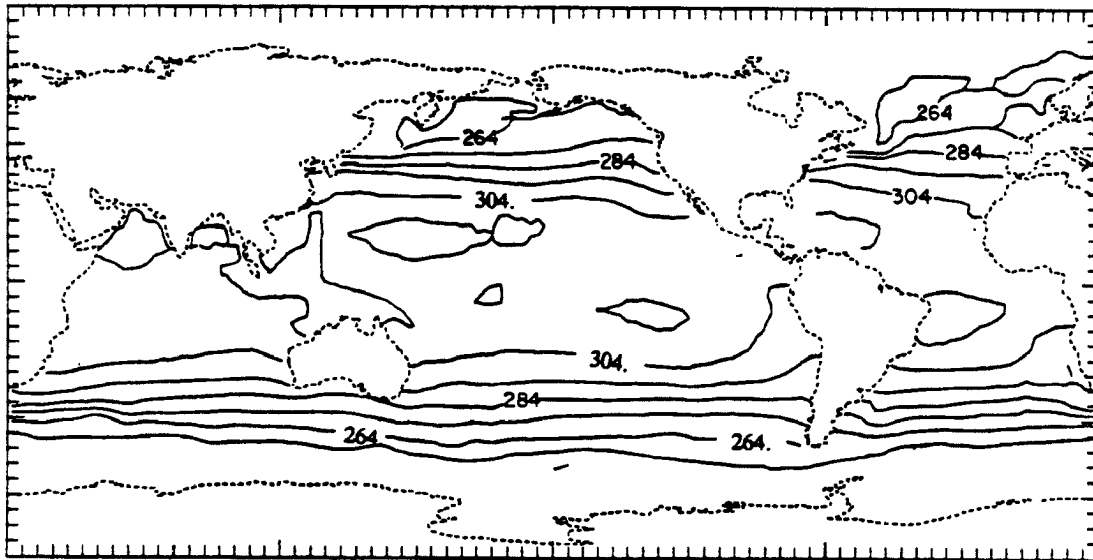
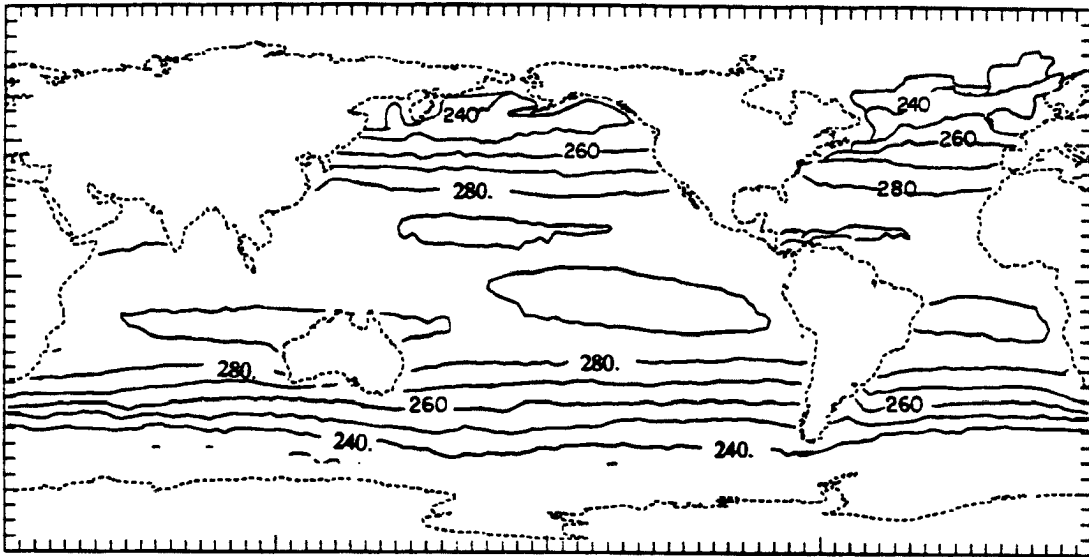


Figure 5.2: ERBS clear sky long wave flux at the top of the atmosphere (top) based on data from June 1985 through May 1986. Model calculated clear sky long wave flux at the top of the atmosphere from the baseline water vapor values based on average temperature and water vapor from July 1983 through June 1989. Units in watts per meter squared.

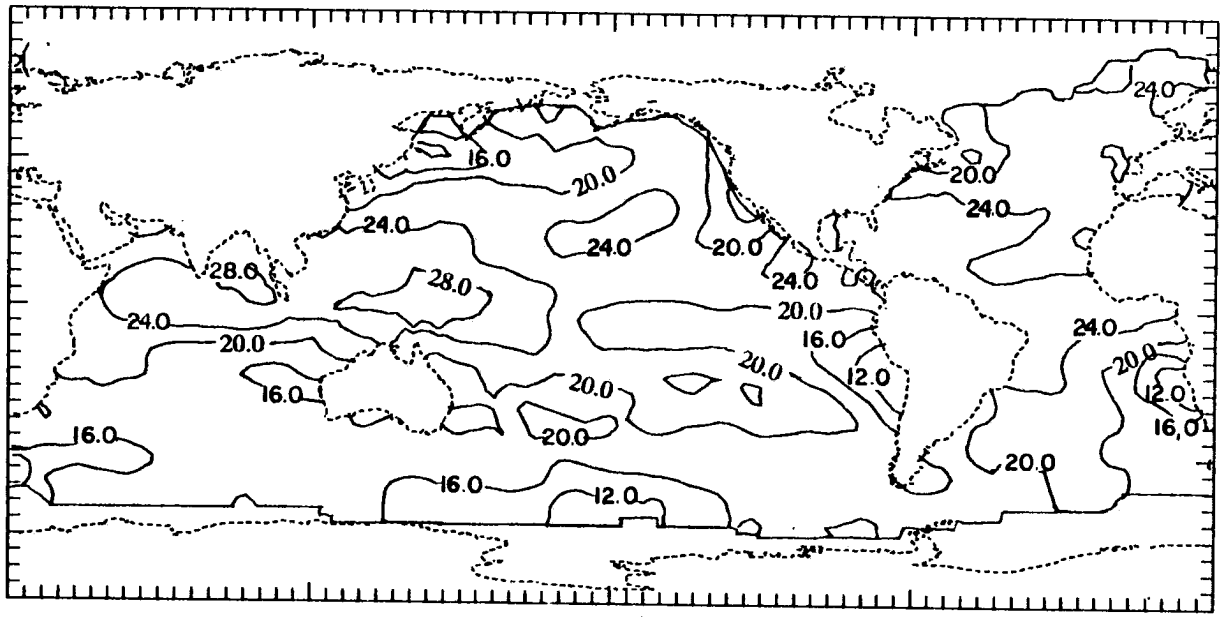


Figure 5.3: Model calculated long wave flux at the top of the atmosphere minus ERBS clear sky long wave flux. Units in $W \cdot m^{-2}$.

To examine the effect that inaccurate baseline water vapor values have on the radiative effects of the same incremental increase in water vapor, a few simple model sensitivity experiments were performed. The model was run in the same mode it was run in for the research. The input data consisted of the temperature and water vapor values for 3 mid Pacific grid points, at 51° North, 1° North, and 34° South. Zonally averaged values for LAD water vapor–SSTA slope at all three levels were added to the water vapor and the model was rerun at each grid point. Then for comparison purposes, the same analysis was run except the initial water vapor content was decreased by 10% first. The result of this sensitivity analysis, shown in Table 5.3, is that a 10% error in the climatological water vapor could result in ~8.5% error in the radiative effect of changes in water vapor associated with a 1°C increase in SSTA. While the magnitude of such errors indicates that they should not be totally ignored in analyzing the results, especially in certain regions where such effects may be large, the errors are small enough to proceed on with analysis of the results.

5.3 Results

5.3.1 Changes in Clear Sky OLR

The changes in water vapor associated with a 1°C increase in SST, shown in Chapter 3, generally decreases clear sky OLR. For ease of reference, the following Tables and Figures are for the change in greenhouse effect: where a decrease in OLR represents an increase in the greenhouse effect. This is in contrast to Chapter 4 where a decrease in OLR was represented simply as a decrease in OLR. As Table 5.4 illustrates, on average over the oceans, the change in water vapor at each level increased the greenhouse effect. The increase is greatest when all three layers of water vapor were used. Of the individual layers, the layer highest in the atmosphere had the greatest radiative effect and the layer lowest in the atmosphere had the smallest radiative effect.

Since Figures 3.5, 3.6, 3.7, and 3.8 illustrate that the lowest P-values were associated with larger magnitudes of the LAD slopes, it comes as no surprise that the radiative effects at grid points with low P-values for the water vapor–SSTA relationship are greater than the average radiative effects of all grid points.

Table 5.3: The sensitivity of the model to baseline water vapor is illustrated by running the model at three different mid-Pacific Ocean grid points with both baseline water vapor and 90% of baseline water vapor. The same zonally averaged change in water vapor determined by LAD analysis (dPW) was added and the model was rerun. The effect of a 10% decrease in baseline water vapor is to increase the radiative effect of the observed changes in water vapor associated with a one degree K increase in SST by $\sim 8.5\%$. Units are $\text{W}\cdot\text{m}^{-2}$ except for the last column which is percent.

Model Run	Flux Up TOA	dPW Effect	% Change
51N Base	267.55		
51N Base + dPW	266.60	0.95	
51N Base - 10%	268.67		8.7%
51N Base - 10% + dPW	267.63	1.04	
1N Base	310.95		
1N Base + dPW	309.87	1.08	
1N Base - 10%	312.82		8.5%
1N Base - 10% + dPW	311.64	1.18	
34S Base	291.01		
34S Base + dPW	290.24	0.77	
34S Base - 10%	292.49		8.3%
34S Base - 10% + dPW	291.65	0.84	

Table 5.4: Average change in clear sky greenhouse effect due to water vapor changes associated with 1°C increase in SSTA. Units are in $\text{W}\cdot\text{m}^{-2}$. P-values are those determined in Chapter 3 for water vapor. Total PW indicates that this change is the result of changes in high, middle, and low water vapor at the same time.

Change Due to	All Grid Points	$P \leq 0.05$ Grid Points
Total PW	0.74	1.41
High PW	0.38	0.70
Mid PW	0.25	0.37
Low PW	0.12	0.15

Figures 5.4 and 5.5 show how the clear sky radiative effects of the changes in water vapor varies with latitude. Again we see that there is a much stronger signal from the grid points with low P-values. For the bulk of the oceans, from 50°N to 45°S, the zonally averaged clear sky greenhouse effect due to changes in water vapor at each level is positive, with the water vapor high in the atmosphere having the greatest effect while water vapor changes low in the atmosphere have the least effect. Within this range of latitudes, the change in clear sky OLR due to changes in water vapor does not show a strong latitudinal dependence. There is a maximum near 20° S and a minimum at 40°N, but there are many secondary maximums and minimums as well. At 60°N, the radiative effect changes sign, which is especially noticeable in Figure 5.5 which plots only grid points with low P-values. As illustrated in Figure 5.4, the zonally averaged change in clear sky greenhouse effect also became negative at 62°S.

Are these negative values directly related to SST? To investigate this, Figures 5.6, 5.7, 5.8, and 5.9 plot the change in clear sky greenhouse effect against yearly average SST for low P-value grid points. The radiative effect of changes in water vapor at all three levels shows only a few grid points that are negative and these are clustered at 5–10 °C and 28–30 °C. The scatter plot of positive values does not show any striking trend in the radiative effect when plotted against SST, though the warmer SST grid points do show a slightly higher average radiative effect. For water vapor high in the atmosphere, the plot is much the same as the plot of total water vapor. The radiative effect of changes in water vapor in the middle of the troposphere shows no average increase with SST of the positive values and again the negative values show a bimodal distribution. For water vapor low in the atmosphere, the radiative effects are smallest but also very interesting. The general trend for the positive values to increase with increasing SST is there, but superimposed on this trend are many strongly negative grid points as well strongly positive grid points at low SSTs.

One of the features that plots of the radiative effect versus SST can't illustrate is the strongly regional characteristic of the clear sky radiative effects of changes in water vapor that can cross gradients of SST. Figures 5.10, 5.11, 5.12, and 5.13 illustrate this regionality.

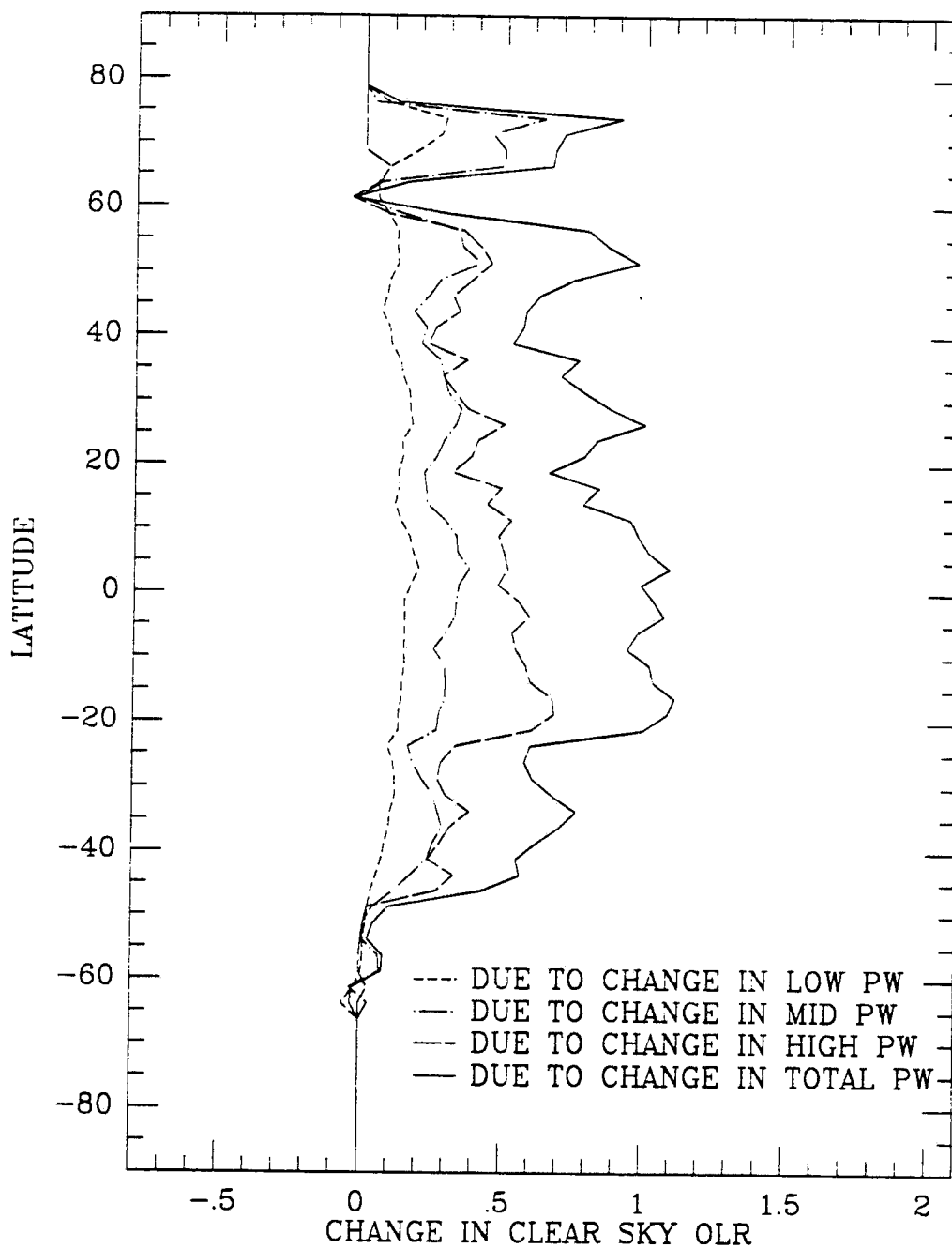


Figure 5.4: The clear sky radiative effect of changes in water vapor as a function of latitude. Units in $W \cdot m^{-2}$, a positive value indicates a decrease in OLR.

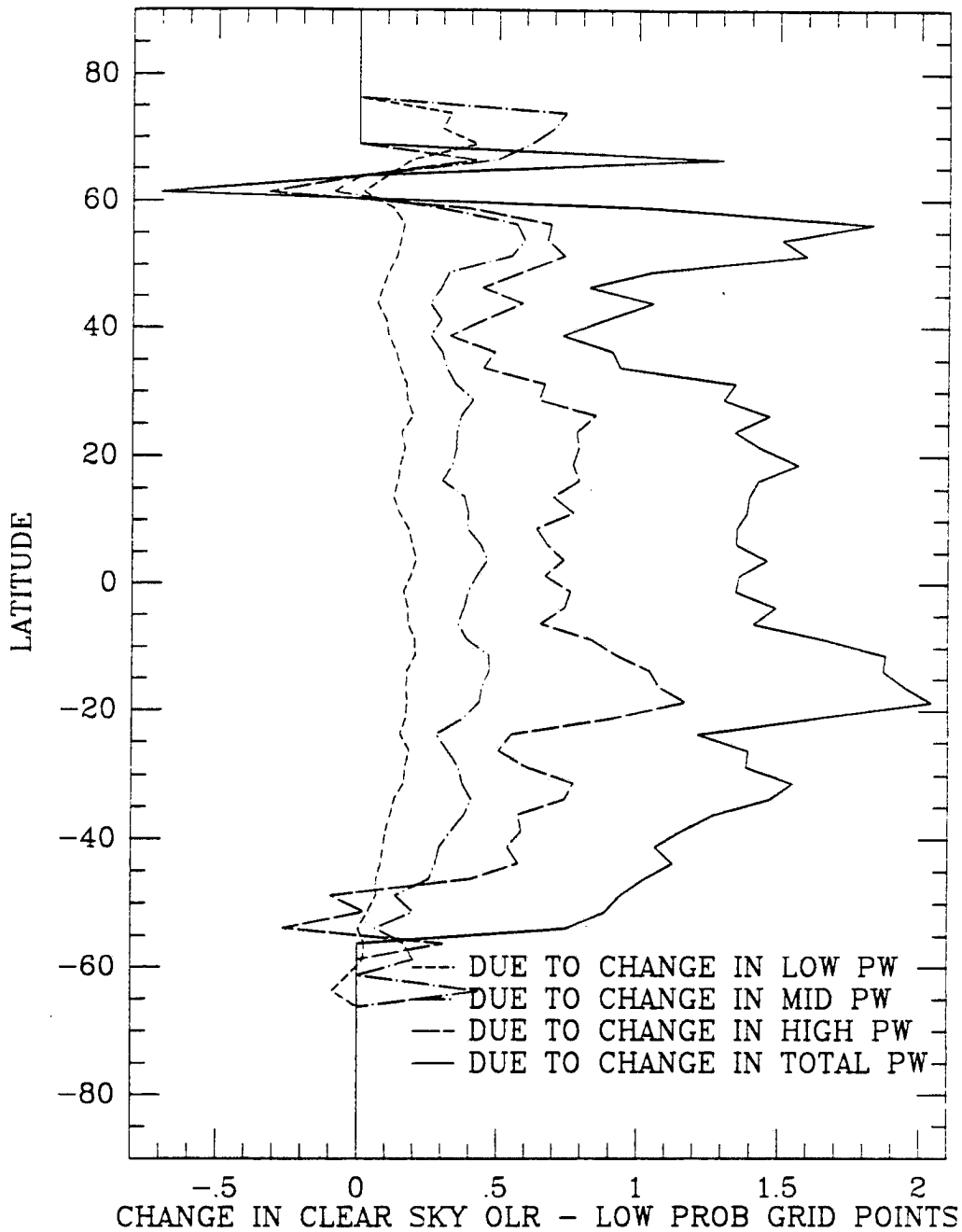


Figure 5.5: The clear sky radiative effect of changes in water vapor as a function of latitude for grid points with water vapor P-values less than or equal to 0.05. Units in $\text{W}\cdot\text{m}^{-2}$, a positive value indicates a decrease in OLR.

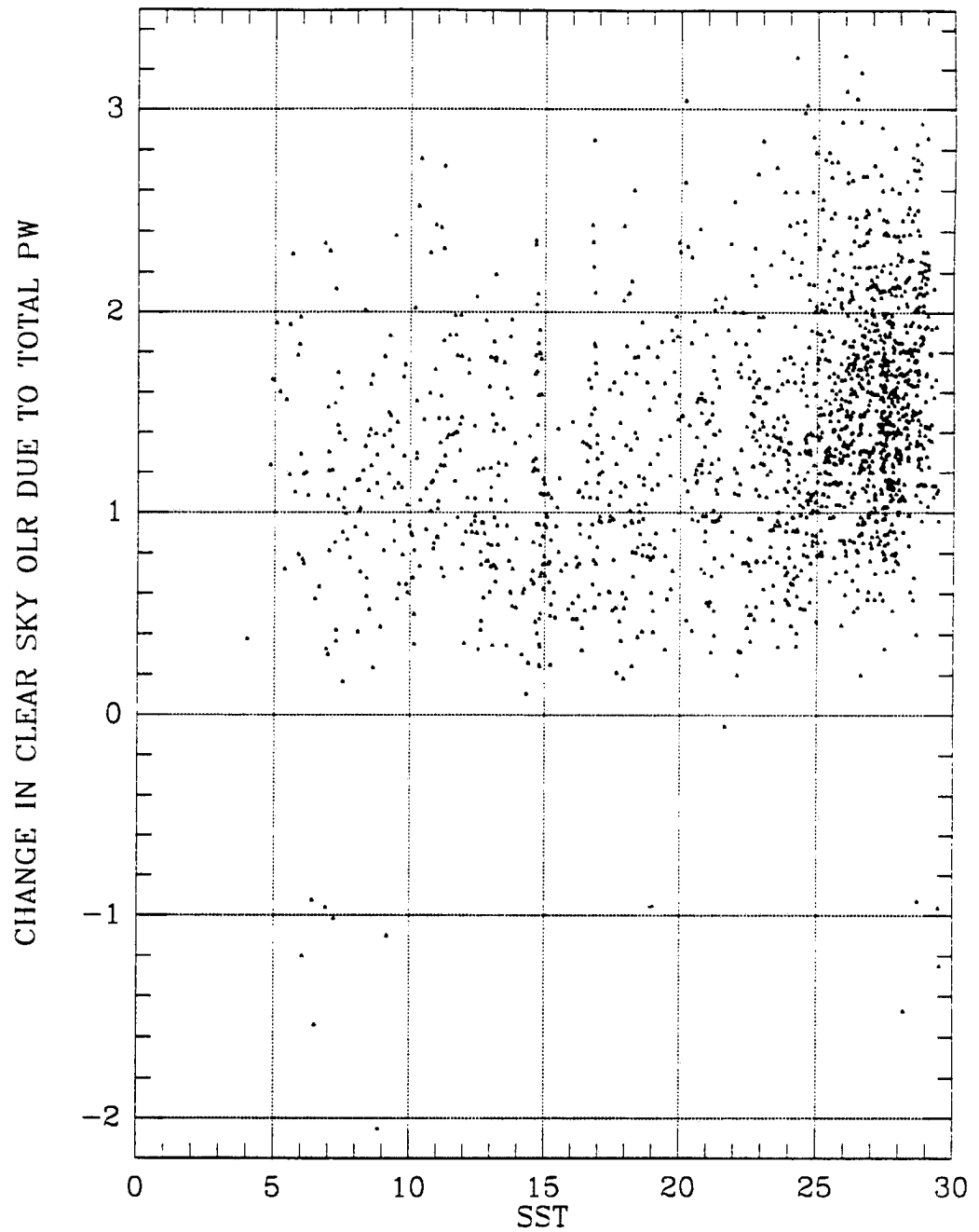


Figure 5.6: The change in clear sky greenhouse effect due to changes in total water vapor as a function of SST. Only grid points with P-values ≤ 0.05 are plotted. Units in $\text{W}\cdot\text{m}^{-2}$, a positive value indicates a decrease in OLR.

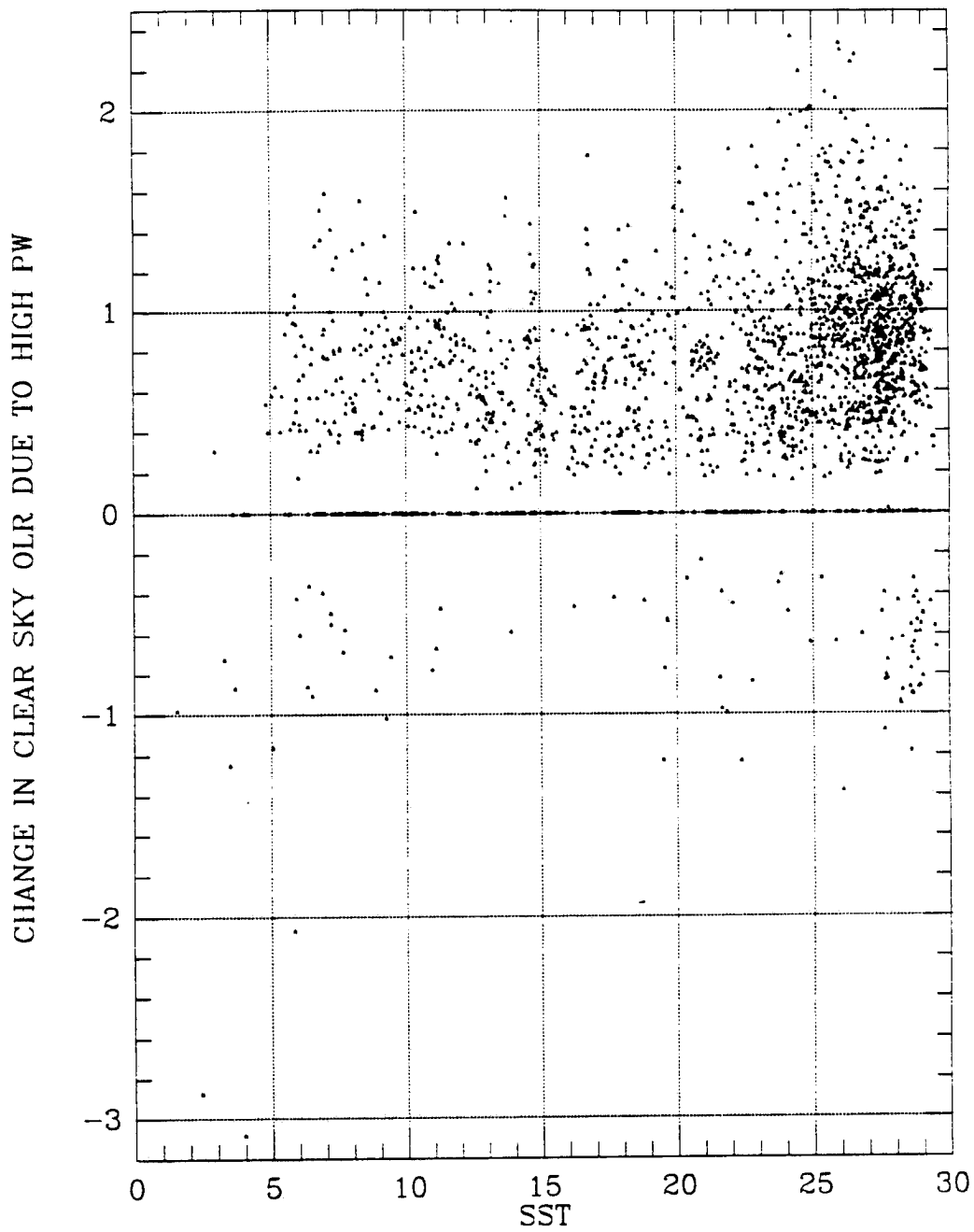


Figure 5.7: The change in clear sky greenhouse effect due to changes in high water vapor as a function of SST. Only grid points with P-values ≤ 0.05 are plotted. Units in $\text{W}\cdot\text{m}^{-2}$, a positive value indicates a decrease in OLR.

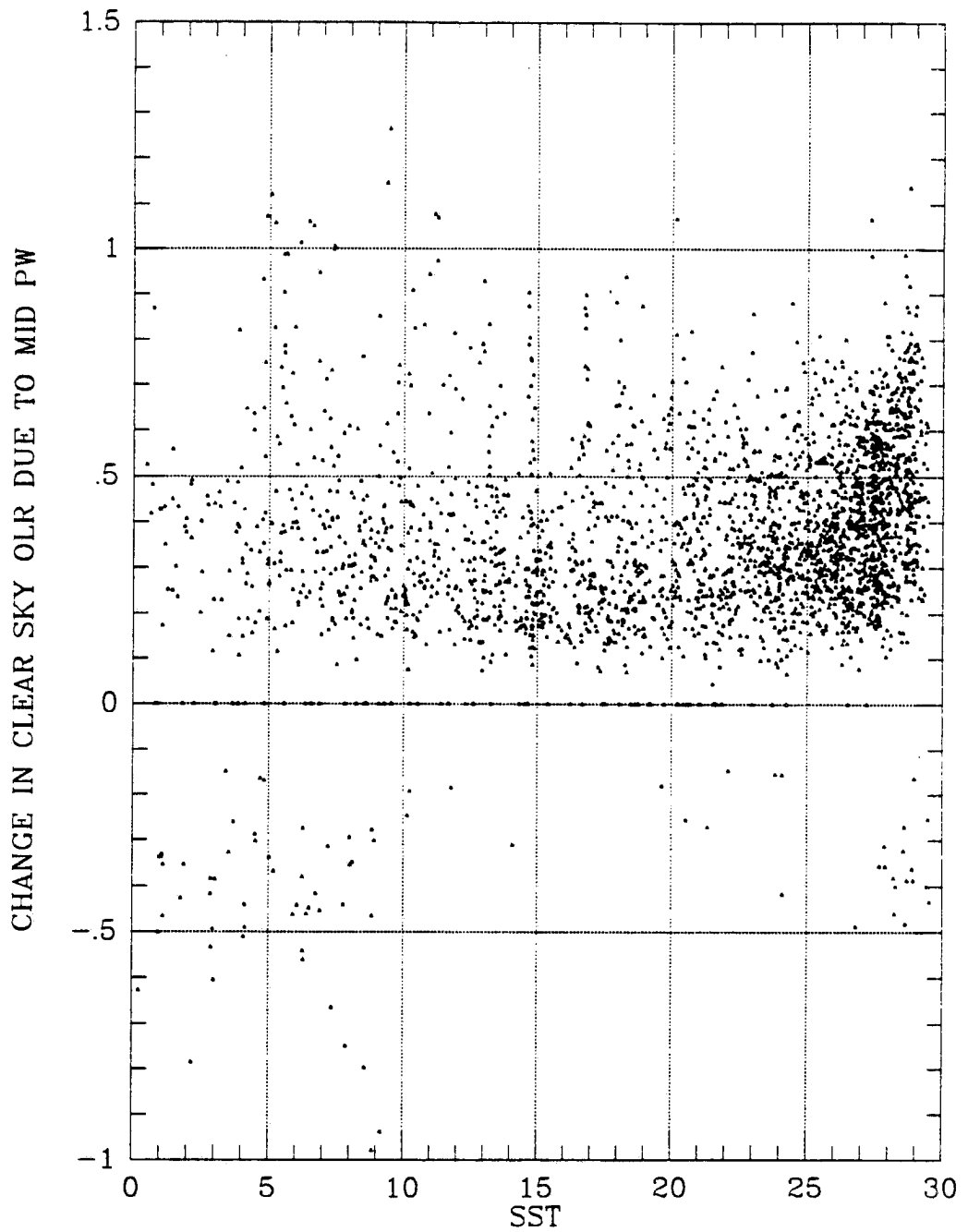


Figure 5.8: The change in clear sky greenhouse effect due to changes in middle level water vapor as a function of SST. Only grid points with P-values ≤ 0.05 are plotted. Units in $\text{W}\cdot\text{m}^{-2}$, a positive value indicates a decrease in OLR.

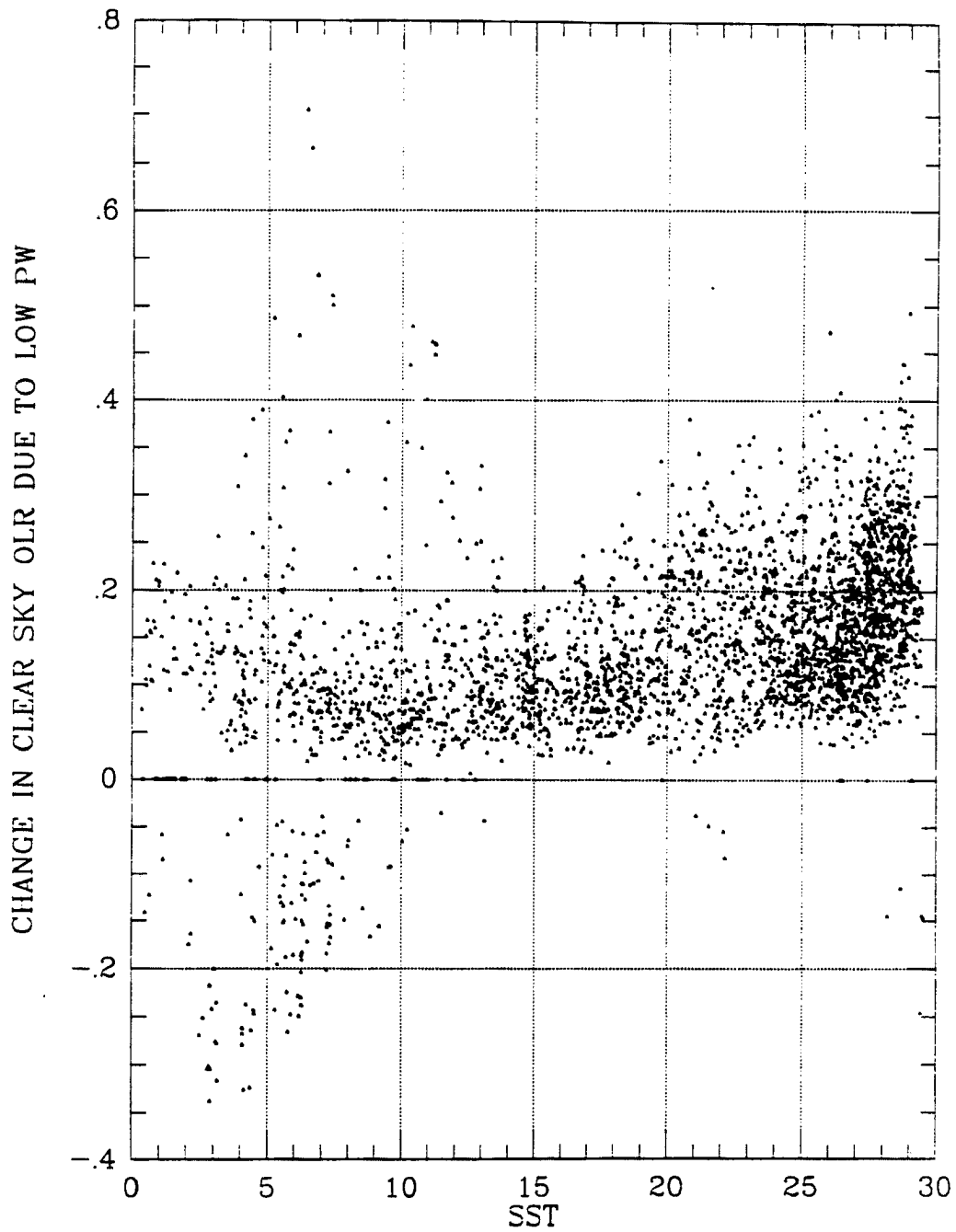


Figure 5.9: The change in clear sky greenhouse effect due to changes in low level water vapor as a function of SST. Only grid points with P-values ≤ 0.05 are plotted. Units in $\text{W}\cdot\text{m}^{-2}$, a positive value indicates a decrease in OLR.

Figure 5.10 has three regions where the change in clear sky OLR due to changes in water vapor associated with a 1 °C increase in SSTA is greater than $2 \text{ W}\cdot\text{m}^{-2}$. These are in the Indian Ocean, central Pacific Ocean, and Atlantic Ocean. For changes in water vapor high in the troposphere, shown in Figure 5.11, the greatest increase, in excess of $1.5 \text{ W}\cdot\text{m}^{-2}$, is in the mid Pacific Ocean. Contour increments appear to link the central Pacific with the central North Atlantic as a region of large increase in the greenhouse effect. Figure 5.12 shows that the increase in the greenhouse effect due to changes in mid level water vapor has a maximum in the North Atlantic near England, though there are many other maxima that aren't quite as high. The effects of changes in low level water vapor, shown in Figure 5.13 indicate several localized maximums in many different parts of the global oceans. A general analysis of these figures indicates that as the radiative effect gets smaller, it gets more geographically diffuse as well, e.g., total and high will have a few distinct regions with localized maxima while low will have many.

5.3.2 Changes in OLR due to changes in clear sky OLR

While the changes in clear sky OLR are important, the values shown in the previous section do not represent the actual changes in OLR due to the changes in clear sky OLR. To calculate these values, the changes in clear sky OLR were multiplied by one minus the average fraction of cloudiness observed at that grid point based on the Nimbus-7 derived cloud data. While the cloud fraction determined from Nimbus-7 data does not totally agree with other cloud retrievals, such as ISCCP, the values work well enough to help determine what the model derived changes in clear sky OLR contributions are to overall OLR changes. It should also be noted that while these values are stated as the effect of water vapor, the radiative effect of changes in water vapor above and below the clouds is not considered. These effects are not considered in part because data for such analysis is not available: the TOVS retrievals are not made in cloudy environments.

The first obvious effect of multiplying changes in clear sky greenhouse effect by the fraction of the sky that is clear is a sharp decrease in average values. As Table 5.5 indicates, these changes resulted in a $\sim 50\%$ decrease in average values. But average values tell only part of the story.

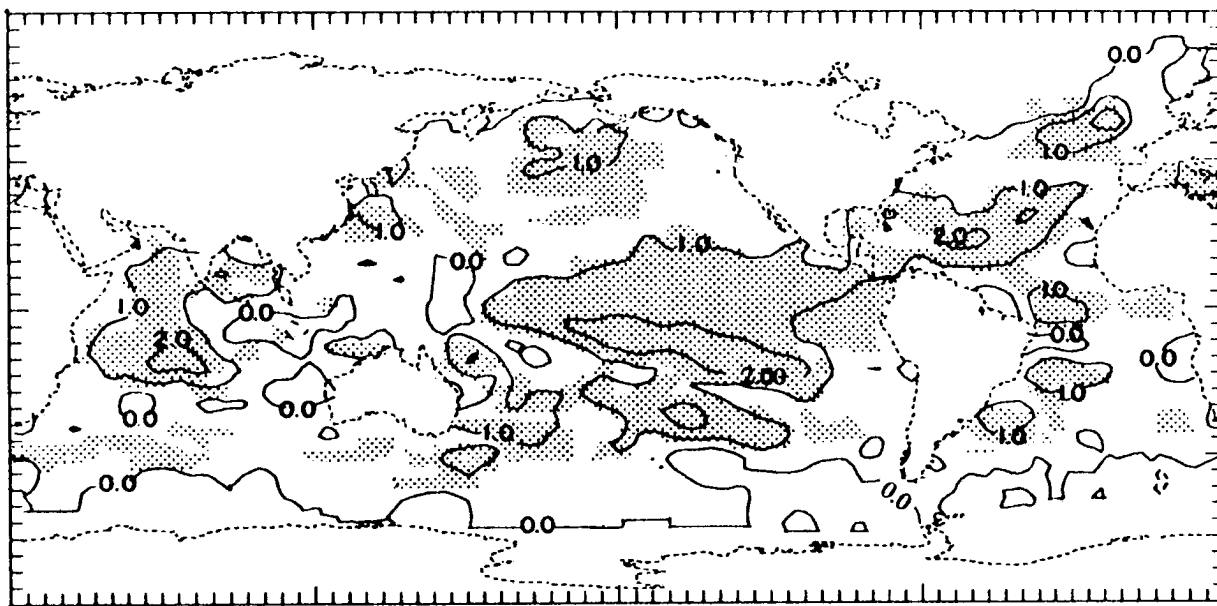


Figure 5.10: Contour plot of the change in clear sky greenhouse effect due to changes in total water vapor. Grid points with P-values ≤ 0.05 indicated by stippling. Units in $\text{W}\cdot\text{m}^{-2}$, a positive value indicates a decrease in OLR. Contour increments are $1 \text{ W}\cdot\text{m}^{-2}$.

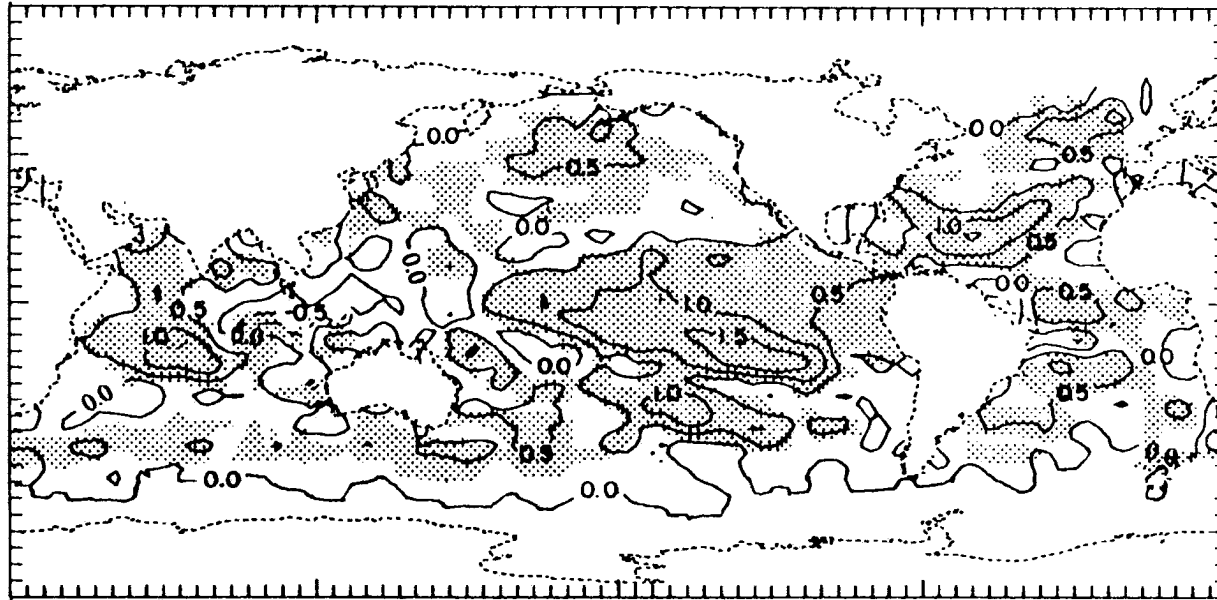


Figure 5.11: Contour plot of the change in clear sky greenhouse effect due to changes in high water vapor. Grid points with P-values ≤ 0.05 indicated by stippling. Units in $\text{W}\cdot\text{m}^{-2}$, a positive value indicates a decrease in OLR. Contour increment $0.5 \text{ W}\cdot\text{m}^{-2}$.

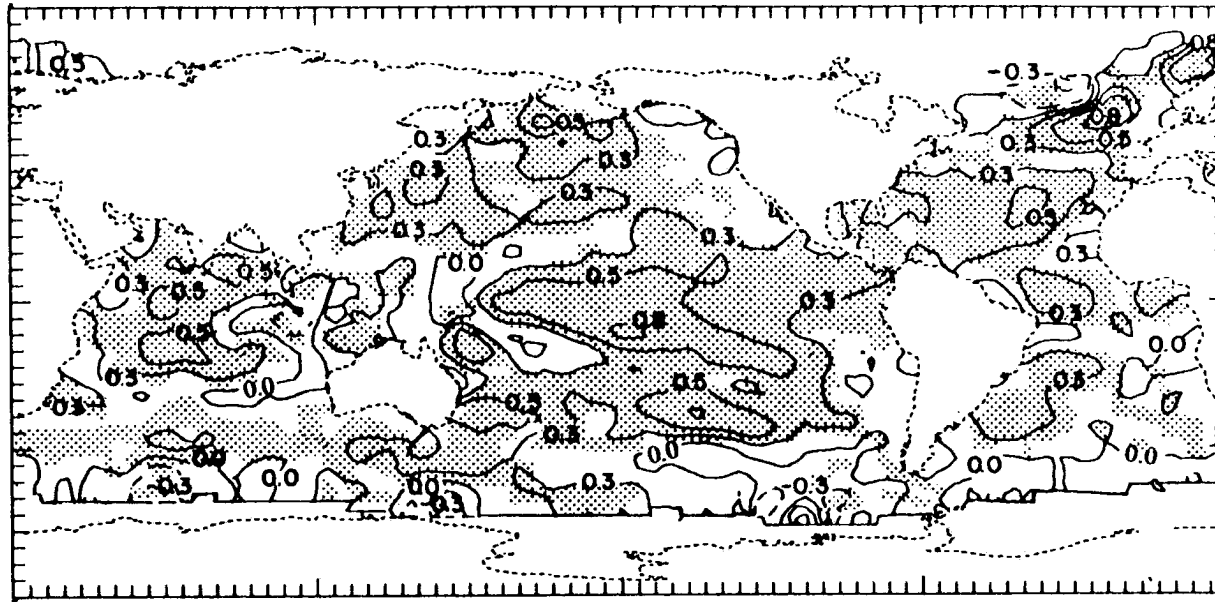


Figure 5.12: Contour plot of the change in clear sky greenhouse effect due to changes in middle level water vapor. Grid points with P-values ≤ 0.05 indicated by stippling. Units in $\text{W}\cdot\text{m}^{-2}$, a positive value indicates a decrease in OLR. Contour increment $0.25 \text{ W}\cdot\text{m}^{-2}$.

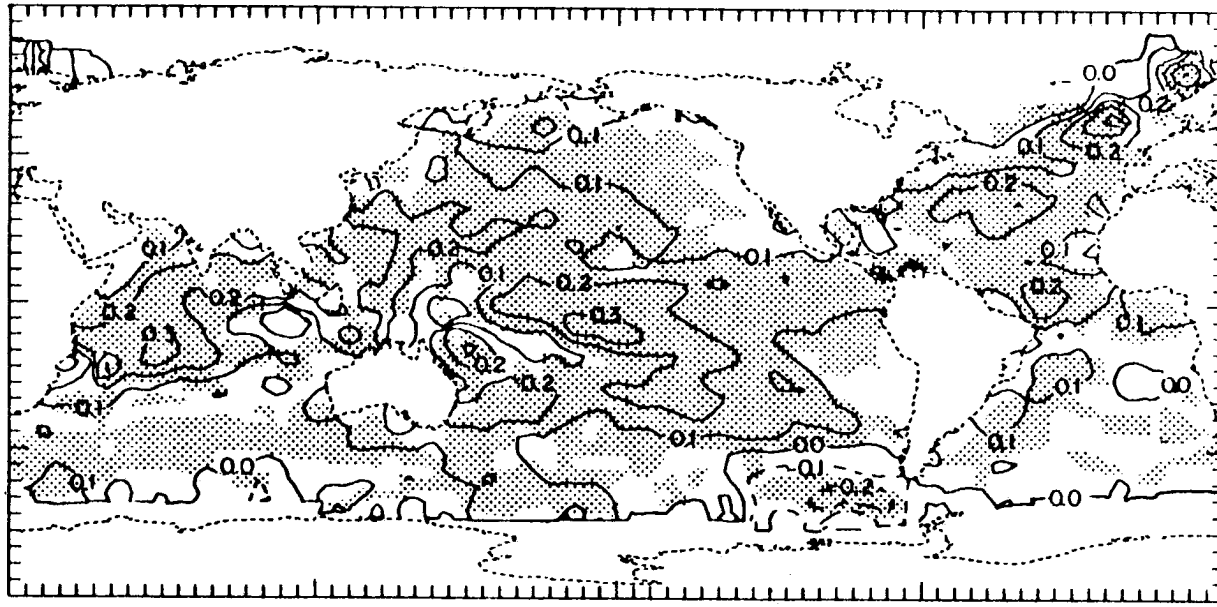


Figure 5.13: Contour plot of the change in clear sky greenhouse effect due to changes in low level water vapor. Grid points with P-values ≤ 0.05 indicated by stippling. Units in $W \cdot m^{-2}$, a positive value indicates a decrease in OLR. Contour increment $0.1 W \cdot m^{-2}$.

Table 5.5: Average change in greenhouse effect due to water vapor changes associated with 1°C increase in SSTA. Units are in $\text{W}\cdot\text{m}^{-2}$. P-values are those determined in Chapter 3 for water vapor–SSTA LAD analysis. A positive change in greenhouse effect represents a decrease in OLR. These values are the same as Table 5.4 except that each grid point's clear sky value was multiplied by the average fraction of clear sky at that grid point. Total PW is the change due to changes in water vapor at all three levels at the same time.

Change Due to	All Grid Points	$P \leq 0.05$ Grid Points
Total PW	0.37	0.71
High PW	0.20	0.36
Mid PW	0.12	0.18
Low PW	0.06	0.07

Figures 5.14 and 5.15 also show marked decreases in the magnitude of the radiative effects of changes in clear sky water vapor. They also show more distinct latitudinal variation caused by strong latitudinal variations in cloudiness. The secondary maximum near 50°N is much reduced. For all grid points, shown in Figure 5.14, the radiative effect is near $0.5 \text{ W}\cdot\text{m}^{-2}$ between 30°N and 20° S. However, for grid points with low P-values, shown in Figure 5.15, there are two distinct maxima at 20°N and 20°S with a value of near $1 \text{ W}\cdot\text{m}^{-2}$.

The change in OLR due to the change in clear sky water vapor shows a much greater dependence on SST than does the change in clear sky OLR. Figure 5.16 shows that the total water vapor radiative effects clearly increases with increasing SST. This same trend is also apparent at for each layer of water vapor as well, as illustrated in Figures 5.17, 5.18, and 5.19.

Figures 5.20, 5.21, 5.22, and 5.23 also show strong regionality. One effect of factoring in the clouds apparent in these figures is the maxima at all levels are now in the tropics. There are fewer regional maxima and there appears to be larger regions defined by these contours. At all levels, the central tropical Pacific is now one region and usually the maximum for the entire data set.

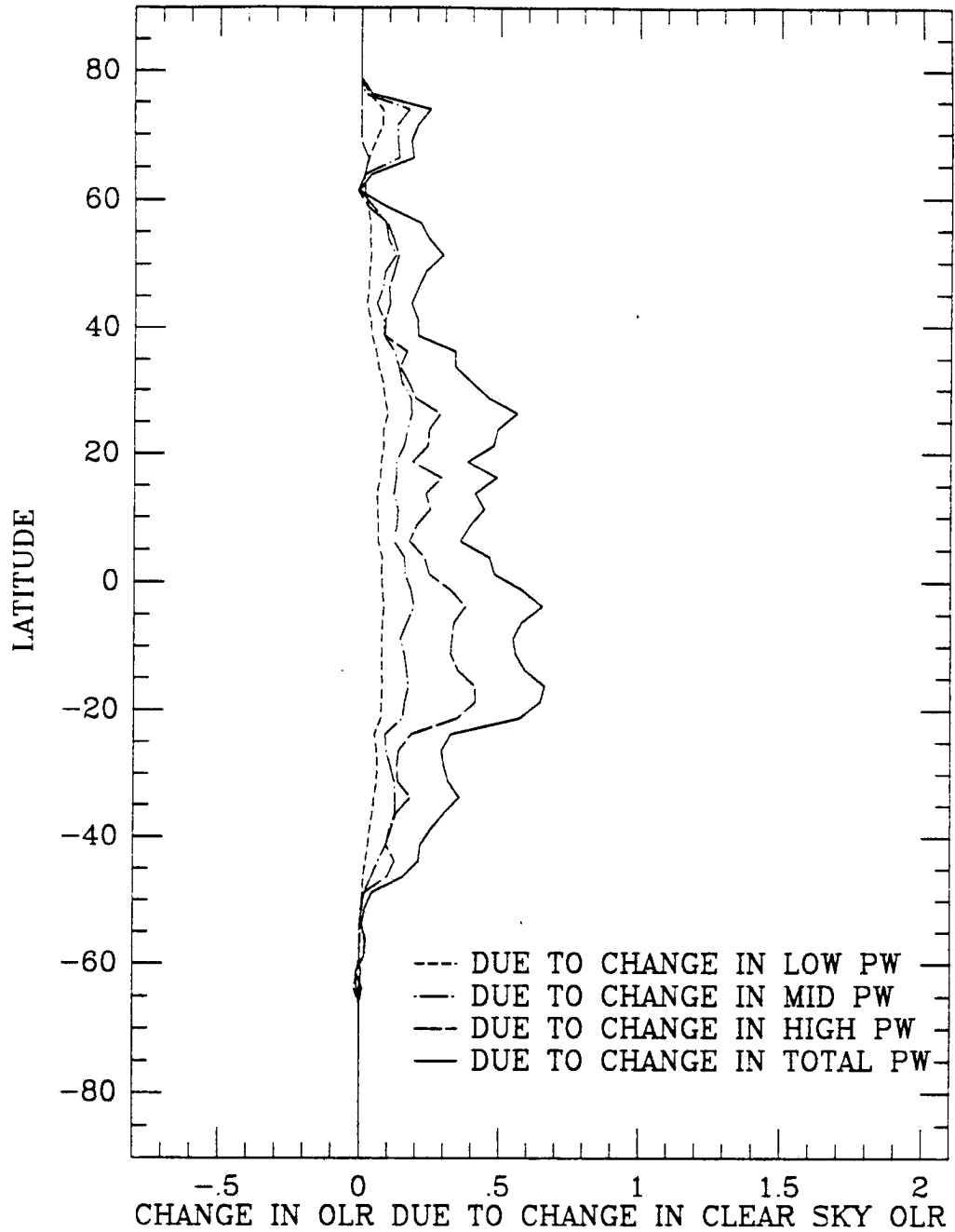


Figure 5.14: The radiative effect due to changes in clear sky water vapor as a function of latitude. Units in $W \cdot m^{-2}$, a positive value indicating a decrease in OLR, and degrees C.

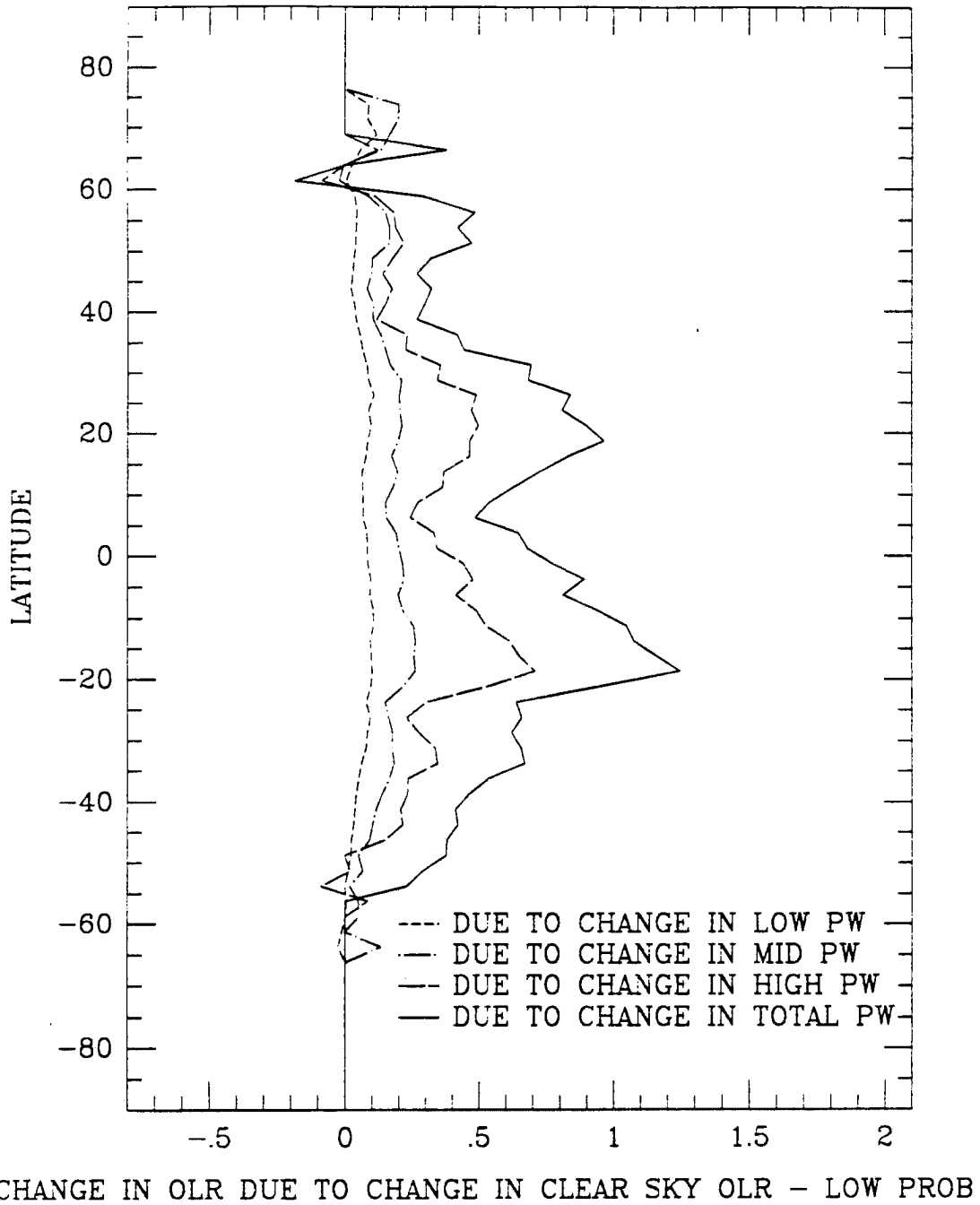


Figure 5.15: The radiative effect due to changes in clear sky water vapor as a function of latitude for grid points with water vapor P-values less than or equal to 0.05. Units in $\text{W}\cdot\text{m}^{-2}$, a positive value indicating a decrease in OLR, and degrees C.

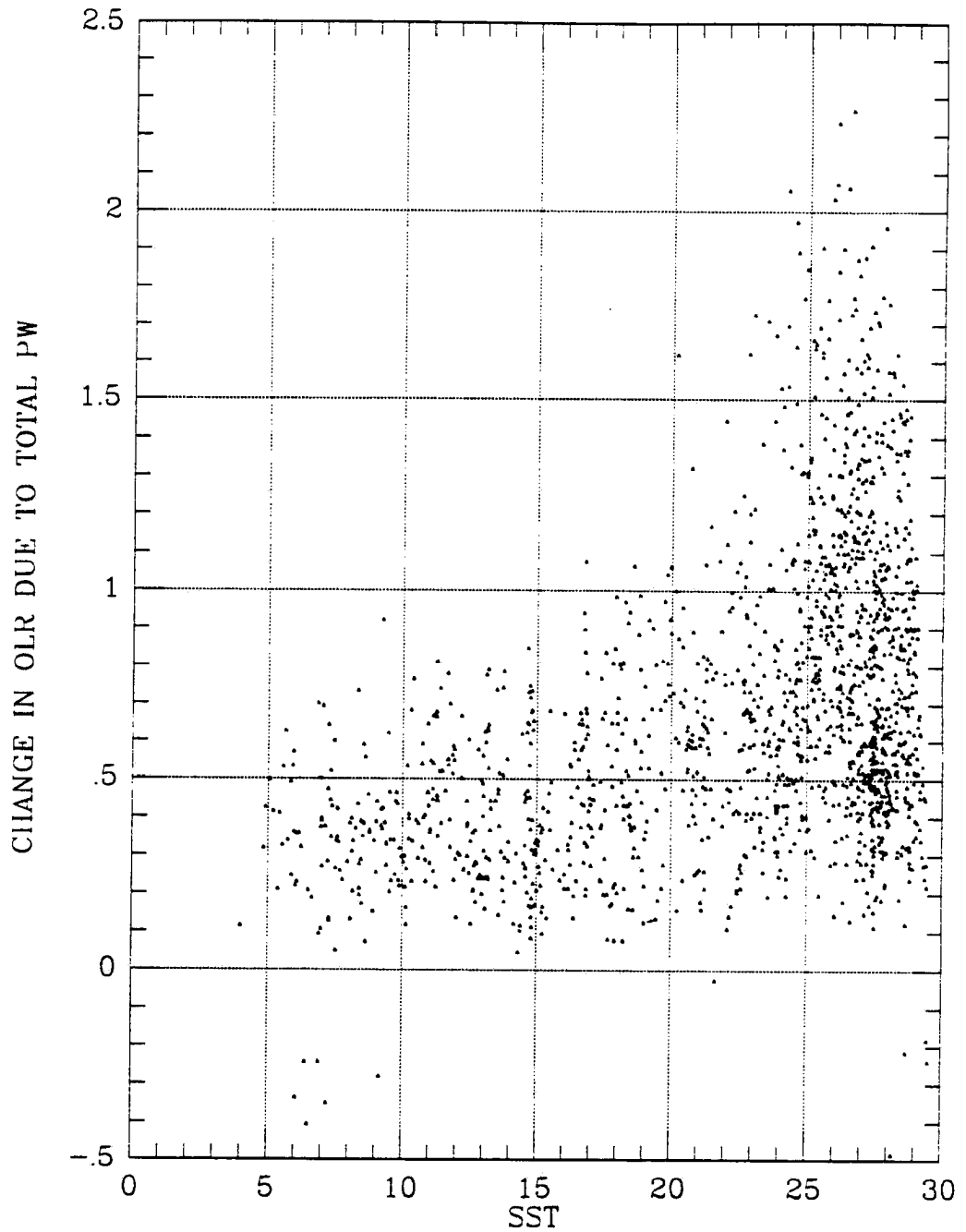


Figure 5.16: The radiative effect due to changes in total water vapor as a function of SST. Only grid points with P-values ≤ 0.05 are plotted. Units in $W \cdot m^{-2}$, a positive value indicating a decrease in OLR, and degrees C.

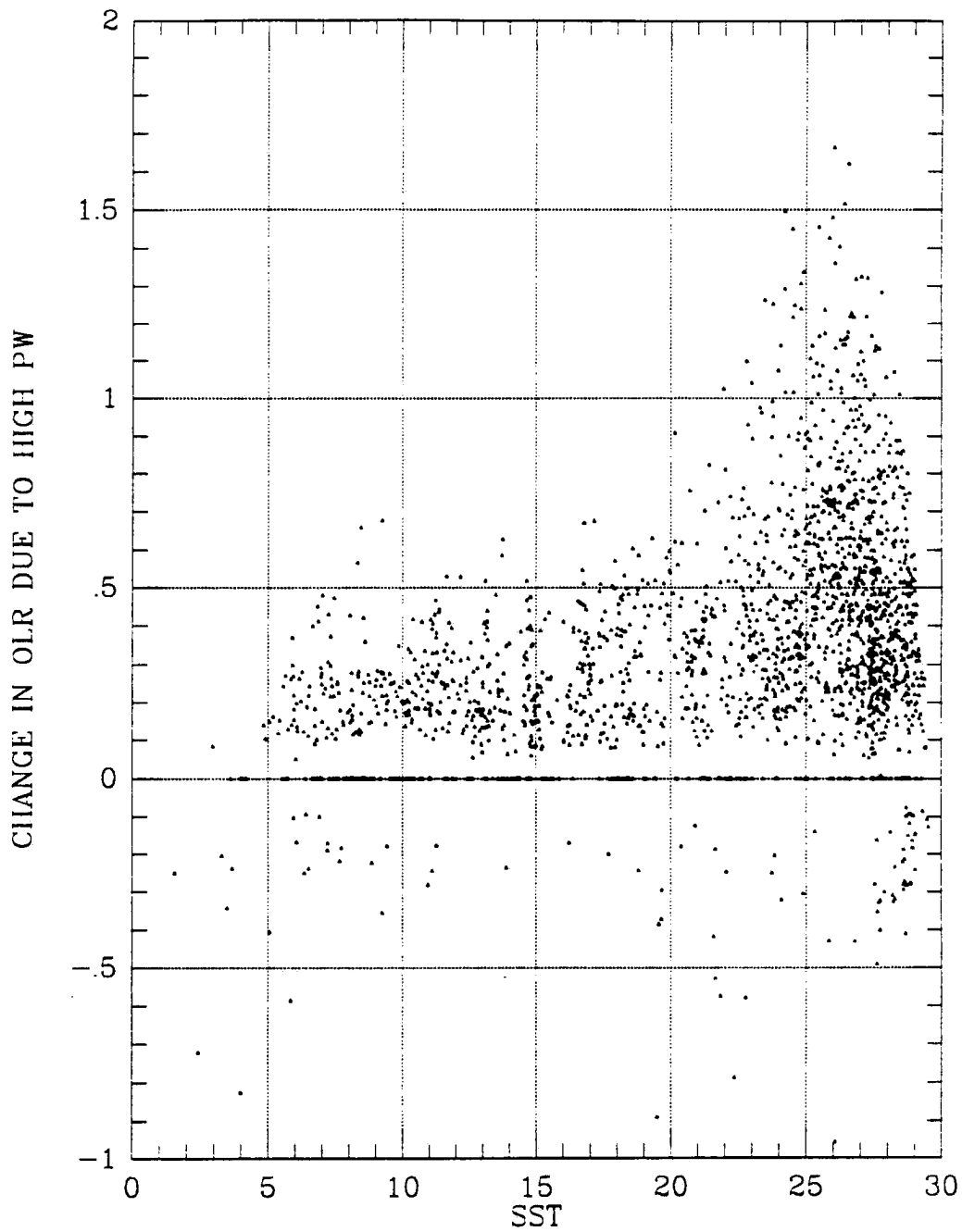


Figure 5.17: The radiative effect due to changes in high water vapor as a function of SST. Only grid points with P-values ≤ 0.05 are plotted. Units in $\text{W}\cdot\text{m}^{-2}$, a positive value indicating a decrease in OLR, and degrees C.

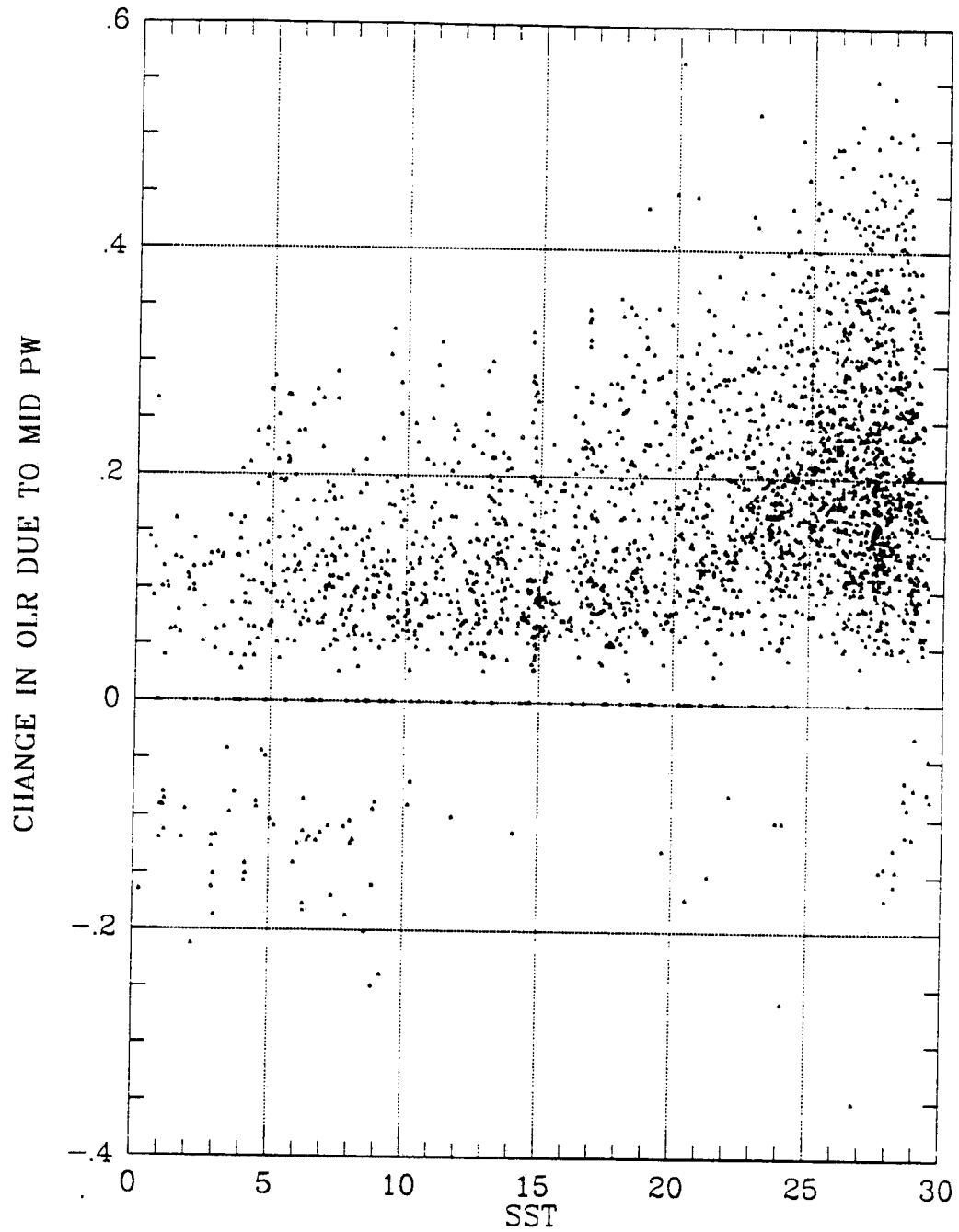


Figure 5.18: The radiative effect due to changes in middle level water vapor as a function of SST. Only grid points with P-values ≤ 0.05 are plotted. Units in $\text{W}\cdot\text{m}^{-2}$, a positive value indicates a decrease in OLR.

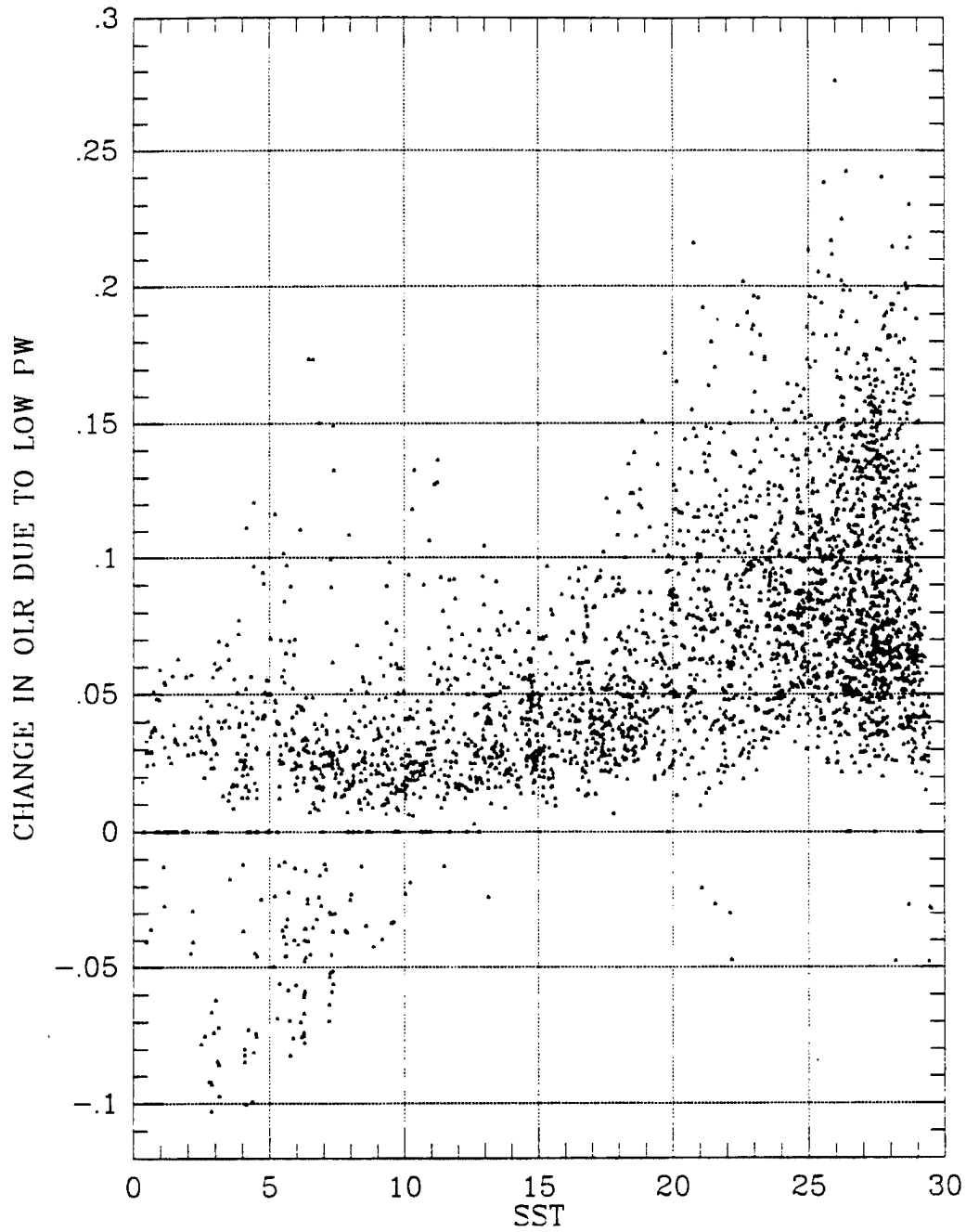


Figure 5.19: The radiative effect due to changes in low level water vapor as a function of SST. Only grid points with P-values ≤ 0.05 are plotted. Units in $\text{W}\cdot\text{m}^{-2}$, a positive value indicates a decrease in OLR.

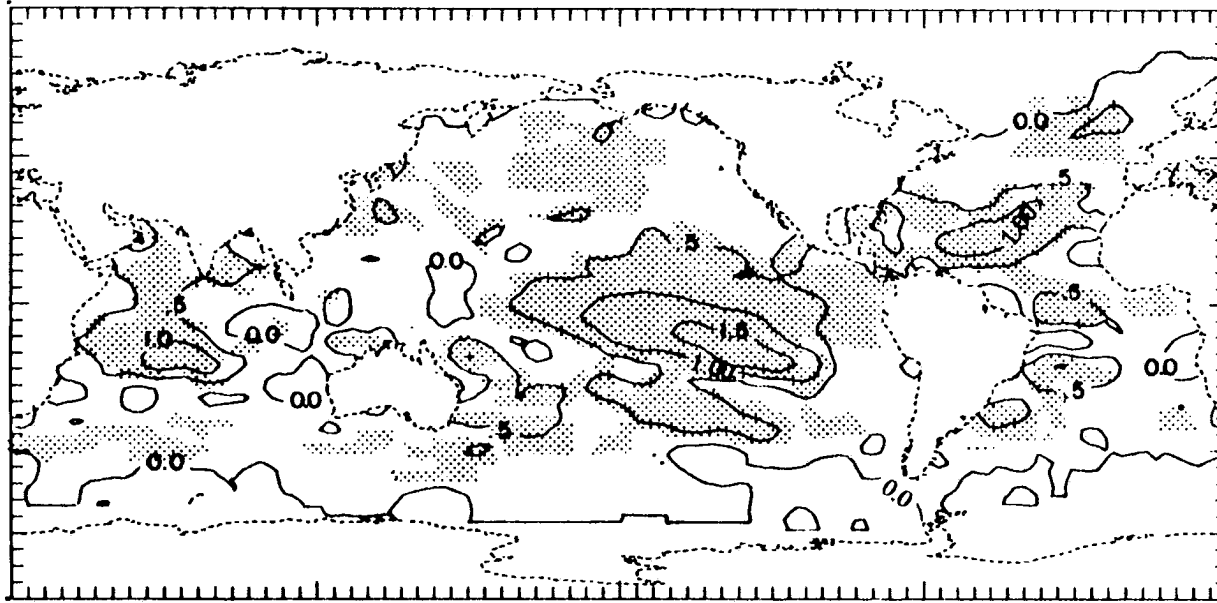


Figure 5.20: Contour plot of the change in greenhouse effect due to changes in total water vapor. Grid points with P-values ≤ 0.05 indicated by stippling. Units in $W \cdot m^{-2}$, a positive value indicates a decrease in OLR. Contour increment $0.5 W \cdot m^{-2}$.

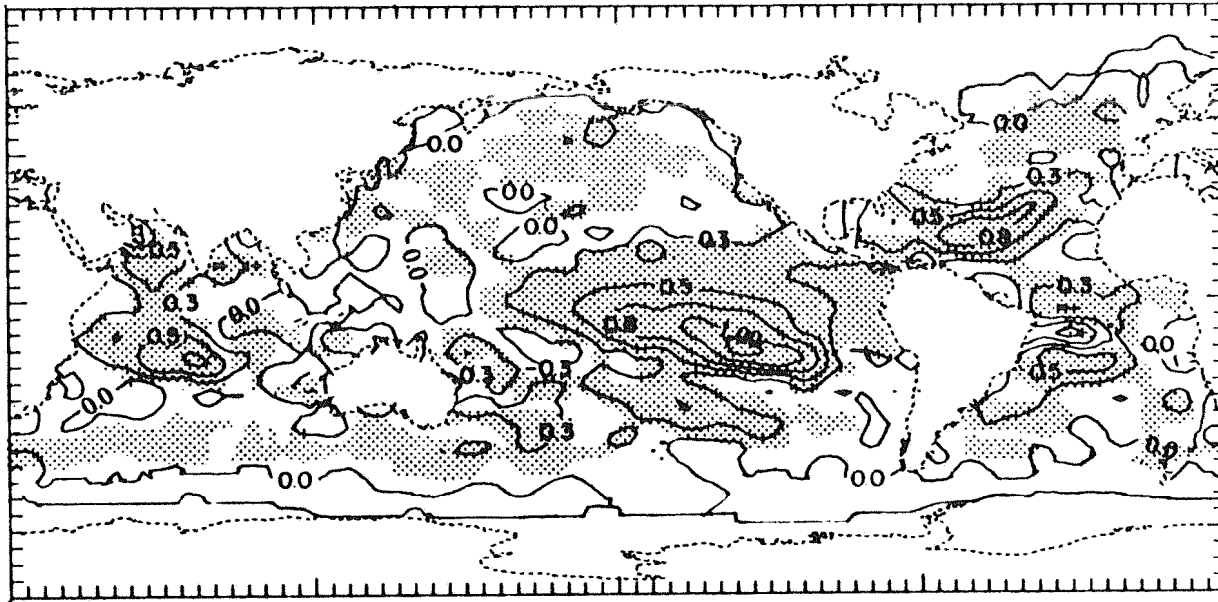


Figure 5.21: Contour plot of the change in greenhouse effect due to changes in high water vapor. Grid points with P-values ≤ 0.05 indicated by stippling. Units in $\text{W}\cdot\text{m}^{-2}$, a positive value indicates a decrease in OLR. Contour increment $0.25 \text{ W}\cdot\text{m}^{-2}$.

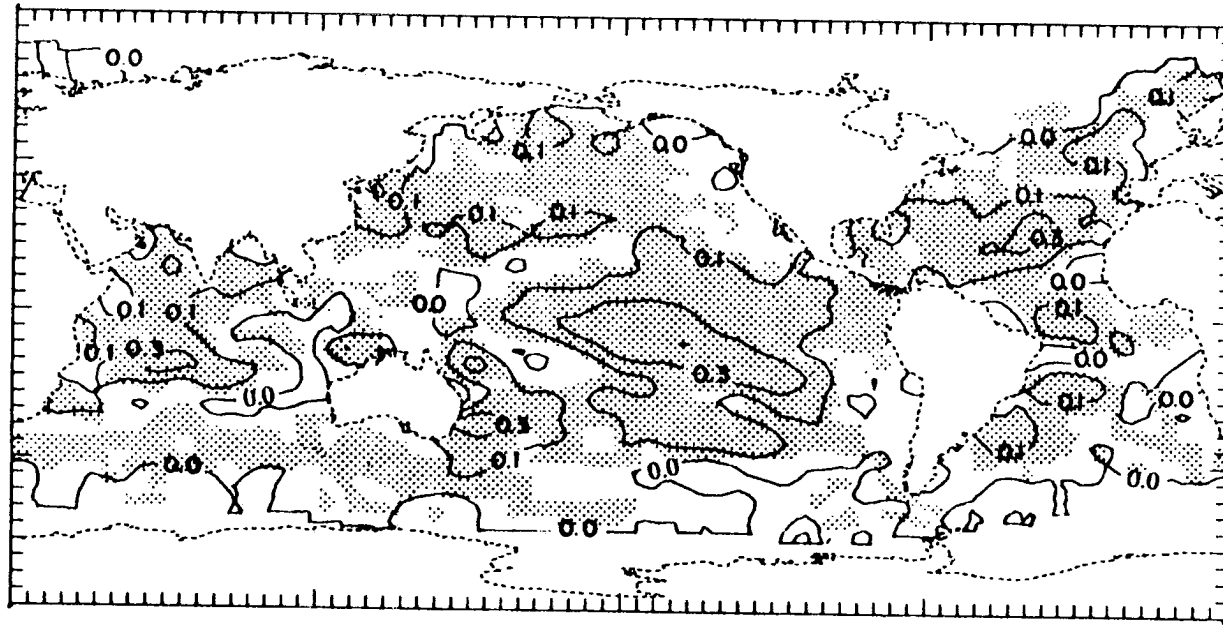


Figure 5.22: Contour plot of the change in greenhouse effect due to changes in middle level water vapor. Grid points with P -values ≤ 0.05 indicated by stippling. Units in $\text{W}\cdot\text{m}^{-2}$, a positive value indicates a decrease in OLR. Contour increment $0.15 \text{ W}\cdot\text{m}^{-2}$.

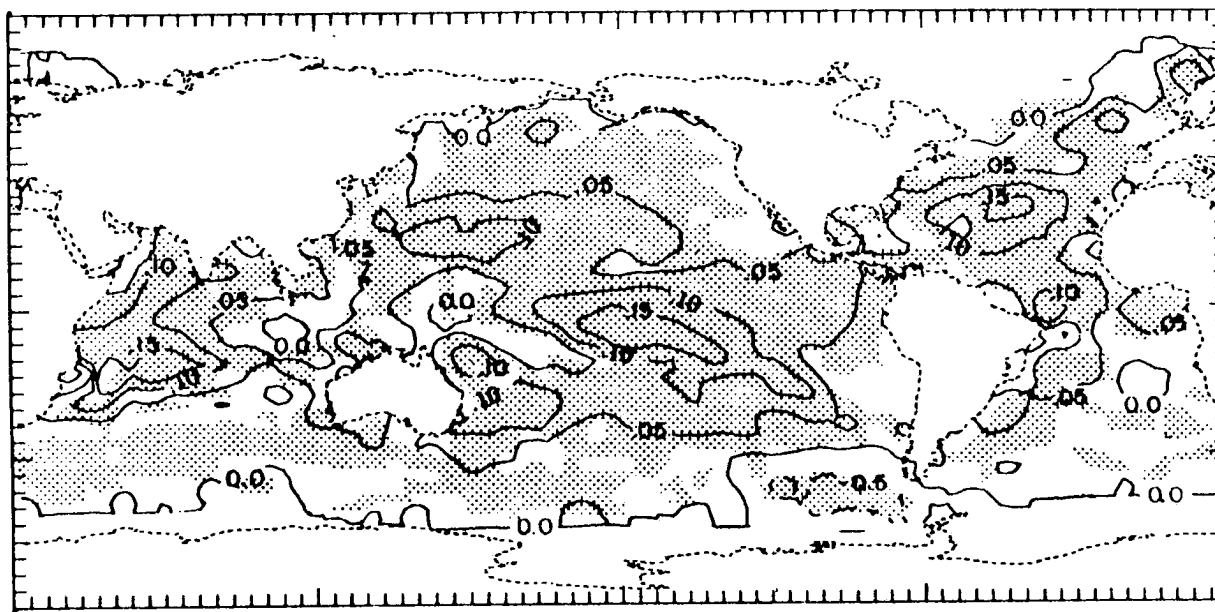


Figure 5.23: Contour plot of the change in greenhouse effect due to changes in low level water vapor. Grid points with P-values ≤ 0.05 indicated by stippling. Units in $\text{W}\cdot\text{m}^{-2}$, a positive value indicates a decrease in OLR. Contour increment $0.05 \text{ W}\cdot\text{m}^{-2}$.

5.3.3 The Contribution of Changes in Clear Sky OLR to changes in OLR

Comparing the radiative effect of changes in clear sky water vapor to the changes in OLR determined in Chapter 4 posed some problems. The approach we chose was to interpolate the OLR-SSTA LAD and probability results to the ISCCP grid. By using only those grid points that had P-values less than or equal to 0.05 from both the OLR-SSTA LAD analysis data set and the clear sky radiative effect (which required a low P-value at that grid point for each of the three water vapor layers—SSTA LAD analyses), we could directly compare valid data from the two data sets.

The problem this causes is that the 4,591 grid points over the ocean are now limited to only 722 valid grid points. Much of this decrease is due simply to the latitudinal limitations of the SST data set during the Nimbus-7 data set time period —when interpolated to the ISCCP grid, the OLR-SSTA LAD analysis only had 3,342 grid points. However, 722 is still only 22% of the potential coverage. This may limit the applicability of “global” averages taken from this data, especially since this data also exhibits strong regionality. Since both the radiative effect of clear sky changes in PW and the OLR-SSTA relationship change sign, Table 5.6 reflects the magnitude of these effects by analyzing only the absolute value of the data. As indicated in this table, the average radiative effect of changes in clear sky water vapor is only 13% of the observed changes in OLR. Since many grid points had negative changes in greenhouse effect despite a positive contribution from the clear sky changes in greenhouse effect, the true magnitude of the contribution to the observed changes in OLR due to clear sky water vapor changes is less than 13%. This is 13% of the observed change (mostly decrease) in OLR without adding in the increase in OLR of about $3.3 \text{ W}\cdot\text{m}^{-2}$ (Cess *et al.*, 1990) that would be expected to be associated with a 1°C increase in surface temperature.

Only one of the 722 grid points shown in Figure 5.24 had a negative clear sky greenhouse effect due to changes in water vapor. That grid point is at a SST of 29.5°C and -1.8 of percent of OLR. All the other negative percent values are from grid points where the radiative effects of changes in clear sky water vapor would increase the greenhouse effect (decrease OLR) yet the observed changes in OLR associated with a 1° increase in SST

Table 5.6: Comparison of the average magnitude of the radiative effect of the change in clear sky water vapor to the average magnitude of the change in OLR associated with a 1°C increase in SSTA. This comparison is of the absolute value of the radiative effect at the same 722 grid points.

Source	Magnitude of Radiative Effect	Percent of Total
Due to Clear Sky	0.78 W·m ⁻²	13%
Total change in OLR	5.93 W·m ⁻²	100%

were such that the greenhouse effect decreased (OLR increased). While there are some outlying points, the radiative effect of changes in clear sky water vapor for the majority of grid points was ~5-20% of the total changes in OLR. Also apparent in Figure 5.24, the warmer the SST, the greater the likelihood that the change in the greenhouse effect would be positive (decrease in OLR). Figure 5.25 clearly shows the regionality in the data.

5.4 Discussion

Raval and Ramanathan (1989) found that the clear sky greenhouse effect “has a strong positive correlation with sea surface temperature”. However, their study used zonally averaged observations which indicated that the observed greenhouse effect increased as one moved from high latitudes to the tropics, which would generally be expected since the amount of water vapor in the atmosphere increases as one moves from high latitudes to the tropics. What they inferred, but could not prove from their data, was that at a given location an increase in SST would lead to an increase in the clear sky greenhouse effect.

The research presented here specifically addressed this question and indicated that for almost all locations, an increase in local SSTA is associated with changes in water vapor that would produce an increase in clear sky greenhouse effect. The globally averaged value for this is ~1 W·m⁻². When multiplied by the fraction of the sky that is clear, the effect on OLR decreases to ~0.5 W·m⁻².

Cess *et al.* (1990) compared 19 atmospheric GCMs by fixing the ocean surface temperature plus and minus 2°C. The sensitivity parameters to water vapor feedback were evaluated. The average “infrared feedback derivatives”, the change in clear sky OLR per

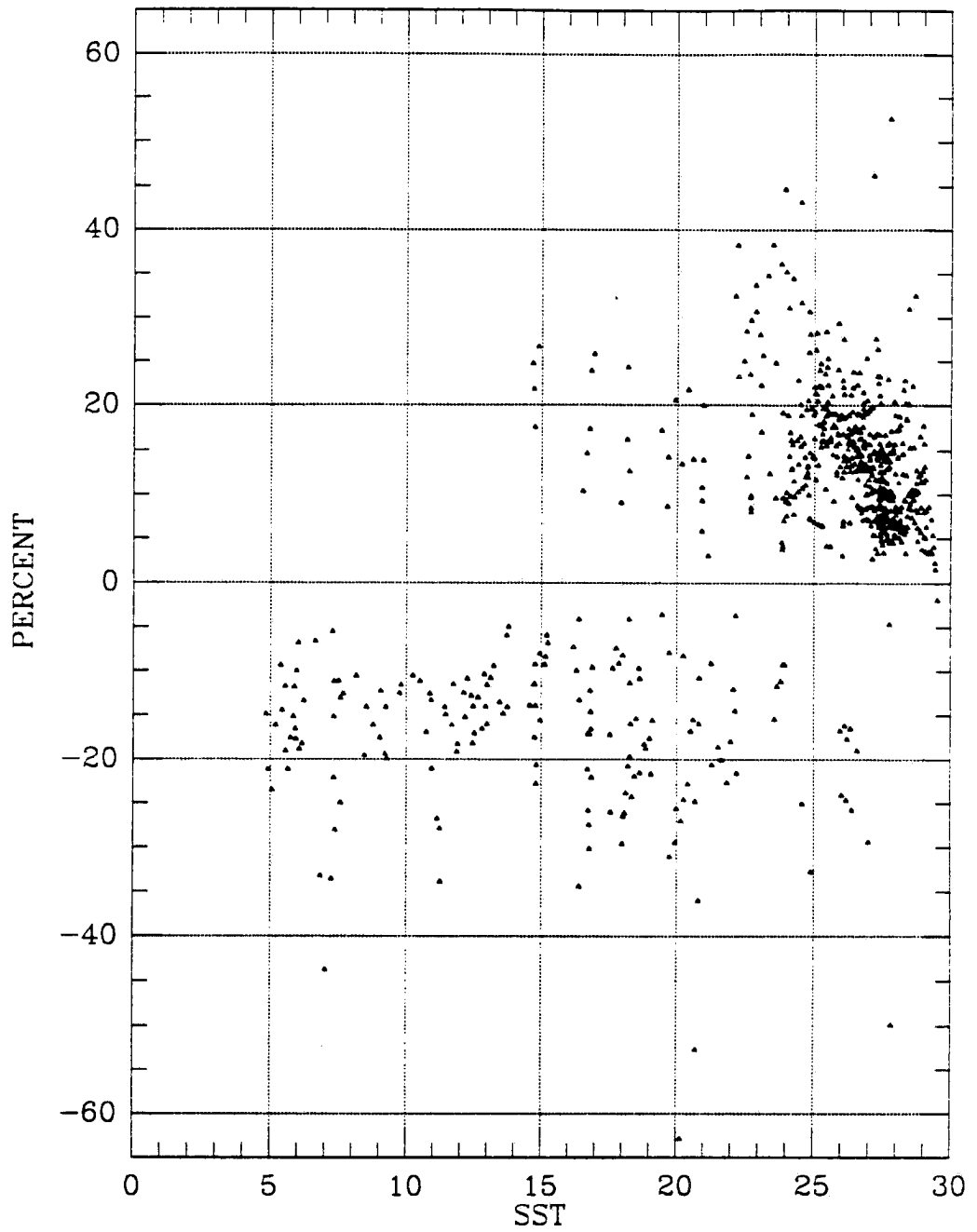


Figure 5.24: The percent of the change in OLR associated with a 1°K increase in SSTA due to changes in clear sky water vapor associated with a 1°K increase in SSTA as a function of SST.

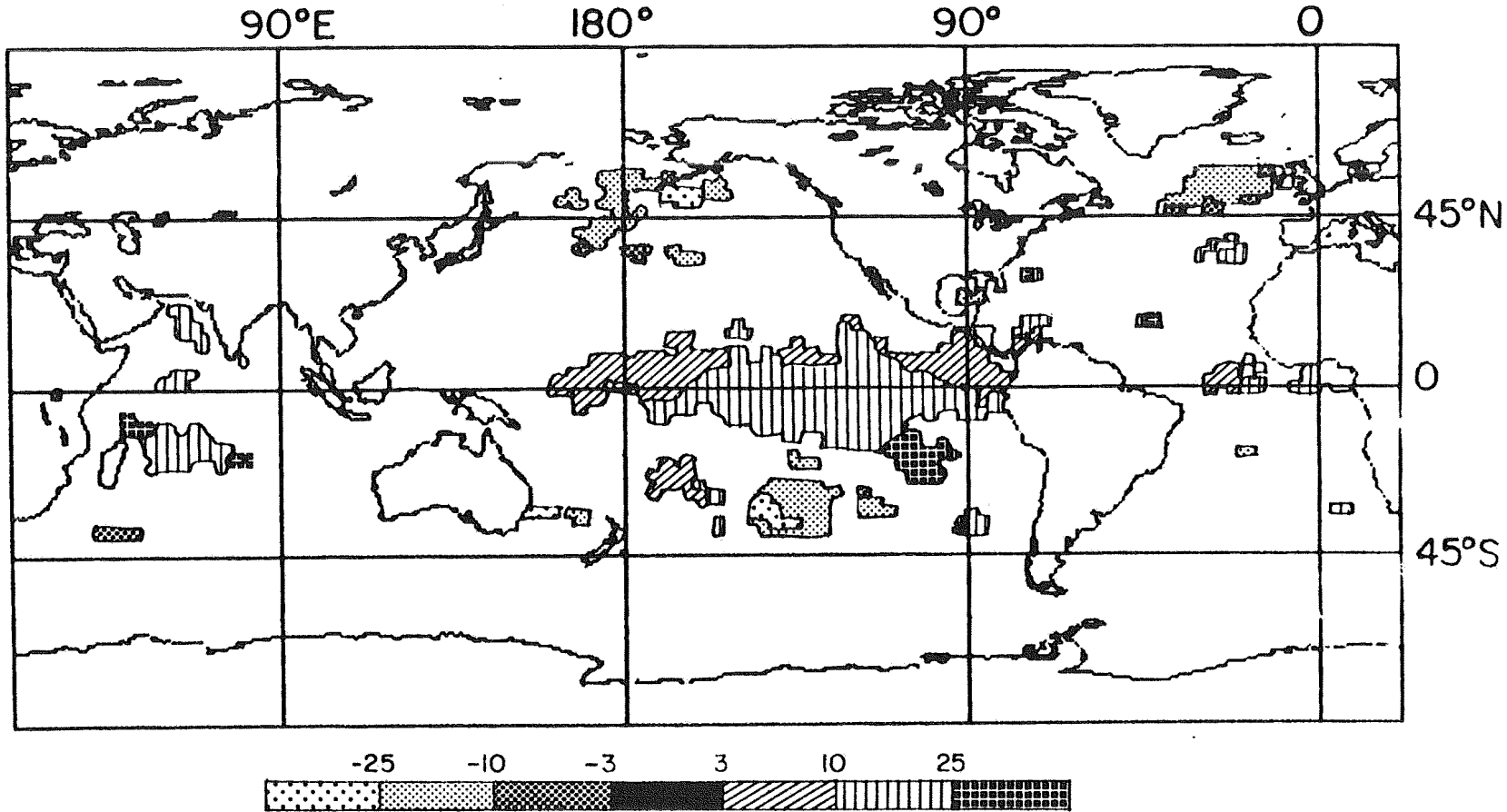


Figure 5.25: Contour plot of the percent of change in OLR due to changes in clear sky water vapor. Only grid points with P-values ≤ 0.05 are plotted. In this case, a positive OLR-SSTA relationship means that the greenhouse effect increased (OLR decrease) with increasing SSTA, as does the value used in the radiative effect of changes in clear sky water vapor associated with a 1° increase in SSTA.

degree increase in SST, was $2.34 \text{ W}\cdot\text{m}^{-2}\cdot\text{K}^{-1}$. For “conditions typical of Earth” without any water vapor feedback, the change in clear sky OLR per degree increase in SST should be $\sim 3.3 \text{ W}\cdot\text{m}^{-2}\cdot\text{K}^{-1}$. This means that the average GCM change in clear sky greenhouse effect due to changes in water vapor associated with a 1° K increase in SST is also $\sim 1 \text{ W}\cdot\text{m}^{-2}$. While the average global GCM results are for over land as well as ocean, the close agreement between the average of 19 GCMs and the results of this observation based analysis should be encouraging to global modelers.

Our results indicate that for the observed range of variability in water vapor in association with SSTAs, the water vapor in the upper levels of the troposphere is definitely the most important influence on changes in clear sky OLR. Yet, water vapor high in the troposphere is probably the hardest for GCMs to accurately handle. In addition, estimating changes in water vapor at this level from integrated water vapor retrievals obtainable from passive microwave satellite data may not be able to help the analysis very much because of the high level of accuracy needed. Therefore, water vapor high in the atmosphere should be a major focus of global modelers, especially since “the positive feedback that arises from using convective parameterizations which tend to moisturize the atmosphere at all levels when there is warming is the most important positive feedback in current large scale climate models — despite the popular emphasis on feedbacks from cloud cover (Arking 1990)” (Lindzen, 1990b).

GCM determined feedbacks notwithstanding, comparing the radiative effects of changes in clear sky OLR due to changes in clear sky water vapor to changes in overall OLR, shown in Figures 5.24 and 5.25, indicates that the radiative effect of changes in clear sky water vapor accounts for only a small portion of the observed changes in OLR. What else could be causing the changes in OLR? Many things: changes in atmospheric temperatures, changes in aerosols due to changes in circulation, and changes in O_3 are all possible. However, the influence that is most likely dominant is the changes in clouds. Since changes in clear sky OLR due to changes in water vapor accounts for $\sim 10\%$ of the changes in OLR, it is likely that IR radiative effect of clouds are much more important. While this analysis neatly separated the clear sky effect from the overall effect, we must keep in mind that water vapor and clouds are not unrelated.

Also, OLR, reflected flux, and net flux are not unrelated. While changes in OLR due to changes in the clear sky greenhouse effect caused by changes in water vapor are small, water vapor's radiative effect appears larger when compared to net radiation. For example, let's take the values at the equator for all grid points shown in Figures 4.19 and 5.4: with a 1°C increase in SST, the radiative effects of changes in clear sky water vapor is $0.5 \text{ W}\cdot\text{m}^{-2}$ which is small compared to a change of $5.5 \text{ W}\cdot\text{m}^{-2}$ for total OLR. Much of this OLR change is due to increases in high clouds which also causes a $4 \text{ W}\cdot\text{m}^{-2}$ change in reflected flux per degree SSTA. Since $4 \text{ W}\cdot\text{m}^{-2}$ of the change in OLR is countered by the change in reflected flux, net radiation is much smaller, only $1.2 \text{ W}\cdot\text{m}^{-2}\cdot\text{K}^{-1}$ at the equator according to Figure 4.19. Therefore, the radiative effect of clear sky water vapor is $\sim 40\%$ of the net change in observed radiation at the equator. Clearly, in certain locations such as the tropics where changes in OLR are largely balanced by changes in reflected flux, the radiative contribution of changes in clear sky water vapor have a major effect on net radiation. But in other regions, such as subtropical stratocumulus decks, the radiative effects of changes in clear sky water vapor can be quite minor. For example, Figure 4.16 indicates that the net radiation-SSTA LAD slope is greater than $5 \text{ W}\cdot\text{m}^{-2}\cdot\text{K}^{-1}$ off the west coasts of the U.S. and southern Africa while Figure 5.20 indicates that the change in OLR due to changes in clear sky water vapor in these same regions is less than $0.5 \text{ W}\cdot\text{m}^{-2}\cdot\text{K}^{-1}$.

Chapter 6

ENSO TELECONNECTIONS AND THE ROLE OF CIRCULATION IN CLOUD-SSTA AND WATER VAPOR-SSTA RELATIONSHIPS

6.1 Introduction

The relationships between clouds and clear sky water vapor to the underlying SSTA, described in Chapters 2 and 3, are incomplete primarily because the role of changes in general circulation was not addressed. Changes in general circulation can cause changes in clouds and water vapor. But trying to separate the role of local SSTAs from the role of changes in general circulation can be exceedingly difficult because changes in SSTAs can cause changes in general circulation and changes in general circulation can cause changes in SSTAs. Never-the-less, in this chapter we will attempt to address this question by using ENSO (El Niño – Southern Oscillation) as an indicator of altered circulation. ENSO is one of the strongest and best understood changes in circulation that we regularly experience, yet it does not fulfill all of the possibilities of altered circulation. Therefore, this method, while helpful to getting a handle on this difficult question, may not be able to totally resolve this issue.

The strong anomalous heating of the eastern tropical Pacific Ocean known as the El Niño has long been recognised to cause major changes in global circulation. “The relatively uniform sea surface temperatures during El Niño are associated with a merger of the atmospheric convergence zones: the ITCZ moves equatorward, the South Pacific Convergence Zone moves northward, and the convergence zone over the western Pacific moves eastward (Pazan and Meyers, 1982). The zonal Walker Circulation is weak during these periods but the meridional Hadley Circulation intensifies. The opposite happens during La Niña when the cold surface waters of the southeastern tropical Pacific stretch far westward in a tongue along the equator” (Philander, 1990).

Horel and Wallace (1981) state that in addition to “enhancement of the Hadley circulation in the Pacific sector (Reiter, 1978)” there are teleconnections to extratropical latitudes which include “a deepening and southward displacement of the Aleutian low during the Northern Hemisphere winter season (Bjerknes, 1966, 1969, 1972; Rowntree, 1972; White and Walker, 1973; Namias, 1976).” In their own work examining upper tropospheric geopotential height anomalies, Horel and Wallace (1981) conclude that during the Northern Hemisphere winters which fall during warm episodes (El Niño), “the following conditions prevail:

“1) The Pacific jet stream is stronger and further to the south than normal so that Hawaii is situated along its anticyclonic flank, in a region of subsidence; this relationship is reflected in the correlation between Hawaiian rainfall and the Southern Oscillation Index of Walker and Bliss (1932), the negative correlation between Hawaiian and Line Island rainfall (Meisner, 1976), and the negative correlation between sea surface temperature averaged over the region 10°N–10°S and 180°W–90°W and Hawaiian rainfall (Wright, 1979).

“2) There are negative mid-tropospheric geopotential height anomalies over the North Pacific, which should be reflected in the sea level pressure field, since low-frequency fluctuations in this region tend to be highly barotropic (Blackmon *et al.*, 1979); hence the pattern ... (of upper tropospheric geopotential height anomalies) is consistent with Bjerknes’ (1966, 1969) and Namias’ (1976) observations concerning the Aleutian low.

“3) There are positive mid-tropospheric geopotential height anomalies over western Canada, which should be more strongly reflected in surface temperature than in sea level pressure since low-frequency fluctuations in this region tend to be highly baroclinic (Blackmon *et al.*, 1979). This is consistent with the teleconnection patterns of Walker and Bliss (1932) and Wright (1978).

“4) There is a negative anomaly centered over the southeastern United States which should be reflected in both surface temperatures and sea-level pressures, since Blackmon *et al.* found that sea level pressure, 500 mb height and 1000-500 mb thickness are all positively correlated with one another in this region. Hence the pattern ... (of upper

tropospheric height anomalies) is consistent with the inclusion of Charleston, South Carolina sea level pressure in the Southern Oscillation Index of Walker and Bliss and with the surface temperature correlations reported by Wright (1978).”

Furthermore, Horel and Wallace (1981) state that there are also “teleconnections to the Southern Hemisphere extratropics. Studies by Pittock (1973), Sreten (1975), Nicholls (1977) and Trenberth (1975, 1976, 1980), among others, have linked tropical fluctuations with changes in the Southern Hemisphere circulation. A detailed analysis of Southern Hemisphere sea level pressure and 700 mb height anomalies by van Loon (1980) has revealed the existence of teleconnections comparable in strength and qualitatively similar, in terms of spatial patterns, to those in Northern Hemisphere.”

In view of these teleconnections, it is not surprising that researchers looking only at teleconnections to cloudiness, such as Angell and Korshover (1987), do indeed find correlations between ENSO and cloudiness in remote locations such as the United States. However, it is important to bear in mind that the purpose of this research is not to undertake an extensive analysis of ENSO teleconnections to clouds, water vapor, and their radiative effects, but rather to use changes in global circulation as indicated by ENSO teleconnections to help determine the role of local SSTA versus altered circulation in causing changes in these atmospheric variables.

6.2 Data

Two different techniques were used to identify ENSO for purposes of this research. One technique used the average SST anomaly for the region 0° to 10° South and from the dateline (180°) to the South American coast ($80 - 82^{\circ}$ West) calculated from the Climate Analysis Centers SST data set. This is the same SST data set used in earlier chapters. The averages used to calculate the anomalies were monthly averages for the time period of the Nimbus-7 cloud data set or the ISCCP TOVS water vapor data set. Therefore, a month that was in both data sets' time periods would have its anomaly calculated from two different averages depending on which data set that anomaly was to be used with. The region used for this SST anomaly calculation is essentially the same region used by

Angell and Korshover (1987) as well as Collimore (1990). However, it is a large region and may create a less precise indication of ENSO altered circulation than desired.

Therefore, another ENSO indicator was used as well, the Southern Oscillation Index (SOI). The SOI is the normalized Tahiti sea level pressure anomaly minus the normalized Darwin sea level pressure anomaly (Trenberth, 1976) calculated and provided by the Climate Analysis Center. The SOI has been widely used as an indicator of ENSO. However, it has considerable noise in the signal. Therefore a 5 month moving average was applied to attempt to get a truer indicator of ENSO (Kousky, 1990).

Time series of these indicators are shown in Figures 6.1 and 6.2. The top of each figure is the SST anomaly. The bottom graph is the smoothed SOI (solid) and raw SOI (dashed). For ease of comparison, the SOI is inverted. Examinations of these two Figures reveals obvious similarities between the two as one would expect. But there are also differences. The atmospheric indicator (SOI) has greater variation and quicker response. There are also noticeable differences between one time period and the other, particularly in the SOI. For example, the very strong 1982-83 El Niño event shows up much stronger on the SOI graphs than any other event while the strength of the SST anomaly is only slightly higher in 1983 than 1987. Also worthy of note is that, based on the SOI, the time corresponding to the Nimbus-7 cloud data set did not have a strong La Niña while the time corresponding to the ISCCP TOVS water vapor data set did have one in 1988-89.

Obviously it would be very helpful to have concurrent data sets, because then they could be analyzed with ENSO events of the same magnitude. This, unfortunately, is not the case. However, both time periods have significant ups and downs in the SOI and eastern tropical Pacific SST anomalies and therefore, evidently, significant changes in circulation.

6.3 Methods

The procedure used to determine the relationship between, for example, total cloudiness and ENSO is the same as that used to determine the relationship between cloudiness and local SSTA: the use of LAD and MRBP. The only difference is that instead of local SST anomalies, all of these analyses were performed with the same SST anomaly,

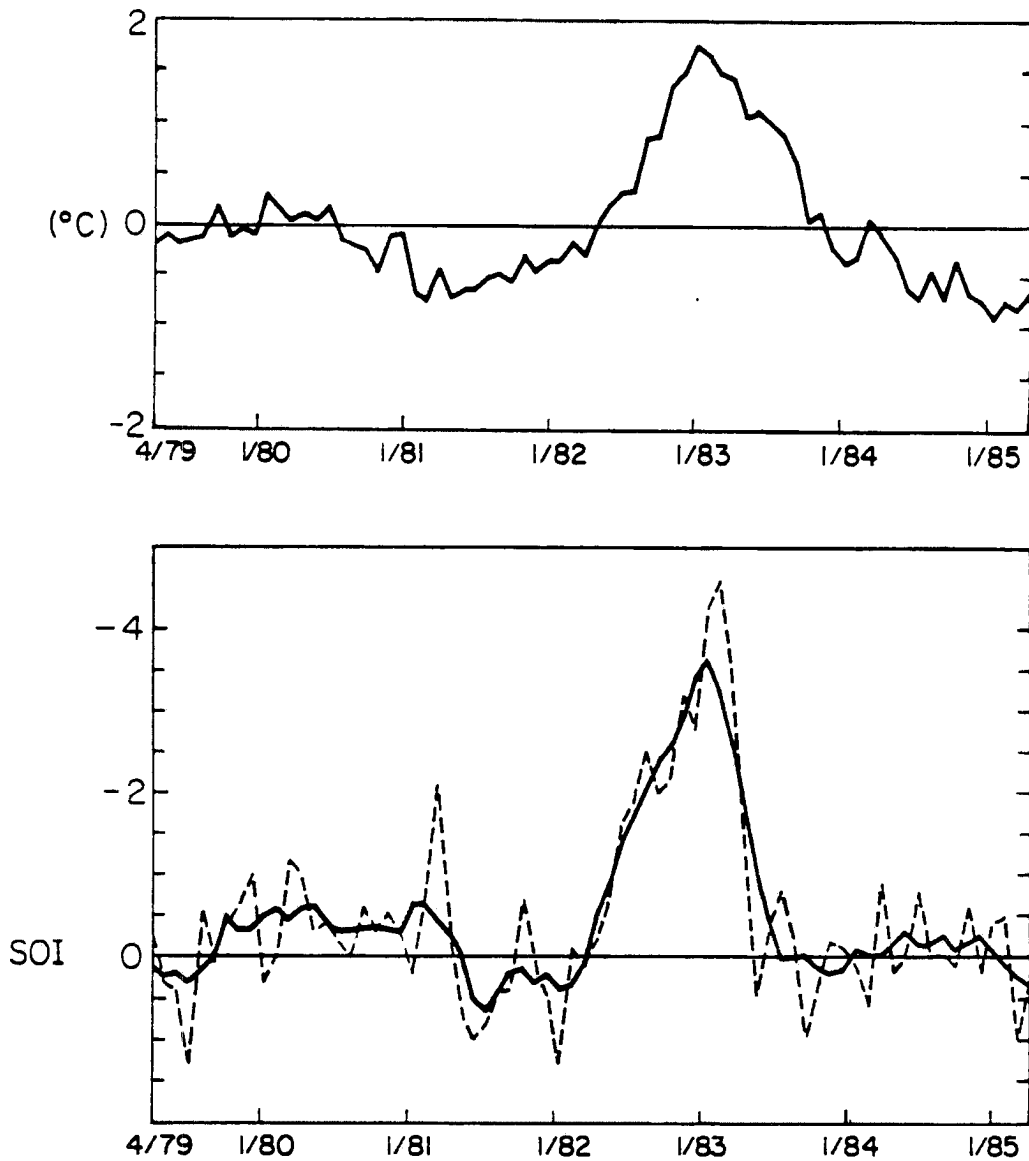


Figure 6.1: Sea surface temperature anomalies from 0° to 10° South and from 180° longitude east to the coast of South America for the times corresponding to the Nimbus-7 cloud data set (top) and the Southern Oscillation Index (SOI) smoothed (solid line) and raw (dashed line) for the same time period (bottom). For ease of comparison, the SOI has been inverted. Units are $^{\circ}\text{C}$ for SST and hPa for the SOI.

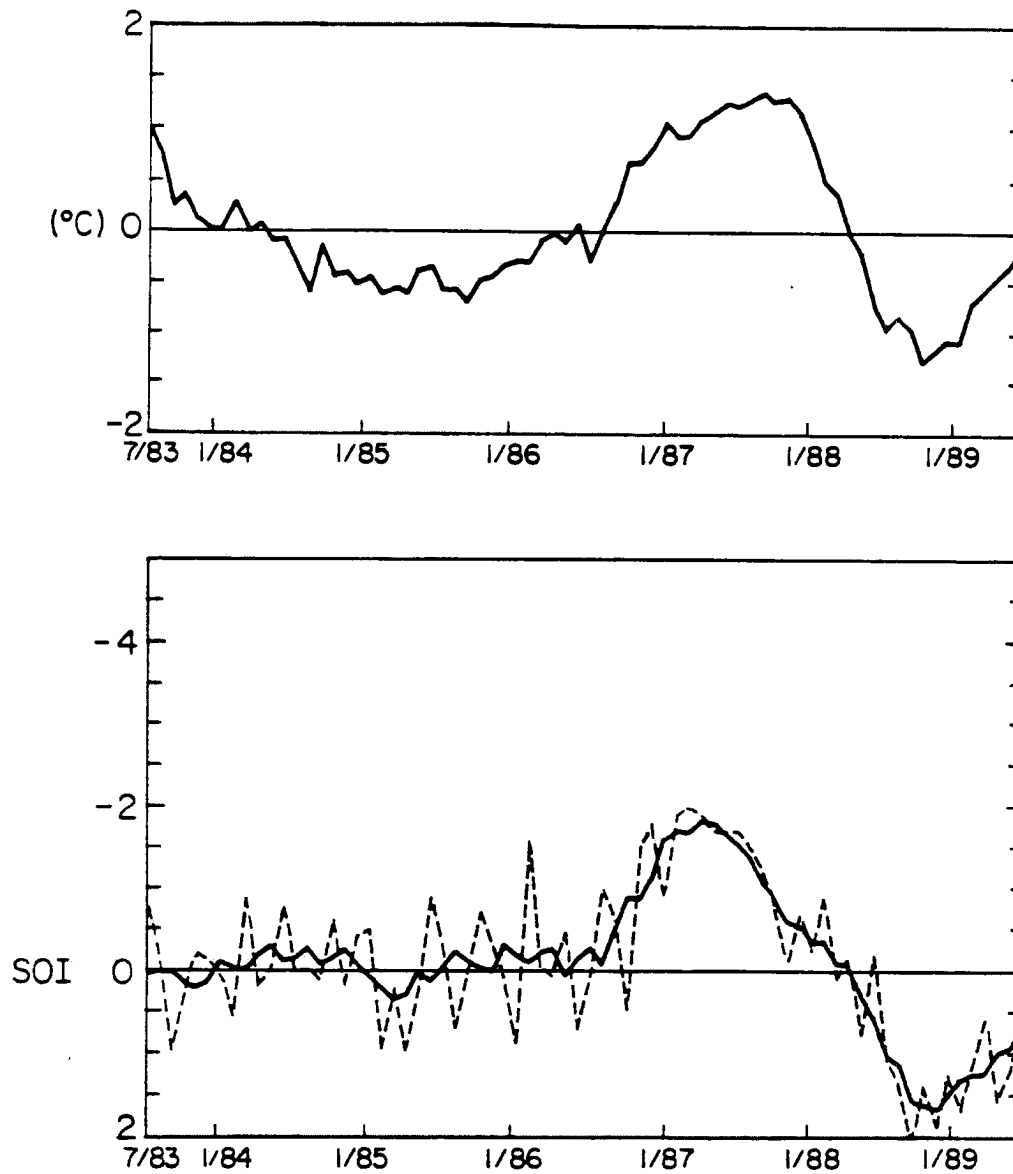


Figure 6.2: Sea surface temperature anomalies from 0° to 10° South and from 180° longitude east to the coast of South America for the times corresponding to the ISCCP TOVS water vapor data set (top) and the Southern Oscillation Index (SOI) smoothed (solid line) and raw (dashed line) for the same time period (bottom). For ease of comparison, the SOI has been inverted. Units are $^{\circ}\text{C}$ for SST and hPa for the SOI.

namely that for eastern tropical Pacific ocean. Also, the SOI was used in place of the SST anomaly. For these analyses, the smoothed SOI was used because the oceanic and general circulation effects associated with ENSO do not fluctuate on the time scales of the monthly fluctuation in the raw SOI and therefore the smoothed SOI was determined to be a better indicator of ENSO related changes.

The LAD and MRBP analyses were performed on cloud, water vapor, and radiation parameters as well as SST throughout the global oceans. The time period for the ENSO signal used in these analyses were shifted forward and back as much as 10 months to see if there was significantly improved correlations for certain lead or lag times. Examination of images resulting of these analyses indicated that some areas had much better correlations with particular lead or lag times, but on a global basis it was difficult to determine the most appropriate lag or lead time to use. For analysis based on the eastern tropical Pacific SST anomaly, the best lag time appeared to be 2 months: that is the atmospheric response lagged two months behind the eastern tropical Pacific SSTA. This means that these analyses were performed using the tropical Pacific SSTA that was for a time period starting two months prior to the start of the data for atmospheric parameter analyzed.

For the SOI, comparative analysis was done with 21 different lag or lead times, from a 10 month lag to a 10 month lead. The results of this analysis for total cloud, total water vapor, and global SST for these data set times are shown in Figures 6.3 and 6.4 by simply plotting the number of grid points with P-values less than or equal to 0.05. It is interesting to note that total cloudiness had a distinct maximum at 0 month lag while total water vapor had a distinct secondary minimum at 0 month lag. When comparing over the same domain, more grid points had highly correlated SSTAs than highly correlated total cloud or total water vapor anomalies. The analysis of the atmospheric or oceanic variable-SOI LAD and MRBP results will focus on 0 or no lag with a little side analysis at 4 month lead which has a maximum in the number of grid points with low P-values for the total water vapor-SOI analysis.

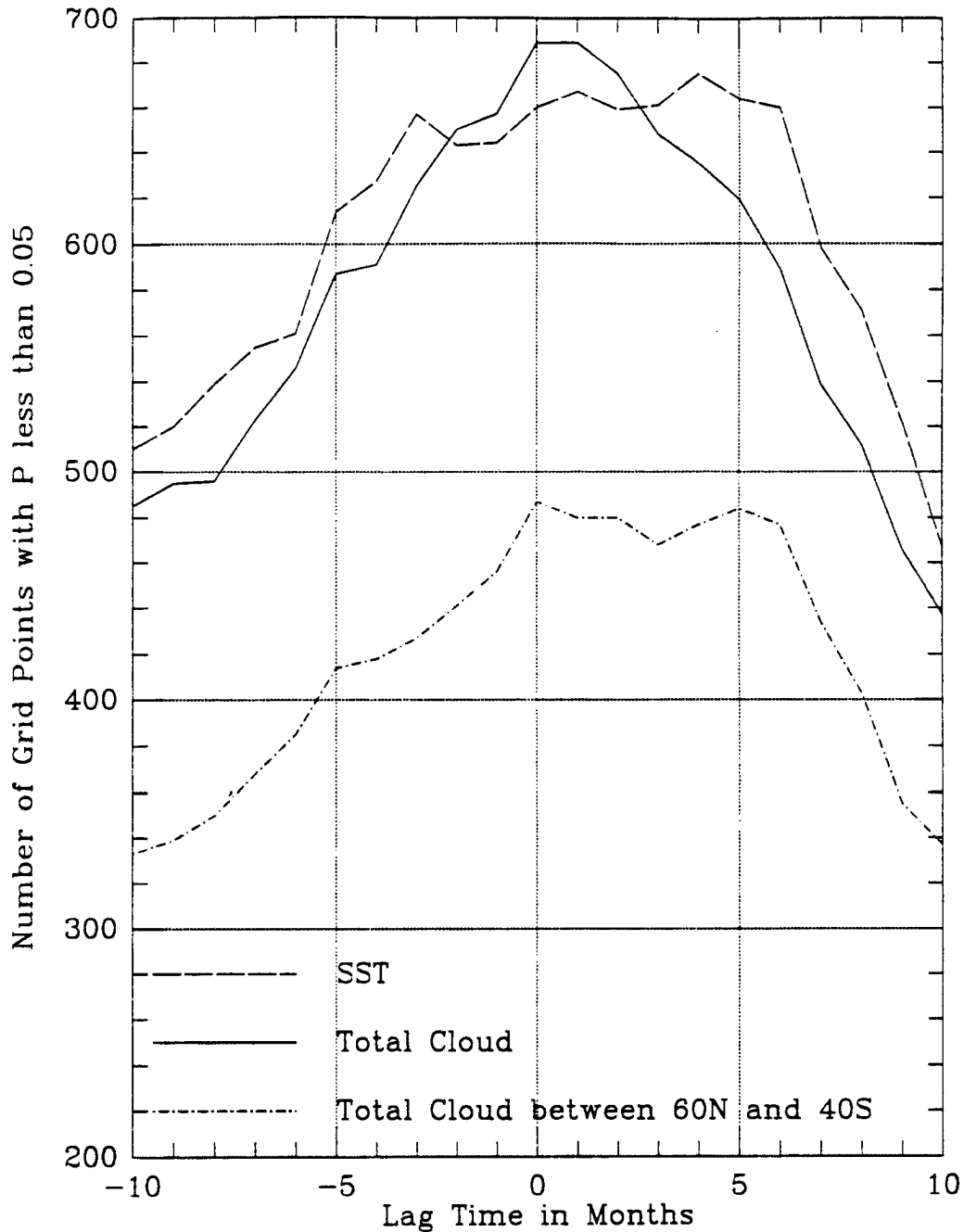


Figure 6.3: The number of grid points with with low P-values for the relationship between the atmospheric or oceanic variable and the SOI at various lags and leads. A 2 month lag time means the atmosphere lags two months behind the SOI, i.e., the time period of the SOI index used in this analysis was 2 months ahead of the atmospheric or oceanic variable. The three curves on this graph are from SSTA, Total Cloud anomaly, and Total Cloud anomaly with a domain limited to the region with valid SST data for that time period, namely 60°N to 40°S. Based on data from April 1979 through March 1985.

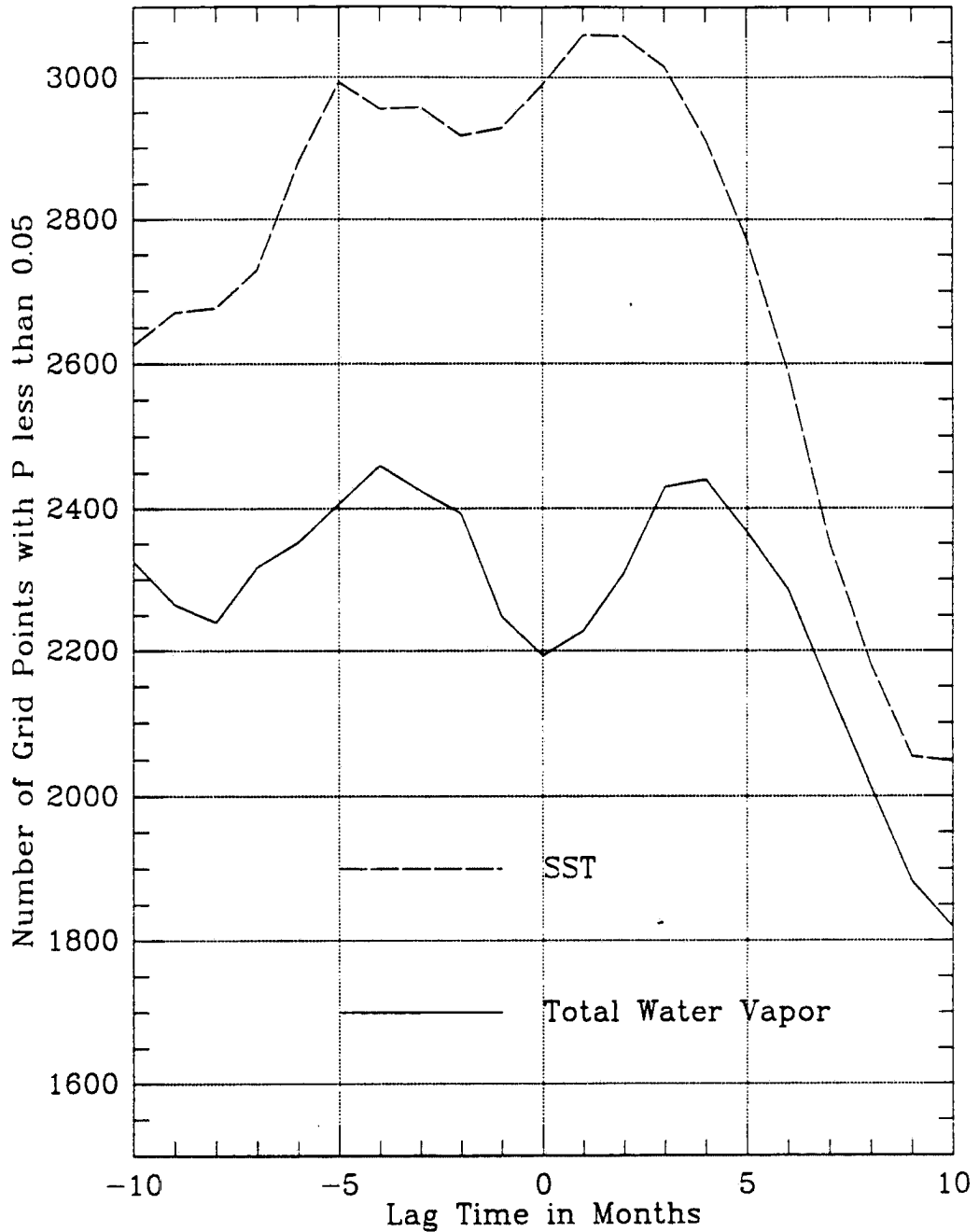


Figure 6.4: The number of grid points with with low P-values for the relationship between the atmospheric or oceanic variable and the SOI at various lags and leads. A 2 month lag time means the atmosphere lags two months behind the SOI, i.e., the time period of the SOI index used in this analysis was 2 months ahead of the atmospheric or oceanic variable. The two curves on this graph are from SSTA and Total ISCCP TOVS water vapor anomaly. Based on data from July 1983 through June 1989.

6.4 Results

The results presented here are primarily for analysis using the SOI as a representative of ENSO. Generally there were better correlations between the atmospheric parameters and the SOI than the eastern tropical Pacific SSTA. The two exceptions to this were high clouds and high water vapor, which showed slightly better correlations with the slower fluctuations of the SSTA. Net radiation was the only variable that showed any substantial differences in the locations of the regions with low P-values between these two analyses. Plots for many the LAD analyses done with the tropical eastern Pacific SSTA are included in the Appendix C.

6.4.1 Global SSTA-ENSO

The first question that needs to be addressed in this research is the relationship between SSTAs and ENSO signals. Differentiating between local SSTA effects and the effect of changes in general circulation will be more difficult at a grid point where the SSTAs also clearly change in association with changes in general circulation. Examination of Figures 6.5 and 6.6 reveals that there are strong relationships between the SOI and SSTA in many parts of the global oceans.

Ideally we should be using data sets for all our parameters from the same time period. This is especially true when analyzing ENSO teleconnections because the 1982-83 El Niño event was unusually strong. It is therefore encouraging that the relationships between global SSTAs and the SOI for the two different time periods, shown in Figures 6.5 and 6.6, are so similar. It is also interesting to note that large regions of the oceans, despite long distances, have SSTA's that can be related to the SOI with low P-values. In fact, as Figures 6.3 and 6.4 make clear, there are more low P-value grid points with SSTA than total clouds or total water vapor. And these grid points are not just in the tropical Pacific, but are often far removed from the tropical Pacific.

The maximum amplitude of the LAD analysis of the SSTAs to the SOI is in the middle and eastern Pacific along the equator where the effect of oceanic equatorial Kelvin waves is greatest, with a LAD slope of $\sim -1^{\circ}\text{C}$ per hPa of SOI. However, the globally

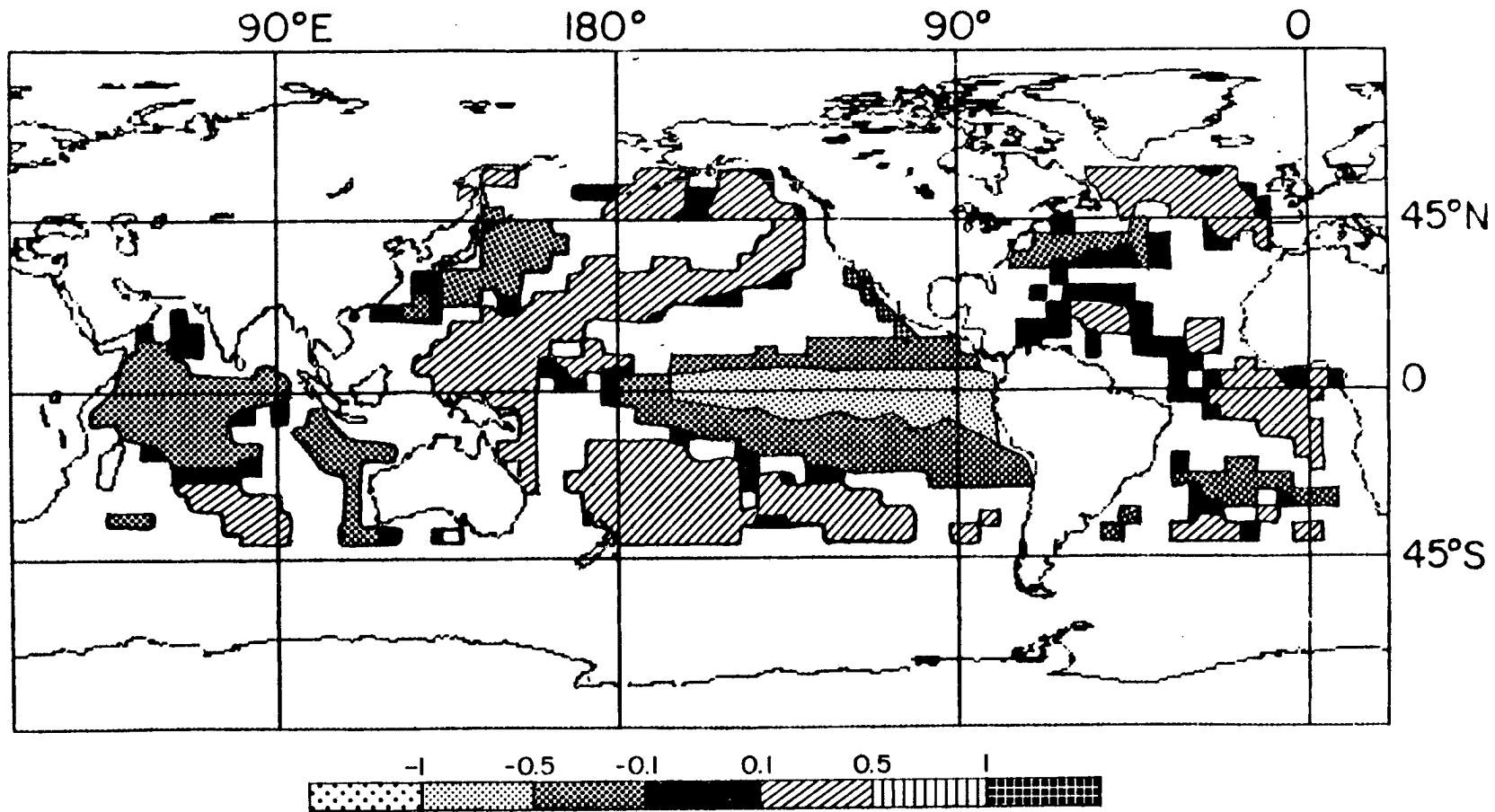


Figure 6.5: SSTA-SOI LAD slope. Contour plot of the LAD slope from the analysis between SSTA and the SOI for the times corresponding to the Nimbus-7 cloud data set. Only those grid points with P-values ≤ 0.05 are plotted. The SST data for this time period is only available from 60°N to 40°S. Units are increase in SSTA in degrees C per hPa increase in SOI. Based on data from April 1979 through March 1985.

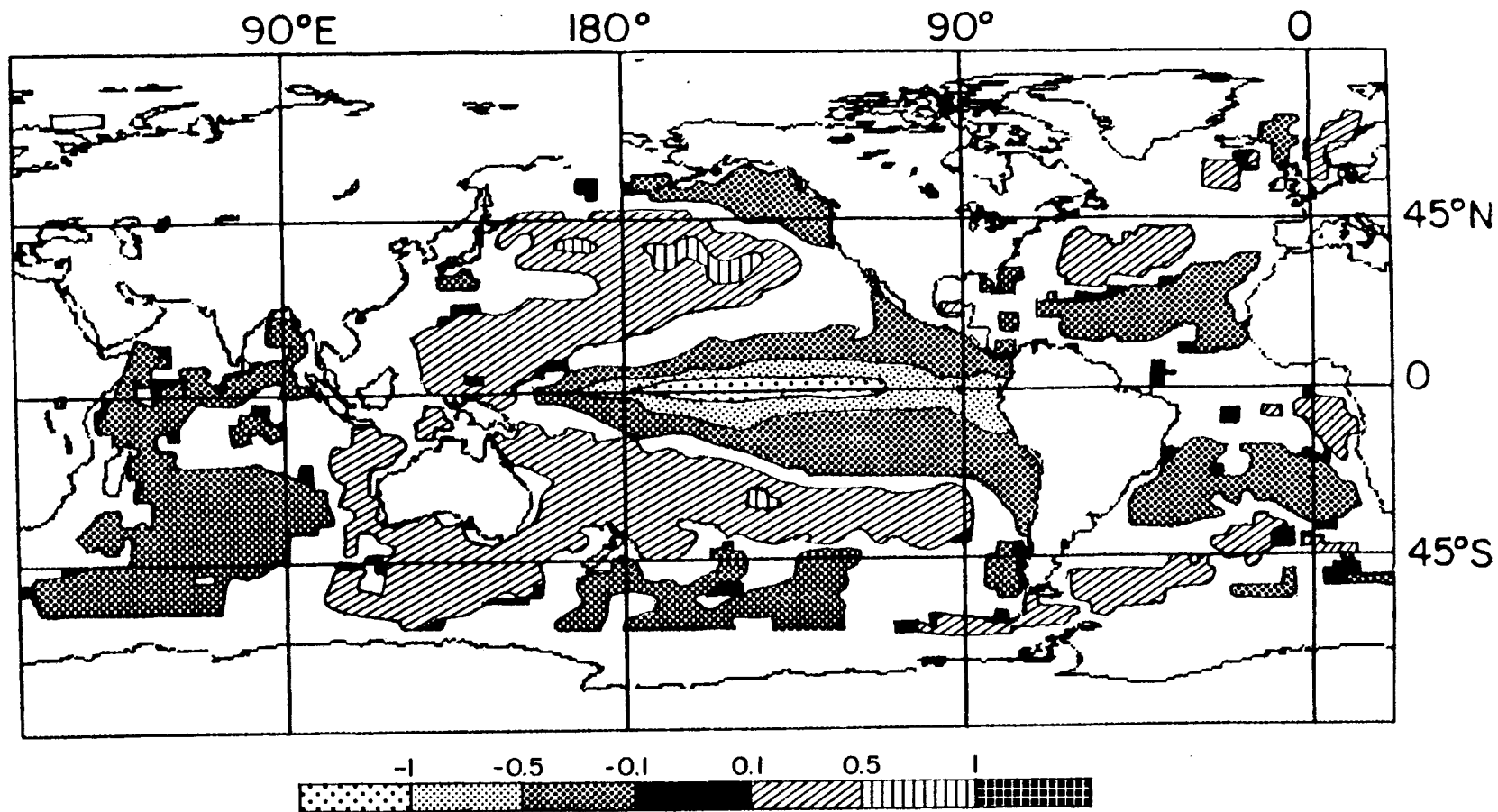


Figure 6.6: SSTA-SOI LAD slope. Contour plot of the LAD slope from the analysis between SSTA and the SOI for the times corresponding to the ISCCP TOVS water vapor data set. Only those grid points with P-values ≤ 0.05 are plotted. Units are increase in SSTA in degrees C per hPa increase in SOI. Based on data from July 1983 through June 1989.

averaged LAD slope values for grid points with $P \leq 0.05$ are only $-0.064 \text{ K}\cdot\text{hPa}^{-1}$ for the Nimbus-7 cloud data set times and $-0.075 \text{ K}\cdot\text{hPa}^{-1}$ for the ISCCP TOVS times due in part to large areas of the ocean having positive LAD slopes.

6.4.2 Clouds–ENSO

Examination of Figures 6.7, 6.8, 6.9, and 6.10 shows that clouds around the globe are related to the Southern Oscillation Index. Certainly the strongest relationship is in the equatorial Pacific. However, regions far removed from the equatorial Pacific, such as over the Indian and Atlantic oceans south of Africa, can also have a strong relationship.

To determine the relative importance of the remote cloud–SOI relationships versus cloud–local SSTA relationships, grid points with P-values for the LAD analysis of less than or equal to 0.05, which indicates that the relationship is unlikely to be random, for both were compared only over the same latitude range: from 60°N to 40°S , the limit of the SST data set for that time period. Table 6.1 compares the number of grid points with $P \leq 0.05$ of each data set. Total and low clouds had more grid points with direct SSTA analysis, but high clouds and mid clouds had more grid points related to the SOI. Of these two data sets, 44% to 69% of the low P-value grid points were points in both data sets. Of these grid points that had low P-values for both cloud–SSTA and cloud–SOI LAD analysis, the vast majority of 73% to 83% also had low P-values for the relationship between local SSTA and the SOI. Furthermore, as the last column in Table 6.1 indicates, almost all these grid points had the sign for the cloud–SOI analysis the way one would expect knowing the sign of the direct cloud–SSTA LAD analysis and the sign of the SSTA–SOI LAD analysis at that grid point. For example, if at a particular grid point the cloud–SSTA LAD slope was positive and the SSTA–SOI LAD slope was positive, then the cloud–SOI LAD slope was positive in almost all cases. Depending on the cloud parameter, only 1–7% of the grid points would have the opposite occur.

This means that for the vast majority of the grid points that the two low P-value data sets have in common, we cannot determine whether the observed changes in clouds is due to changes in local SSTA or changes in circulation because all three are related to each

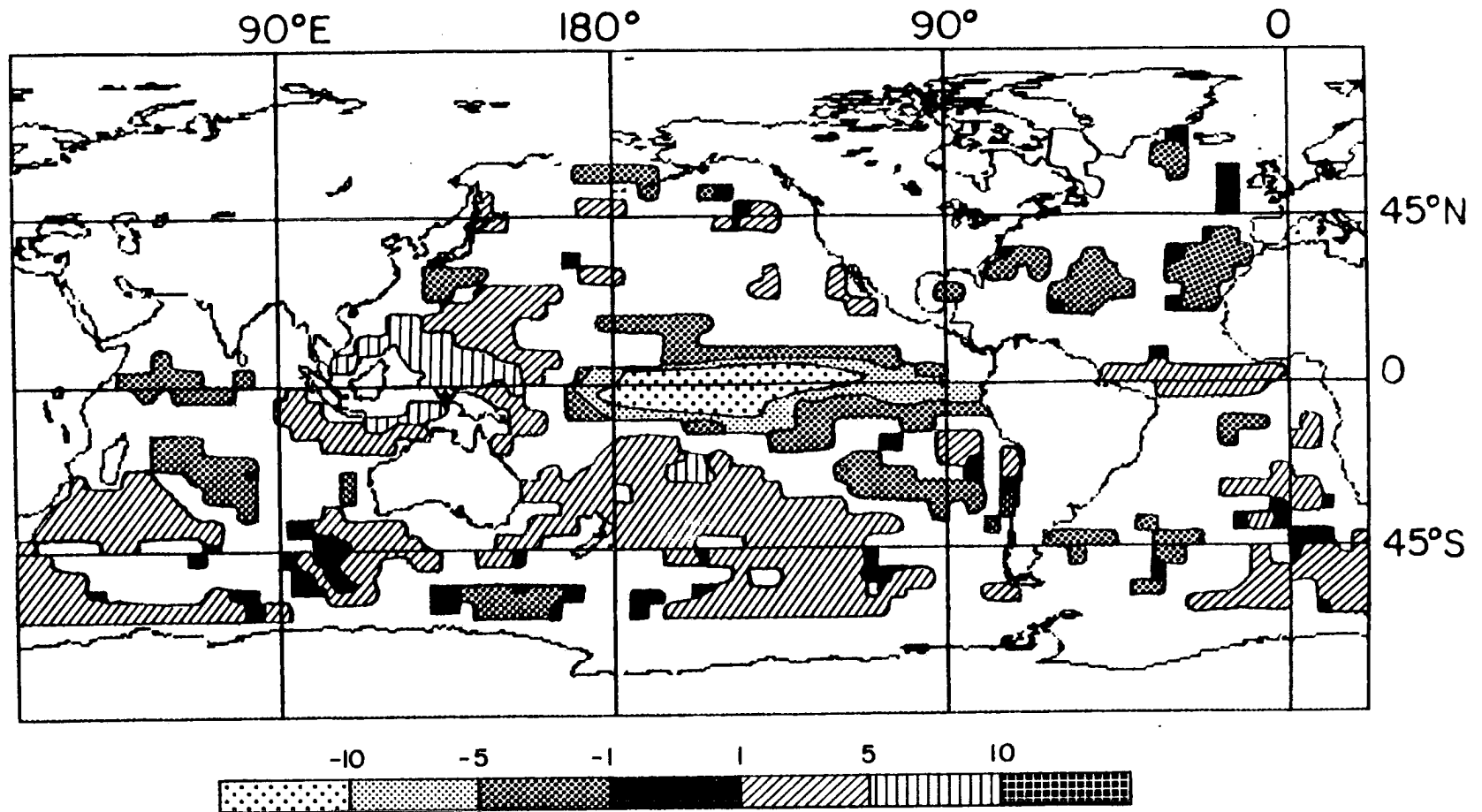


Figure 6.7: Total cloud-SOI LAD slope. Contour plot of the LAD slope from the analysis between total cloudiness and the SOI. Only those grid points with P-values ≤ 0.05 are plotted. Units are the increase in percent of cloudiness per hPa increase in the SOI. Based on data from April 1979 through March 1985.

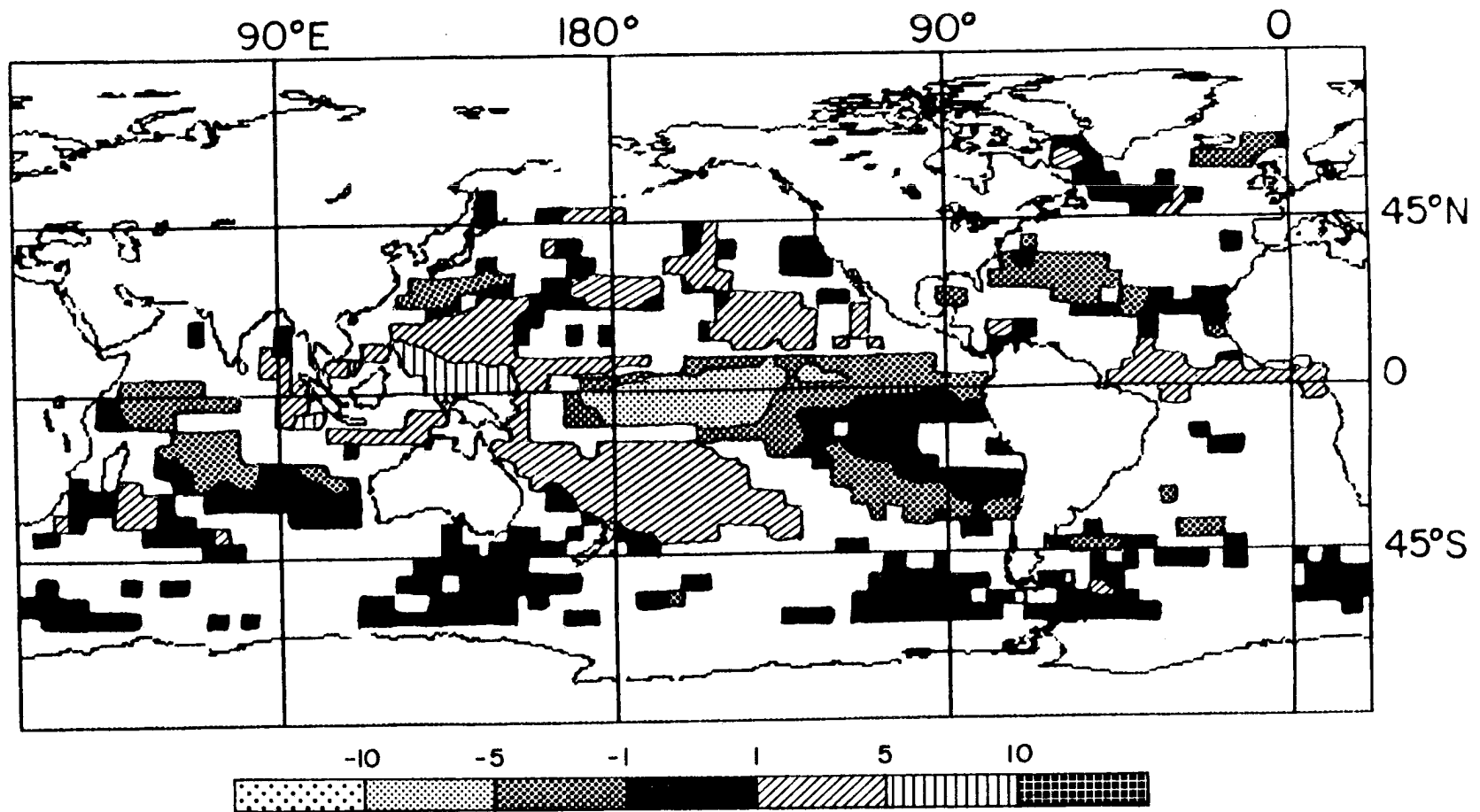


Figure 6.8: High cloud-SOI LAD slope. Contour plot of the LAD slope from the analysis between high clouds and the SOI. Only those grid points with P-values ≤ 0.05 are plotted. Units are the increase in percent of high clouds per hPa increase in the SOI. Based on data from April 1979 through March 1985.

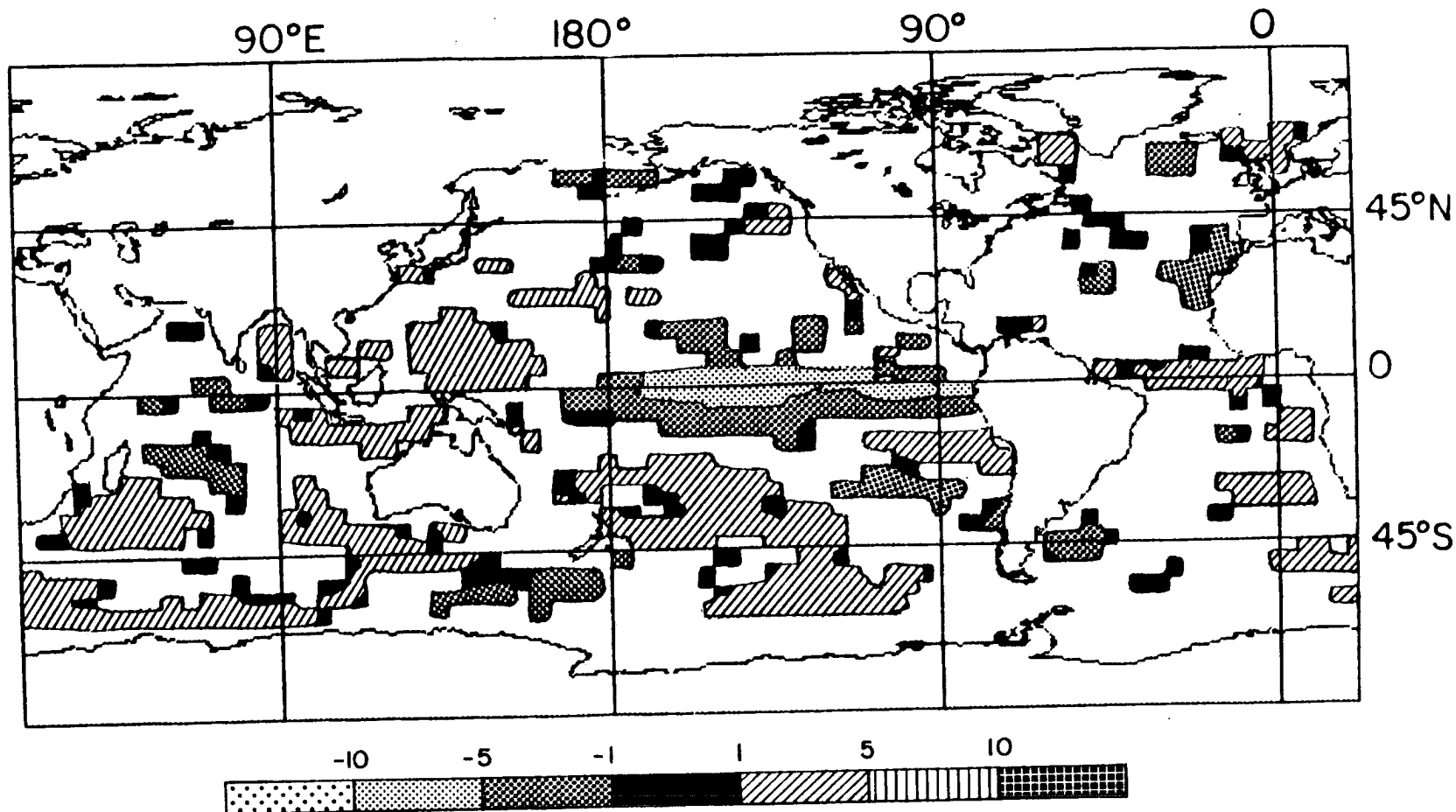


Figure 6.9: Mid cloud-SOI LAD slope. Contour plot of the LAD slope from the analysis between middle level clouds and the SOI. Only those grid points with P-values ≤ 0.05 are plotted. Units are the increase in percent of middle level clouds per hPa increase in the SOI. Based on data from April 1979 through March 1985.

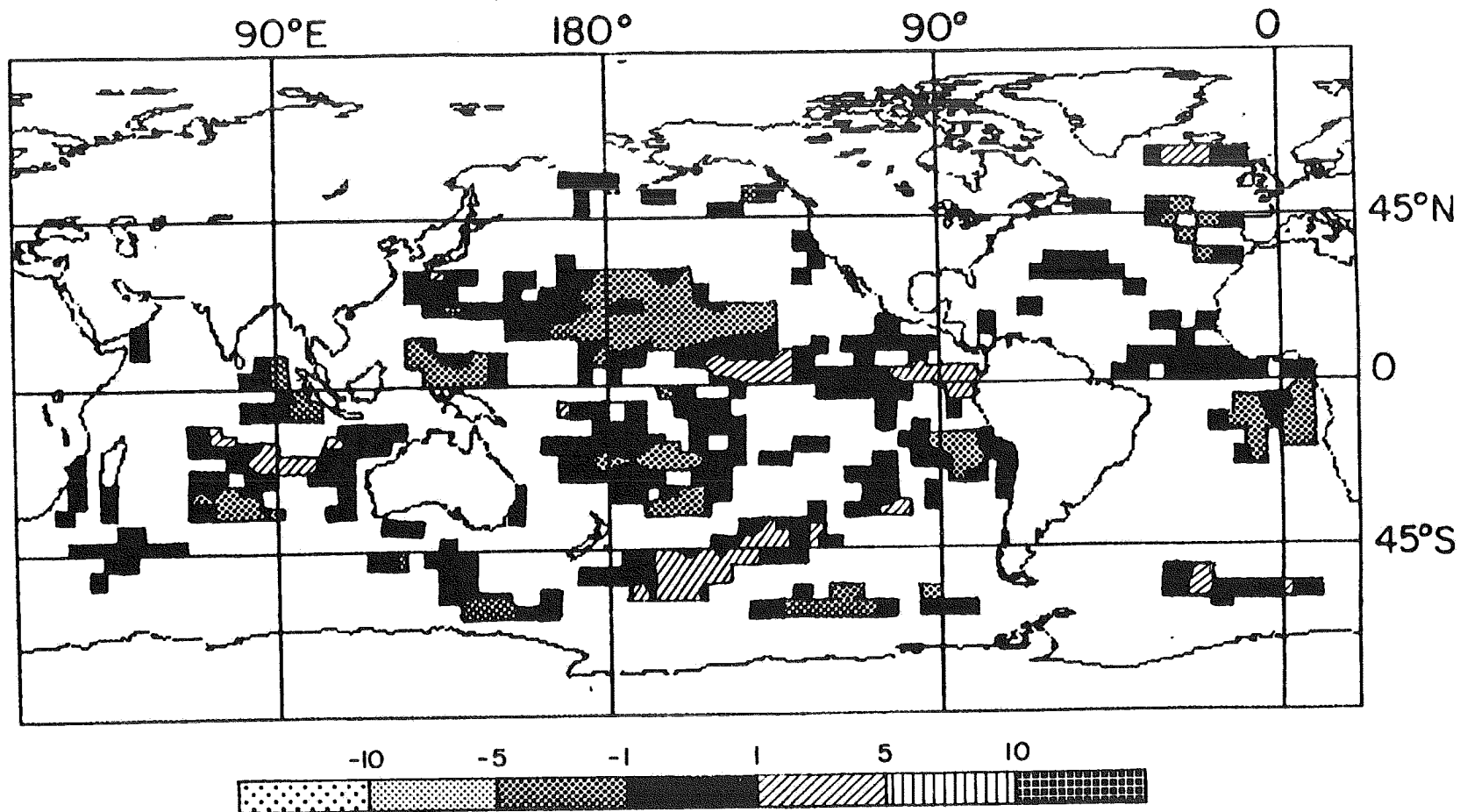


Figure 6.10: Low cloud-SOI LAD slope. Contour plot of the LAD slope from the analysis between low clouds and the SOI. Only those grid points with P-values ≤ 0.05 are plotted. Units are the increase in percent of low clouds per hPa increase in the SOI. Based on data from April 1979 through March 1985.

Table 6.1: Number of cloud LAD analysis grid points with P-value ≤ 0.05 . Column 2 is for LAD analysis using the Southern Oscillation Index, column 3 uses underlying SSTAs (from Chapter 2), column 4 is the number of low P-value grid points that SOI and direct SSTA analysis have in common, column 5 is the number of these grid points that also have low P-values for the LAD analysis of the underlying SSTA with the SOI, column 6 is the percent of the grid points in column 4 that are in column 5. The last column is the percent of the grid points that are in common for the three data sets, where the sign of the LAD for the atmospheric variable–SOI analysis is not the sign one would expect knowing the sign of the LAD analysis at that grid point for the atmospheric variable–local SSTA and the sign of the LAD analysis for the local SSTA–SOI. To make for more accurate comparisons, the grid points in column 2 are only those within the 60°N to 40°S domain that limit columns 3 and 4 due to geographical limits to the SST data set for this time period. There is a total of 1,040 possible grid points. Based on data from April 1979 through March 1985.

Cloud Parameter	SOI	Direct	In Common	IC + SST	Percent	Reverse Value
Total Clouds	487	515	267	212	79%	3%
High Clouds	561	425	292	232	79%	1%
Mid Clouds	453	436	205	171	83%	4%
Low Clouds	407	463	203	148	73%	7%

other. Where the two data sets diverge, we can determine which has the greater effect on clouds.

In regions where any LAD slope value switches sign (e.g., where the LAD slope is positive to the south and negative to the north), the LAD regression analysis is likely to have a high probability of being random (high P-value). These are frequently the regions where cloud–SSTA analysis has a low P-value while cloud–SOI analysis has a high P-value and vice-versa. For analysis involving total clouds, cloud–local SSTA analysis had better representation of stratocumulus decks off the west coast of continents and for a region in the North Atlantic near 45°N than did cloud–SOI analysis. The total cloud–SOI analysis did not have any large, distinct regions not in common with total cloud–SSTA analysis though high cloud analyses did. Low P-value high cloud–SSTA analysis grid points that were not in common with low P-value high cloud–SOI grid points were scattered, isolated points compared to the distinct regions where high cloud–SOI analysis had low P-values for grid points not in common with low P-value high cloud–SSTA grid points. The main regions where the high cloud–SOI had better representation were a much broader SPCZ

and regions which normally have subtropical subsidence and very few high clouds. Middle cloud direct SSTA analysis had a region in the tropical Pacific between areas where the middle cloud-SOI analysis went from a positive value south of Japan to a negative value east of the dateline and a region north and north east of Hawaii that was not in common with the middle cloud-SOI analysis. The middle cloud-SOI analysis only had scattered grid points which were not in common with direct SSTA analysis. For low clouds, direct SSTA analysis had better representation in stratocumulus decks while low cloud-SOI analysis had better representation in a region near and south of Hawaii.

6.4.3 Water Vapor-ENSO

Water vapor over much of the globe has a strong relationship with the Southern Oscillation Index. These are shown in Figures 6.11, 6.12, 6.13, and 6.14. For the Pacific Ocean, there is a very strong similarity between the figures for total water vapor-, low water vapor-, and SSTA-SOI analyses (Figures 6.11, 6.14, and 6.6). It is also interesting to note that in the central tropical Pacific, as one moves up from low level to high level water vapor, the region of negative water vapor-SOI LAD analysis with low P-values moves farther north of the equator.

In the North Atlantic ocean, there are two regions of low P-value LAD regression analysis for SSTA-SOI, one positive and one negative. Yet low level water vapor LAD slopes are uniformly positive there, while high water vapor-SOI LAD slopes are negative. The relationship between water vapor and the SOI seems to be poorest for the Indian ocean and South Atlantic ocean, though some of this is a function of the decision to use no lead or lag time for this analysis. Examination of LAD analyses for a 4 month lead reveals a stronger water vapor-SOI relationships for the tropical Indian ocean, especially for low levels. This occurs despite a weak relationship between SSTA and the SOI in most of the Indian ocean with a 4 month lead. The South Atlantic has a few more low P-value water vapor-SOI LAD analysis grid points with a 4 month lead, but the number of low P-value grid points remains small.

The number of grid points with P-values less than or equal to 0.05 for both SOI analysis and direct local SSTA analysis are shown in Table 6.2. Again, the vast majority

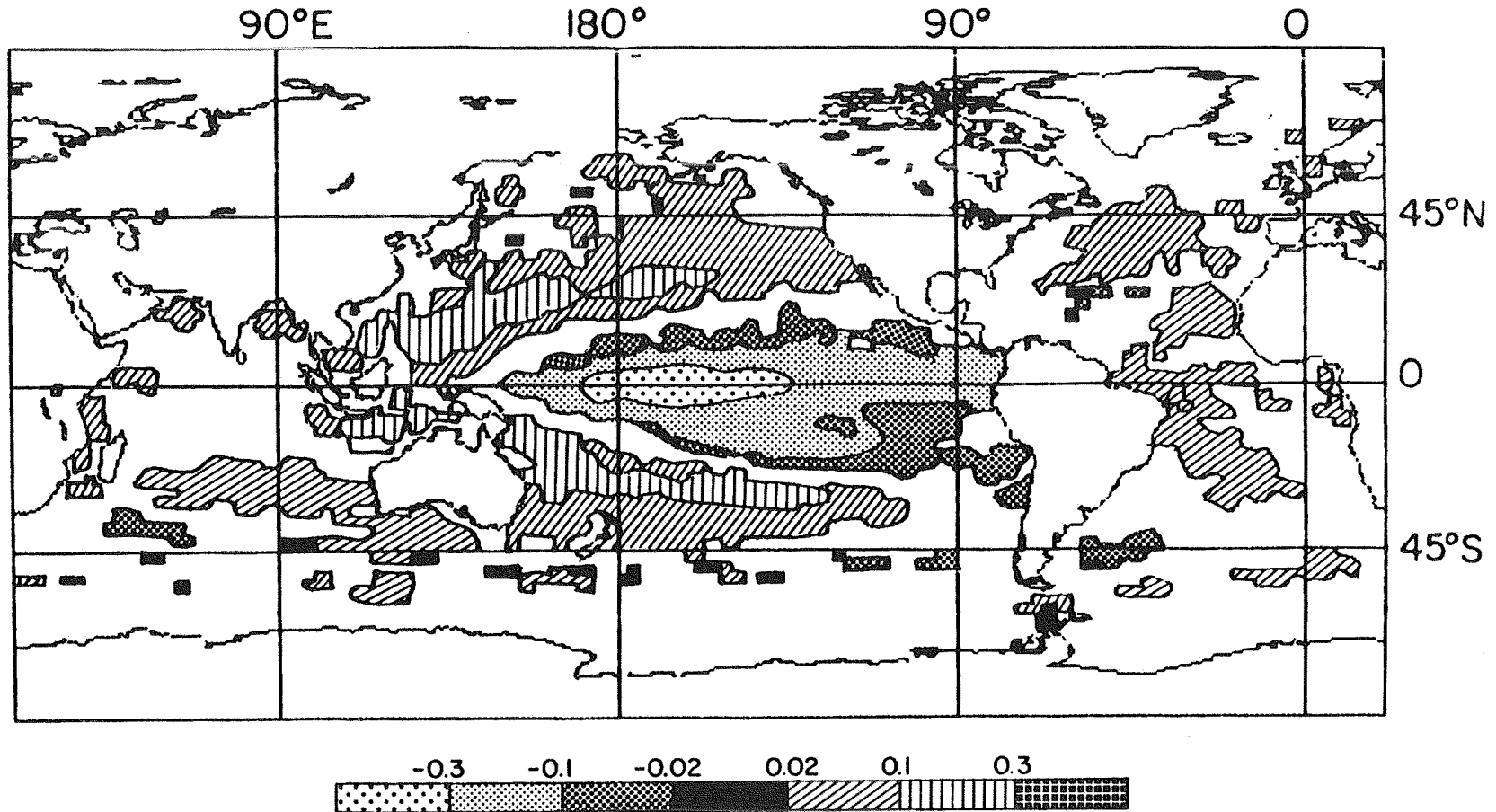


Figure 6.11: Total PW-SOI LAD slope. Contour plot of the LAD slope from the analysis of total water vapor and the SOI. Only those grid points with P-values ≤ 0.05 are plotted. Units are the increase in cm precipitable water per hPa increase in the SOI. Based on data from July 1983 through June 1989.

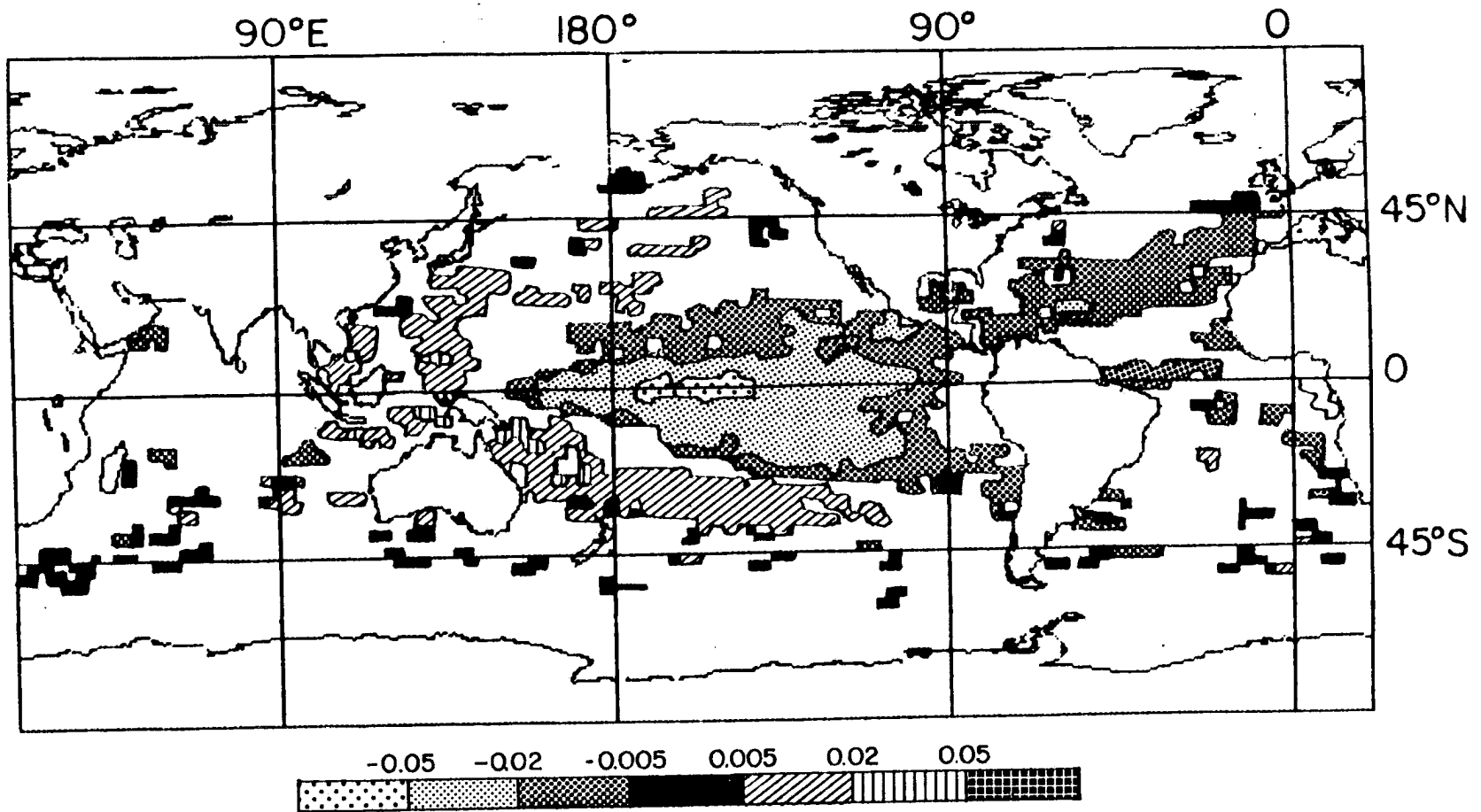


Figure 6.12: High PW-SOI LAD slope. Contour plot of the LAD slope from the analysis of high water vapor and the SOI. Only those grid points with P-values ≤ 0.05 are plotted. Units are the increase in cm precipitable water per hPa increase in the SOI. Based on data from July 1983 through June 1989.

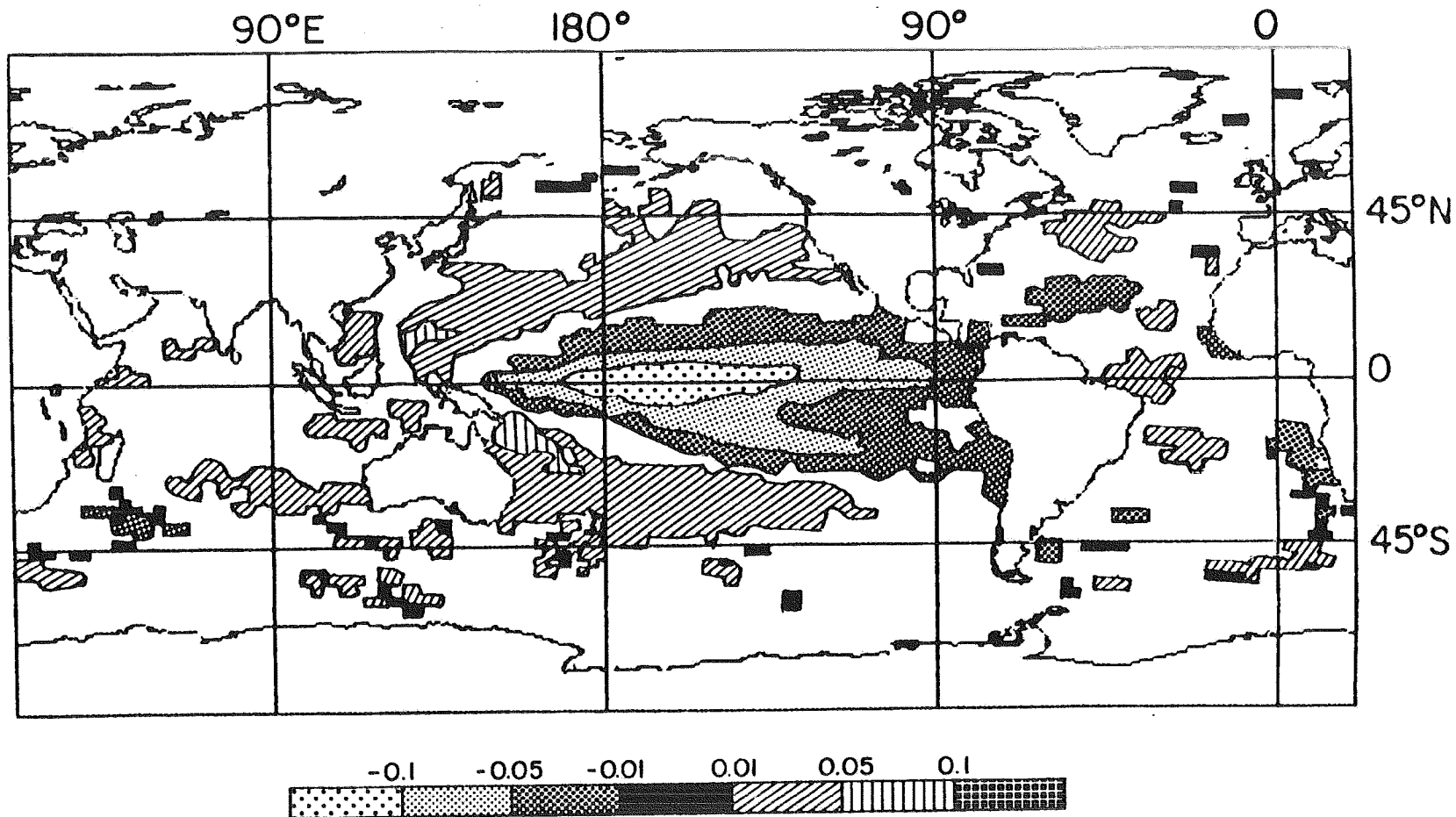


Figure 6.13: Mid PW-SOI LAD slope. Contour plot of the LAD slope from the analysis of middle level water vapor and the SOI. Only those grid points with P-values ≤ 0.05 are plotted. Units are the increase in cm precipitable water per hPa increase in the SOI. Based on data from July 1983 through June 1989.

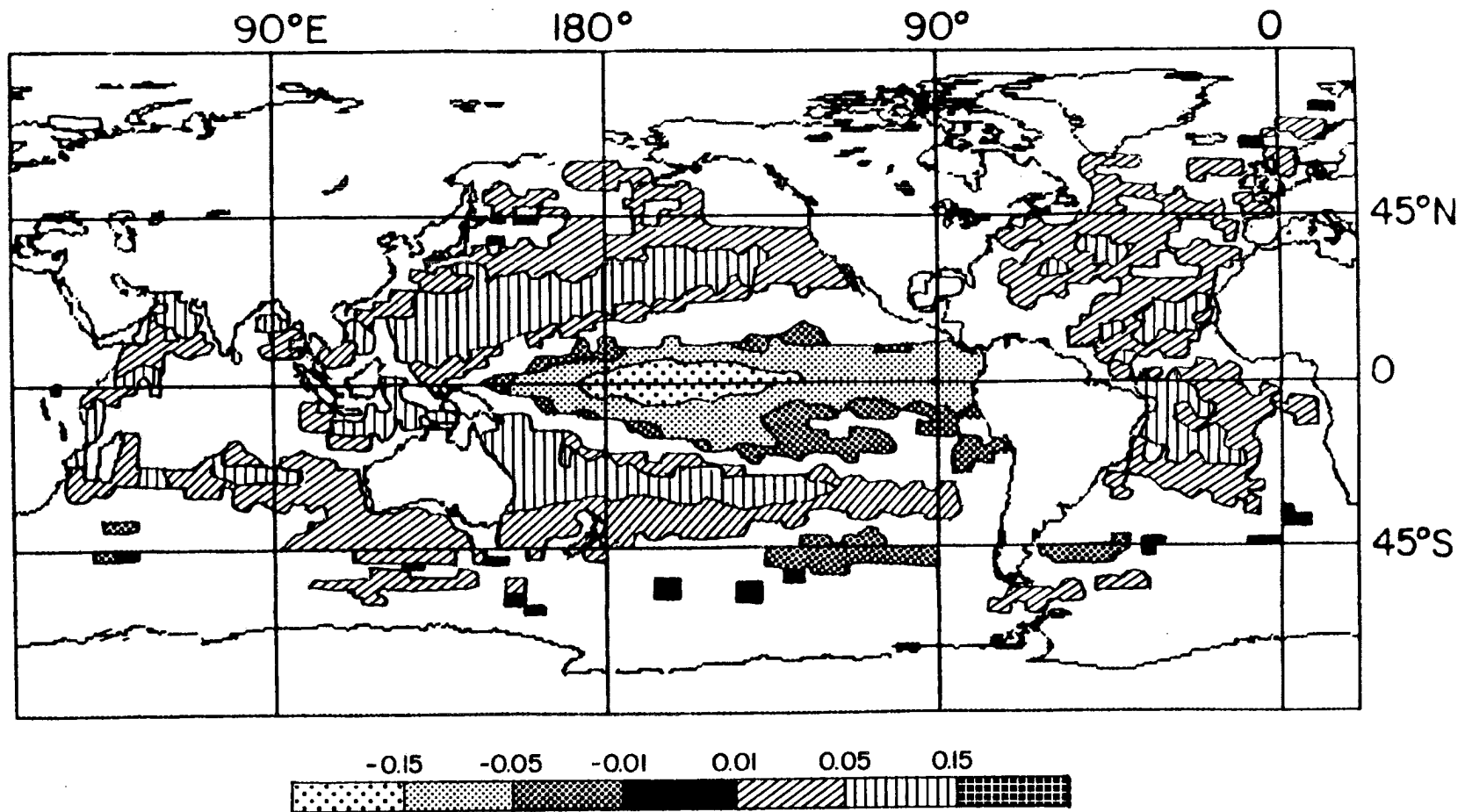


Figure 6.14: Low PW-SOI LAD slope. Contour plot of the LAD slope from the analysis of low water vapor and the SOI. Only those grid points with P-values ≤ 0.05 are plotted. Units are the increase in cm precipitable water per hPa increase in the SOI. Based on data from July 1983 through June 1989.

Table 6.2: Number of water vapor LAD analysis grid points with P-value ≤ 0.05 . Column 2 is for LAD analysis using the Southern Oscillation Index, column 3 uses underlying SSTAs (as done in Chapter 3), column 4 is the number of low P-value grid points that SOI and direct SSTA analysis have in common, column 5 is the number of these grid points that also have low P-values for the LAD analysis of the underlying SSTA with the SOI, column 6 is the percent of the grid points in column 4 that are in column 5. The last column is the percent of the grid points that are in common for the three data sets but where the sign of the LAD for the atmospheric variable–SOI is not the sign one would expect knowing the sign of the LAD analysis at that grid point with for water vapor–SSTA and the sign of the LAD analysis of local SSTA–SOI. There is a total of 4,591 possible grid points. Based on data from July 1983 through June 1989.

Water Vapor Para	SOI	Direct	In Common	IC + SST	Percent	Rev Val
Total PW	2193	3078	1689	1326	79%	10%
High PW	1723	2069	1137	894	79%	6%
Mid PW	1960	2710	1371	1110	81%	6%
Low PW	2605	3340	2072	1541	74%	16%

of the grid points that both SOI and direct SSTA analyses have low P-values, analysis of SSTA–SOI also have low P-values. As noted earlier, however, some of these grid points may, for example, show a cooling of the water with SOI yet an increase in water vapor with SOI at the same location despite direct analysis indicating negative SSTAs are associated with negative water vapor anomalies at that grid point. As indicated by the last column in Table 6.2, the number of grid points where the sign of the water vapor–SOI LAD regression analysis is the reverse of what would be expected based on SSTA–SOI LAD and water vapor–local SSTA LAD analysis is 6–16% of the grid points that have P-values less than or equal to 0.05 in all three data sets.

Examination of the low water vapor–SOI LAD regression grid points that had the opposite sign of what might be expected revealed that the majority of these grid points fell in three locations: in the tropical Indian Ocean along the east coast of Africa and in the subtropical North and South Atlantic Oceans. These locations all had positive low water vapor–local SSTA LAD slopes, SSTAs that decreased with increasing SOI (they were warmer during El Niño events), and positive low water vapor–SOI LAD slopes (decreased water vapor during El Niño events).

The location of the grid points that the two data sets (PW-SOI LAD analysis and PW-SSTA LAD analysis) do not both have low P-values are again in bands where the LAD value of one or the other data sets is changing sign. The points where SOI analysis has low P-values while direct SSTA analysis has high P-values are generally in small isolated groups. The same is not true for opposite case. Direct water vapor-SSTA analysis has low P-values in the large parts of the Indian ocean that the SOI analysis does not. In addition there are several other regions of good coverage. These include the negative water vapor-SSTA LAD analysis regions off the SW tip of South America and SE coast of Greenland, and a region south of New Zealand.

6.4.4 Basic Radiation Parameters-ENSO

Figures 6.15, 6.16, and 6.17 show how three basic radiation parameters, outgoing long wave radiation, reflected flux, and net radiation change in relation to the SOI. The general configuration is not particularly surprising after looking at the earlier figures of the relationship of SOI to clouds. Close analysis of the radiation figures reveals some interesting features. One of these features is in Figure 6.15 where there is a distinct region in the northern Pacific which has a relationship to outgoing longwave radiation. Yet, this area does not show up in Figure 6.16 of reflected solar radiation. This perhaps indicates that the changes in OLR there are associated with high, thin cirrus which wouldn't show up as well on reflected flux or occurred primarily at night or in wintertime when there is less incoming solar radiation for the change in clouds to reflect.

Once again, as Table 6.3 reveals, the majority of the grid points with strong relationships between radiation parameters and both direct SSTA and the SOI also have a strong SSTA-SOI relationship. Also, most of these grid points have the sign of the radiation parameter-SOI LAD slope the way it would be expected. However, this table also indicates that there are many grid points that are not in common.

Examination of where the data sets diverge reveals that the OLR-SOI analysis has a stronger relationship near the maritime continent than direct OLR-SSTA analysis has, while direct SSTA analysis has regions in the Pacific and Atlantic oceans north of 45° that SOI analysis does not. For reflected flux, direct SSTA analysis includes not only

Table 6.3: Number of radiation parameter LAD analysis grid points with P-value ≤ 0.05 . Column 2 is for LAD analysis using the Southern Oscillation Index, column 3 uses underlying SSTAs (as done in Chapter 4), column 4 is the number of low P-value grid points that SOI and direct analysis have in common, column 5 is the number of these grid points that also have low P-values for the LAD analysis of the underlying SSTA with the SOI, column 6 is the percent of the grid points in column 4 that are in column 5. The last column is the percent of the grid points that are in common for the three data sets but where the sign of the LAD for the radiation variable–SOI is not the sign one would expect knowing the sign of the LAD analysis at that grid point with radiation variable–local SSTA and the sign of the LAD analysis between local SSTA and the SOI. To make for more accurate comparisons, the grid points in column 2, labeled SOI, are only those grid points within the 60°N to 40°S domain that limits columns 3 and 4 due to the geographical extent of SST data set for this time period. There is a total of 1,040 possible grid points. Based on data from April 1979 through March 1985.

Radiation Para	SOI	Direct	In Common	IC + SST	Percent	Rev Val
Albedo	497	514	262	197	75%	5%
Reflected Flux	477	526	250	183	73%	7%
OLR	525	451	271	203	75%	9%
Net Flux	322	443	140	97	69%	14%

stratocumulus decks, but also regions in the Pacific and Atlantic north of 25-30° that do not have low P-values for SOI analysis. The reflected flux–SOI analysis in return, has better relationships near the maritime continent and scattered areas of the southern Pacific and Indian ocean.

Examination of Table 6.3 reveals that for regions with strong relationships (low P-values) for net flux, the two data sets (net–SSTA LAD and net–SOI LAD results) have less than 50% of their grid points in common. Also, 14% of the grid points they do have in common do not have the net radiation–SOI LAD slope the sign that would be expected. Therefore, when it comes to net flux, there are evidently different processes at work. The locations where these data sets are not in common are quite different. The direct net radiation–SSTA relationship is much stronger in the stratocumulus decks off the west coast of continents. These are regions with very little relationship between SSTA and OLR but a strong relationship between SSTA and reflected flux. The regions that SOI analysis indicates a strong relationship to net radiation but direct SSTA analysis does not are regions in the west-central north and central south Pacific where there are distinct

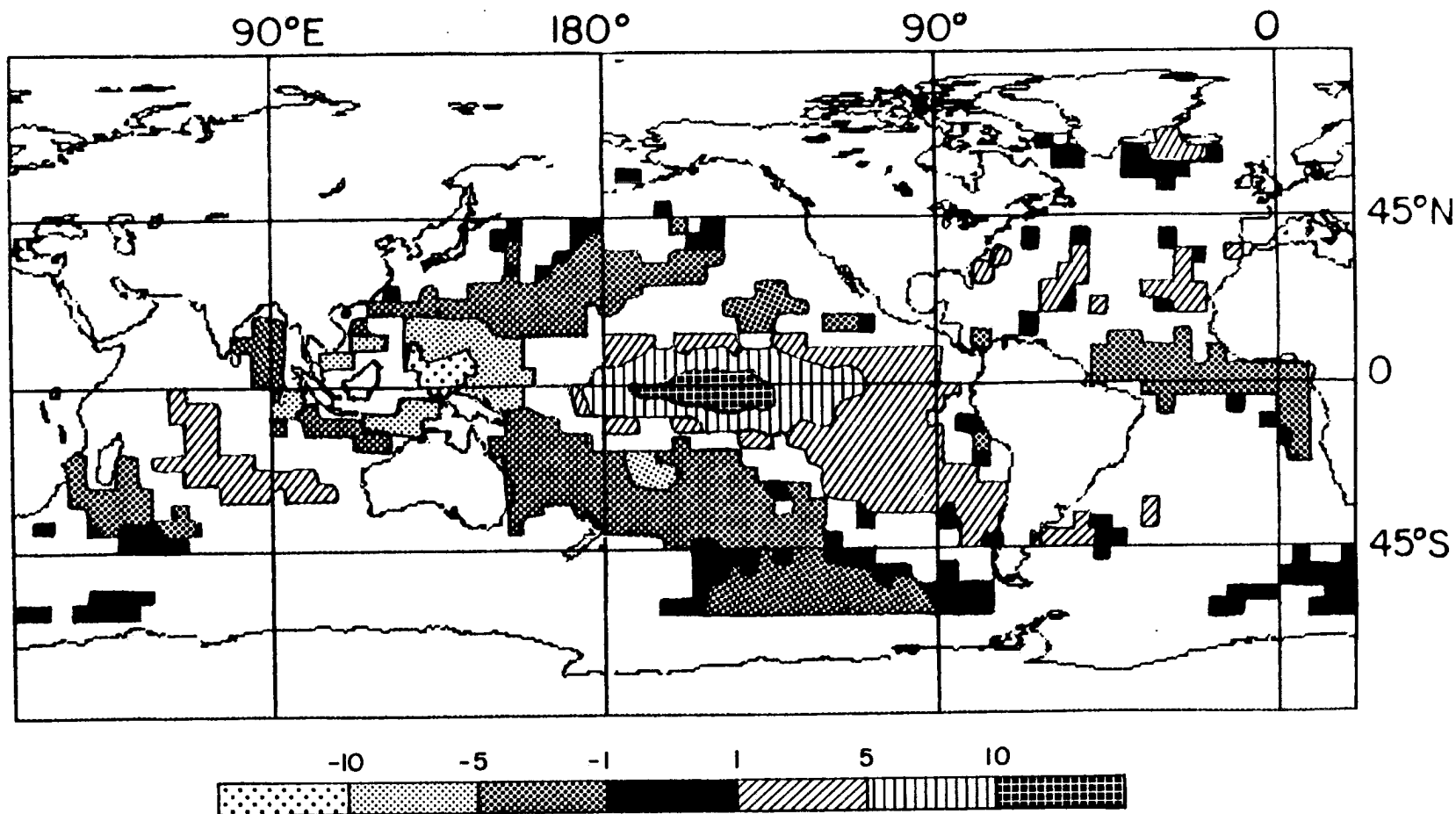


Figure 6.15: OLR-SOI LAD slope. Contour plot of the LAD slope from the analysis between OLR and the SOI. Only those grid points with P-values < 0.05 are plotted. Units are the increase OLR in $W \cdot m^{-2}$ per hPa increase in the SOI. Based on data from April 1979 through March 1985.

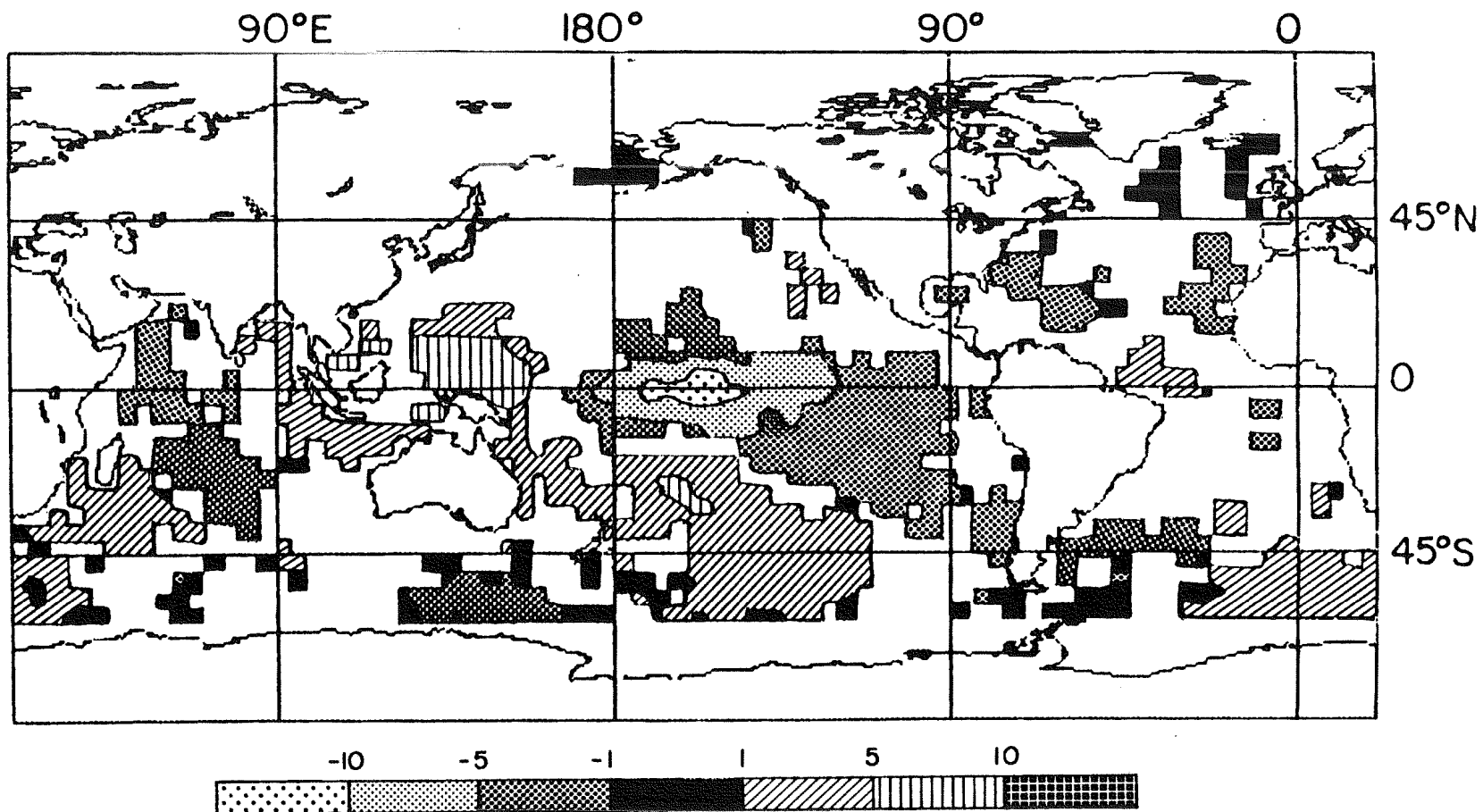


Figure 6.16: Reflected flux-SOI LAD slope. Contour plot of the LAD slope from the analysis between reflected flux and the SOI. Only those grid points with P-values ≤ 0.05 are plotted. Units are the increase reflected flux in $\text{W}\cdot\text{m}^{-2}$ per hPa increase in the SOI. Based on data from April 1979 through March 1985.

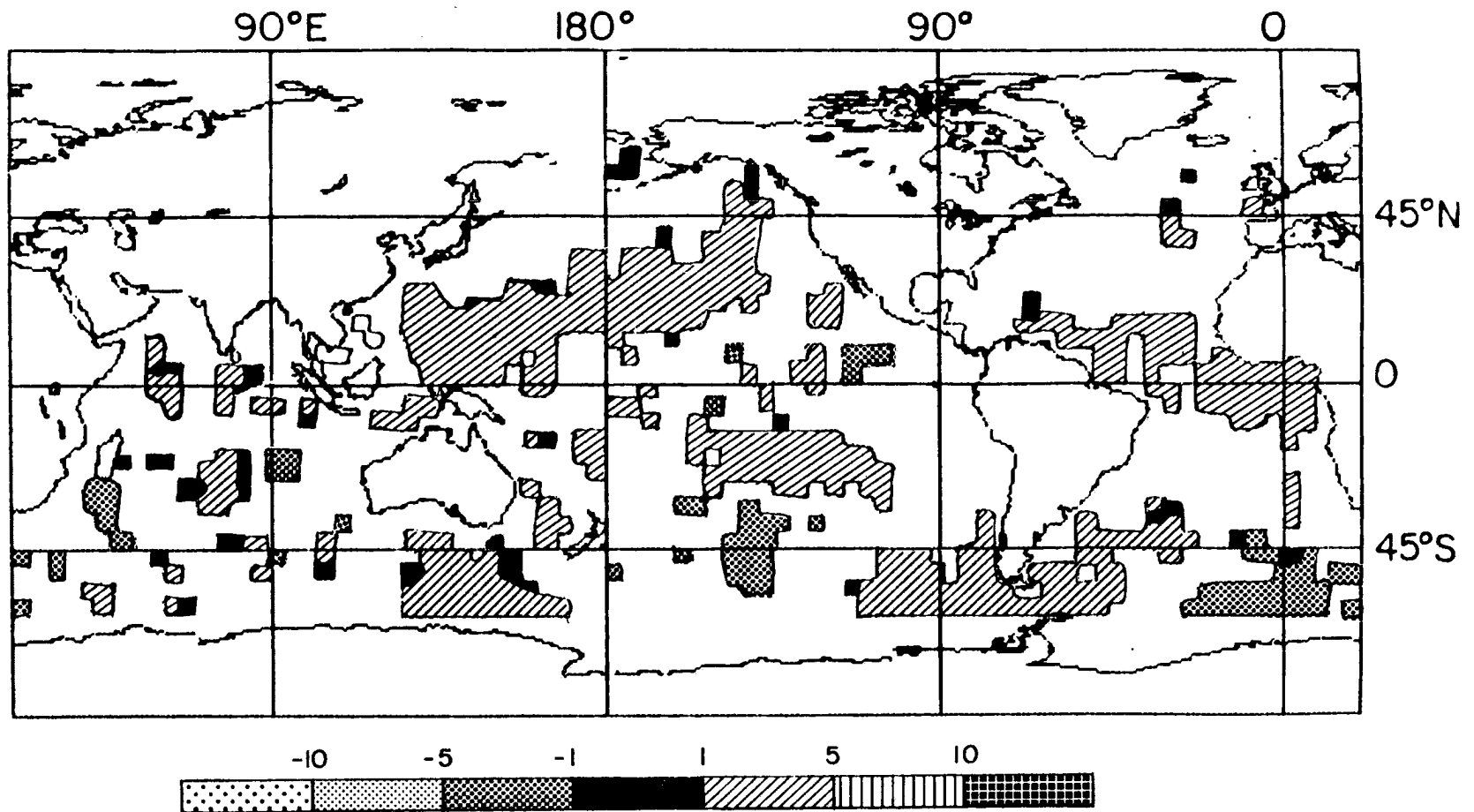


Figure 6.17: Net flux-SOI LAD slope. Contour plot of the LAD slope from the analysis between net flux and the SOI. Only those grid points with P-values ≤ 0.05 are plotted. Units are the increase net flux in $\text{W}\cdot\text{m}^{-2}$ per hPa increase in the SOI. Based on data from April 1979 through March 1985.

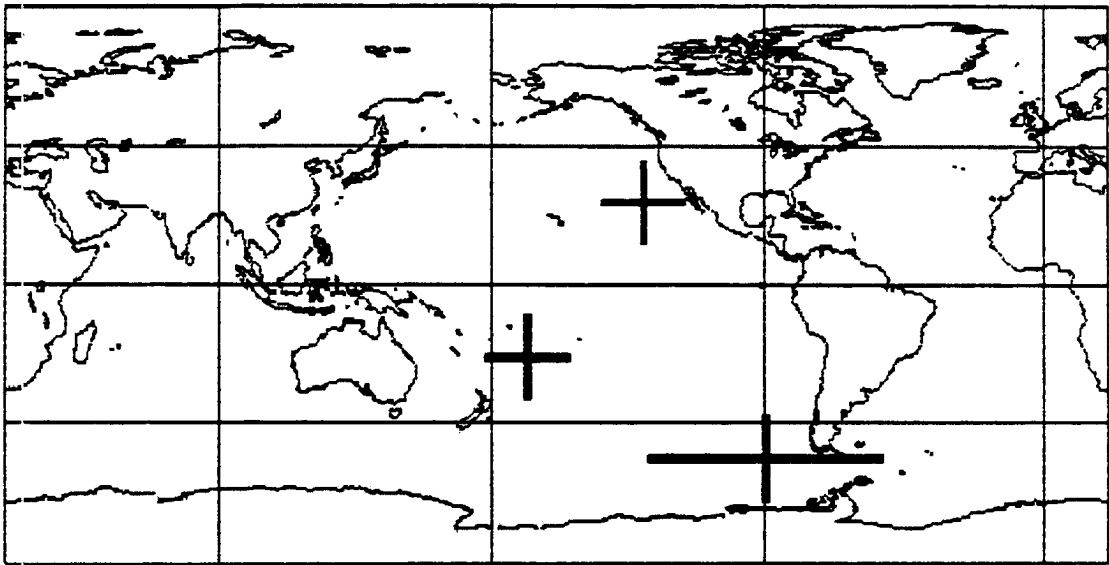


Figure 7.1: Case study regions.

changes in OLR. Furthermore, there are distinct differences in the location of the low P-value grid points between net flux–SOI analysis and net flux–eastern tropical Pacific SSTA analysis (see Figure C.18). Though, like the SOI analysis, the eastern tropical Pacific SSTA analysis does not have many low P-value grid points in stratocumulus decks and instead tends to be in regions with changes in high cloudiness.

6.5 Discussion

In the equatorial Pacific, changes in circulation and changes in SSTAs are so closely related that they are impossible to separate. In other parts of the world where relationship between changes in circulation and SSTAs are not as closely linked or as well understood, it can still be impossible to separate the role of altered circulation in changing clouds and clear sky water vapor versus the role of changes in local SSTAs in changing clouds and clear sky water vapor. For example, a decrease in clouds at some grid point may be associated with negative SSTA and with the El Niño while a decrease in local SSTA is also associated with the El Niño. Where the role of general circulation versus local SSTA can be clearly separated is at grid points where the signs of these three associations are not compatible.

The number of grid points with signs that are the reverse of expectations were most common for low water vapor and were grouped in 3 regions. The region in the tropical Indian Ocean along the African coast might be due to alteration of circulation advecting dry air off the African continent over warmer waters. The two regions in the subtropical North and South Atlantic Oceans may be due to changes in subsidence: an increase in subsidence would dry the air while a decrease would weaken the trade wind inversion allowing for deeper mixing of the moist air and greater potential for cloud formation.

Whatever the cause for these regions, it is clear that such regions are definitely in the minority of the low P-value grid points that both data sets share. Low P-value grid points which the two data sets do not have in common are places where the relative importance of local SSTA versus circulation effects can be determined easily. For cloud analysis this is ~50% of the grid points while for water vapor it is ~30% of the grid points. Therefore, for

the vast majority of the grid points with strong cloud or water vapor–SSTA relationships determined in Chapters 2 and 3, the role of altered circulation in causing this relationship is either not important or impossible to separate from local SSTA relationships.

Reflected flux and OLR changes are in keeping with the analysis for clouds: the majority of the low P-value grid points for direct SSTA relationships indicate that the cloud–SSTA relationship is either not affected much by changes in circulation or it is impossible to separate out the effect of changes in circulation. Net flux, however, is a special case.

Changes in net flux are often small changes resulting from large and somewhat balancing changes in OLR and reflected flux. For example, changes in the thickness of cirrus clouds can easily change the net flux. As one might expect, therefore, the largest differences between –SOI and –SSTA analyses occurred with net flux. Net flux–ENSO relationships were primarily located in regions with cirrus clouds while the prime regions for net flux–local SSTA relationships, as shown in Chapter 4, were associated with low clouds. Therefore, it would appear that for the most important parameter from an Earth radiation budget perspective, changes in net radiation, the relationship to local SSTAs determined earlier are largely unaffected by ENSO changes in circulation.

One other interesting feature uncovered by this research is the time scale of changes in high water vapor and high clouds compared to water vapor and clouds lower in atmosphere. As noted earlier, high clouds and high water vapor appeared to have better relationships to the eastern tropical Pacific SSTA than the SOI. Examination of Figures 6.1 and 6.2 reveals that one of the prime differences between the smoothed SOI and the eastern tropical Pacific SSTA is the broader, slower rise and fall of the SSTA compared to the SOI. The better relationship between high clouds and high water vapor with the slower changing Pacific SSTA could be an indication that the time scales for climatological changes in high clouds and high water vapor are longer than that for lower clouds and lower water vapor.

Chapter 7

CASE STUDY ANALYSES

7.1 Introduction

The preceding chapters have pointed out strong regionally varying relationships between SSTAs and clouds, water vapor, and their radiative effects by using climatological analysis of 72 months of data. However, there are some questions that such analysis cannot answer. This is where in-depth analysis of 3 specific regions comes in. The regions chosen were the negative cloud–SSTA LAD regression slope stratocumulus region off the west coast of North America, the positive cloud–SSTA LAD slope area associated with the South Pacific Convergence Zone (SPCZ), and the region with negative water vapor–SSTA LAD slope off the southwestern tip of South America.

Because of natural variations in the atmosphere, one must be careful when drawing climatological conclusions from analysis of data that is very limited in time. However, case study analysis can help answer several questions that we have been unable to answer in earlier analysis, partly because it can use data sets that are too short to use for multi-year analysis. The case study analysis presented here will focus on 4 specific questions:

1) What is the diurnal variability of the response determined in earlier chapters? For example, is the observed change in clouds with SSTAs primarily due to changes that occur at noon while there is very little change in clouds with SSTA for some other time of day?

2) Is the change in cloudiness a function of a decrease or increase in clouds over a large region, or simply a function of clouds within a region moving to that part which is most favored?

3) What are the changes in optical thickness of the clouds? For example, in a region where high clouds increase with increasing SSTAs, does the optical thickness of these clouds increase as well?

4) How reliable is the data? This question will particularly be focused on the negative low water vapor-SSTA LAD slope region in the SE Pacific Ocean.

7.2 Data

The cloud data set used for this analysis is ISCCP data. The ISCCP cloud data is available on a 3 hour basis compared to Nimbus-7's 12 hour intervals. This will provide much better temporal resolution. Furthermore, ISCCP's 2.5° by 2.5° grid also provides finer horizontal resolution than Nimbus-7's. Even the vertical resolution, 7 cloud layers, is finer than Nimbus-7's. In fact, ISCCP's cloud data set would have been used in this entire research project except that the currently available time span of ISCCP cloud data was too short.

The ISCCP cloud analysis procedure has been described very well by Rossow and Schiffer (1991):

“The ISCCP cloud analysis procedure has three principal parts: cloud detection, radiative model analysis, and statistical analysis (Rossow *et al.*, 1988). Cloud detection refers to the separation of the image pixels into cloudy and clear scenes. (Each image pixel is about 4-8 km in size, but the Stage B data have been sampled to a pixel spacing of about 30 km. Because of navigation uncertainties, the pixel location is not more precise than about 30 km and is variable within this range. Hence, in the cloud analysis, each image pixel is treated as representing a specific scene about 30 km across.) This process is performed by what is often referred to as a cloud algorithm; intercomparisons of several existing cloud algorithms were conducted to facilitate the design of a global analysis method (Rossow *et al.*, 1985). Each scene is then compared to calculations of a radiative transfer model that simulates the radiances that should be measured by the satellites as a function of surface visible reflectance and temperature (clear scenes) and cloud optical thickness and cloud top temperature (cloudy scenes). The effects on the radiances of the atmosphere are accounted for using the TOVS data for each location and time. All the results from each satellite are reduced to a spatial resolution of about 280 km by collecting statistics (mean, standard deviation and distributions) of the spatial variability of the

surface and clouds and by merging the results from all the satellites. These data are called the Stage C1 data, which report global results every three hours. Monthly averages of the C1 data are also produced, called C2 data.

“This cloud analysis is considered to be experimental, though state-of-the-art; hence, the strategy is to report more about the results than the ‘answer’. The cloud detection procedure is an inherently statistical decision process, in that all the attributes used to make the decision are obtained from the distribution of radiances over space and time. Therefore, the results are expected to be ‘correct’ only in a statistical sense, though the errors at any one place and time are estimated and reported in the data. In addition to uncertainties in detection, there are uncertainties in the interpretation of the radiances (see Rossow, 1989). The most important of these is the assumption that all image pixels containing cloud are completely covered by a single, homogeneous layer. We do not have a better scheme yet, but we have tried to preserve enough additional information to allow for later improvement of the results.

“The cloud detection step examines all the B3 radiance data for one month to collect statistics on the space/time variation of the VIS and IR radiances. The key assumptions used in the analysis are that the radiances in clear scenes are less variable than in cloudy scenes and that it is the clear scenes that compose the ‘darker’ and ‘warmer’ parts of the VIS and IR radiance distributions, respectively (cf., Rossow *et al.*, 1985; Rossow *et al.*, 1989; Sèze and Rossow 1990). Based on these statistics, estimates are made of the clear values of VIS and IR for each location and time. The maps of these values are referred to as the ‘clear sky composites’. This approach is novel in two respects. First, all the complicated tests are used to detect cloudiness directly, many of which were first proposed by other investigators (cf., Rossow *et al.*, 1989 for a review), are here used to eliminate clouds to find clear scenes. The advantages are that the tests can be stricter, because only an estimate of clear radiances is required not a decision in each image at each location, and that the results can be more directly validated by other measurements of the surface properties that dominate the clear radiances. Second, the use of time variations at one location to detect cloudiness is new (cf. Desbois and Sèze 1984; Rossow *et al.*, 1985; Gutman *et al.*, 1987; Sèze and Desbois 1987).

“After estimates of clear radiances are obtained for each place and time, the entire B3 radiance data set is examined again to compare each radiance value to its corresponding clear value. The differences are compared to the uncertainties in estimating the clear radiances: if the differences are larger than the uncertainty and in the ‘cloudy direction’ at either wavelength (colder IR or brighter VIS), then the pixel is labeled cloudy. In fact, each pixel is labeled to indicate the position of its radiance values relative to the clear values. The radiance plane is divided by intervals that represent the magnitude of the uncertainty in the clear radiances; the lower and upper ranges extend all the way to the minimum and maximum possible values.

“Since the precise value of the threshold (magnitude of clear radiance uncertainty) is also uncertain, one estimate of the error in the identification is given by counting the frequency of radiance values that are ‘close’ to the dividing line between the clear and cloudy categories. These pixels are defined by threshold flag values of 4 in both channels. We refer to these pixels as ‘marginally cloudy’, since they are just barely detected. This category includes very thin cirrus clouds and very low-level broken cloudiness (more low-level cloudiness is included in this category at night when only IR data are available). We believe that these ‘marginal clouds’ are actually clouds, since we set the thresholds to the uncertainty in the clear radiances; i.e., this approach avoids spurious detections of clouds, but misses some clouds. However, the interpretation of these clouds is uncertain, because partial coverage of the radiometer field-of-view can lead to intermediate radiance values that are arbitrarily close to the clear radiance values. Hence, the frequency of these ‘marginal clouds’ may also be used to correct for resolution-dependent effects on the cloud amount” (Rossow and Schiffer, 1991).

Comparison of ISCCP cloud amounts with the Nimbus-7 THIR/TOMS cloud analysis used for the climatological part of this research indicates that ISCCP global cloud amount is about 10% higher than that of Nimbus-7 while comparison to surface observations indicates that ISCCP cloud amounts are a “few percent” lower than surface observations (Rossow and Schiffer, 1991).

To maintain approximately equal statistical significance, the original ISCCP grid is an equal-area grid with each grid box encompassing 2.5 degrees of latitude (cf., Rossow

and Garder 1984). Prior to use in the case study analysis, this grid was interpolated in the x direction into a $2.5^\circ \times 2.5^\circ$ equal angle grid.

The ISCCP cloud data is in 7 different layers: from 1000-800, 800-680, 680-560, 560-440, 440-310, 310-180, and 180-0.5 hPa. To be able to present this data easier, we combined these 7 levels into 3: low (1000-680), middle (680-440), and high (440-0.5 hPa). These levels do not correspond directly to the Nimbus-7 cloud levels or to the high, middle and low ISCCP-TOVS water vapor levels. The Nimbus-7 cloud levels were from the surface to 2 km (~ 800 hPa) for low clouds and above 7 km (~ 410 hPa) for high clouds. The decision to include the two lowest ISCCP cloud levels as low clouds was based on evidence that stratocumulus, traditionally considered low clouds, were sometimes classified as middle clouds by the Nimbus-7 classification scheme. High clouds in this classification can have cloud tops slightly lower than the Nimbus-7 high cloud classification.

The water vapor data set used for case study analysis is the same ISCCP TOVS water vapor data set used in Chapter 3. The SST data is again the monthly mean Climate Analysis Center's blended *in situ* and remotely sensed SST data that was used in earlier research. In addition, results of some earlier research will be used in the case study analysis.

Another ISCCP data set used in the case study analysis is cloud optical thickness. Clearly cloud optical thickness can be an important parameter: even with no change in height or percentage of clouds, a change in cloud optical thickness can have major radiative impacts. ISCCP data includes cloud optical depth which is calculated from a visible radiance corrected for sun-earth distance and ozone absorption, the viewing/illumination geometry, a surface reflectance (from the retrieval using the visible radiance value from the clear sky composite) and the cloud top pressure (Rossow *et al.*, 1988b). ISCCP provides a matrix of 7 layers of clouds each with 5 categories of optical thickness: 0.02-1.27, 1.27-3.55, 3.55-9.38, 9.38-22.63, and 22.63-119.59. Use of this data directly allows analysis of the effect of changes in SSTA on one cloud layer's optical thickness distribution without the complicating factors of changes in the mix of clouds, therefore averages and anomalies of this highly variable parameter were not used.

7.3 Methods

Two months were selected for detailed comparative analysis at each of the 3 case study locations. To be used, the months needed to: 1) be included in the Nimbus-7 cloud data set times as well as the ISCCP TOVS times, 2) be the same month of the year, 3) have fairly similar Southern Oscillation Index values, and 4) have different SSTAs in the case study regions. Based on this criteria, March 1984 and March 1985 were selected.

The center location point for each analysis area was chosen based on examination of results of seasonal and full data set LAD analysis of cloud-SSTA and, in the case of the SE Pacific region, water vapor-SSTA relationships. The latitudes and longitudes of the center point of the three analysis regions are 26.25°N, 131.25°W for region 1; 23.75°S, 168.75°W for region 2; and 56.25°S, 91.25°W for region 3. The analysis focuses on both a north/south and an east/west cross section through the regions. The regions analyzed in this manner are shown in Figure 7.1. Note that in the SE Pacific, for the latitudinal cross section to extend outside of the region of strong negative water vapor-SSTA LAD slopes, a greater number of grid boxes were needed.

Because the prime data sets used in this analysis are on the ISCCP grid, the results from the Nimbus-7 LAD analyses were interpolated to the finer resolution ISCCP grid for use in the case study analysis.

7.4 Results

One of the criteria used in selecting March 1984 and March 1985 for this analysis was that the SOI was not too different. For March 1984, the smoothed SOI (see Chapter 6 for reasons and effects of smoothing the Southern Oscillation Index) was 0.00 while for March 1985 it was 0.38 hPa. Compared to a minimum of -3.64 (during the strong El Niño of '82-83) and a maximum of 1.68 over the time period of the cloud and water vapor data sets, these two months were fairly close.

In preparing data for these case study analyses, we acquired many relevant data files. For example, we have 7 levels of clouds, as well as combined high, middle, low, and total clouds, at 8 different times during the day, for two different months with means and

differences. The eventual total was ~ 350 different data sets available to be used. Clearly this many data sets are impossible and unnecessary to present for both cross sections at each of the 3 case study regions. Therefore, only the data that are most relevant to each analysis will be presented.

7.4.1 Region 1: California Stratocumulus Deck

Case study region one is centered at 26.25°N and 131.25°W in the Pacific Ocean southwest of California. Figure 7.2 shows the average conditions for clouds, water vapor, and SST for the two months of the case study, March 1984 and March 1985. SST decreases to the north and to the east towards the coast of North America. In the east/west cross section, clear sky water vapor increases very slightly towards the east while it increases dramatically at all levels towards the south. This is a region of considerable cloudiness with total cloudiness averaging $\sim 75\%$. Primarily these are low clouds. However, not all clouds are low: there are small but significant amounts of middle and high clouds with high clouds more common in the southern part of the area.

As the scatter of data points around the LAD slope shown in Figure 2.2 indicate, it is quite possible for an individual month not to behave as the LAD slope would predict. With that caveat aside, Figure 7.3 indicates the prediction of how clouds and clear sky water vapor should behave over the region with an increase in SSTA according to the LAD analyses presented in Chapters 2 and 3. In addition to plots of the LAD slope, plots of the probability are also included. Generally, the lower the probability, the greater the likelihood that the data will behave as predicted with a simple 0.05 (5%) cut off P-value often used in this research to indicate the reliable LAD slope relationships. The predicted change in high clouds with increases in SSTA are very small and high clouds also have very high P-values indicating that we should put little faith in the LAD slope values for the high clouds-SSTA relationship. The LAD slopes for middle, low, and total clouds are all negative throughout the region, indicating that we should expect a decrease in cloudiness in association with an increase in SSTA. However, as indicated by the P-values for these relationships, the relationships are very strong in only part of the region: for low clouds it is strong in the northern and western part of the region, for middle clouds the

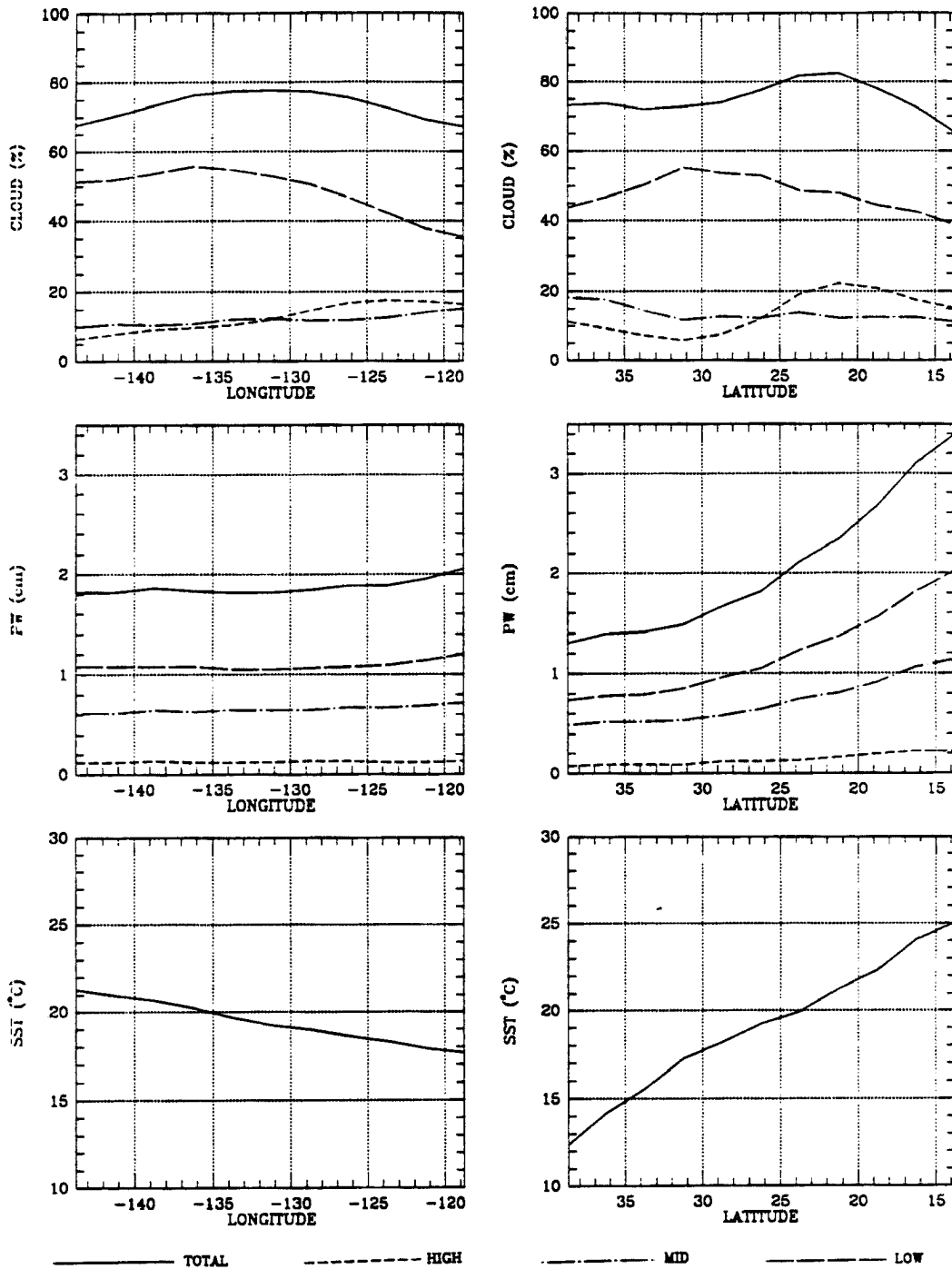


Figure 7.2: Average conditions of clouds, precipitable water, and SST for March 1984 and March 1985 at case study region one.

western half of the region, and for total clouds it is the western two thirds of the region for the east/west cross section and the center part for the north/south cross section. For precipitable water, the probabilities indicate that relationships are poor for the center part of the region while it is stronger in the western and southern part where there are increases in clear sky water vapor associated with increases in SSTAs.

To look at the differences between March 1984 and March 1985, the monthly averages of ISCCP clouds, ISCCP TOVS precipitable water vapor, and SST for March 1985 were subtracted from the values for March 1984 at each grid point. The results are shown in Figure 7.4. Readily apparent from this figure is a large positive SSTA for most of this region. Clear sky water vapor anomalies show distinct trends across the domain, but were not predicted to be linked very directly with SSTAs. As predicted for total cloudiness, cloudiness decreases over the whole region. However, the relationship is more complex when one looks at cloudiness at various levels.

While the average high cloudiness in this region, shown in Figure 7.2 indicates a low percentage of high clouds, there is considerable change in high clouds from one month to the other. Looking at the two plots of cloud anomalies in Figure 7.4, it is clear that low cloud anomalies and high cloud anomalies have a very strong out of phase relationship. This is most likely because high clouds obscure the satellite's view of low clouds. Since the high cloud-SSTA P-values indicate that the relationship between high cloud anomalies and SSTAs is likely to be random and the strong out of phase relationship between high cloud anomalies and low cloud anomalies, it is inappropriate to draw any strong conclusions between low clouds and SSTA from the data from these two particular months. However, rather than casting a doubt on the low cloud-SSTA LAD slope's ability to predict the low cloud anomalies' response to SSTAs, this data would indicate that the relationship is actually stronger than predicted. The high cloud-SSTA LAD was small and the P-value high, hence the effect of high cloud obscuration of low clouds would input noise into the low cloud data. The fact that the statistical techniques could pull out a strong signal despite this added noise, indicates that most likely the signal is even stronger than stated.

One of the questions case study research was to address was: If the cloud-SSTA LAD analysis indicated a strong positive or negative cloud-SSTA relationship, how is this

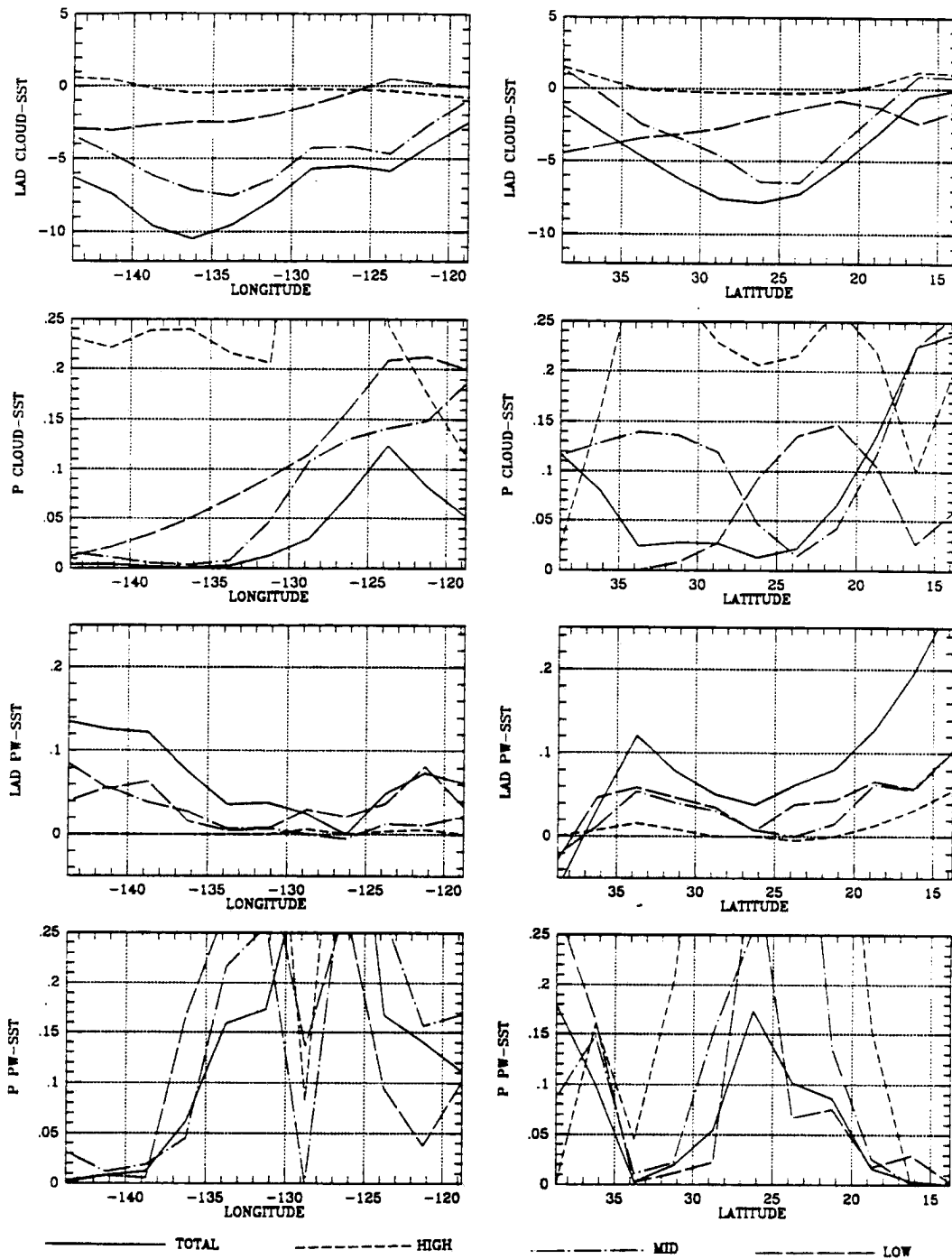


Figure 7.3: LAD slope and the Probability that the a distribution of data points around the LAD slope more extreme than the observed could be caused by random chance for the cloud-SSTA and PW-SSTA relationships at case study region one.

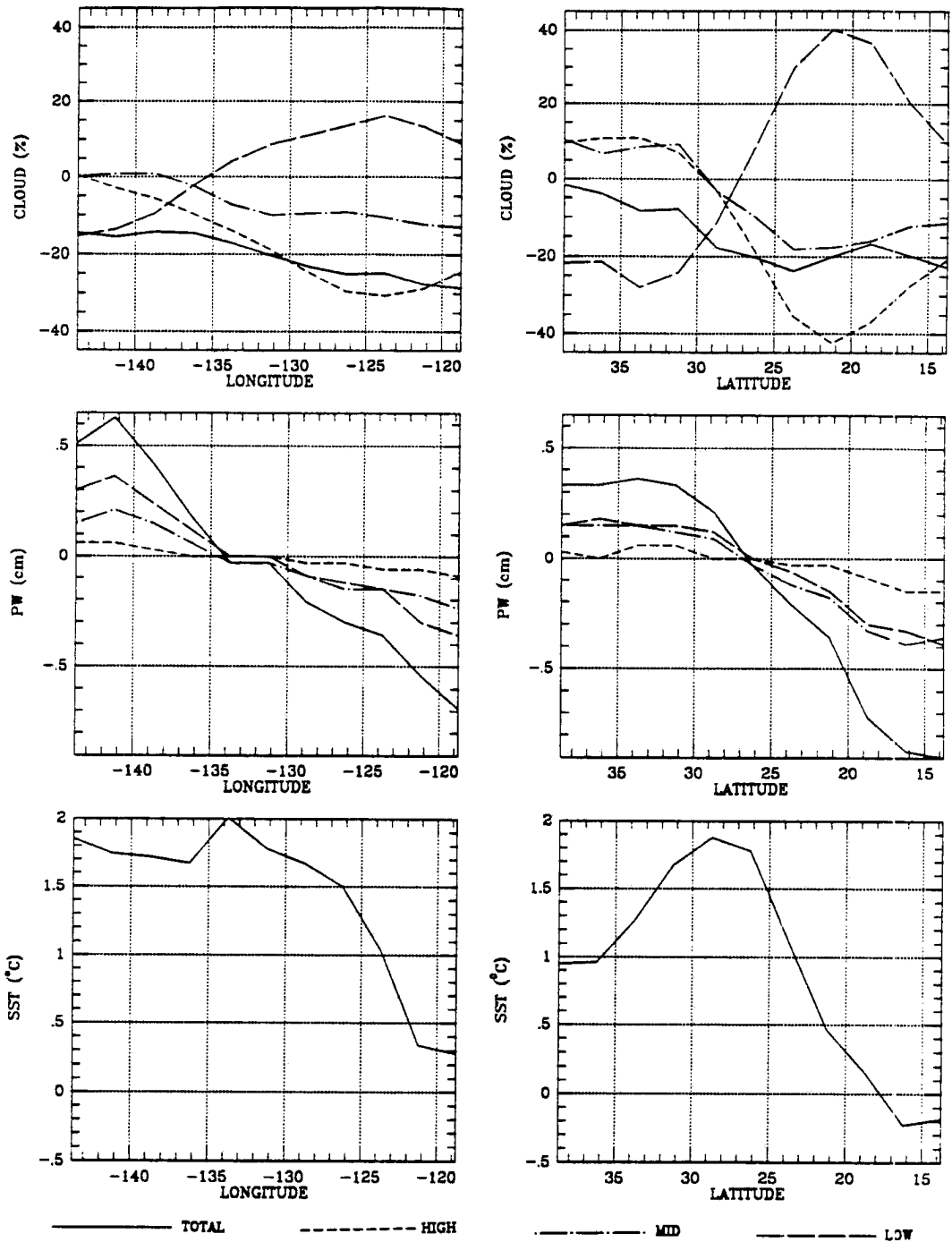


Figure 7.4: The difference in observed clouds, clear sky precipitable water, and SST between March 1984 and March 1985 (March 1984 minus March 1985) at case study region one.

relationship distributed during the day? Of prime concern in region one is the change in low clouds. Since, as noted earlier, the change in low clouds for these two months over much of this region seem to be directly related to the change in high clouds, it is important to look at a part of this region where the influence of changes in high clouds do not impact the changes in low clouds very much. This occurs in the far western part of the E/W cross section. This is a region of negative low clouds–SSTA LAD slope with low P-values. High clouds decrease (March 84 minus March 85) slightly in this area yet low clouds decrease even more. Therefore, to look at the diurnal variation in this decrease in low clouds, an average of the 3 westernmost grid boxes was used. These three grid boxes are centered at 26.25°N and 141.25°W.

The change in low clouds as a function of time of day is shown in the bottom of Figure 7.5. There is a clear and strong diurnal variation to this change: the magnitude of the decrease in low clouds is smaller during the day than at night. The top graph in Figure 7.5 shows the average low clouds as a function of time of day for the same location. This too undergoes a diurnal variation, with less low clouds present in the afternoon, but the magnitude of the change in average low clouds, 6.4%, is less than the diurnal variation in the change in low clouds, 12.6%.

These same three grid points were used in the analysis of the change in optical thickness. Again, since low clouds are of prime concern in this case study region, the optical thickness analysis involved the lowest of ISCCP's 7 cloud layers, the 800-1000 hPa layer. Since the amount of low clouds varies between March 1984 and March 1985 at these grid points, the values plotted in Figure 7.6 are normalized for that month. As illustrated in Figure 7.4, March 1985 had lower SST and more low clouds at these grid points. In Figure 7.6, it is clear that at these grid points, March 1985's 800-1000 hPa clouds tended to have lower optical thicknesses than March 1984's.

7.4.2 Region 2: South Pacific Convergence Zone

The center point of this region was chosen based on LAD slope values of seasonal and full data set analyses of clouds–SSTA, not based on an objective analysis of where the SPCZ (South Pacific Convergence Zone) is located in March. The center point is located

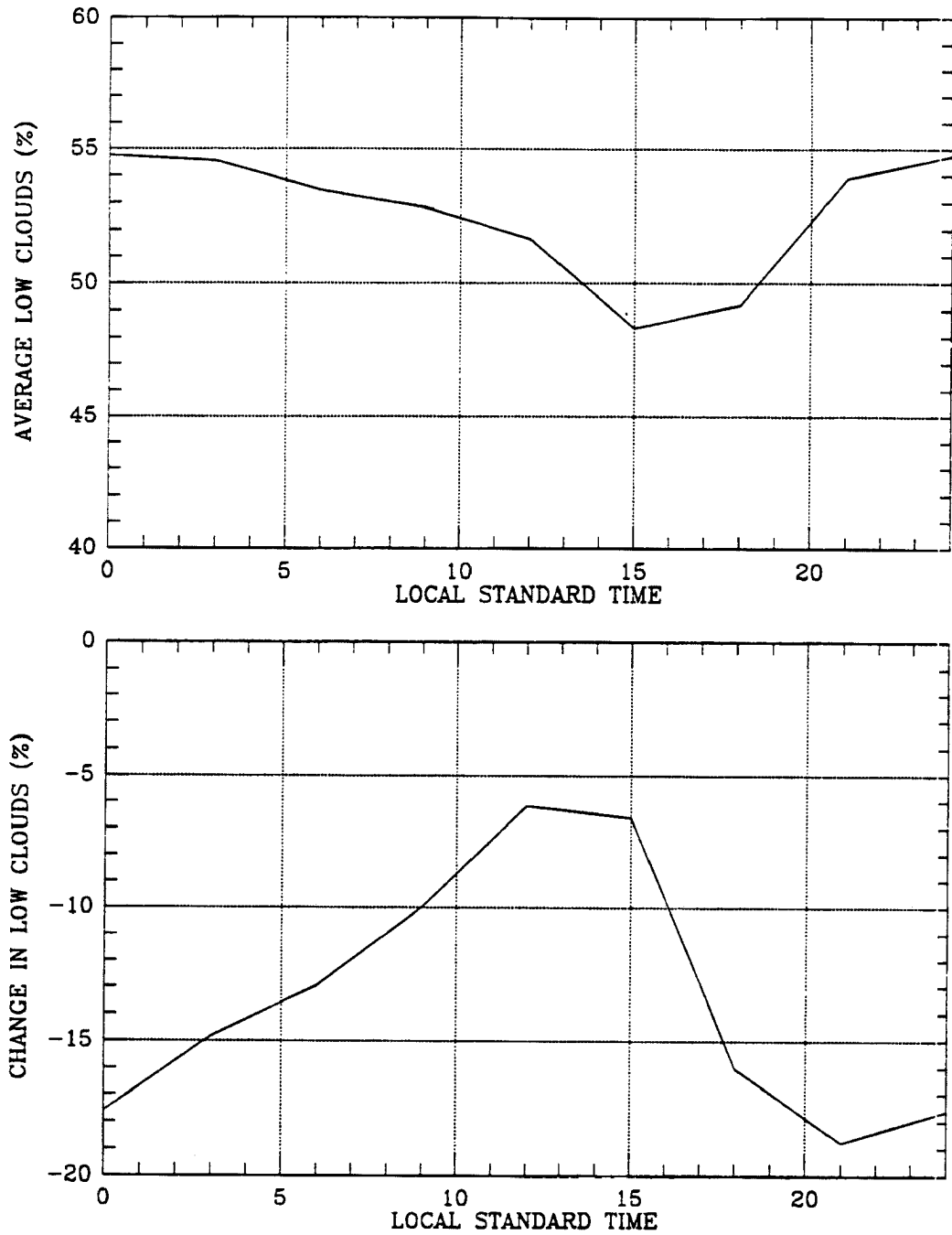


Figure 7.5: The average low clouds for March 1984 and March 1985 (top) and the difference in observed low clouds between March 1984 and March 1985 (March 1984 minus March 1985) as a function time of day for the three westernmost grid boxes in case study region one which are centered at 26.25°N and 141.25°W .

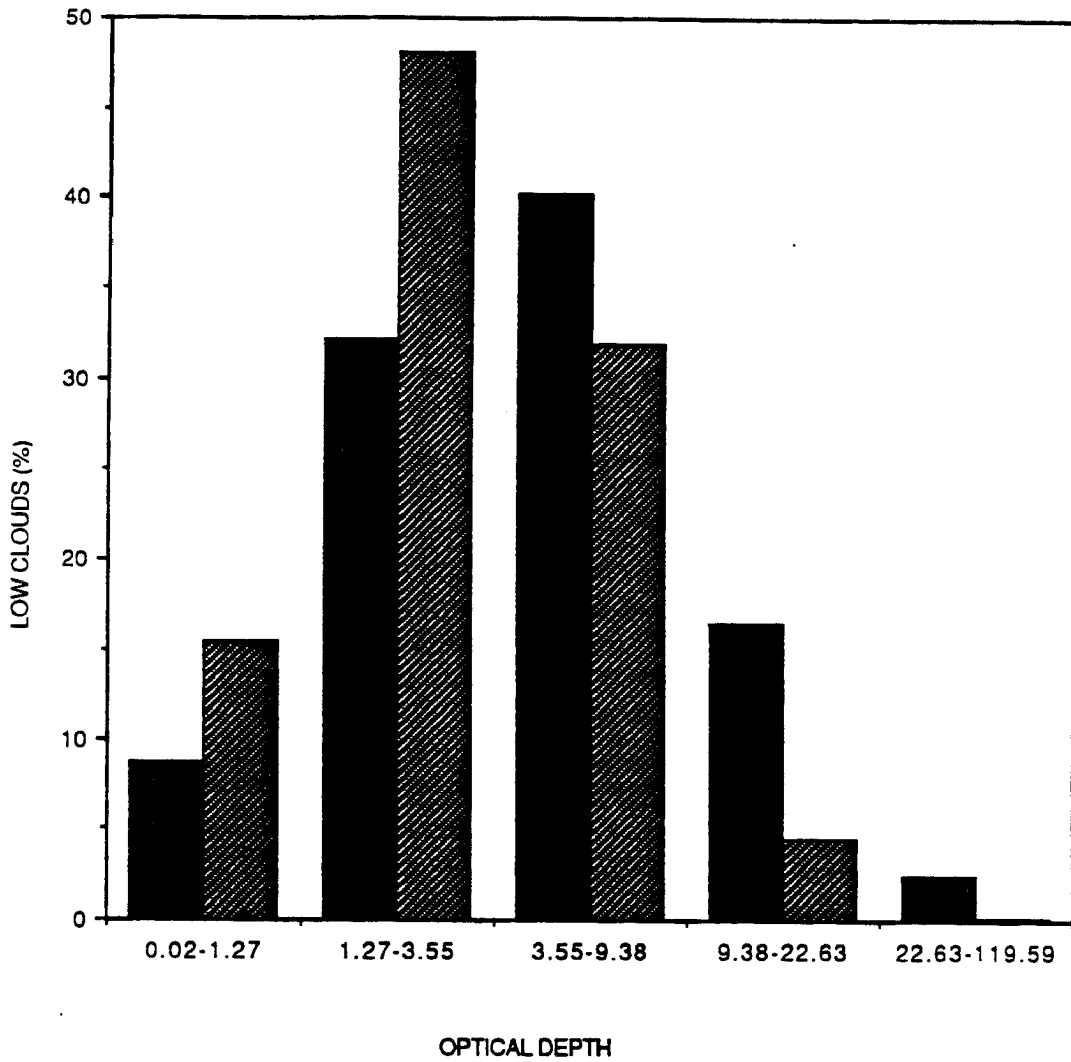


Figure 7.6: Normalized percent of 800-1000 hPa clouds falling in ISCCP's 5 optical thickness categories for March 1984 (solid) and March 1985 (striped) for the average of three E/W cross section grid points centered at 26.25°N and 141.25°W in case study region one.

at 33.75°S and 168.75°W in a region of strong positive total cloud–SSTA LAD slopes. As stated in Chapter 2, the LAD analysis revealed a NW/SE oriented band of strongly positive total cloud–SSTA LAD slopes that appeared to correspond to the SPCZ. The center point is near the location of the highest value of the total cloud–SSTA LAD slopes. Since this band was oriented along a NW/SE axis, both the east/west and north/south cross sections would pass out of the band.

The average conditions for the two months of this case study are shown in Figure 7.7. The SST is warm, $\sim 27^{\circ}\text{C}$ at the center point and throughout the entire east/west oriented cross section. The north/south cross section indicates a marked decrease in SST as one moves south. Clear sky water vapor stays very constant at all levels in the E/W direction, while water vapor at all levels decrease towards the south. In the E/W direction, the percent of cloudiness stays fairly uniform at $\sim 65\%$ total cloudiness. In the N/S direction, the center of the research area has a lower percent of total clouds than either the northern or southern end of the cross section. The mix of different level clouds varies somewhat, with the center of the region having $\sim 30\%$ low clouds, $\sim 25\%$ high clouds, and $\sim 10\%$ middle clouds. Towards the southern end of the research area the percentage of low clouds increases, while towards the northern end high and middle cloud percentages increase.

Examination of the 4 graphs of probability in Figure 7.8 reveals very low probabilities for the center of the research area for both cloud–SSTA and water vapor–SSTA LAD analyses. In the center area, the LAD slope would predict that water vapor anomalies would increase at all levels in association with increases in SSTA. For clouds, the LAD slopes indicate that for the center of the region total clouds would increase $\sim 8\%$ with a 1°C increase in SSTA. Most of this increase is due to increases in high cloudiness. Middle clouds have a slight increase while low clouds decrease in association with increases in SSTA. This latter effect may be because the strong changes in high clouds altering the satellite's ability to view low clouds.

Examination of Figure 7.9 indicates that March 1984 SST minus March 1985 SST was positive in the west and negative in the east, while the N/S cross section had negative values in the center of the region with positive values at both the northern and southern

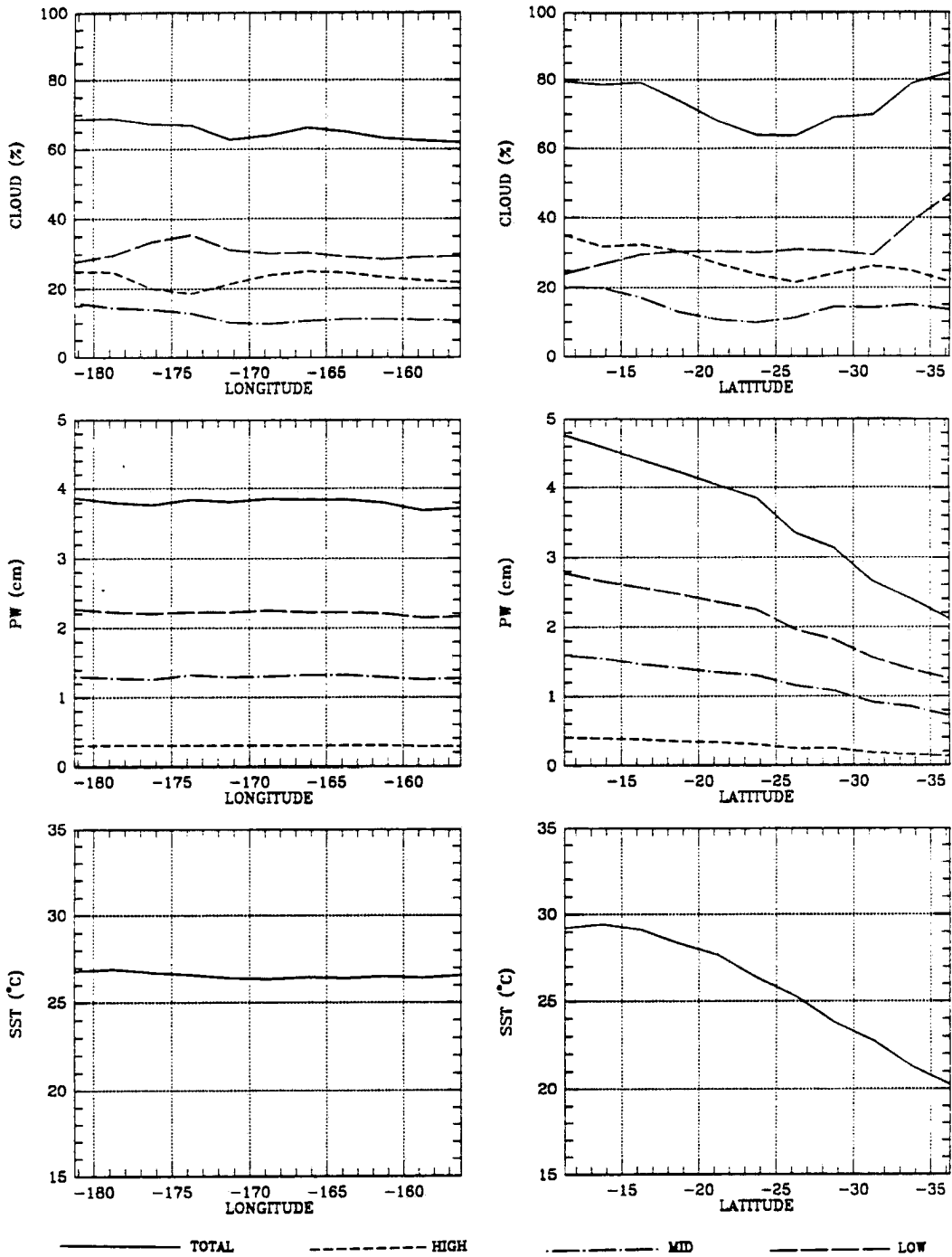


Figure 7.7: Average conditions of clouds, precipitable water, and SST for March 1984 and March 1985 at case study region two.

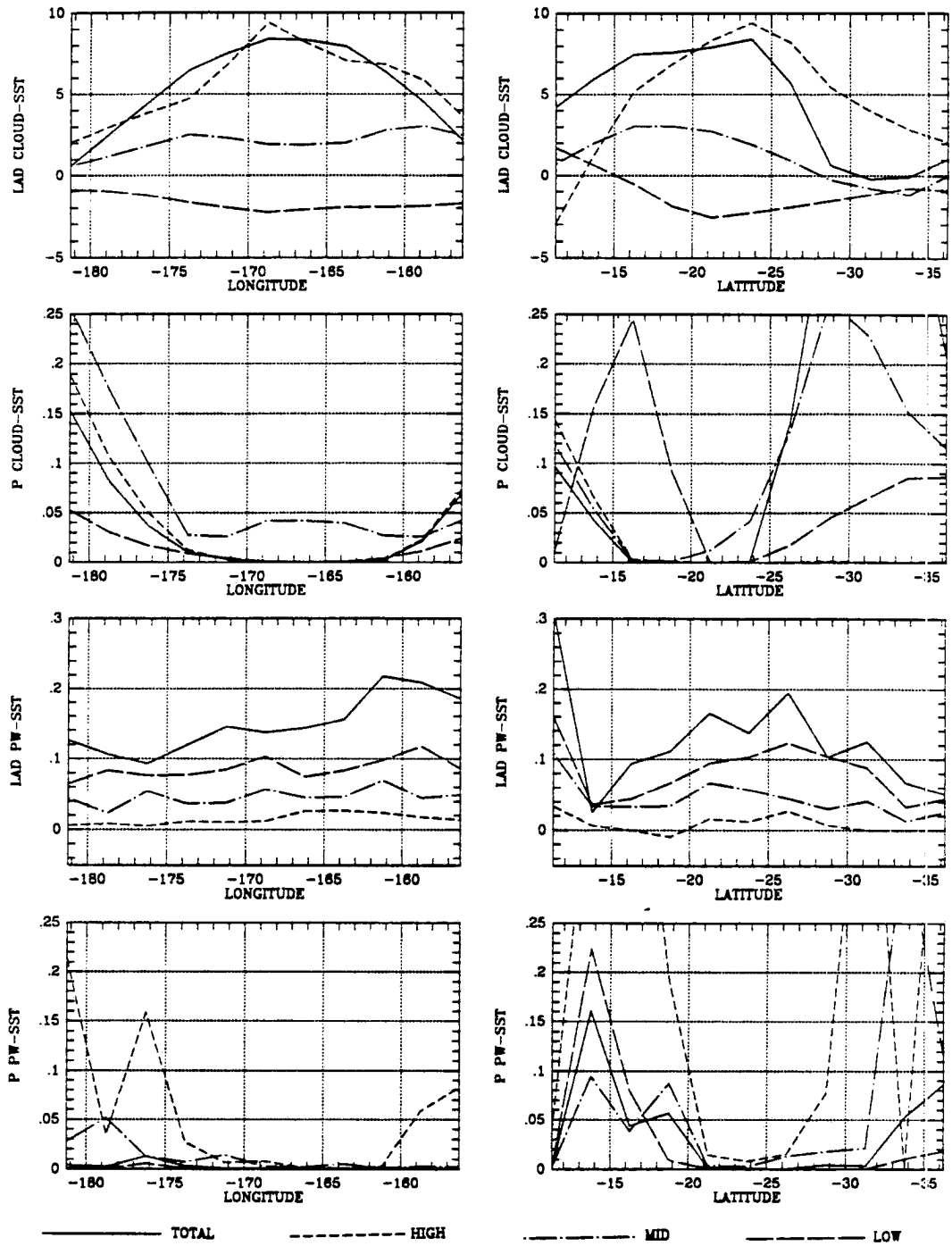


Figure 7.8: LAD slope and the Probability that the a distribution of data points around the LAD slope more extreme than the observed could be caused by random chance for the cloud-SSTA and PW-SSTA relationships at case study region two.

ends. The center of the region, 170° to 165°W, 20° to 25°S, had SSTAs in the range of -0.2 to -0.7°C . This same region also had negative clear sky water vapor anomalies as predicted by the LAD analysis. However, the magnitude of the water vapor anomalies were greater than predicted by the LAD analysis. For example, this area's total water vapor-SSTA LAD slope was $\sim 0.15 \text{ cm K}^{-1}$, therefore, for a SSTA of -0.5° , the expected water vapor anomaly would be $\sim -0.075 \text{ cm}$ while the observed total water vapor anomaly exceeded -0.2 cm . Total clouds and high clouds had negative anomalies in the center of the region, which again were expected based on the LAD regression analysis. Though again the magnitude of these cloud anomalies exceed what might have been predicted based on the cloud-SSTA LAD analysis. In the center part of the region, the low cloud anomaly generally was positive, though fairly small in value. And indeed the LAD slope for low clouds was much lower in magnitude than high clouds and of the opposite sign.

One of the questions that this section was to address was: Is the change in cloudiness a function of a decrease (increase) in clouds over a large region, or simply a function of clouds with in a region moving to that part which is most favored? For example, did high clouds simply move over 5 or 10 degrees of longitude to a region more favorable to formation of clouds, e.g., with a higher SSTA? The answer based on these two months of data appears to be no. In the E/W cross section, the high cloud-SSTA LAD was strongly positive and the P-value was small for region from 175° to 160°W. The average SSTA for this region was decidedly negative, though the value ranged from $+0.2$ to -1.5°C . If the positive high cloud-SSTA LAD slope was a response to deep clouds moving 15° to a region with higher SSTAs, one would expect negative high cloud anomalies at 160°W with compensating strongly positive high cloud anomalies at 170-175°W where the SSTA is near 0. What one observes, though, is negative high cloud anomalies in the range of 15-25% over the entire region. Though the lower negative anomalies are over the region of lower negative SSTAs.

To look at the diurnal variation in the change in clouds, data from 5 grid points in the E/W cross section between 171°W and 161°W were used. These 5 grid points all had positive high clouds-SSTA LAD slopes, low P-values (averaging 0.0012), moderate

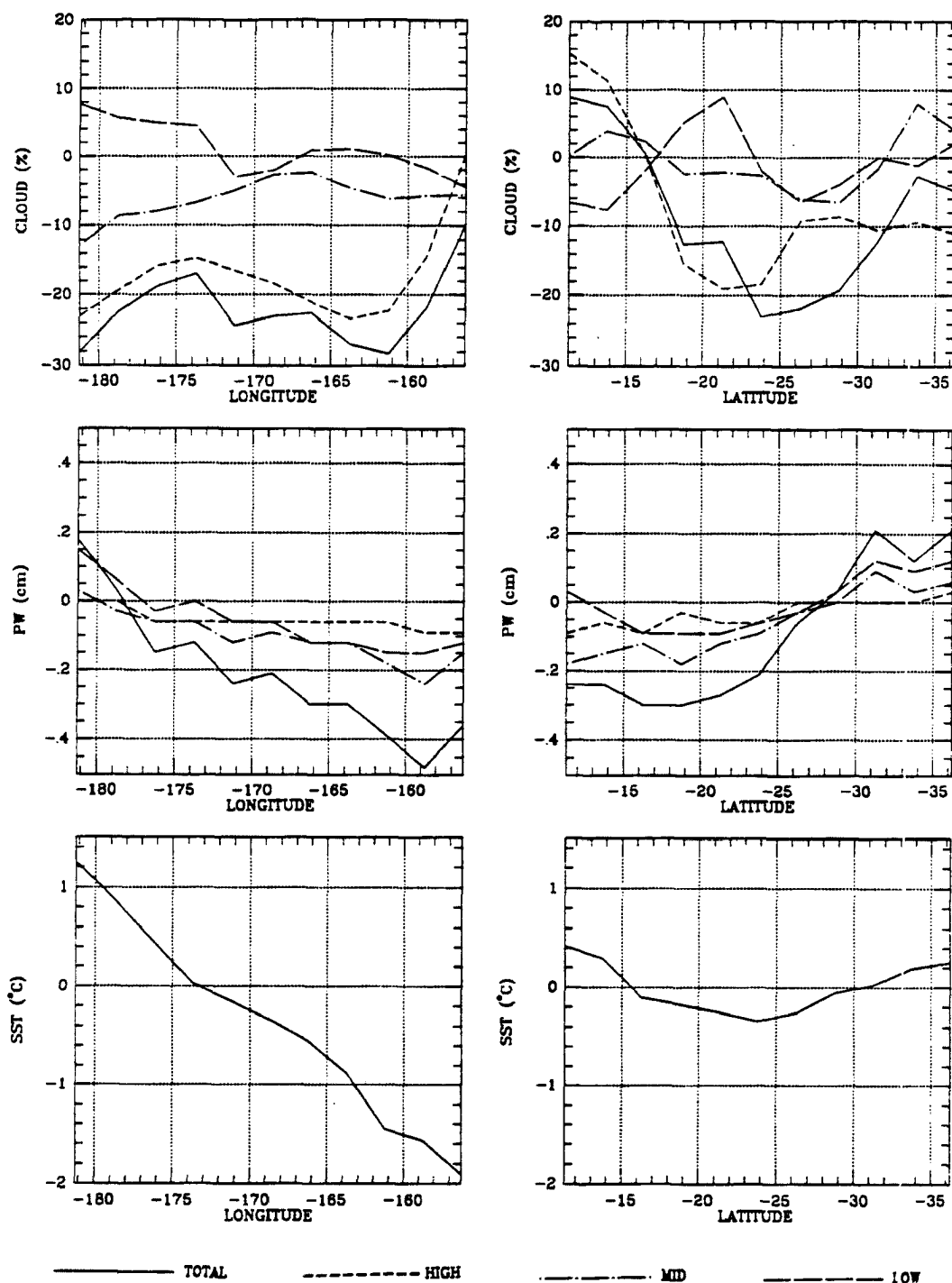


Figure 7.9: The difference in observed clouds, clear sky precipitable water, and SST between March 1984 and March 1985 (March 1984 minus March 1985) at case study region two.

decrease in SST (March 84 minus March 85), and marked decrease in high clouds. For this case study region, high clouds are the prime concern, and therefore only the diurnal variation in the change in high clouds is examined. The results, shown in Figure 7.10, indicate that there is very little diurnal variation in the change in high clouds and little diurnal variation in the average amount of high clouds for at this location for these two months.

Figure 7.11 shows that for ISCCP's 180-310 hPa cloud layer, March 1985's optical thickness tended to be less than March 1984's. This analysis was performed on the same grid points used in the diurnal analysis of high clouds. March 1984 when SSTs were cooler had fewer clouds with cloud tops at this level, but these clouds had higher optical depth. The major changes are in the highest optical depth category and the lowest optical depth category. This implies that cold SSTAs are associated with a lower percentage of the clouds at this level being thin cirrus and a higher percentage being thick towering cumulus.

7.4.3 Region 3: The Southeastern Pacific Ocean

This case study region was chosen because of its strong negative low water vapor-SSTA. Since this relationship extends in the E/W direction farther in terms of longitude than the two previous case study regions, the E/W domain of this case study region was increased to extend beyond the domain of the negative low water vapor-SSTA LAD slopes. The center point of the region is at 56.25°S and 91.25°W. The average conditions for these two months, shown in Figure 7.12 reveals a steady decrease in SST as one goes towards the pole with the southernmost temperature being below 0°C (the freezing point of sea water is -1.8°C). In the E/W cross section, SSTs are higher in the center than towards the ends and has an average SST of ~6°C. Clear sky water vapor is fairly uniform in the E/W direction, but does decrease in the eastern edge. In the N/S cross section, water vapor dramatically decreases towards the pole. This again is a very cloudy region with total clouds ~80%. Low and middle clouds dominate, with high clouds only ~10%.

The results of the cloud-SSTA LAD analyses described in Chapter 2 are not available for this case study region because the SST data set available for the time corresponding

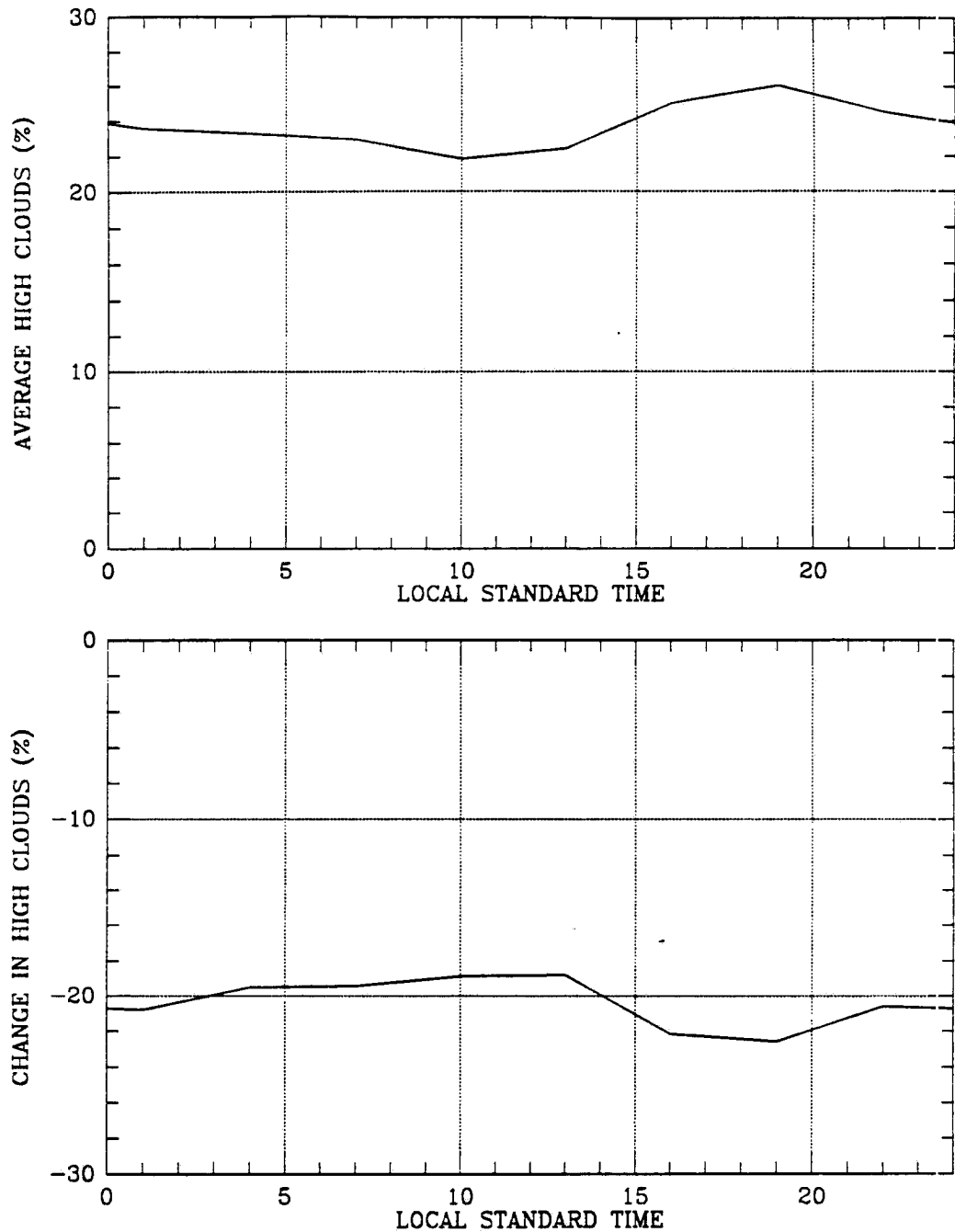


Figure 7.10: The average high clouds for March 1984 and March 1985 (top) and the difference in observed high clouds between March 1984 and March 1985 (March 1984 minus March 1985) as a function time of day for 5 grid points in the center of case study region 2. These 5 grid points are all at latitude 33.75°S and centered on longitude 166.25°W .

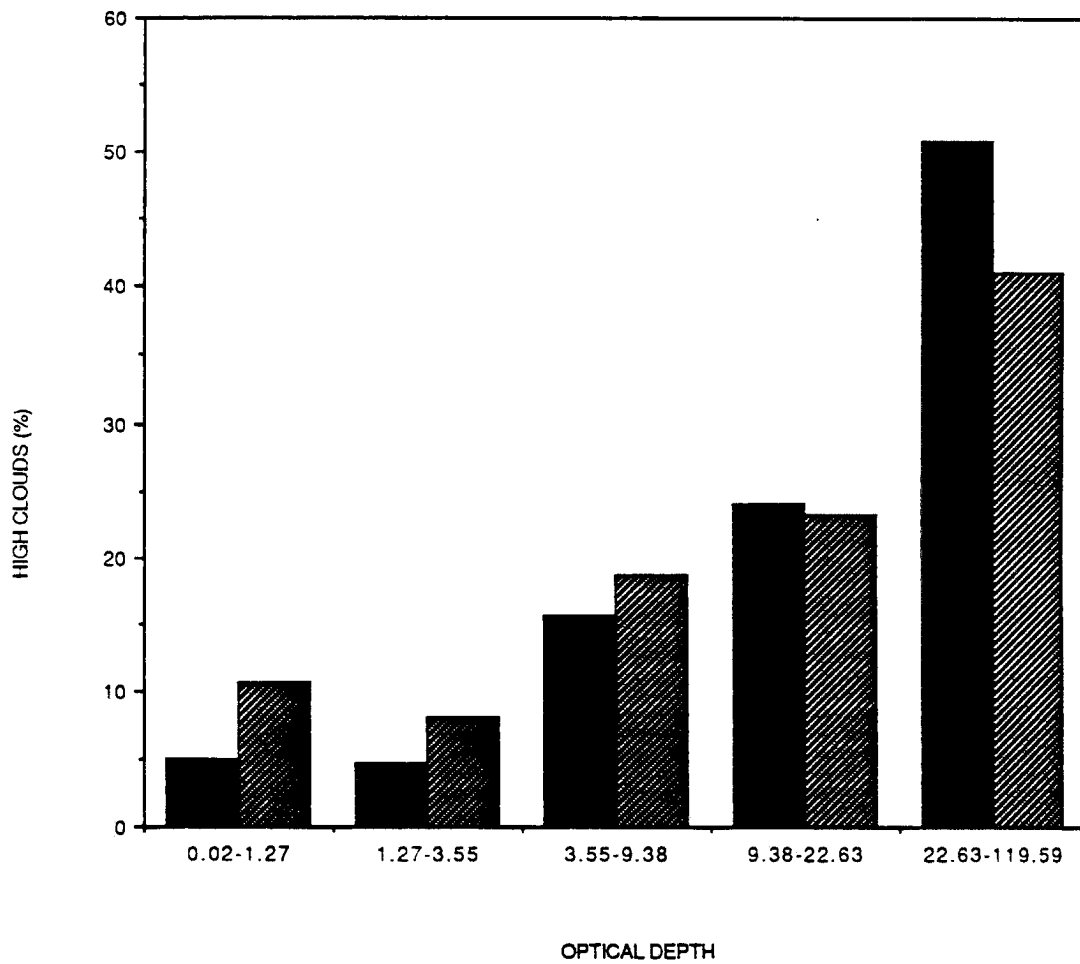


Figure 7.11: Normalized percent of 180-310 hPa clouds falling in ISCCP's 5 optical thickness categories for March 1984 (solid) and March 1985 (striped) for the average of five E/W cross section grid points centered at 33.75°S and 166.25°W in case study region 2.

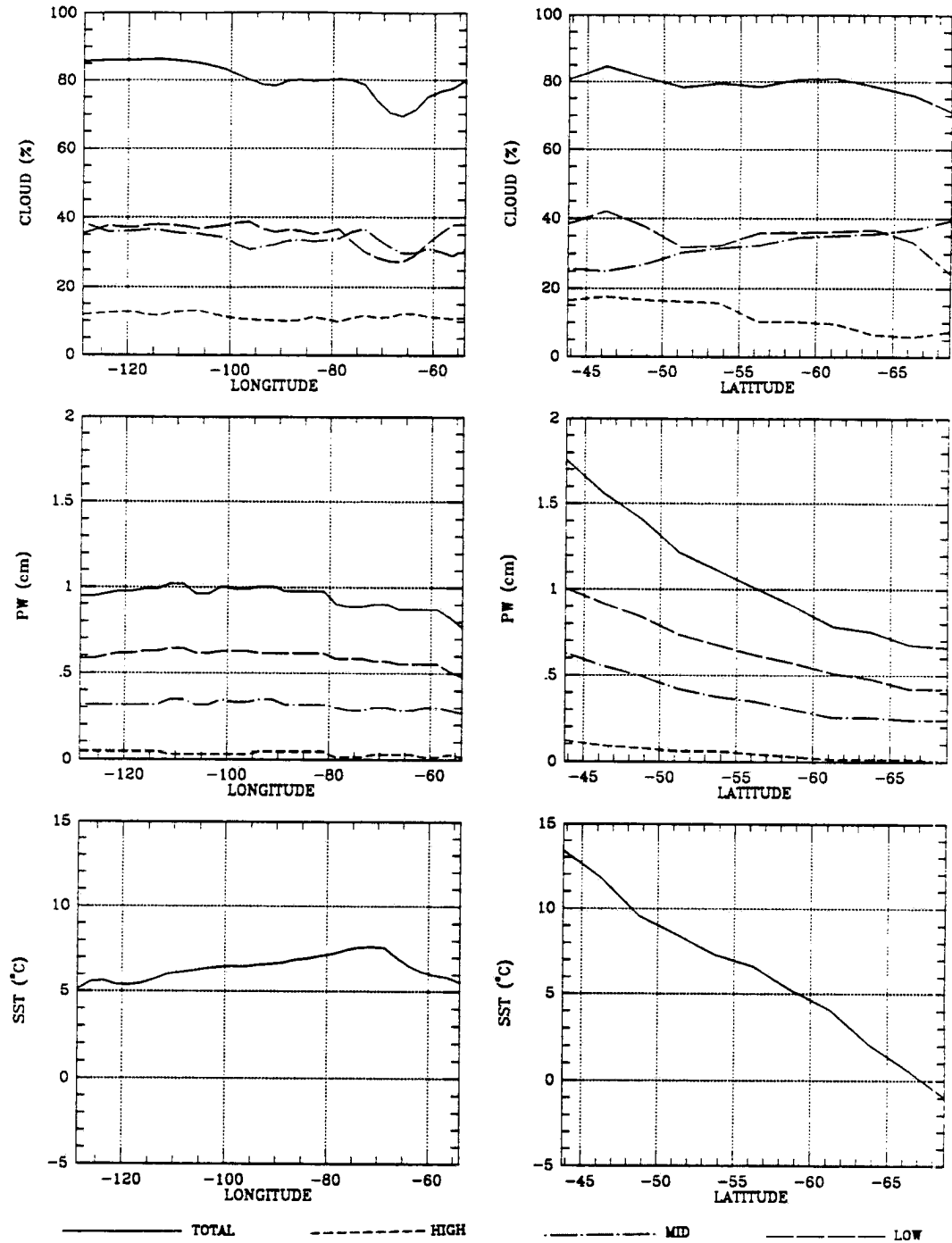


Figure 7.12: Average conditions of clouds, precipitable water, and SST for March 1984 and March 1985 at case study region three.

to the Nimbus-7 cloud data set was limited to 60°N to 40°S. Therefore Figure 7.13 only presents results of the LAD analyses of clear sky water vapor–SSTA and the corresponding P-values. Examination of the N/S cross section presented in this figure reveals that the LAD analyses based of the complete data set did not go farther south than 64°S: to avoid contamination of the results by air-sea-ice interactions, no analysis was made where part of the grid box was likely to be covered with ice during any one of the 72 months in the data set. Also, two grid points near 70°W longitude in the E/W cross section do not have LAD results because these two grid boxes have greater than 5% of their area land. The important information in Figure 7.13 is that in the center of the case study region water vapor anomalies low in the atmosphere decrease in association with increases in SSTA and the P-values for low water vapor–SSTA LAD analysis are quite low in the center of the region. Total water vapor displays a similar relationship, probably in response to the changes in low water vapor because the relationship between SSTAs and mid and high water vapor have LAD slopes at or near 0 and high P-values in this region.

The differences between March 1984 and March 1985 are shown in Figure 7.14. Cloud anomalies fluctuate from positive to negative on a scale that does not appear to be related to SST anomaly fluctuations. However, as graphically revealed once again in the E/W cross section, high and low cloud anomalies have a distinct out of phase relationship. In the center part of the two cross sections, low water vapor anomalies were negative as were the SST anomalies. This is the opposite of the relationship predicted by the LAD slope. However, in the center of the E/W cross section from 110°W to 70°W, the trend from west to east is for the SST anomaly to decrease while the total and low water vapor anomalies tend to increase. And this trend would be predicted by the negative PW–SSTA LAD slopes.

One of the specific questions the case study analysis was to address was the question of data quality in case study region 3. To examine what is different about the data at this location versus other locations at the same latitude, data along the whole latitude band centered at 56.25°S was analyzed. The top chart on Figure 7.15 shows the value of the low water vapor–SSTA LAD regression analysis slope along the whole latitude band. Only

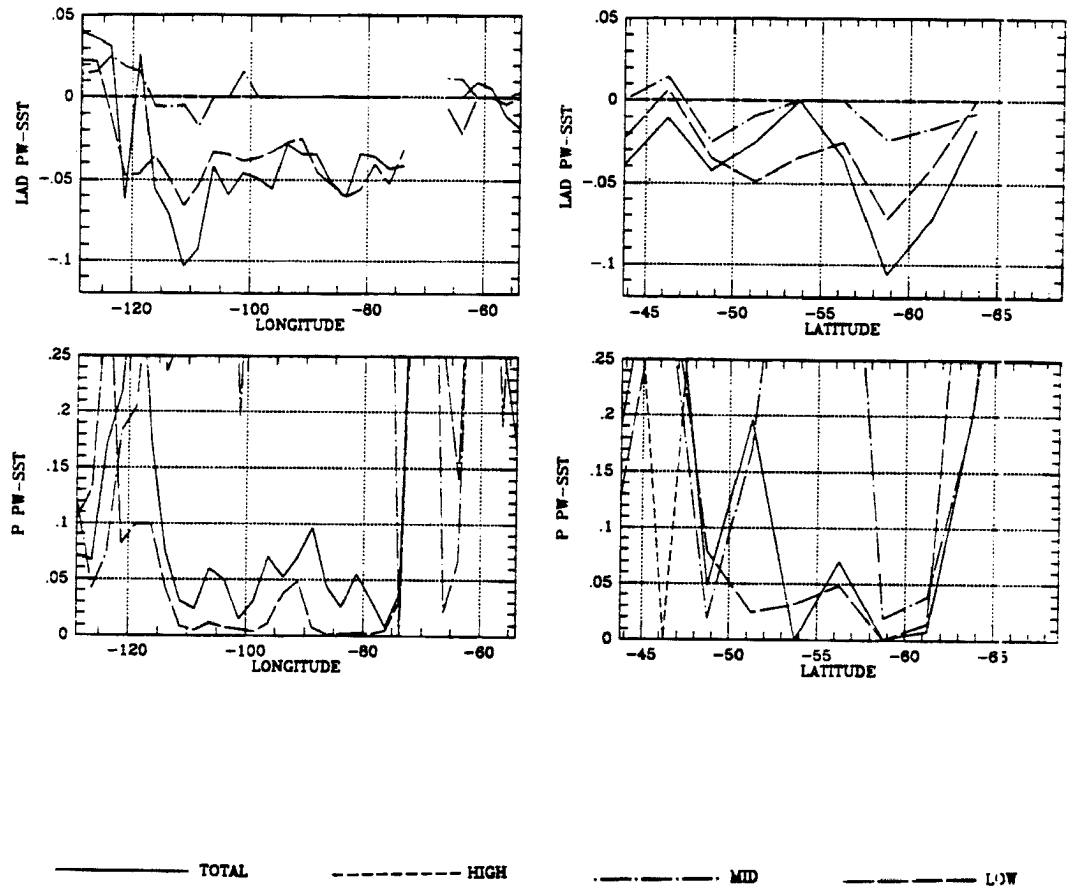


Figure 7.13: LAD slope and the Probability that the a distribution of data points around the LAD slope more extreme than the observed could be caused by random chance for the PW-SSTA relationships at case study region three.

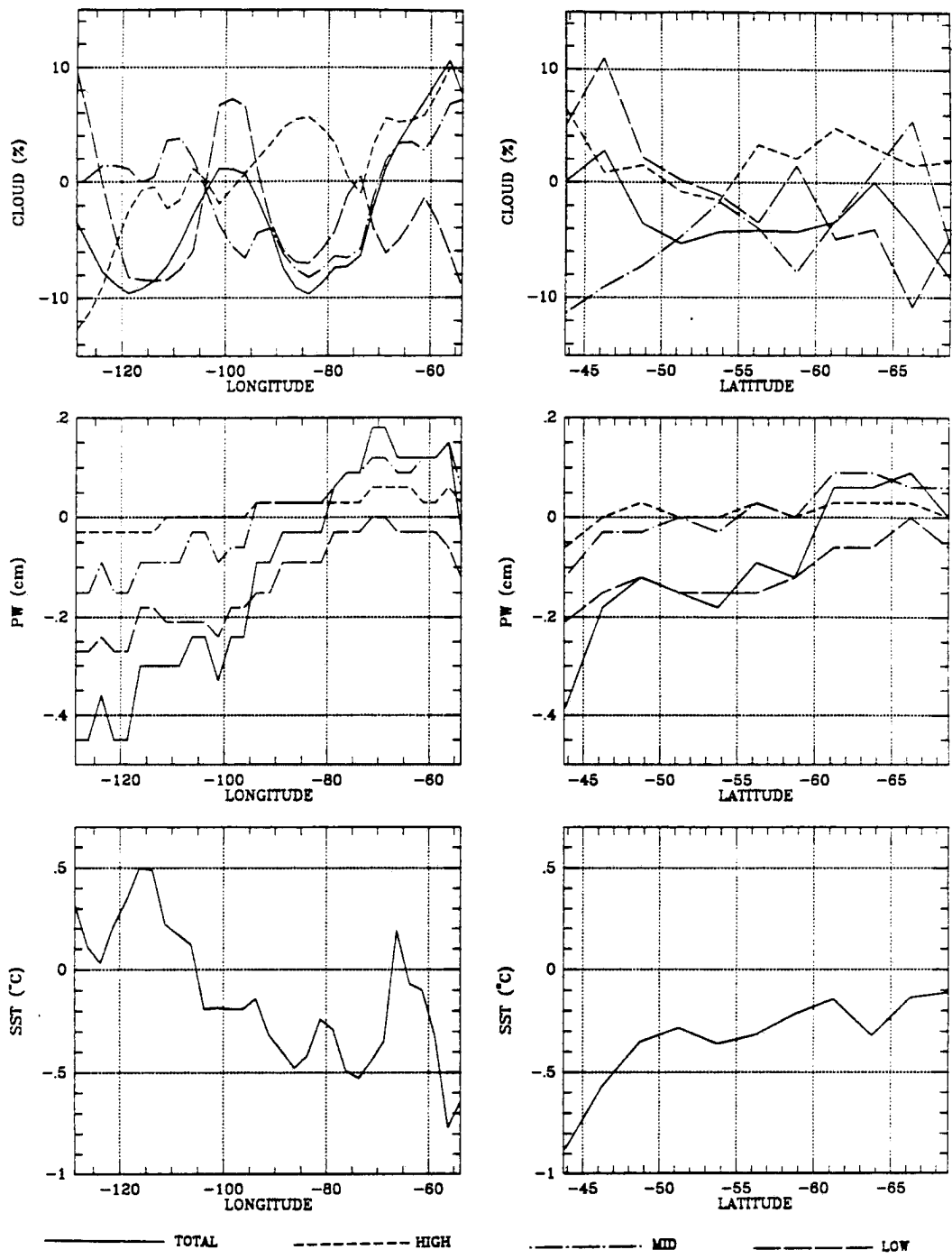


Figure 7.14: The difference in observed clouds, clear sky precipitable water, and SST between March 1984 and March 1985 (March 1984 minus March 1985) at case study region three.

two regions had negative LAD slope values. As the middle chart on Figure 7.15 indicates, though many grid points had low P-values, only the region between -115° to -70° E longitude had low P-values associated with the negative LAD slopes. The bottom chart on this figure indicates which grid boxes were open ocean and hence had LAD analysis performed on them and which did not have LAD analysis performed on them due to either (1) 5% or more of the $2.5^{\circ} \times 2.5^{\circ}$ grid box being land or (2) part of the grid box was ice covered for one or more of the 72 months of the analysis.

Clearly the -115 to -70° region has a unique combination of negative low level clear sky water vapor-SSTA LAD slopes and low P-values, but what other factors make it unique? Figure 7.16 shows the average value from 72 months worth of data for total clouds, low clouds, low PW, and SST. The cloud values is from the Nimbus-7 derived cloud data set interpolated to the finer resolution ISCCP grid. Total clouds can impact on data quality by decreasing the number of valid satellite observations of SST and low water vapor. However, there are actually less total clouds from -115 to -70° than the zonal average. Low clouds can affect data quality because cloud top can be mistaken for ocean surface by satellite instruments. Here the cloud amount remains fairly even for the entire latitude belt. The average quantity of water vapor low in the atmosphere is high over this region, but so is the average SST and in neither case are the values from -115 to -70° unique.

More specific examination of data quality is shown in Figure 7.17. The top chart in this figure is the number of TOVS soundings taken in each grid box over the course of 72 months. More accurately, it is the number of daily ISCCP TOVS grids that had actual data based on TOVS soundings for that day at that grid box. Since data was actually based on 71 months of analysis (one month had no data), 1400 TOVS soundings represents an average of 20 soundings per month. The area weighted average for the entire open ocean was 1116 TOVS soundings per grid box. The higher than average coverage of this latitude band is because the satellite trajectories increase the coverage at high latitudes. There is also a very good inverse correlation between the number of TOVS soundings and the percent of total clouds.

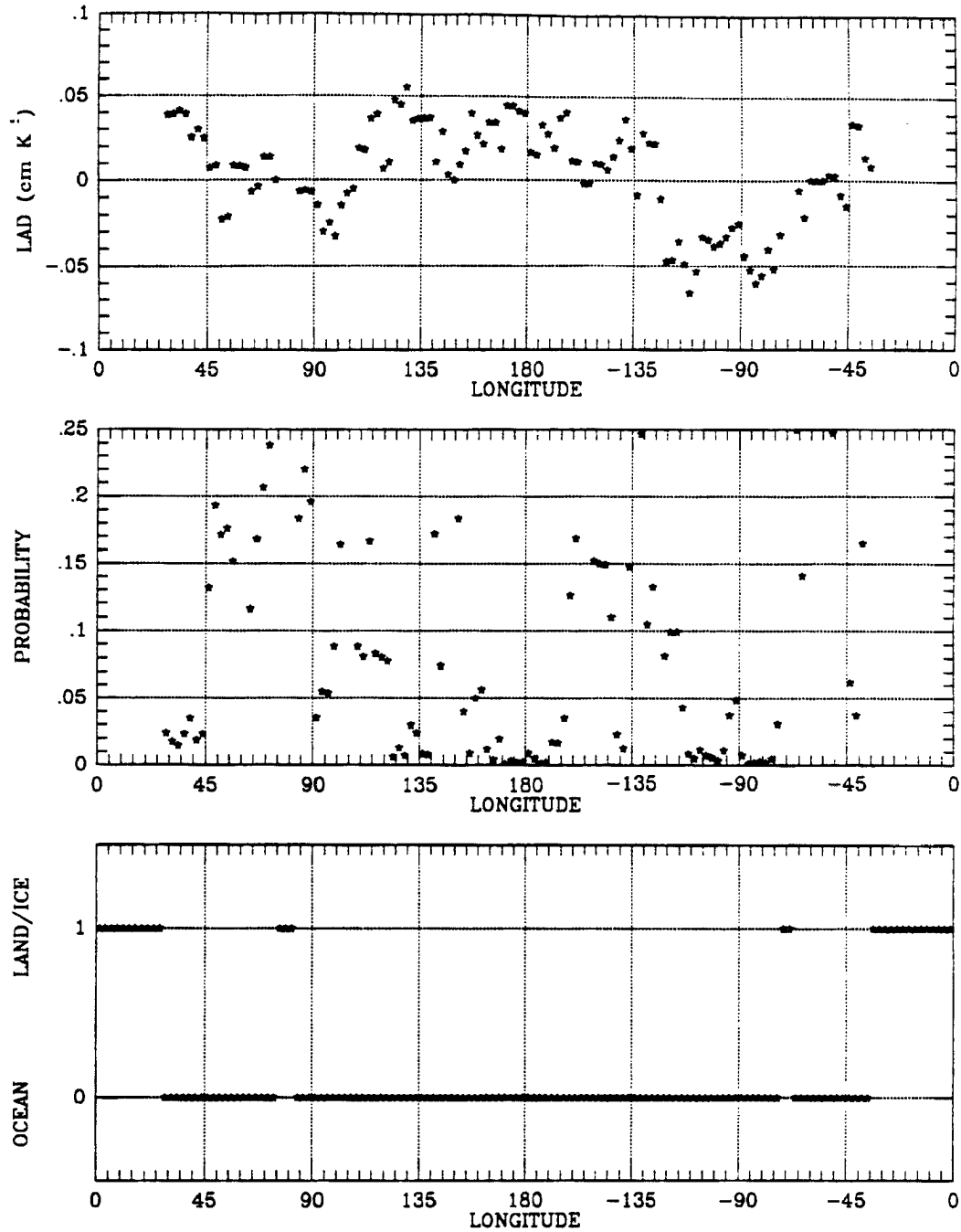


Figure 7.15: Values for low water vapor-SSTA LAD regression analysis slopes (top) and the Probability calculated from that analysis (middle) for the one 2.5° grid box wide latitude band centered at 56.25°S. The bottom chart indicates grid boxes where there was open ocean and hence the analysis was performed versus where the LAD analysis was not performed due to land occupying greater than 5% of the area or at least one month had sea ice in the grid box.

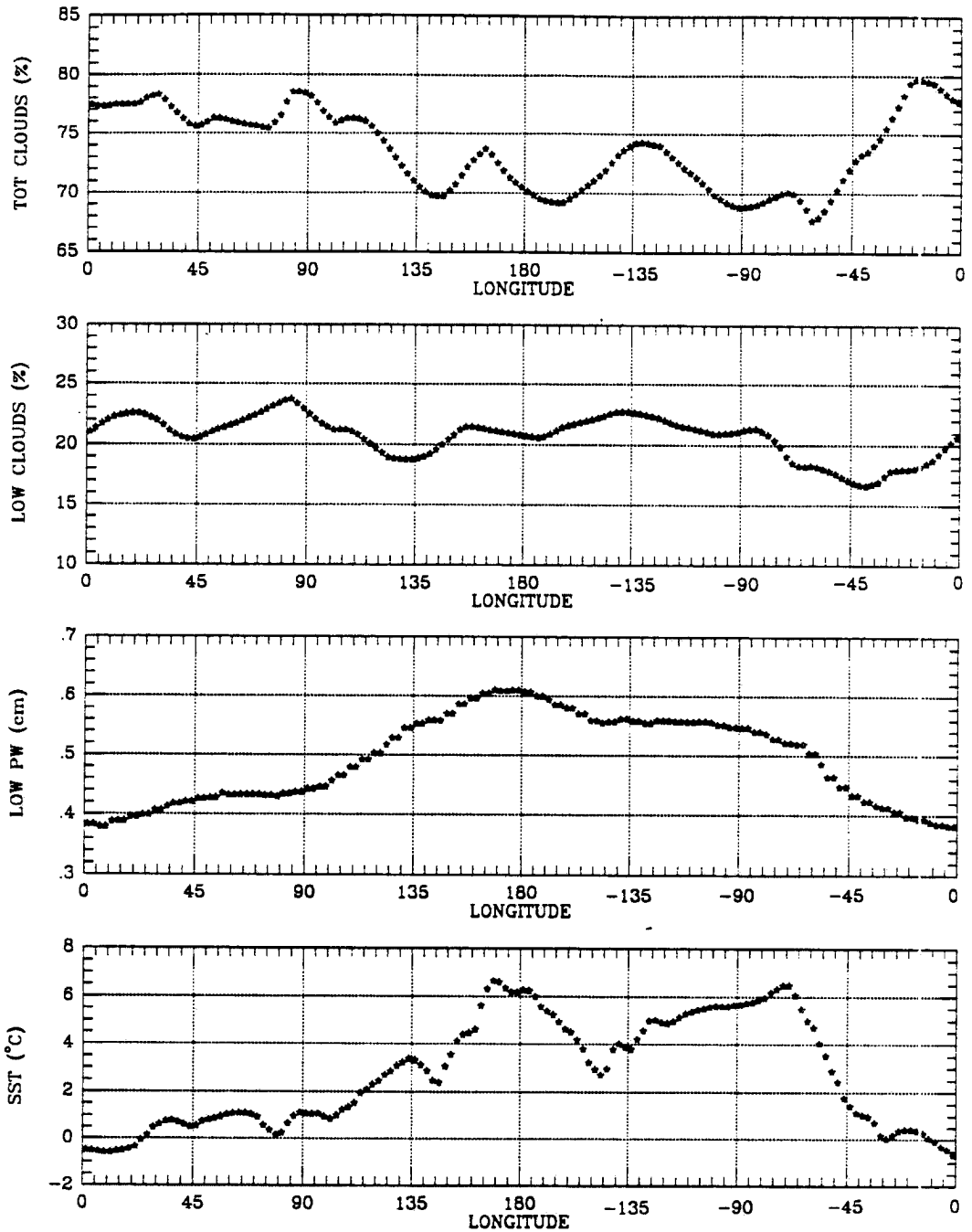


Figure 7.16: Average percent of Total Clouds (top), average percent of Low Clouds, average low clear sky precipitable water, and average SST along a latitude band centered at 56.25°S. All quantities are 72 month averages. PW and SST from July 1983 to June 1989. Clouds are from the Nimbus-7 derived cloud amounts from April 1979 to March 1985, interpolated to the ISCCP grid.

The CAC has several different techniques for deriving their monthly average SST value depending on the availability of various types of data. Each month's SST data has a flag for each grid box indicating which type of analysis was used to determine it. For type 1, the blended SST value is anchored by *in situ* analysis and there are at least 5 *in situ* observations per month. Type 5's SST value is determined by relaxation of the *in situ* analysis with satellite forcing and the number of satellite observations is at least 10 per month. For type 6, the blended SST value is determined by relaxation of the *in situ* analysis with the satellite forcing set to zero and there are less than 10 satellite observations per month (Reynolds, 1988). The CAC SST analysis is on a 2 x 2 degree grid so when the number of months for each type of SST data were interpolated to the 2.5 x 2.5 degree ISCCP grid, the values were no longer integers.

It is interesting to note that even at 56°S, there are still several months with 5 or more *in situ* observations. Again there is a distinct relationship between total clouds and the type of SST analysis. Specifically, there are more type 6 analyses where there are more clouds. The region from -115 to -70° has several type 1 analyses and above the zonal average of type 5 analyses. Based on the numbers and quality of observations, the region from -115 to -70° would appear to have better than zonal average data quality. Though as one would expect at this latitude, the SST data quality is not as good as the area weighted global average which is 25 type 1, 44 type 5, and 2 type 6.

Another data quality problem occurs when the range of the observed variation is so small that instrument noise seriously degrades the signal. To look at this question, Figure 7.18 shows the standard deviation of monthly low clear sky water vapor and monthly SST. The data sets used to calculate the standard deviations are the anomaly data sets used in Chapter 3. These anomalies are based on the average for that month, therefore, the seasonal signal is removed from the standard deviation calculation. Again the region from -115 to -70° does not stand out as unique. The area weighted average for the standard deviation of low PW over the global oceans is 0.1 cm. This latitude belt has lower standard deviations, but it also has lower average low water vapor, ~0.5 cm for this latitude belt versus an area weighted global ocean average of 1.6 cm. The standard deviation for SST in this latitude belt is not far from the global average of 0.5°C.

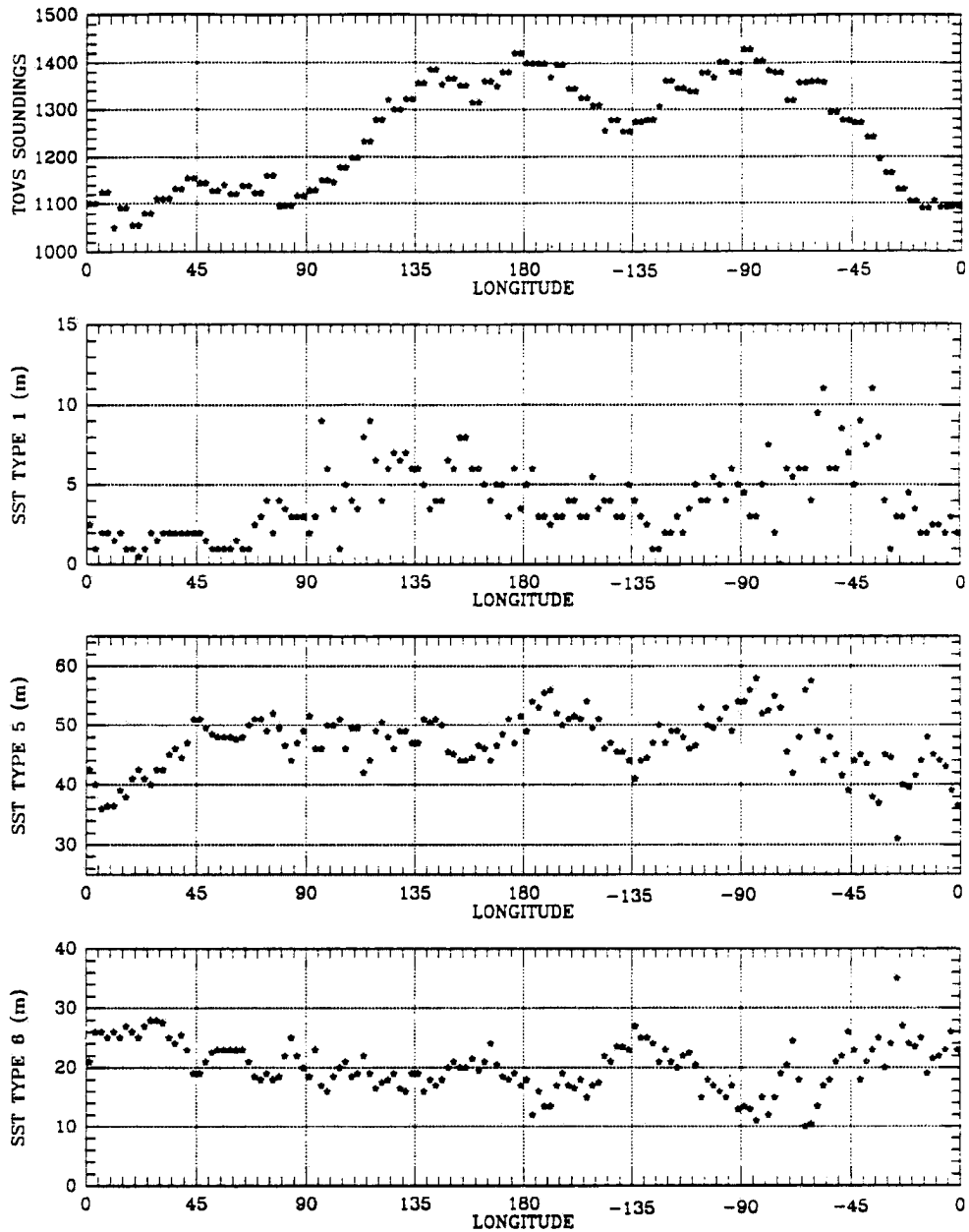


Figure 7.17: Number of days in 72 months of the ISCCP-TOVS data set used in analysis involving clear sky water vapor that the grid box reported data based on TOVS soundings from that day (top). The concurrent SST data was calculated by several different methods. In type 1, the blended SST value was anchored by the *in situ* analysis, of which there were at least 5 *in situ* observations for that month. Type 5 analysis was determined by relaxation of the *in situ* analysis with satellite forcing with the number of satellite observations numbering at least 10 per month. With type 6 analysis, the SST value was determined by relaxation of the *in situ* analysis with the satellite forcing set to zero and the number of satellite observations less than 10 per month. The results plotted are the number of months in each category for the 2 x 2 degree SST grid interpolated to the 2.5 x 2.5 degree ISCCP grid.

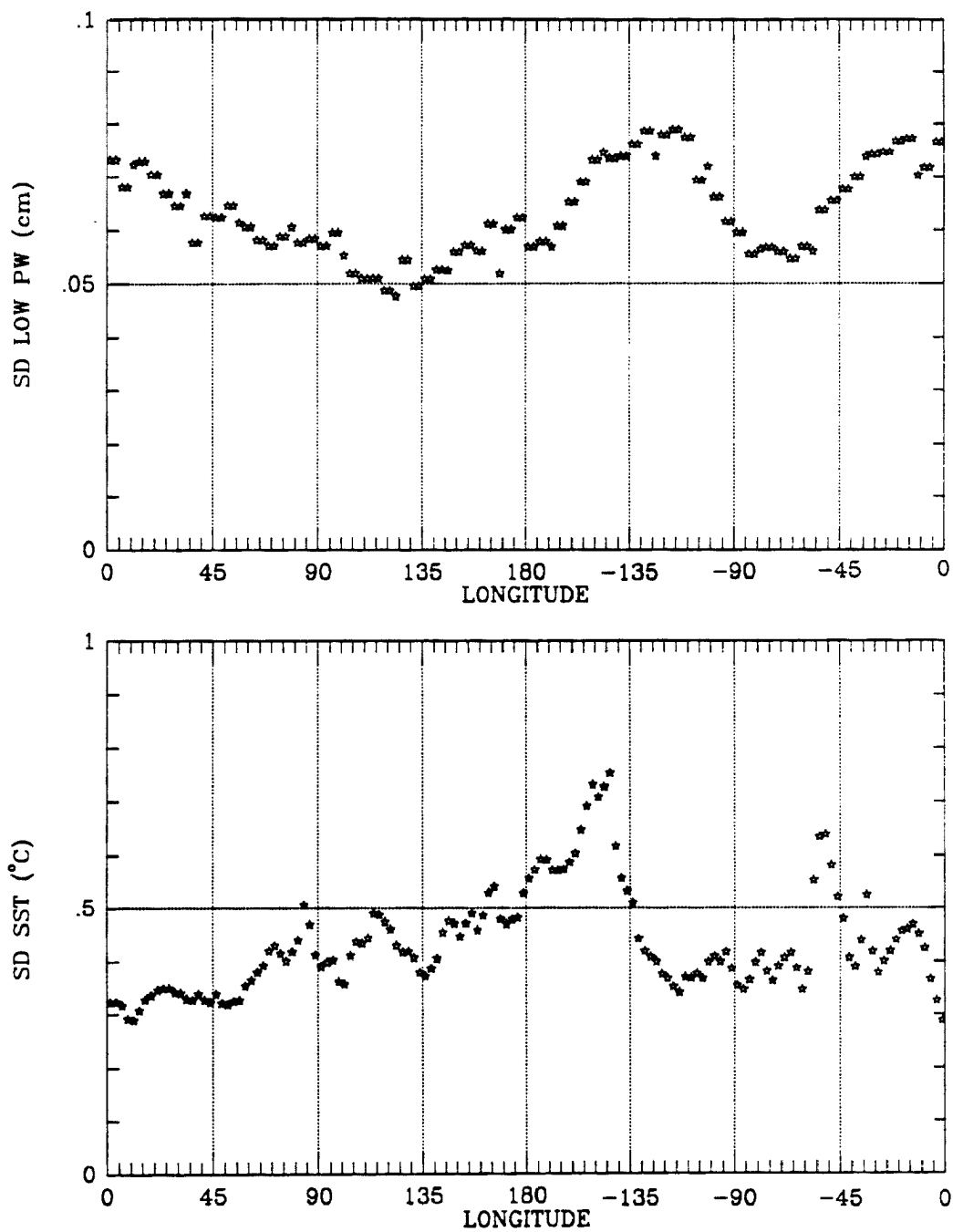


Figure 7.18: The standard deviation of low level clear sky water vapor (top) and SST (bottom) along the latitude band centered at 56.25°S.

Analysis of data quality revealed no smoking gun such as a marked increase in low clouds in the same region as a marked increase in TOVS soundings. That does not eliminate the question of data quality, but it can provide no reason to suspect data quality would be the cause for this strong negative low PW–SSTA relationship particularly when compared to the other values in this latitude zone. This leads us to seek physical explanations for this relationship. Here are two such explanations:

1) Increases in SSTA leads to increases in instability leading to an increase in clouds and precipitation which decreases the water vapor in the atmosphere.

2) This is a region of strong surface winds (the “furious fifties” as mariners named this latitude band). Where there are strong winds, evaporation is not related so much to surface temperature but rather to spray (Gray, 1990a). The stronger the wind, the more spray, and hence more evaporation and higher low level water vapor. At the same time, stronger winds cause deeper mixing of the ocean, and hence cooling of the surface and negative SSTAs.

The problem with both of these explanations is that they do not indicate why these explanations should apply only to the region from 115° to 70°W longitude and not to the rest of the latitude band. Oceanographic explanations involving gradients in salinity or ocean/atmosphere interactions along oceanic frontal or current boundaries offers potential for regionally varying explanations. However, due to scarcity of *in situ* oceanographic data in this region, confirming any theory may be impossible at the present time. For purposes of the central theme of this research, an explanation may be only tangentially important because, as shown in Chapter 5, the radiative effects of these changes in low level clear sky water vapor are quite minor, $\sim 0.07 \text{ W}\cdot\text{m}^{-2}$, because of low surface temperatures, a high percentage of cloud cover, and the negative water vapor–SSTA relationship being limited to low levels of the troposphere.

7.5 Discussion

While the strong climatological relationships between SSTA and cloud and water vapor anomalies determined using 72 months of data may not be revealed in any two

particular months, this case study analysis of two months did reveal some features that climatological analysis could not. The case study analysis focused on 4 specific questions that were not, or could not have been, addressed in the earlier climatological analysis. These questions were:

1) What is the diurnal variability of the response determined in earlier chapters? The ISCCP TOVS water vapor data does not provide diurnal resolution, however, the ISCCP cloud data does. Examination of this data revealed that there is very little diurnal variability in the response of high clouds to SSTAs in the region with positive high cloud-SSTA LAD slopes. However, in the region of negative low cloud-SSTA LAD slopes, there is a distinct diurnal variability in the response to SSTAs. The decrease in low clouds in response to positive SSTAs is much smaller during the day than at night. Therefore, the radiative effect of changes in low clouds—which is due mainly to the change in albedo—is therefore less than would be expected based on the response of low clouds to increases SSTA averaged over all 24 hours.

2) Is the change in cloudiness in response to changes in SSTAs a function of a decrease or increase in clouds over a large region or simply a function of clouds within a region moving to that part which is most favored? Due to the effect of changes in high clouds, this question could not be answered for case study region 1. In region 2, the case study data indicates that the change in cloudiness in response to changes in SSTAs is a large-scale phenomena. There is no indication that cloudiness simply moves 5 or 10 degrees to a portion of the region that is more favored for cloud formation. The global change implications of this are that large-scale changes in sea surface temperatures may well have major radiative effects due to changes in clouds over a large region.

3) What are the changes in cloud optical depth associated with changes in SSTAs? In case study region 1, a decrease in SSTA was associated with a decrease in low cloud optical depth. In case study region 2, a decrease in SSTA was associated with an increase in high cloud optical depth. The radiative implication in case study region one is that while warm SSTAs are associated with fewer low clouds, those low clouds may be more reflective and hence at least partially mitigate the radiative effect of decreases in low level clouds. In

case study region 2 the radiative effects are likely due to an increase in thin cirrus at this level. The radiative implication of increases in thin cirrus is a positive feedback to warming of the ocean surface.

4) How reliable is the data? This question was focused on the negative low water vapor-SSTA LAD slope region in the SE Pacific Ocean. Examination of the data in this region revealed no indications of problems in data quality. Since this is a fairly data sparse region, determining the cause of this negative LAD slope using other data is difficult. However, the radiative effects of this relationship is minor compared to the strong cloud-SSTA and water vapor-SSTA relationships determined elsewhere in the world.

Caution, however, must be exercised in determining how much weight to attach to these case study results. For example, the cloud optical depth analysis may have major implications on the radiative effects expected to be associated with CO₂ increases, but it was performed on only a few grid points for two months. Clearly much more research on the relationship between cloud optical depth and SSTAs is needed before any firm conclusions should be drawn.

Chapter 8

SUMMARY AND CONCLUSIONS

Most of the research related to CO₂ induced global warming are numerical experiments using GCMs. As the earth and atmosphere warm through increased greenhouse effect caused by increases in CO₂, evaporation from the ocean surface, clear sky water vapor, and clouds would all be expected to change. The changes in water vapor and clouds would have radiative effects creating either positive or negative feedbacks to the global warming. The magnitude and even sign of these feedbacks are currently the subject of much research and debate. While the physics of various parameterizations in GCMs can be discussed, refined, and numerically tested, the need for observational analysis is not diminished. The problem is that observations of yet to occur global warming are impossible. However, observational analogies to global warming are possible. For this research, we used local SSTAs as a surrogate for climate change. The objectives of this research were to identify and quantify the relationships of clouds, water vapor, and their radiative effects to underlying SSTAs.

This research was therefore limited to the global oceans. To avoid complicating the analyses with the effects of sea/land and sea/ice interfaces, the research was further limited to the atmosphere over the open, ice free oceans. In addition, due to data availability, the analyses of clouds and basic radiation parameters needed to be limited to the oceans from 60°N to 40°S. The relationship between cloud, water vapor, and basic radiation parameter anomalies and SSTAs was determined by using LAD regression analysis of the 72 month, monthly anomaly data sets at each grid point over the global oceans. How well the data was represented by the LAD regression line was determined using a MRBP test at each grid point. The radiative effect of changes in clear sky water vapor was determined

by using a two stream radiative transfer model at each grid point with the model input varying depending on the water vapor–SSTA relationship determined by the water vapor–SSTA LAD regression analyses at that grid point. The radiative effects of the changes in clouds were assumed to be the difference between the basic radiation parameters–SSTA LAD slope and radiative effects of changes in clear sky water vapor.

The results of this research indicate that clouds, water vapor, and their radiative effects have strong and regionally varying relationships to SSTAs. It was determined that in much of the tropics and along the South Pacific Convergence Zone (SPCZ), high clouds increased with increasing SSTAs at a rate of about 5% high cloud cover per degree increase in SSTA while in subtropical stratocumulus regions, low clouds decreased with increasing SSTAs at a rate of about 4% low cloud cover per degree increase in SSTA. Averaged for the entire data area, total cloudiness increased 1–2% in association with a 1°C increase in SSTA. For almost the entire global ocean, clear sky water vapor increased with increasing SSTA with an average increase of about 0.1 cm of precipitable water per degree increase in SSTA.

Examination of basic radiation parameters revealed that outgoing longwave radiation (OLR) decreased as SSTAs increased in the tropics and SPCZ where high clouds increased. The magnitude of this change varied with the region, but values of $-10 \text{ W}\cdot\text{m}^{-2}\cdot\text{K}^{-1}$ were common. Some of this change in OLR was due to increases in the clear sky greenhouse effect resulting from increases in water vapor. The magnitude of this effect was determined to average about $0.5 \text{ W}\cdot\text{m}^{-2}\cdot\text{K}^{-1}$ over our entire data area, only a small fraction ($\sim 10\%$) of the total change in OLR. Where clouds increased with increasing SSTA, the reflected flux increased as well. This offset much of the change in OLR in the tropics and SPCZ. Therefore, an analysis of the net radiative effect associated with increases in SSTAs did not reveal a very good statistical relationship in the tropics and SPCZ. The net radiation anomaly–SSTA relationship averaged $\sim 2-3 \text{ W}\cdot\text{m}^{-2}\cdot\text{K}^{-1}$ and was strongest in subtropical stratocumulus regions where the decrease in low clouds with increasing SSTA produced a net gain in energy, with values as high as $8 \text{ W}\cdot\text{m}^{-2}\cdot\text{K}^{-1}$ being common in these area. Averaged for the entire data area, reflected flux decreased $\sim 0.4 \text{ W}\cdot\text{m}^{-2}\cdot\text{K}^{-1}$ despite total

cloudiness increasing. This occurred because low, optically thick clouds decreased while high optically thin clouds increased.

Chapters 6 and 7 addressed two questions that needed to be answered before it would be appropriate to draw general conclusions applicable to global warming from this research. The first question is, how much of these analyses are actually examining the role of altered circulation and how much are the role of local SSTAs. The answer revealed in Chapter 6 is that the observed atmospheric anomaly–SSTA relationship is either related to local SSTA and not altered circulation or, in regions where SSTAs and altered circulation are closely related such as the eastern tropical Pacific, it is impossible to isolate the two relationships. The second question involves the scale of the interactions involved in these relationships. For example, in the South Pacific Convergence Zone (SPCZ) high clouds were found to increase with increasing SSTAs. If this relationship is a very localized phenomenon, where high clouds decrease at one grid point while they increase at the next grid point in response to gradients in SSTAs, then the cloud feedback when averaged over a large region may be negligible and the results of the research may not be relevant to large scale climate change induced warming of the ocean surface. Examination of this question described in Chapter 7 revealed that the observed relationships are large scale phenomena: that even if averaged over a large region, which the global warming–positive SSTA analogy implies, the feedback would still be apparent.

Therefore, the observational analogy to global climate change used for this research, while not perfect by any means, does have some validity. Based on this analogy, if the entire ocean surface warmed 1°C, the ensuing changes in clouds and water vapor would result in the earth–atmosphere system gaining $\sim 2\text{--}3 \text{ W}\cdot\text{m}^{-2}$ over the ice-free open oceans. This gives observational evidence to support the position that the cloud and water vapor radiative feedback loops are positive.

However, such global averages based on an average predicted change in SST do not take into consideration important regional differences. For example, ocean surface temperature changes resulting from increased CO₂ depend not only on the direct radiative effects of CO₂ and the associated cloud and water vapor radiative feedbacks, but also on

the changes in global circulation. Clearly in regions of coastal upwelling, changes in winds can have a much greater effect on SSTAs than changes in net radiation. SSTA should properly be considered a co-dependent variable rather than a true independent variable. This research does not attempt to predict SSTs. That we will leave to coupled ocean-atmosphere circulation models. By identifying the strong regionally varying cloud- and water vapor-SSTA relationships, this research clearly demonstrates the need for realistic oceans in coupled ocean-atmosphere GCMs. While not attempting to predict SSTAs, this research can indicate, in a very quantitative fashion, what changes in clouds, water vapor and their radiative effects a GCM should see for a particular SSTA at any particular location in the global ocean. In this regard, it is interesting to note here that the radiative effect of changes in clear sky water vapor per degree increase in SSTA predicted by 19 atmospheric general circulation models (Cess *et al.*, 1990) is in very good agreement with the observational-radiative transfer modeling results of this research.

The debate between Lindzen (1990a, 1990b) and Betts (1990) highlighted the importance of understanding the relationship between upper tropospheric clear sky water vapor and clouds. Our research concurs: for the observed variation of water vapor in association with observed SSTAs, the layer highest in the troposphere has the greatest radiative effect. Lindzen (1990a) argued that where tropical clouds grow deeper, the upper tropospheric clear sky around the clouds gets dryer. Our research clearly indicates that just the opposite happens: it gets more moist.

Another key feature this research pointed out is where the largest net radiative feedback occurs: subtropical stratocumulus regions. These regions will clearly need to be a focus of future global climate change research using both observations and numerical simulations. As Slingo (1990) pointed out, "the top-of-atmosphere radiative forcing by doubled carbon dioxide concentrations can be balanced by modest relative increases of $\sim 15\text{-}20\%$ in amount of low clouds and $20\text{-}35\%$ in liquid-water path, and by decreases of $15\text{-}20\%$ in the mean drop radius (depending on the version of the model)." This emphasis on drop size and liquid-water path as well as cloud amount implies that a potentially fruitful line of future research would be to extend this current research into cloud optical depth. It

is quite possible that cloud optical depth has a strong relationship to SSTAs. Since a long term cloud optical depth data set was not available for this research, a climatological analysis of a possible relationships between cloud optical depth and SSTAs could not be made. However, as more years of the ISCCP cloud data become available, such analysis will be possible.

Chapter 9

REFERENCES

- Angell, J. K., and J. Korshover, 1987: Variability in United States cloudiness and its relation to El Niño. *J. Climate Appl. Meteor.*, **26**, 580-584.
- Arking, A., 1990: Feedback processes and climate response. *Proceedings of the Conference on Climate Impacts of Solar Variability*, NASA Conference Publications CP-3086.
- Berry, K. J., and P. W. Mielke, 1985: Subroutines for computing exact chi-square and Fisher's exact probability tests. *Educ. Psychol. Meas.*, **45**, 153-159.
- Betts, A. K., 1990: Greenhouse warming and the tropical water budget. *Bull. Amer. Meteor. Soc.*, **71**, 1464-1465.
- Bjerknes, J., 1966: A possible response of the atmospheric Hadley circulation to equatorial anomalies of ocean temperature. *Tellus*, **18**, 820-829.
- Bjerknes, J., 1969: Atmospheric teleconnections from the equatorial Pacific. *Mon. Wea. Rev.*, **97**, 163-172.
- Bjerknes, J., 1972: Large-scale atmospheric response to the 1964-65 Pacific equatorial warming. *J. Phys. Oceanogr.*, **2**, 212-217.
- Blackmon, M. L., R. A. Madden, J. M. Wallace and D. S. Gutzler, 1979: Geographical variation in the vertical structure of geopotential height fluctuation. *J. Atmos. Sci.*, **36**, 2450-2466.
- Brower, R. L., H. S. Gorband, W. G. Pichel, T. L. Signore and C. Walton, 1976: Satellite derived sea-surface temperatures from NOAA spacecraft, *Tech. Memo. NESS 78*, NOAA, Washington, DC, 74 pp.
- Bryson, R. A., 1977: *Climates of hunger: mankind and the world's changing weather*. U. of Wisc. Press, Madison, 171 pp.
- Budyko, M. I., 1982: *The Earth's climate: past and future*. Academic Press, New York, 307 pp.
- Campbell, G. G., 1990: Personal communication.
- Cess, R. D., G. L. Potter, J. P. Blanchet, G. J. Boer, A. D. Del Genio, M. Déqué, V. Dymnikov, V. Galin, W. L. Gates, S. J. Ghan, J. T. Kiehl, A. A. Lacis, H. Le Treut,

- X.-Z. Liang, B. J. McAvaney, V. P. Meleshko, J. F. B. Mitchell, J.-J. Morcrette, D. A. Randall, L. Rikus, E. Roeckner, J. F. Royer, U. Schlese, D. A. Sheinin, A. Slingo, A. P. Sokolov, K. E. Taylor, W. M. Washington, R. T. Weatherald, I. Yagai, and M.-H. Zhang, 1990: Intercomparison and interpretation of climate feedback processes in 19 atmospheric general circulation models. *J. Geophys. Res.*, **95**, 16,601-16,615.
- Chan, P. H. and K. M. Lau, 1988: Relationships between sea surface temperature and outgoing longwave radiation over the tropical ocean. *Preprints of the Seventh Conference on Ocean-Atmosphere Interaction*, February 1-5, 1988, 83-85.
- Charlson, R. J., J. E. Lovelock, M. O. Andreae, and S. G. Warren, 1987: Oceanic phytoplankton, atmospheric sulphur, cloud albedo and climate. *Nature*, **326**, 655-661.
- Charney, J. G., 1979: *Carbon dioxide and climate: A scientific assessment*. National Academy Press, Washington, D.C., 33 pp.
- Chou, M.-D. and A. Arking, 1980: Computation of infrared cooling rates in the water vapor bands. *J. Atmos. Sci.*, **37**, 855-867.
- Chou, M.-D. and A. Arking, 1981: An efficient method for computing the absorption of solar radiation by water vapor. *J. Atmos. Sci.*, **38**, 798-807.
- Chou, M.-D. and A. Arking, 1983: A parameterization of the absorption in the 15 μm spectral region with application to climate sensitivity studies. *J. Atmos. Sci.*, **40**, 2183-2192.
- Collimore, C. C., 1990: *Association between West Pacific Equatorial Zonal Winds and East Pacific SST Anomalies*. Colorado State University Atmospheric Science Paper Number 468, 103 pp.
- Colorado State University, 1982: *Workshop on Satellite Meteorology*. July 19-23, 1982, Fort Collins, Colorado.
- Cotton, W. R., 1991: Personal communication.
- Daniels, J. M. and A. D. Vernekar, 1988: Influence of sea surface temperature on intra- and inter-annual variations of ITCZ. *Preprints of the Seventh Conference on Ocean-Atmosphere Interaction*, February 1-5, 1988, J61-J64.
- Fisher, R. A., 1958: *Statistical Methods for Research Workers*. Thirteenth Edition. Hafner, New York, 356 pp.
- Flatau, P. J., and G. L. Stephens, 1988: On the fundamental solution of the radiative transfer equation. *J. Geophys. Res.*, **93**, 11037-11050.
- Fleming, H. E., 1991: Personal communication.
- Gadgil, S., P. V. Joseph, and N. V. Joshi, 1984: Ocean-atmosphere coupling over monsoon regions. *Nature*, **312**, 141-143.
- Gardner, T., 1991: Personal communication.

- Gray, W. M., 1990a: Personal communication.
- Gray, W. M., 1990b: Strong association between west African rainfall and U.S. landfall of intense hurricanes. *Science*, **249**, 1251-1256.
- Gruber, A., and C. D. Watkins, 1979: Preliminary evaluation of initial atmospheric moisture from the TIROS-N sounding system. *Satellite Hydrology, Proc. Fifth Ann. Symp. on Remote Sensing*, Mineapolis, Amer. Water Resources Assoc., 115-123.
- Harrison, E. F., D. R. Brooks, P. Minnis, B. A. Wielicki, W. F. Staylor, G. G. Gibson, D. F. Young, F. M. Denn, and the ERBE Science Team, 1988: First estimates of the diurnal variation of longwave radiation from the multiple-satellite Earth Radiation Budget Experiment (ERBE). *Bull. Am. Meteor. Soc.*, **69**, 1144-1151.
- Harrison, E. F., P. Minnis, B. R. Barkstrom, V. Ramanathan, R. D. Cess, and G. G. Gibson, 1990: Seasonal variation of cloud radiative forcing derived from the Earth Radiation Budget Experiment. *J. Geophys. Res.*, submitted.
- Heath, D., A. J. Krueger, and H. Park, 1978: The solar backscatter ultraviolet (SBUV) and total ozone mapping spectrometer (TOMS) experiment. *The Nimbus-7 User's Guide*, C.R. Madrid, Ed., NASA, Goddard Space Flight Center, 175-211.
- Horel, J. D. and J. M. Wallace, 1981: Planetary-scale atmospheric phenomena associated with the Southern Oscillation. *Mon. Wea. Rev.*, **109**, 813-829.
- Intergovernmental Panel on Climate Change, 1990: *Scientific Assessment of Climate Change*. John Houghton, Chairman, IPCC Working Group I, World Meteorological Organization, Geneva, 26 pp.
- Jacobowitz, H., H. V. Soule, H. L. Kyle, F. B. House, and the Nimbus-7 ERB Experiment Team, 1984: The Earth Radiation Budget (ERB) Experiment: An overview. *J. Geophys. Res.*, **89**, 5021-5038.
- Jenne, R. L., H. L. Crutcher, H. van Loon and J. J. Taljaard, 1974: A selected climatology of the southern hemisphere: Computer methods and data availability. *Tech. Note NCAR-TN/STR-92*, Boulder, CO., 91 pp.
- Kerr, R. A., 1989: Hansen vs. the world on the greenhouse threat. *Science*, **224**, 1041-1043.
- Khalsa, S. J. S., and E. J. Steiner, 1987: Vertical structure in the near-equatorial atmosphere from the TIROS Operational Vertical Sounders (TOVS). *17th Conf. on Hurricanes and Tropical Meteorology*, Miami, Amer. Meteor. Soc., 137-141.
- Kidwell, K. B., ed., 1988: *NOAA Polar Orbiter Data Users Guide*, U.S. Dept. of Commerce, Washington, D.C., 184 pp.
- King, M. D. and Harshvardhan, 1986: Comparative accuracy of selected multiple scattering approximations. *J. Atmos. Sci.*, **43**, 784-801.
- Kneizys, F. X., E. P. Shettle, W. O. Gallery, J. H. Chetwynd, Jr., L. W. Abreu, J. E. A. Selby, R. W. Fenn, and R. A. McClatchey, 1980: Atmospheric transmit-

tance/Radiance: computer code LOWTRAN. *Report No. AFGL-TR-80-0067*, Air Force Geophysics Lab, Hanscom AFB, MA., 200 pp.

Kousky, V., 1990: Personal communication.

Kyle, H. L., P. E. Ardanuy, and E. J. Hurley, 1985: The status of the *Nimbus-7* Earth Radiation Budget data set. *Bull. Amer. Meteor. Soc.*, **66**, 1378-1388.

Lauritson, L., G. J. Nelson, and F. W. Porto, 1979: Data extraction and calibration of TIROS-N/NOAA Radiometers. *NOAA Tech. Memorandum NESS 107*, U.S. Dept. of Commerce, Washington, D.C.

Lindzen, R. S., 1990a: Some coolness concerning global warming. *Bull. Amer. Meteor. Soc.*, **71**, 288-299.

Lindzen, R. S., 1990b: Response. *Bull. Amer. Meteor. Soc.*, **71**, 1465-1467.

Love, G., 1985: A study of the linear relationships between the monthly mean fields of sea surface temperature, mean sea level pressure and cloudiness over the Northwest Pacific. *J. Meteor. Soc. Japan*, **63**, 201-209.

Lovelock, J. E., 1979: *Gaia: A new look at life on Earth*. Oxford University Press, New York, 157 pp.

Lovelock, J. E., 1986: Geophysiology: A new look at Earth Science. *Bull. Amer. Meteor. Soc.*, **67**, 392-397.

McClatchey, R. A., R. W. Fenn, J. E. A. Selby, F. E. Voltz, and J. S. Garing, 1972: *Optical properties of the atmosphere*, 3rd ed. AFCRL-72-0497, 108 pp.

Meador, W. E. and W. R. Weaver, 1980: Two stream approximations to radiative transfer in planetary atmospheres: A unified description of existing methods and a new improvement. *J. Atmos. Sci.*, **37**, 630-643.

Meisner, K. N., 1976: A study of Hawaiian and Line Island rainfall. *Rep. UHMET-76-04*, Department of Meteorology, University of Hawaii, 83 pp.

Mielke, P. W., 1984: Meteorological applications of permutation techniques based on distance functions. *Handbook of Statistics, Vol. 4*, P.R. Krishnaiah and P.K. Sen, eds, North Holland, Amsterdam, 813-830.

Mielke, P. W., 1986: Non-metric statistical analyses: Some metric alternatives. *J. Statist. Plann. Inference*, **13**, 377-387.

Mokhov, I. I., 1985: Global relationship between cloudiness and temperature as revealed by data on their interannual variability. *Izv. Acad. Sci. USSR, Atmos. Ocean. Phys.*, **21**, 700-704.

Mokhov, I. I., 1990a: Global cloudiness: Tendencies of change. *Il Nuovo Cimento*, submitted.

- Mokhov, I. I., 1990b: Tendencies of the global and polar cloudiness changes on satellite data. *WGRF-III/Doc. 2, Appendix*, 15 pp.
- Namias, J., 1976: Some statistical and synoptic characteristics associated with El Niño. *J. Phys. Oceanogr.*, **6**, 130-138.
- Namias, J., X. Yuan, and D. R. Cayan, 1988: Persistence of North Pacific sea surface temperature and atmospheric flow patterns. *J. Climate*, **1**, 682-703.
- Narula, S. C., and J. F. Wellington, 1982: The minimum sum of absolute errors regression: A state of the art survey. *Int. Statist. Rev.*, **50**, 317-326.
- Nicholls, N., 1977: Tropical-extratropical interactions in the Australian region. *Mon. Wea. Rev.*, **105**, 826-832.
- Nitta, T., 1986: Long-term variations of cloud amount in the western Pacific region. *J. Meteor. Soc. Japan*, **64**, 373-390.
- Pazan, S. E. and G. Meyers, 1982: Pacific trade wind fluctuations and the Southern Oscillation Index. *Mon. Weather Rev.*, **110**, 587-600.
- Philander, S. G., 1990: *El Niño, La Niña, and the Southern Oscillation*. Academic Press, San Diego, 293 pp.
- Pittock, A. B., 1973: Global meridional interactions in stratosphere and troposphere. *Quart. J. Roy. Meteor. Soc.*, **99**, 424-437.
- Platt, C. M. R., 1981: The effect of cirrus of varying optical depth on the extraterrestrial net radiative flux. *Quart. J. Roy. Met. Soc.*, **107**, 671-678.
- Preisendorfer, R. W., 1976: *Hydrologic Optics V. Properties*, NOAA, PMEL. 296 pp.
- Ramanathan, V., R. D. Cess, E. F. Harrison, P. Minnis, B. R. Barkstrom, E. Ahmad, and D. Hartmann, 1989: Cloud-radiative forcing and climate: results from the Earth Radiation Budget Experiment. *Science*, **243**, 57-63.
- Randall, D. A., 1980: Conditional instability of the first kind upside-down. *J. Atmos. Sci.*, **37**, 125-130.
- Randall, D. A., 1990a: Atmospheric and surface cloud radiative forcing: results from climate models. *Proceedings from the International Society for Optical Engineering's Conference on Long-Term Monitoring of the Earth's Radiation Budget*, 16-27.
- Randall, D. A., 1990b: Personal communication.
- Randel, D. L., 1990: *Earth radiation budget variability and the relationship to changes in the general circulation*. Colorado State University Atmospheric Science Paper Number 478, 114 pp.
- Raval, A. and V. Ramanathan, 1989: Observational determination of the greenhouse effect. *Nature*, **432**, 758-761.

- Reiter, E. A., 1978: Long-term wind variability in the tropical Pacific; its possible causes and effects. *Mon. Wea. Rev.*, **106**, 324-330.
- Reynolds, R., 1988: A real-time global sea surface temperature analysis. *J. Climate*, **1**, 75-86.
- Robertson, F. R., 1991: Personal communication.
- Robertson, F. R. and C. Cohen, 1990: Global analyses of water vapor, cloud and precipitation derived from a diagnostic assimilation of SSM/I geophysical retrievals. *Fifth Conference on Satellite Meteorology and Oceanography*, September 3-7, 1990, London, England, 262-264.
- Rossow, W. B., 1989: Measuring cloud properties from space: A review. *J. Climate*, **2**, 201-213.
- Rossow, W. B., and L. C. Garder, 1984: Selection of a map grid for data analysis and archival. *J. Climate Appl. Meteor.*, **23**, 1253-1257.
- Rossow, W. B. and B. Kachmar, 1988: *International Satellite Cloud Climatology Project (ISCCP) Description of Atmospheric Data Set*. Available from NOAA NESDIS, Washington, D.C., 30 pp.
- Rossow, W. B. and R. A. Schiffer, 1991: ISCCP cloud data products. *Bull. Amer. Meteor. Soc.*, **72**, 2-20.
- Rossow, W. B., F. Mosher, E. Kinsella, A. Arking, M. Desbois, E. Harrison, P. Minnis, E. Ruprecht, G. Sèze, C. Simmer and E. Smith, 1985: ISCCP cloud algorithm intercomparison. *J. Climate Appl. Meteor.*, **24**, 877-903.
- Rossow, W. B., L. C. Garder, P.-J. Lu, and A. Walker, 1988: *International Satellite Cloud Climatology Project (ISCCP) Documentation of Cloud Data*. Available from NOAA NESDIS, Washington, D.C., 78 pp.
- Rossow, W. B., L. C. Garder, and A. A. Lacis, 1989: Global, seasonal cloud variations from satellite radiance measurements. Part I: Sensitivity of analysis. *J. Climate*, **2**, 419-458.
- Rowntree, P. R., 1972: The influence of tropical east Pacific Ocean temperature on the atmosphere. *Quart. J. Roy. Meteor. Soc.*, **98**, 290-321.
- Schneider, S. H., 1990: The global warming debate heats up: an analysis and perspective. *Bull. Amer. Meteor. Soc.*, **71**, 1292-1304.
- Schwalb, A., 1978: The TIROS-N/NOAA A-G Satellite Series, *NOAA Technical Memorandum NESS 95*, U.S. Dept. of Commerce, Washington, D.C., 75 pp.
- Senta, E., 1983: The weighted median and multiple regression. *Austral. J. Statist.*, **25**, 370-377.
- Sèze, G., and W. B. Rossow, 1991: Time-cumulated visible and infrared radiance histograms used as a descriptor of cloud cover. *Int. J. Remote Sensing*, in press.

- Slingo, A., 1990: Sensitivity of the Earth's radiation budget to changes in low clouds. *Nature*, **343**, 49-51.
- Smith, W. L., and H. M. Woolf, 1976: The use of statistical covariance matrices for interpreting satellite sounding radiometer observations. *J. Atmos. Sci.*, **33**, 1127-1140.
- Somerville, R. C. J., S. Iacobellis, and S. M. Isakari, 1989: Tropical cirrus and climate stability. *Preprints from the 18th Conference on Hurricanes and Tropical Meteorology*. 3B 1-2.
- Stackhouse, P. W., Jr. and G. L. Stephens, 1989: *A Theoretical and Observational Comparison of Cirrus Cloud Radiative Properties*, Colorado State University Atmospheric Science Paper Number 452, 117 pp.
- Stackhouse, P. W., Jr. and G. L. Stephens, 1991: A theoretical and observational study of the radiative properties of cirrus: Results from FIRE 1986. *J. Atmos. Sci.*, in press.
- Stephens, G. L., 1984: The parameterization of radiation for numerical weather prediction and climate models. *Mon. Wea. Rev.*, **112**, 826-867.
- Stephens, G. L., 1988: Radiative transfer through arbitrarily shaped optical media. Part I: A general method of solution. *J. Atmos. Sci.*, **45**, 1818-1836.
- Stephens, G. L., 1990a: On the relationship between water vapor over the oceans and sea surface temperature. *J. Climate*, **3**, 634-645.
- Stephens, G. L., 1990b: Personal communication.
- Stephens, G. L. and T. J. Greenwald, 1991a: Observations of the Earth's radiation budget in relation to atmospheric hydrology. Part I: Clear sky greenhouse effect and water vapor feedback. *J. Geophys. Res.*, submitted.
- Stephens, G. L. and T. J. Greenwald, 1991b: Observations of the Earth's radiation budget in relation to atmospheric hydrology. Part II: Cloud effects and cloud feedback. *J. Geophys. Res.*, submitted.
- Stephens, G. L., and S.-C. Tsay, 1990: On the cloud absorption anomaly. *Quart. J. Roy. Meteor. Soc.*, **116**, 671-704.
- Stephens, G. L., S.-C. Tsay, P. W. Stackhouse, Jr., and P. J. Flatau, 1990: The relevance of the microphysical and radiative properties of cirrus clouds to climate and climate feedback. *J. Atmos. Sci.*, **47**, 1742-1753.
- Stowe, L. L., C. G. Wellemeyer, T. F. Eck, H. Y. M. Yeh, and the Nimbus-7 Cloud Data Processing Team, 1988: Nimbus-7 global cloud climatology. Part I: Algorithm and validation. *J. Climate*, **1**, 445-470.
- Stowe, L. L., H. Y. M. Yeh, T. F. Eck, C. G. Wellemeyer, H. L. Kyle, and The Nimbus-7 Cloud Data Processing Team, 1989: Nimbus-7 global cloud climatology. Part II: First year results. *J. Climate*, **2**, 671-709.

- Streten, N. S., 1975: Satellite derived inferences to some characteristics of the South Pacific atmospheric circulation associated with the Niño event of 1972-73. *Mon. Wea. Rev.*, **103**, 989-995.
- Tjemkes, S., 1990: Personal communication.
- Trenberth, K. E., 1975: A quasi-biennial standing wave in the Southern Hemisphere and interrelations with sea-surface temperature. *Quart. J. Roy. Meteor. Soc.*, **101**, 55-74.
- Trenberth, K. E., 1976: Spatial and temporal variations of the Southern Oscillation. *Quart. J. Roy. Meteor. Soc.*, **102**, 55-74.
- Trenberth, K. E., 1980: Planetary waves at 500 mb in the Southern Hemisphere. *Mon. Wea. Rev.*, **108**, 1378-1389.
- Van Loon, H., 1980: The Southern Oscillation in the Southern Hemisphere. *Proc. Fifth Annual Climate Diagnostics Workshop*, U.S. Department of Commerce, Washington, DC, 176-179.
- Walker, G. T. and E. W. Bliss, 1932: World weather. *V. Mem. Roy. Meteor. Soc.*, **4**, 53-84.
- Washington, W. M., 1990: Where's the heat? *Natural History*, March, 66-72.
- Werbowetzki, A., 1981: Atmospheric sounding users guide. *NOAA Tech. Rep. NESS 83*, U.S. Dept. of Commerce, Washington, D.C.
- White, W. B. and A. E. Walker, 1973: Meridional atmospheric teleconnections over the North Pacific from 1950 to 1972. *Mon. Wea. Rev.*, **101**, 817-822.
- Wittmeyer, I. L., 1990a: Satellite based precipitable water measurements and poleward latent heat transport using satellite data and model analysis. *Colorado State University M.S. Thesis*, Fort Collins, Colorado, 77 pp.
- Wittmeyer, I. L., 1990b: Personal communication.
- Wright, P. B., 1979: Hawaiian winter rainfall related to Pacific sea surface temperature. *Mon. Wea. Rev.*, **107**, 492-495.
- Wright, P. B., 1978: The Southern Oscillation. *Climatic Change and Variability*, A. B. Pittock, L. A. Frakes, D. Jenssen, J. A. Paterson and J. W. Zillman, Eds., Cambridge University Press, Cambridge, 180-185.
- Wong, R. K. W., C. Schneider and P. W. Mielke, 1989: Geometric consistency for regression model estimation and testing in climatology and meteorology. *Atmos. Ocean*, **27**, 508-520.
- Zdunkowski, W. G., R. M. Welch, and G. Korb, 1980: An investigation of the structure of typical two-stream-methods for the calculation of solar fluxes and heating rates in clouds. *Contrib. Atmos. Phys.*, **53**, 147-166.

Appendix A

LIST OF ACRONYMS AND ABBREVIATIONS

CAC: Climate Analysis Center. The source for the SST data used in our research.

ECMWF: European Centre for Medium Range Weather Forecasts.

ENSO: El Niño – Southern Oscillation.

ERBS: Earth Radiation Budget Satellite.

FOV: Field Of View.

GCM: Global Circulation Model.

HIRS/2: High Resolution Infrared Radiation Sounder. One of the TOVS instruments.

ISCCP: International Satellite Cloud Climatology Project. A multi-year cloud data project using data from many geostationary and polar orbiting satellites. The cloud data is divided into 7 layers on a 2.5 x 2.5 degree grid on an every 3 hours basis.

ISCCP TOVS: This is a version of the TOVS water vapor and temperature retrievals where the ~8,000 daily TOVS soundings are put on the ISCCP grid, with temperatures and water vapor interpolated to the levels used with ISCCP.

ITCZ: Intertropical Convergence Zone.

LAD: Least Absolute Deviations regression analysis. LAD analysis will essentially determine the best fit line through a scatter plot of the data. It is similar to the more commonly used LSD, but has the advantage of not working in squared space which gives inordinate weight to a few far outlying points.

MRBP: Multivariate Randomized Block Permutation test. This test is very helpful in determining how well the model results fits the observed. As used in this research, the model results are the LAD regression line, and the MRBP is used to see how well that line

represents the observed distribution of data by returning a P-value. One major advantage of this permutation technique is that it makes no prior assumption of the distribution of the data.

MSU: Microwave Sounding Unit. One of the TOVS instruments.

NESDIS: National Environmental Satellite, Data, and Information Service.

OLR: Outgoing Longwave Radiation.

P, P-value, Probability: The probability is a number between 0 and 1 which is the likelihood of an event more extreme than the observed occurring by random chance alone. A P-value of 0.25 means there is a 25% chance that an event more extreme could occur just by random chance. P-values calculated in this research range from ~ 0.4 where no significance was attached to those results to $\sim 6 \times 10^{-89}$ where the relationship definitely was not random. The frequently used cut off value for significance at a particular grid point was 0.05. The P-value in this research was determined by the MRBP or the Fisher's Exact test.

PW: Precipitable water vapor. In this research, the units used are cm of equivalent liquid.

SOI: Southern Oscillation Index.

SPCZ: South Pacific Convergence Zone.

SSU: Stratospheric Sounding Unit. One of the TOVS instruments.

SST: Sea Surface Temperature.

SSTA: Sea Surface Temperature Anomaly.

THIR: Temperature Humidity Infrared Radiometer on the Nimbus-7 satellite.

TIROS: A series of polar orbiting satellites known as the Television and Infrared Observation Satellite.

TOMS: Total Ozone Mapping Spectrometer on the Nimbus-7 satellite.

TOS: TIROS Operational System.

TOVS: TIROS Operational Vertical Sounder.

Appendix B

STATISTICAL TECHNIQUES

Three different statistical procedures were used in the course of this research. The actual FORTRAN code used in all of these procedures was written by Professor Mielke. The following three sections provide some background on these procedures.

B.1 LAD: Least Absolute Deviations

The Least Absolute Deviations (LAD) is very similar to the more common Least Squared Deviations (LSD) in that it tries to determine the best fit straight line through the data points as illustrated in Figure 2.2. The difference between LAD and LSD is that LAD is performed in Euclidean space while LSD is performed in squared space. That is, LAD tries to minimize

$$\sum_{i=1}^n |e_i|$$

while LSD tries to minimize

$$\sum_{i=1}^n e_i^2.$$

The practical result of this difference is that the effect of far outlying data points are much smaller for LAD than LSD. But the main reason for using LAD over LSD is the fundamental difference between Euclidean and squared space. To illustrate, consider three data points with the same value on the x axis but with y axis values of 1, 3, and 4. The distance from 3 to 4 is 1 for both LAD and LSD ($1^2 = 1$). However, the distance from 1 to 3 is 2 in LAD analysis but 4 ($2^2 = 4$) in LSD analysis. As used in our research, the y axis represents a physical quantity such as percent of cloudiness, cm of precipitable water vapor, or temperature. By using Euclidean space, as LAD does, we use a direct representation

of the physical quantity while LSD working in squared space does not. Though LAD is used less commonly than LSD, it is not the use of LAD that needs justification. Rather, the use of LSD should require some justification as to why use a technique that sees the distance from 1 to 3 as 4 when clearly the distance represents 2 (degrees, percent, etc.). Twenty years ago, one could have used the justification that, although LSD does not use an accurate representation of the physical data, LSD was used because it is less computationally intensive. However, the improvement in computer resources over the last several years makes this justification less valid.

B.2 MRBP: Multivariate Randomized Block Permutation

Multivariate Randomized Block Permutation (MRBP) procedure is often used to compare models. Each model would be a different block. In our case, the LAD regression line is one block and the observed data is another block. For each observed SSTA x_i , we have a (e.g.) cloud anomaly y_i and a predicted cloud anomaly \hat{y}_i (the LAD regression line value at x_i). For our full data set analysis (as opposed to seasonal) we have 2 blocks (b) and 72 treatments (g). The MRBP statistic is given by

$$\delta = [g \binom{b}{2}]^{-1} \sum_{i=1}^g \sum_{r < s} \Delta(x_{ir}, x_{is})$$

where $\sum_{r < s}$ is the sum of all r and s such that $1 \leq r < s \leq b$ and $\Delta(x, y)$ is a symmetric distance measure value for the two objects with measurements $x' = (x_1, \dots, x_m)$ and $y' = (y_1, \dots, y_m)$.

The null hypothesis of MRBP assigns an equal probability to each of the

$$M = (g!)^b$$

possible allocations of the g treatments to the g objects within each of the b blocks. The permutation distribution of δ under the null hypothesis is the collection of all δ values of these M equally likely allocations.

A small value of δ indicates a concentration of similar response measurements for some of the g treatments. Thus the P-value associated with an observed value of δ (say δ_0) is the probability under the null hypothesis given by $P(\delta \leq \delta_0)$ (Mielke, 1986).

Table B.1: An example of a 2 x 2 cross-classification table: The sum of the first row (column) cells is a (b) and n is the sum of all 4 cells.

	$P \leq 0.05$	$P > 0.05$	Total
$ \text{latitude} \leq 12^\circ$	x	$a - x$	a
$ \text{latitude} > 12^\circ$	$b - x$	$n - a - b + x$	$n - a$
Total	b	$n - b$	n

B.3 Fisher's Exact Test

The Fisher's Exact test was used in this research as a probability test for a 2 x 2 cross-classification table. The two classifications we used in the table were the probability as determined by the MRBP analysis (e.g., was $P >$ or ≤ 0.05 for that grid point) and latitude (e.g., was $|\text{latitude}| >$ or $\leq 12^\circ$) as shown in Table B.1. The numerical value used in each of the 4 cells on the 2 x 2 cross-classification table in Fisher's Exact was the number of grid points from the LAD and MRBP analysis for that atmospheric parameter that would be classified as belonging in that box. Each grid point in the MRBP analysis is counted in one of the 4 boxes on the 2 x 2 table as shown in Table B.1.

In the Fisher's Exact test,

$$P(x|a, b, n) = \frac{\binom{a}{x} \binom{n-a}{b-x}}{\binom{n}{b}} = \frac{a!b!(n-a)!(n-b)!}{n!x!(a-x)!(b-x)!(n-a-b+x)!}$$

where $\max(0, a + b - n) \leq x \leq \min(a, b)$. The P-value equals $\sum P(x|a, b, n)$ such that x is associated with a $P(x|a, b, n) \leq P(x_0|a, b, n)$ where x_0 is the observed value.

Appendix C

THE RELATIONSHIPS BETWEEN THE EASTERN TROPICAL PACIFIC SSTA AND GLOBAL SSTAS, CLOUDS, WATER VAPOR, AND RADIATION PARAMETERS

C.1 Introduction

Chapter 6 primarily looked at the relationship between water vapor, clouds, and radiation parameters to the Southern Oscillation Index. As noted in that chapter, a similar analysis was performed on the eastern tropical Pacific SSTA. This anomaly was calculated from the monthly means of the region from the equator to 10°S and from the dateline (180°) to the South American coast (80-82° West) using the Climate Analysis Center's SST data. Like the SOI, this SSTA is closely associated with the ENSO phenomena. However, there are some differences between these two ENSO signals, the prime one being that the SSTA over this large area fluctuates more slowly than the smoothed SOI.

C.2 Methods

The same methods which are described in Chapter 6 are used in this analysis, except instead of performing the LAD analysis at each remote grid point with that grid point's atmospheric variable and the SOI, the SOI was replaced with the eastern tropical Pacific SSTA.

C.3 Results

The relationship between global clouds, water vapor, radiation parameters, and global SSTAs with the eastern tropical Pacific SSTAs are similar, but not identical to those related to the SOI. The analysis of the relationship between this tropical SSTA and the remote atmospheric and oceanic variable was performed 9 times, each with a different lead

or lag time ranging from a 4 month lead to a 4 month lag. A 4 month lead means the atmosphere leads the SSTA by 4 months, e.g. March 1982's atmospheric phenomena is paired with July 1982's eastern tropical Pacific SSTA when performing a LAD analysis. Figures C.1, C.2, and C.3 show the total cloud–eastern tropical Pacific SSTA LAD analysis at the two extreme times of the analysis (4 month lead and 4 month lag) and the time that appeared to be best correlated which is a 2 month lag. Figures C.4, C.5, and C.6 show the same two extreme times with total clear sky water vapor–eastern tropical Pacific SSTA LAD analysis and the time with the best correlation, which again is a 2 month lag.

All the remaining figures are for a two month lag, where the remote variable lags two months behind the eastern tropical Pacific SSTA. Figures C.7 and C.8 show the relationship between the eastern tropical Pacific SSTA and remote sea surface temperature anomalies for the time span corresponding to the cloud and radiation analyses presented in Chapters 2 and 4 and the water vapor analyses in Chapter 3. The global SSTAs used in Figure C.7 are available only from 60°N to 40°S.

Figures C.9, C.10, and C.11 show the relationship between the eastern tropical Pacific SSTA and clouds at all three levels while Figures C.12, C.13, and C.14 show this relationship with all three levels of clear sky water vapor. The analyses with the radiation parameters albedo, reflected flux, OLR, and net radiation are shown in Figures C.15, C.16, C.17, and C.18

C.4 Discussion

A discussion of the differences between these analyses and the SOI analyses can be found in Chapter 6. The prime difference is that all parameters appear to have a better relationship to the quicker varying SOI than the average SSTA over this large region of the tropical Pacific except clouds high in the troposphere and water vapor high in the troposphere.

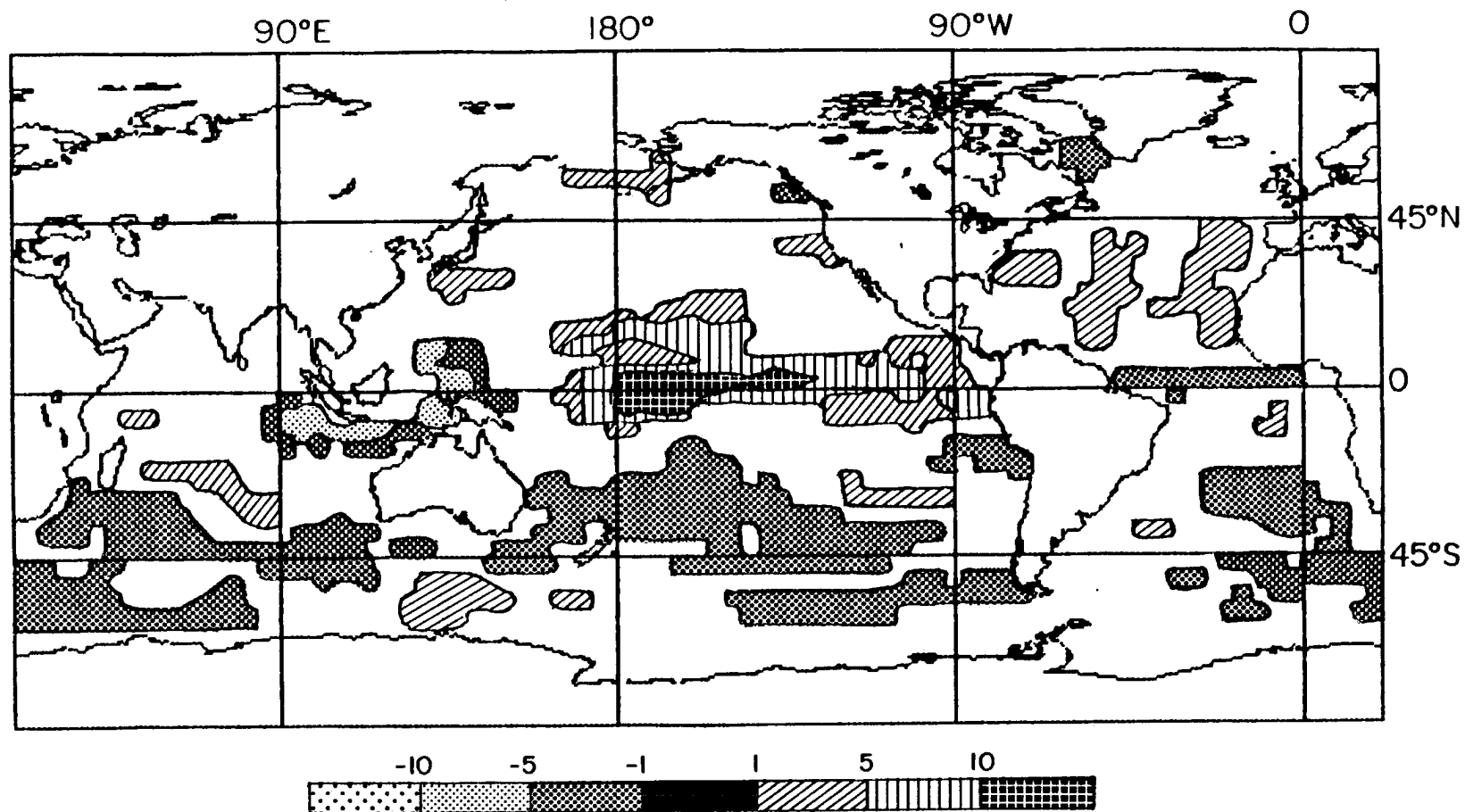


Figure C.1: A global plot of the LAD slope between total clouds and the eastern tropical Pacific SSTA analyzed with the atmospheric variable leading 4 months ahead of the SSTA. Only grid points with a P-value of less than or equal to 0.05 are plotted. Units are $\% \cdot K^{-1}$. Based on data from April 1979 through March 1985.

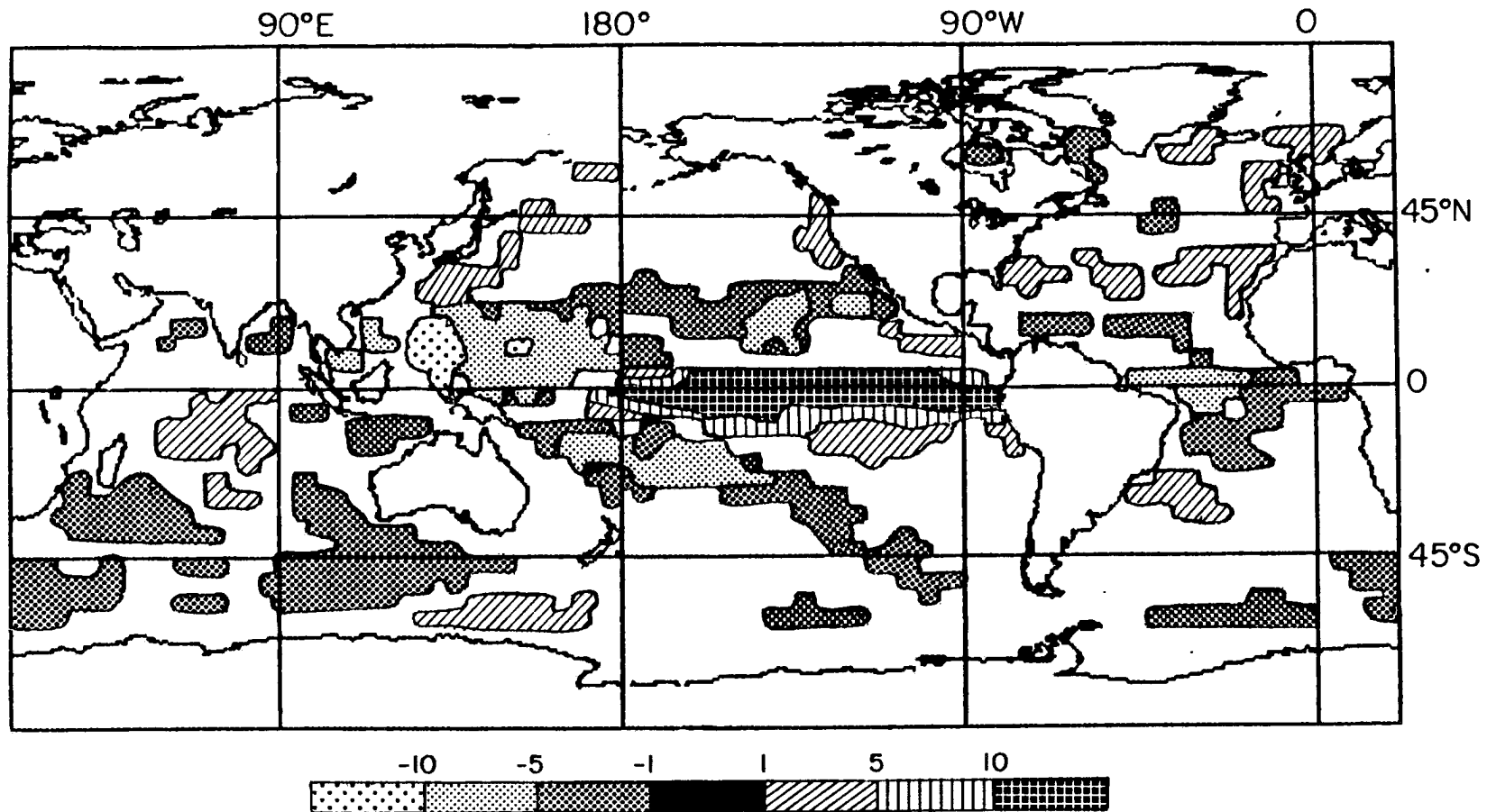


Figure C.2: A global plot of the LAD slope between total clouds and the eastern tropical Pacific SSTA analyzed with the atmospheric variable lagging 4 months behind the SSTA. Only grid points with a P-value of less than or equal to 0.05 are plotted. Units are $\% \cdot K^{-1}$. Based on data from April 1979 through March 1985.

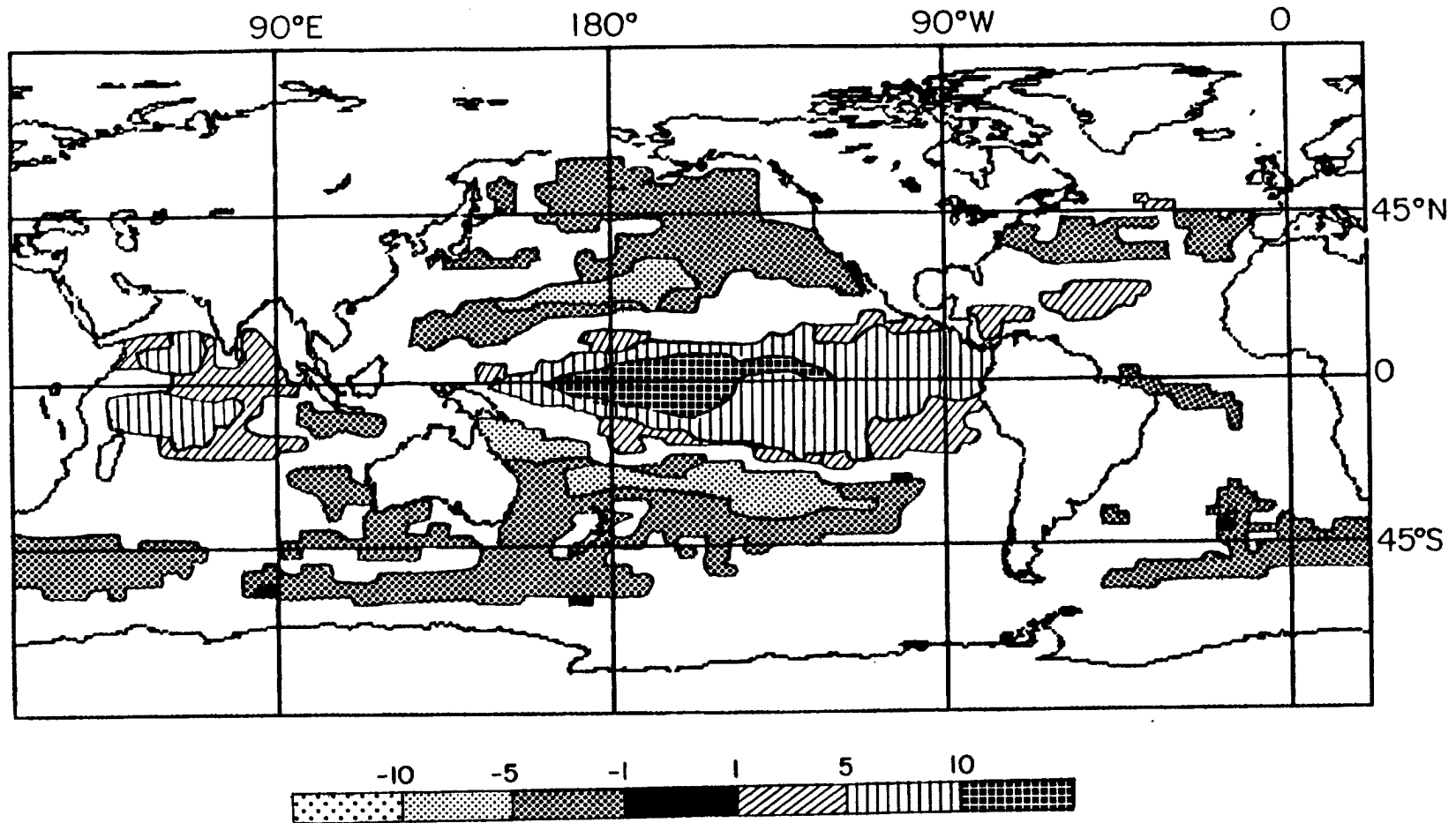


Figure C.3: A global plot of the LAD slope between total clouds and the eastern tropical Pacific SSTA analyzed with the atmospheric variable lagging 2 months behind the SSTA. Only grid points with a P-value of less than or equal to 0.05 are plotted. Units are $\% \cdot K^{-1}$. Based on data from April 1979 through March 1985.

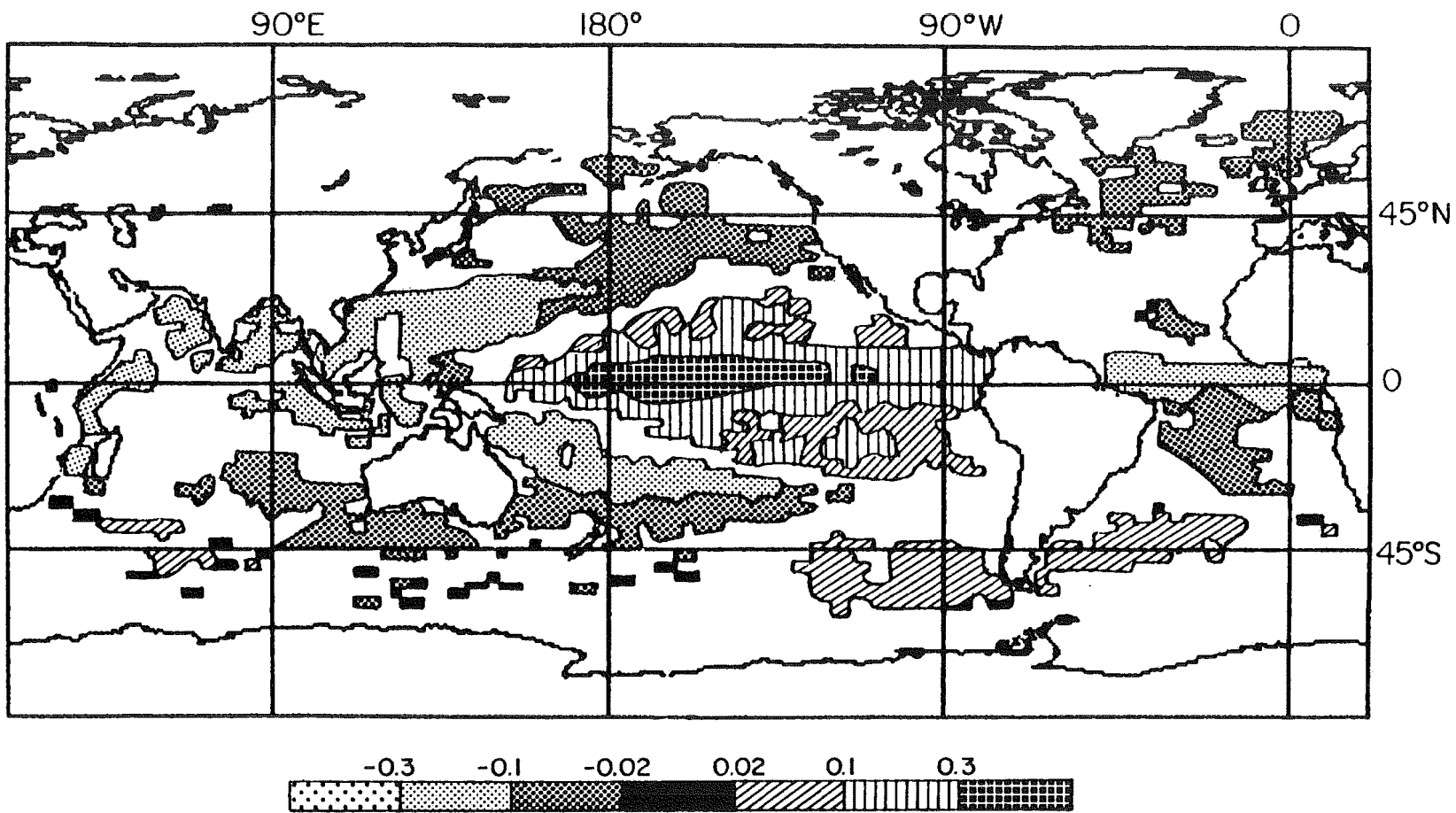


Figure C.4: A global plot of the LAD slope between total clear sky water vapor and the eastern tropical Pacific SSTA analyzed with the atmospheric variable leading 4 months ahead of the SSTA. Only grid points with a P-value of less than or equal to 0.05 are plotted. Units are $\text{cm}\cdot\text{K}^{-1}$. Based on data from July 1983 through June 1989.

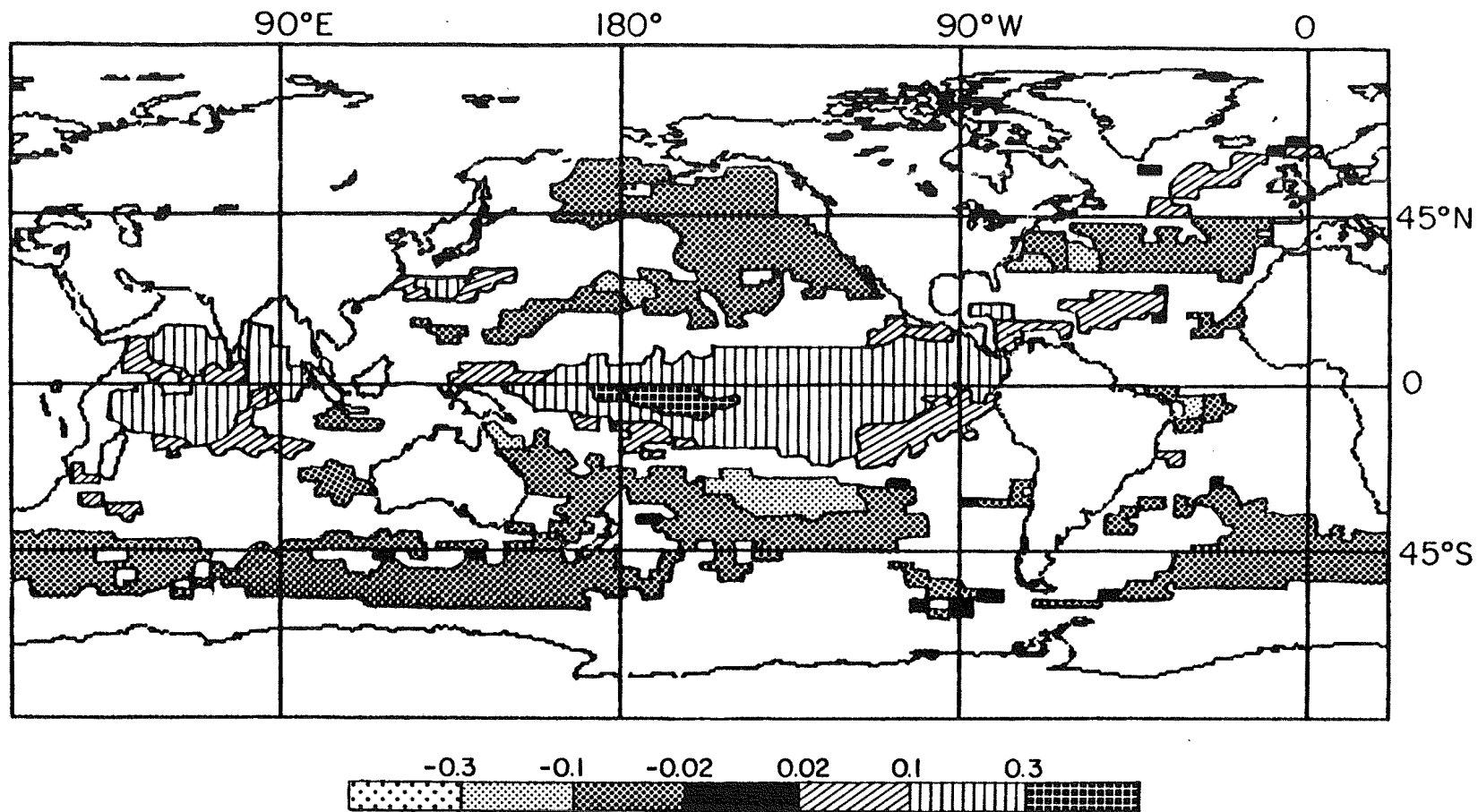


Figure C.5: A global plot of the LAD slope between total clear sky water vapor and the eastern tropical Pacific SSTA analyzed with the atmospheric variable lagging 4 months behind the SSTA. Only grid points with a P-value of less than or equal to 0.05 are plotted. Units are $\text{cm}\cdot\text{K}^{-1}$. Based on data from July 1983 through June 1989.

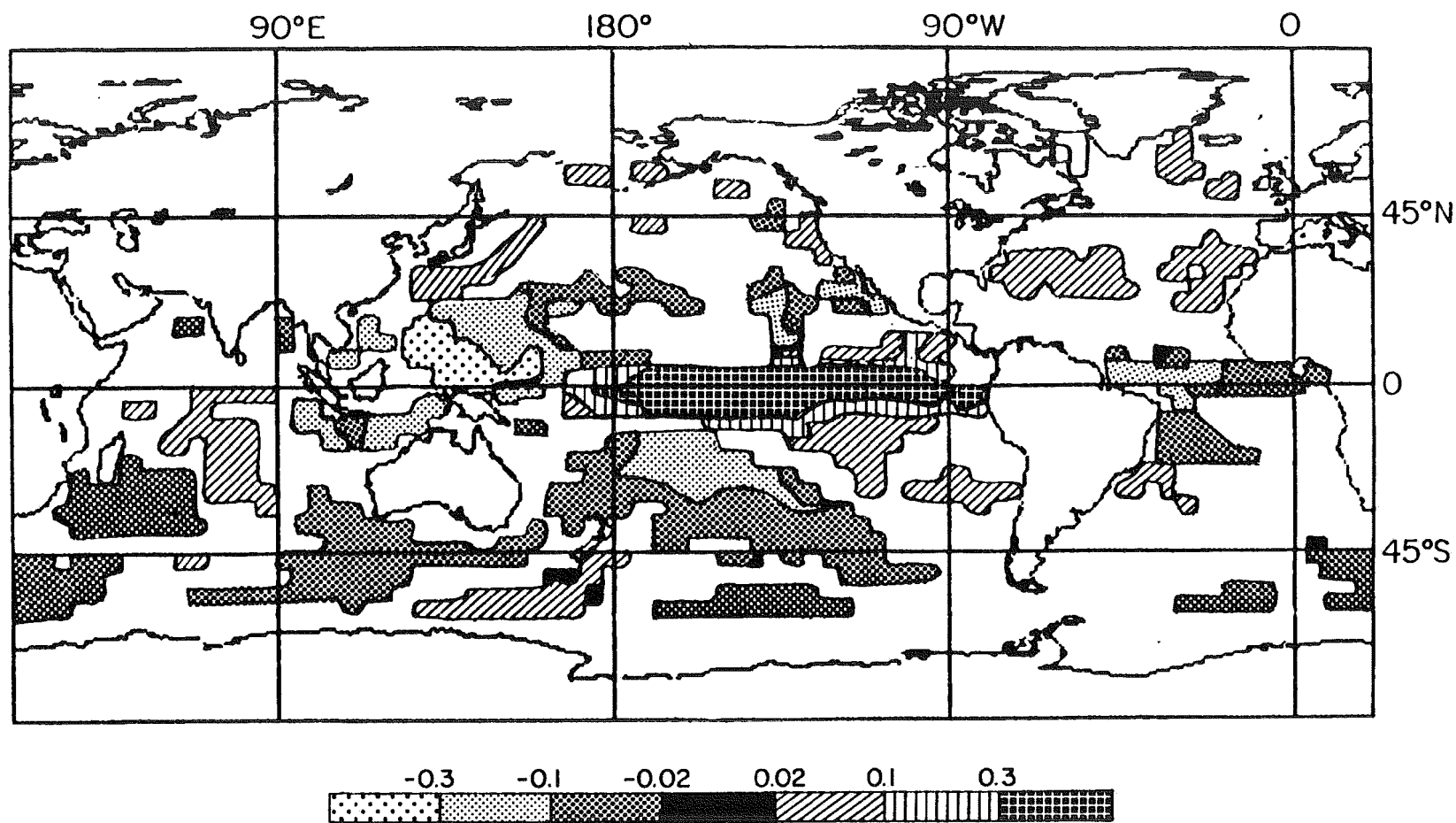


Figure C.6: A global plot of the LAD slope between total clear sky water vapor and the eastern tropical Pacific SSTA analyzed with the atmospheric variable lagging 2 months behind the SSTA. Only grid points with a P-value of less than or equal to 0.05 are plotted. Units are $\text{cm}\cdot\text{K}^{-1}$. Based on data from July 1983 through June 1989.

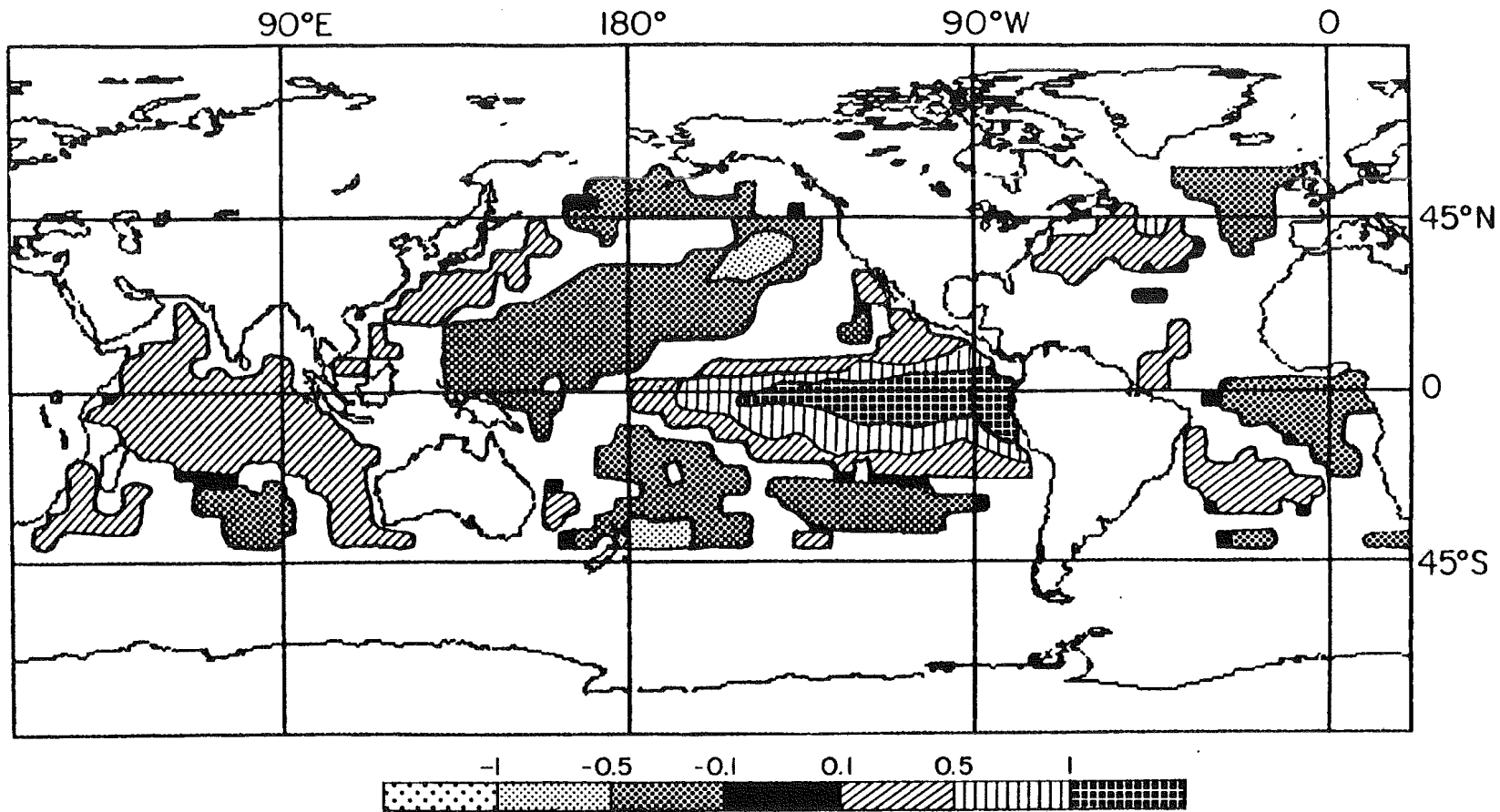


Figure C.7: A global plot of the LAD slope between global SSTA and the eastern tropical Pacific SSTA analyzed with the global SSTA lagging 2 months behind the eastern tropical Pacific SSTA. Only grid points with a P-value of less than or equal to 0.05 are plotted. Units are in change of $^{\circ}\text{C}$ of local SSTA per $^{\circ}\text{C}$ of eastern tropical Pacific SSTA. Based on data from April 1979 through March 1985, the time period corresponding to the Nimbus-7 cloud data set.

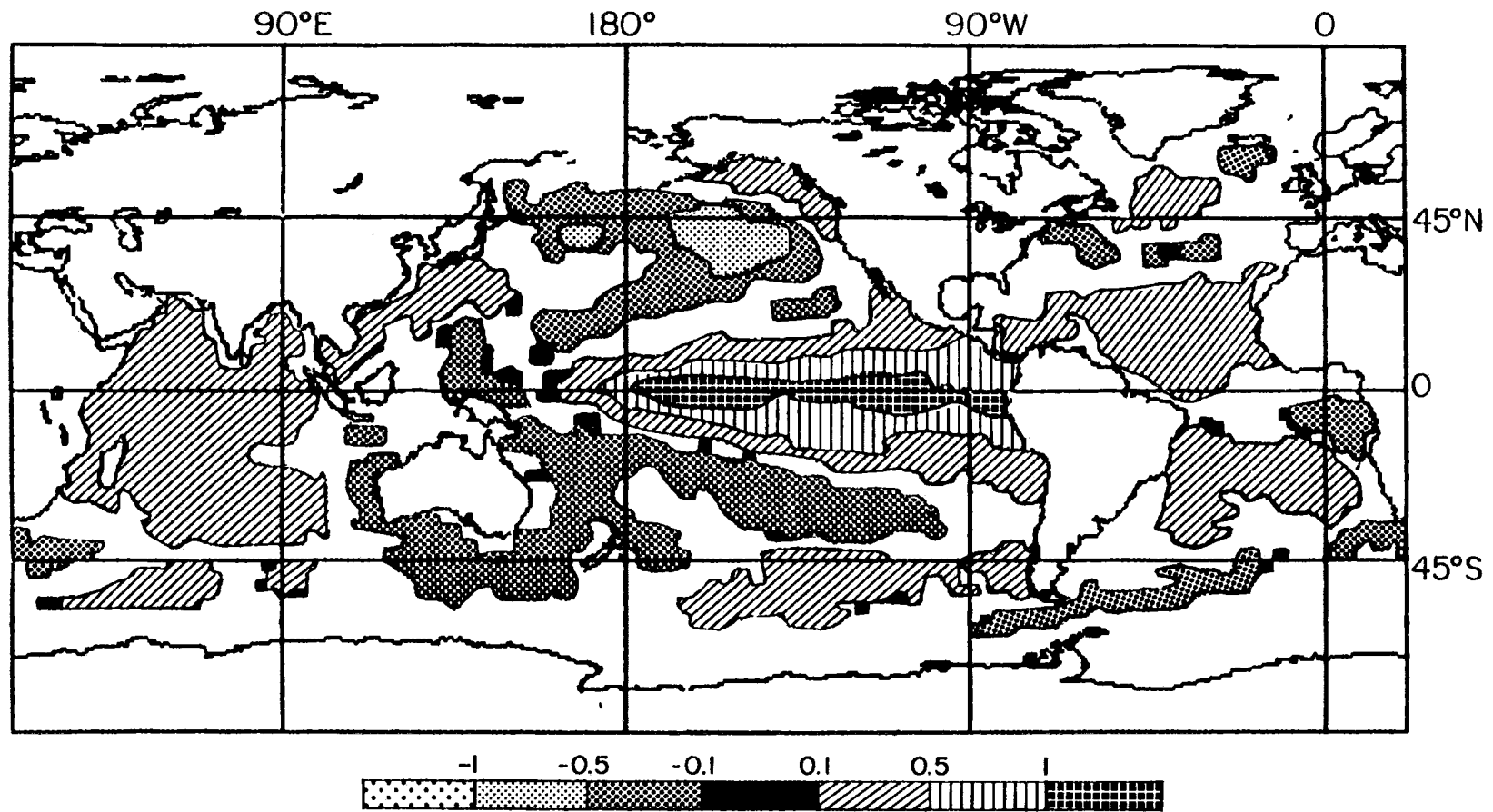


Figure C.8: A global plot of the LAD slope between global SSTAs and the eastern tropical Pacific SSTA analyzed with the global SSTA lagging 2 months behind the eastern tropical Pacific SSTA. Only grid points with a P-value of less than or equal to 0.05 are plotted. Units are in change of °C of local SSTA per °C of eastern tropical Pacific SSTA. Based on data from July 1983 through June 1989, the time period corresponding to the ISCCP TOVS water vapor data set.

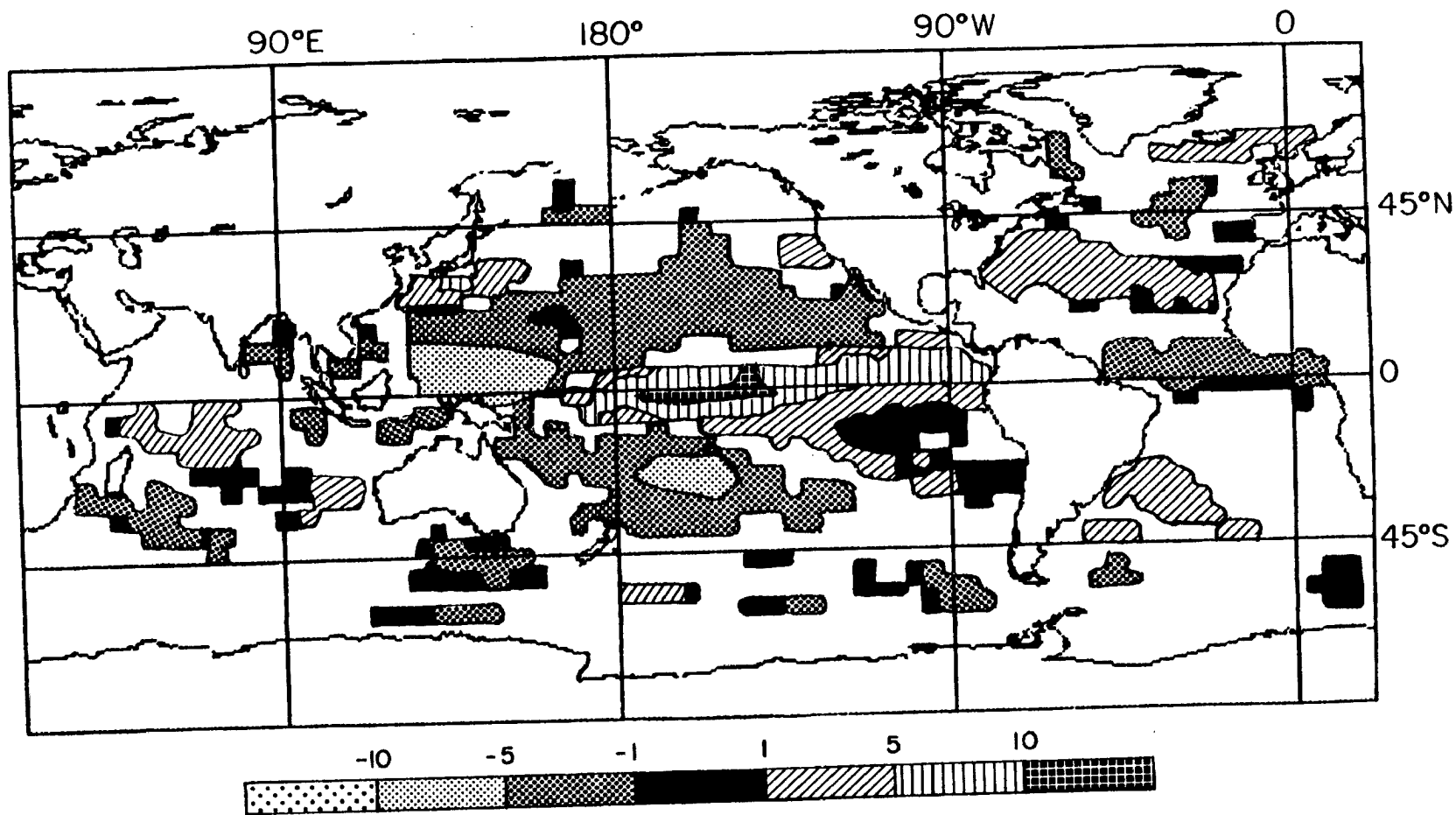


Figure C.9: A global plot of the LAD slope between high clouds and the eastern tropical Pacific SSTA analyzed with the atmospheric variable lagging 2 months behind the SSTA. Only grid points with a P-value of less than or equal to 0.05 are plotted. Units are $\% \cdot K^{-1}$. Based on data from April 1979 through March 1985.

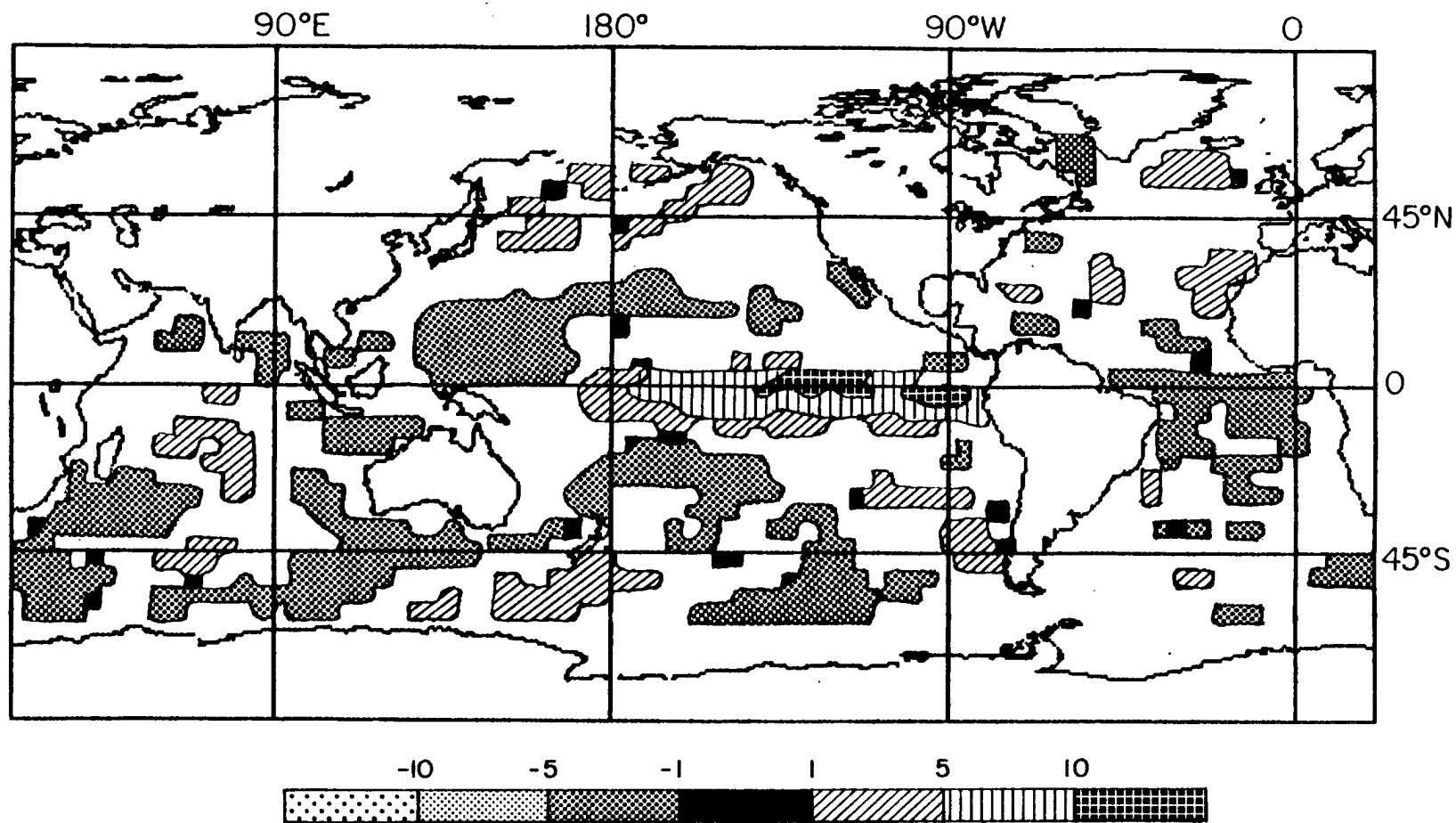


Figure C.10: A global plot of the LAD slope between middle clouds and the eastern tropical Pacific SSTA analyzed with the atmospheric variable lagging 2 months behind the SSTA. Only grid points with a P-value of less than or equal to 0.05 are plotted. Units are $\% \cdot K^{-1}$. Based on data from April 1979 through March 1985.

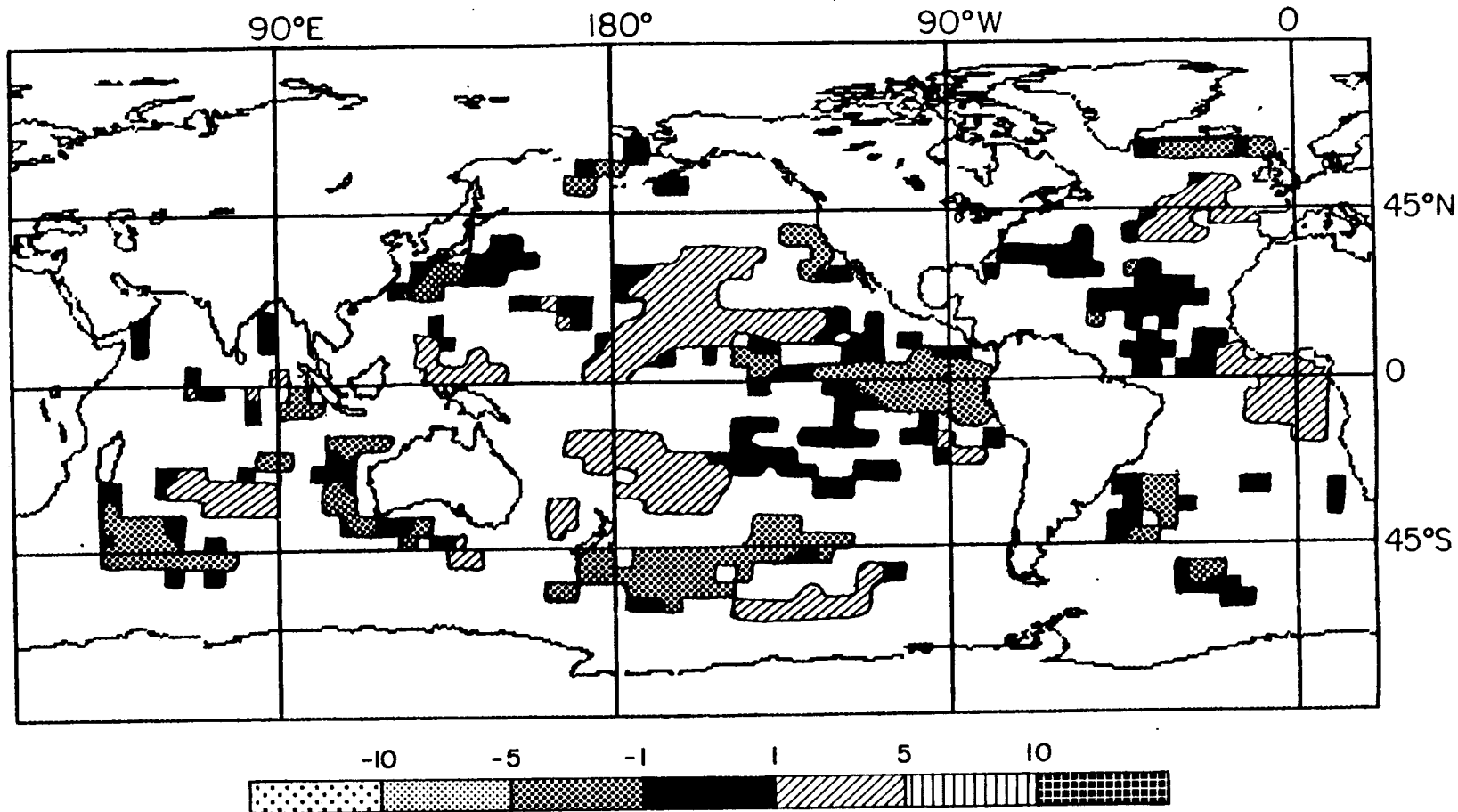


Figure C.11: A global plot of the LAD slope between low clouds and the eastern tropical Pacific SSTA analyzed with the atmospheric variable lagging 2 months behind the SSTA. Only grid points with a P-value of less than or equal to 0.05 are plotted. Units are $\% \cdot K^{-1}$. Based on data from April 1979 through March 1985.

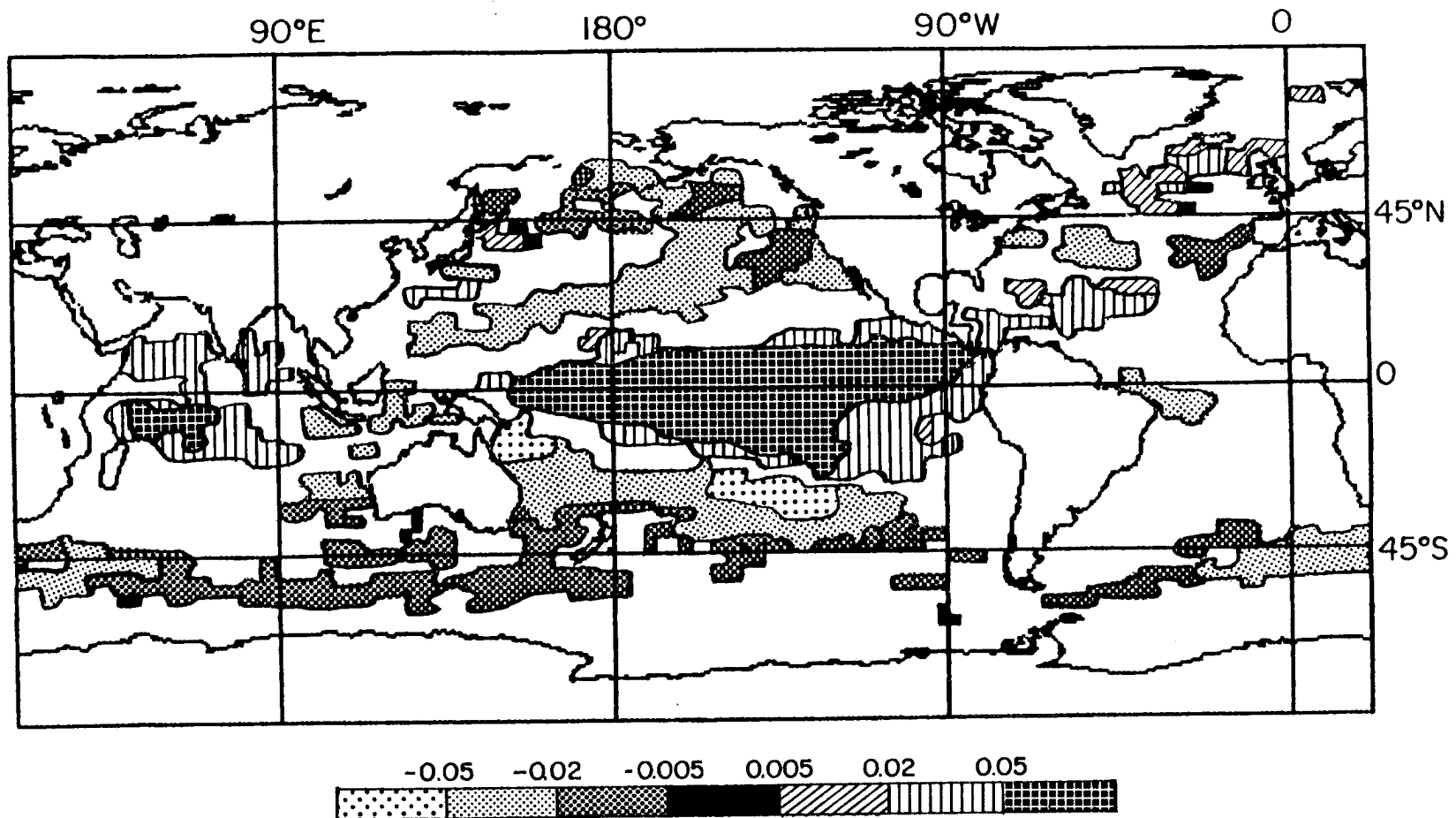


Figure C.12: A global plot of the LAD slope between high clear sky water vapor and the eastern tropical Pacific SSTA analyzed with the atmospheric variable lagging 2 months behind the SSTA. Only grid points with a P-value of less than or equal to 0.05 are plotted. Units are $\text{cm}\cdot\text{K}^{-1}$. Based on data from July 1983 through June 1989.

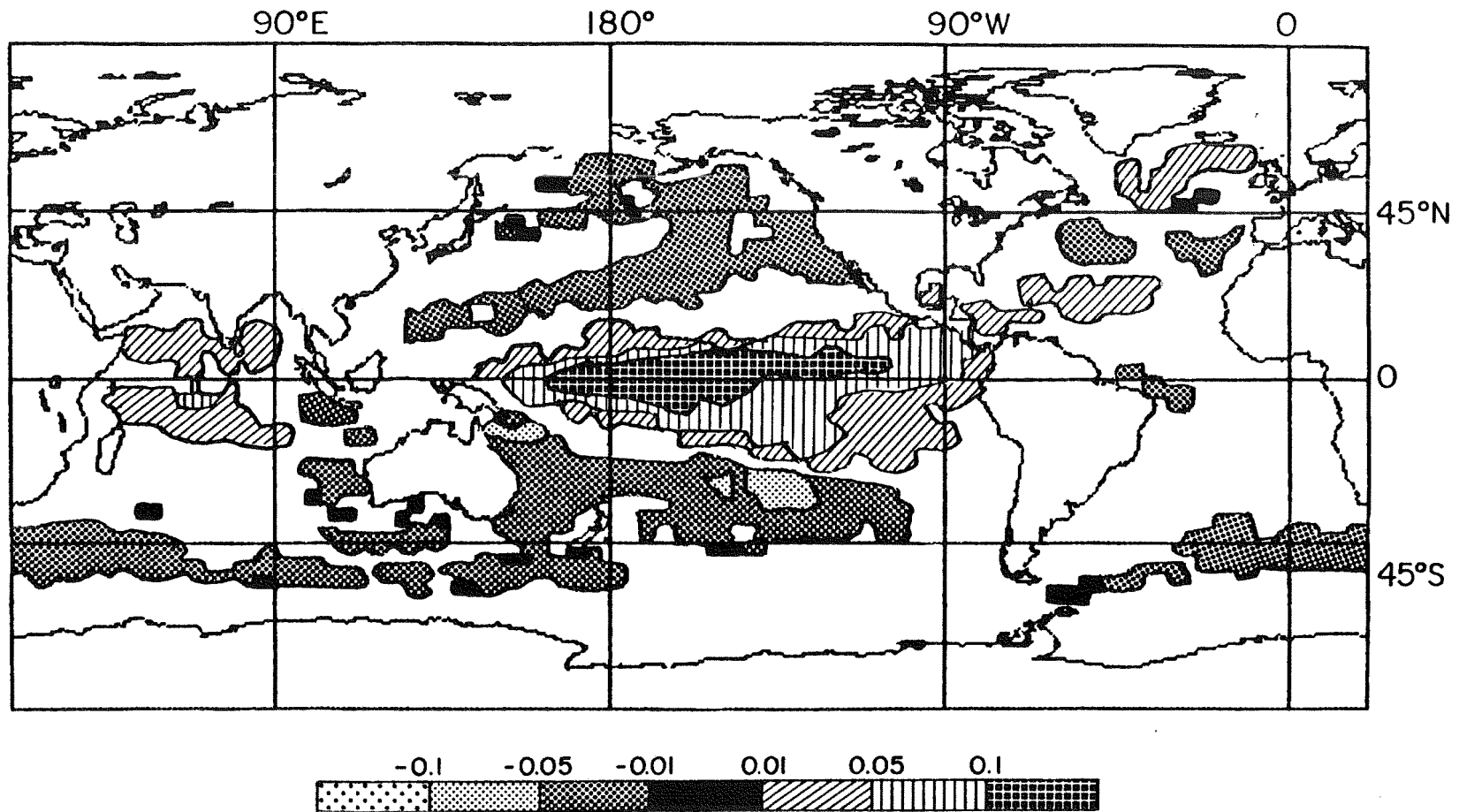


Figure C.13: A global plot of the LAD slope between middle level clear sky water vapor and the eastern tropical Pacific SSTA analyzed with the atmospheric variable lagging 2 months behind the SSTA. Only grid points with a P-value of less than or equal to 0.05 are plotted. Units are $\text{cm}\cdot\text{K}^{-1}$. Based on data from July 1983 through June 1989.

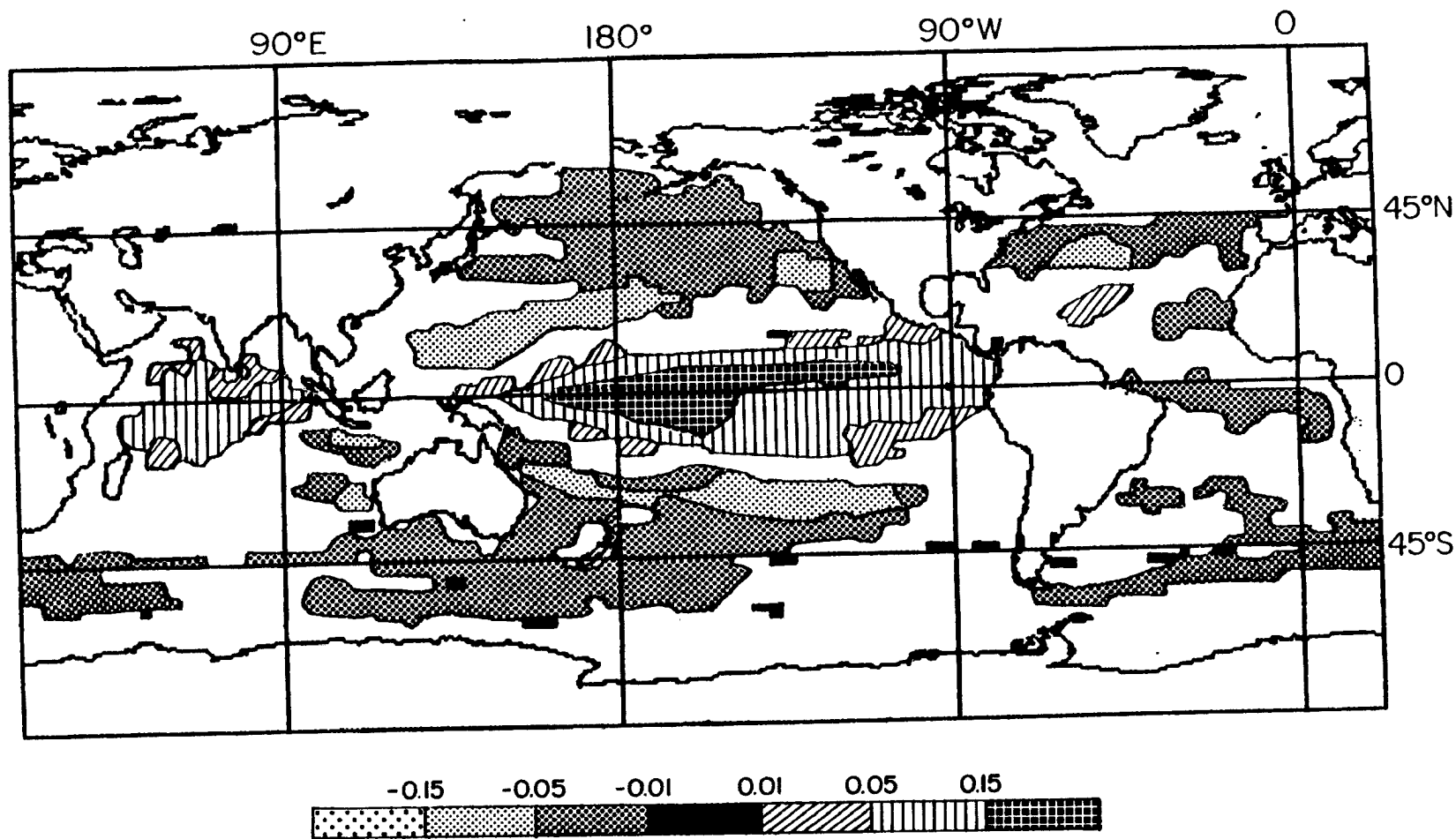


Figure C.14: A global plot of the LAD slope between low level clear sky water vapor and the eastern tropical Pacific SSTA analyzed with the atmospheric variable lagging 2 months behind the SSTA. Only grid points with a P-value of less than or equal to 0.05 are plotted. Units are $\text{cm}\cdot\text{K}^{-1}$. Based on data from July 1983 through June 1989.

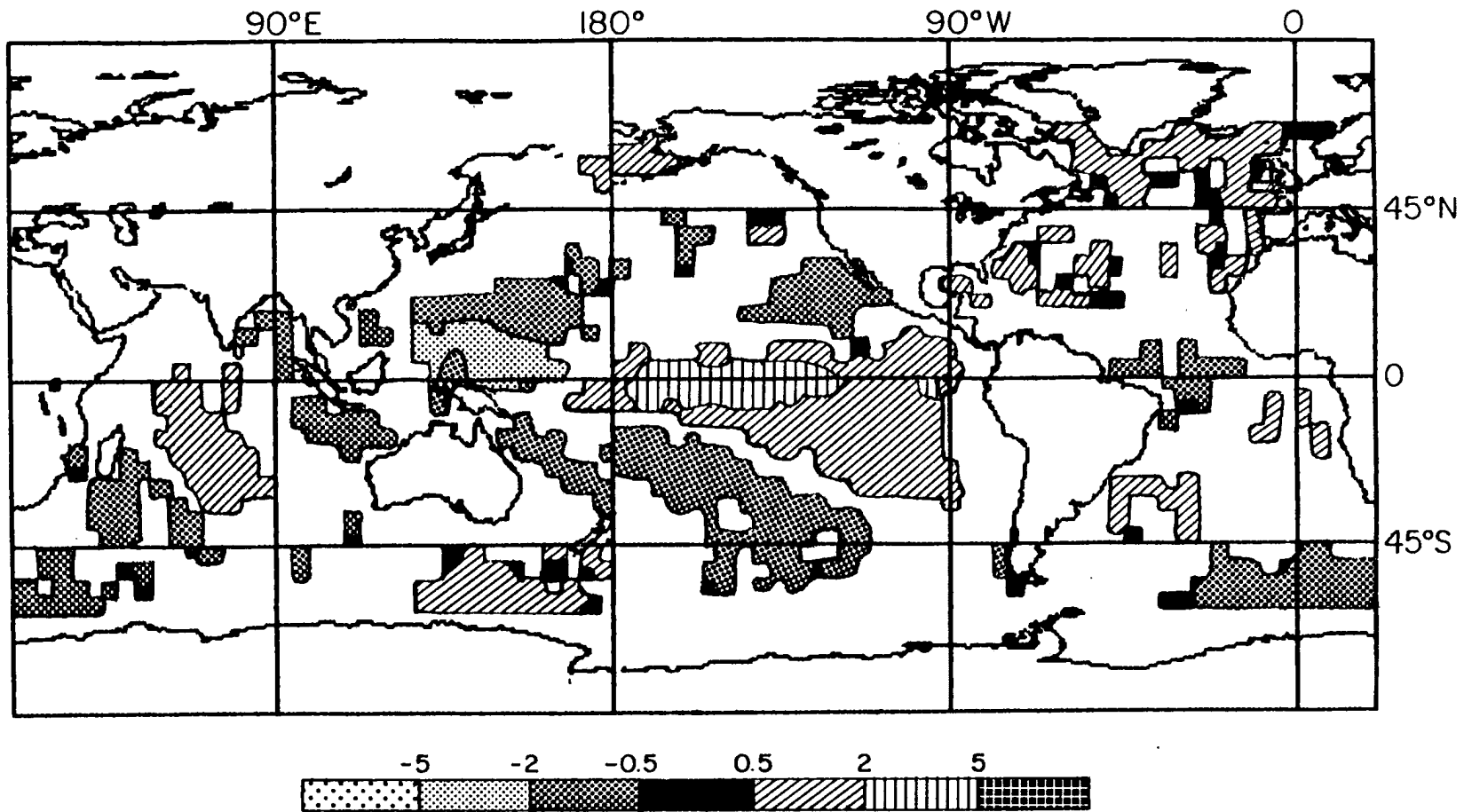


Figure C.15: A global plot of the LAD slope between albedo and the eastern tropical Pacific SSTA analyzed with the radiation variable lagging 2 months behind the SSTA. Only grid points with a P-value of less than or equal to 0.05 are plotted. Units are $\% \cdot K^{-1}$. Based on data from April 1979 through March 1985.

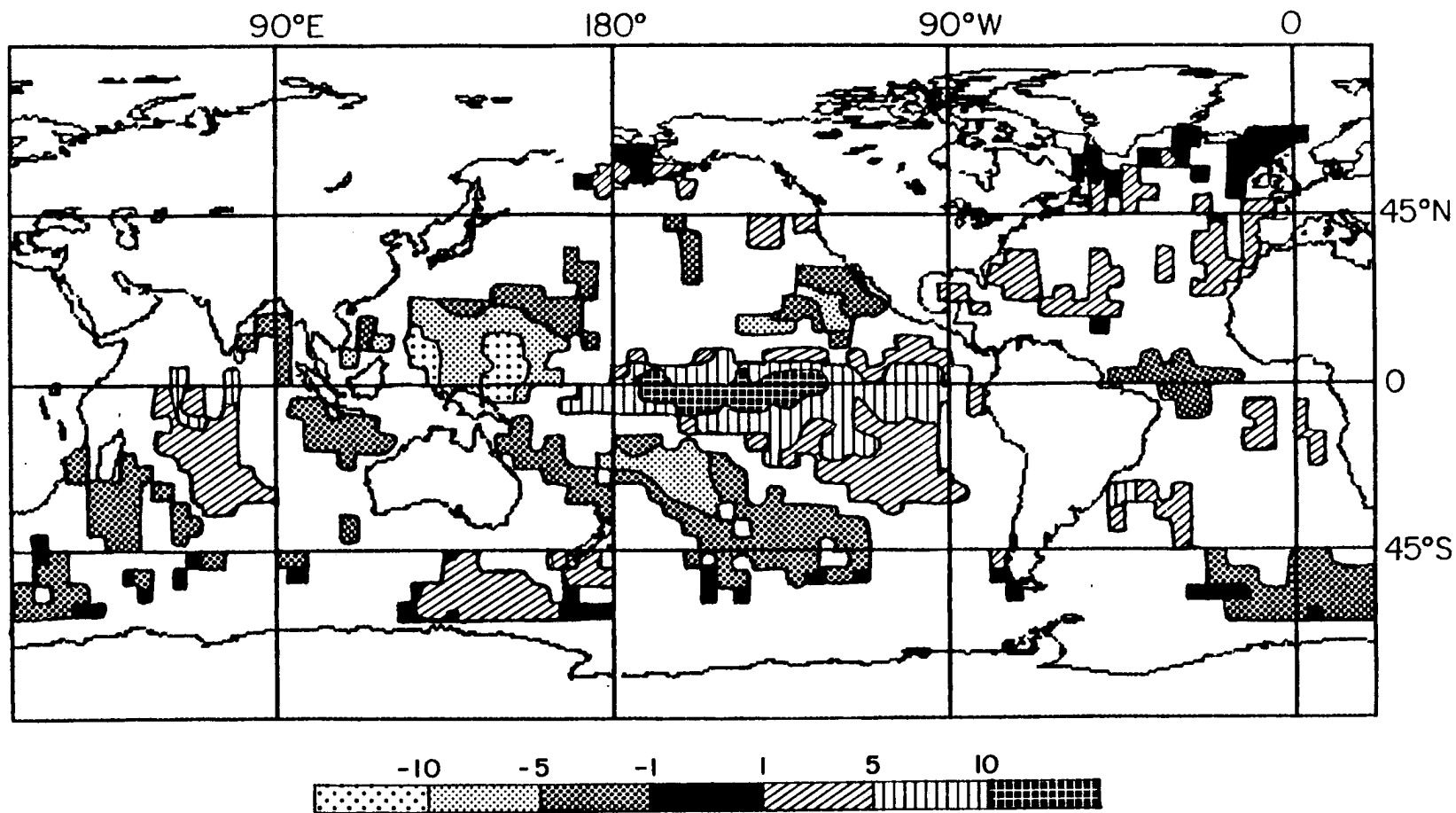


Figure C.16: A global plot of the LAD slope between reflected flux and the eastern tropical Pacific SSTA analyzed with the radiation variable lagging 2 months behind the SSTA. Only grid points with a P-value of less than or equal to 0.05 are plotted. Units are $\text{W}\cdot\text{m}^{-2}\cdot\text{K}^{-1}$. Based on data from April 1979 through March 1985.

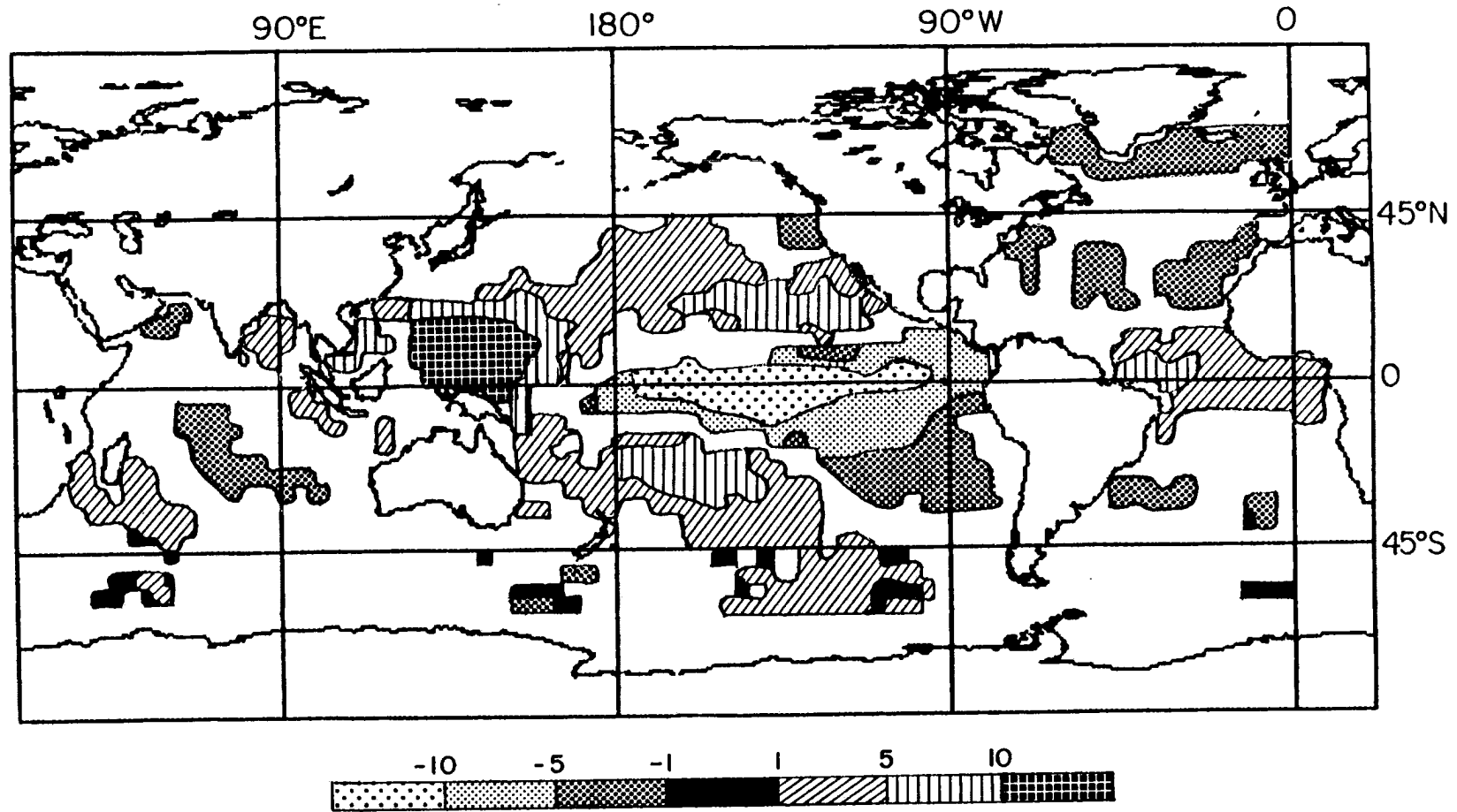


Figure C.17: A global plot of the LAD slope between OLR and the eastern tropical Pacific SSTA analyzed with the radiation variable lagging 2 months behind the SSTA. Only grid points with a P-value of less than or equal to 0.05 are plotted. Units are $W \cdot m^{-2} \cdot K^{-1}$. Based on data from April 1979 through March 1985.

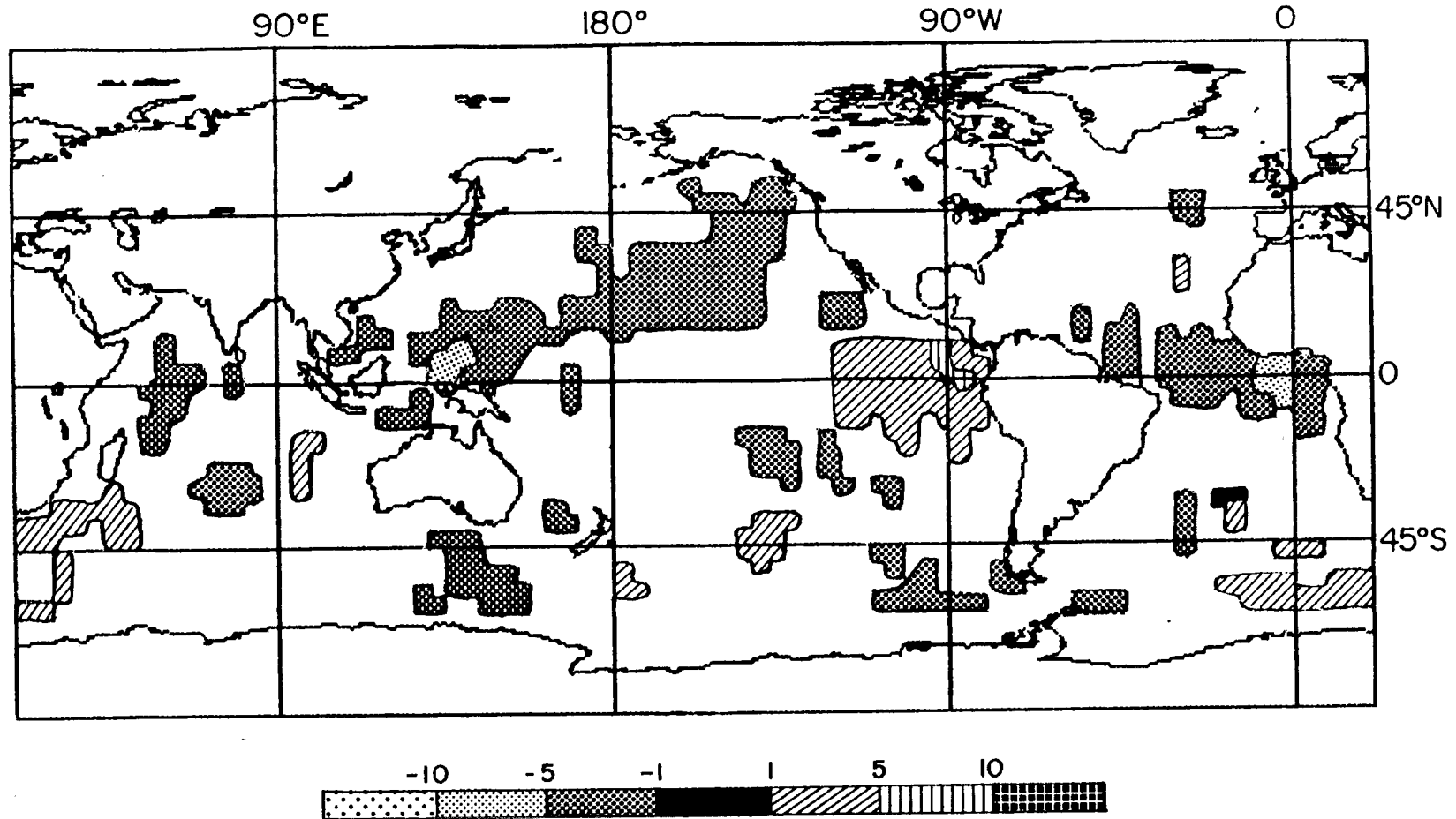


Figure C.18: A global plot of the LAD slope between net radiation and the eastern tropical Pacific SSTA analyzed with the radiation variable lagging 2 months behind the SSTA. Only grid points with a P-value of less than or equal to 0.05 are plotted. Units are $W \cdot m^{-2} \cdot K^{-1}$. Based on data from April 1979 through March 1985.